Investigation of Degradation Mechanisms of LSCF Based SOFC Cathodes — by CALPHAD Modeling and Experiments

Zhang, Weiwei; Barfod, Rasmus

Publication date:
2012

Document Version
Publisher's PDF, also known as Version of record

Investigation of Degradation Mechanisms of LSCF Based SOFC Cathodes — by CALPHAD Modeling and Experiments

Weiwei Zhang

Ph.D. Thesis

December 2012

Department of Energy Conversion and Storage

Technical University of Denmark

Academic advisors

Ming Chen, Senior Scientist

Department of Energy Conversion and Storage, Technical University of Denmark, DK-4000 Roskilde, Denmark

Peter Vang Hendriksen, Professor, Head of Programme

Department of Energy Conversion and Storage, Technical University of Denmark, DK-4000 Roskilde, Denmark

Rasmus Gottrup Barfod, Group Manager and Technology Supervisor

Topsoe Fuel Cell, DK-2800 Lyngby, Denmark

Acknowledgements

My first debt of gratitude must go to my principal supervisor, Dr. Ming Chen. He patiently provided the vision, encouragement and advice necessary for me to proceed through the PhD project and complete my dissertation, which led to my successful Ph.D. study at DTU. I would like to express my heartfelt gratitude to my co-supervisors, Prof. Peter Vang Hendriksen and Dr. Rasmus Barfod. I have benefited greatly from them for academic guidance, financial support and all kinds of helps.

Many thanks to Dr. Erwin Povoden-Karadeniz and Prof. Ernst Kozeschnik at Institute of Materials Science and Technology, Vienna University of Technology, for accepting me as a visiting student during 22 Feb. to 18 Mar., 2012, in Austria. I have benefited greatly from the suggestions and helps from Erwin on thermodynamic modeling of the oxide systems. And I am grateful for the chance to visit the laboratory. I also would like to thank Dr. James E. Saal, Mei Yang and Prof. Zi-Kui Liu in the Penn State University for providing thermodynamic database for discussion.

The financial support from HyFC – The Danish Hydrogen and Fuel Cell Academy and Topsoe Fuel Cell A/S is acknowledged. I am grateful for the support from STT foundation and CALPHAD scholarship for attending conferences.

It has been a great privilege to spend three years in the Department of Energy Conversion and Storage at DTU (previously Fuel Cells and Solid State Chemistry Division, Risø National Laboratory for Sustainable Energy), and colleagues here will always remain dear to me. Huge credit to former and present colleagues, Ruth, Jason, Karl, Ebtisam, Ragnar, Kion …. Their hard work made my study here without a hitch. My friends in Denmark, China and other parts of the world were sources of joy, inspiration and support. Special thanks go to Lei, Mingyuan, Alfred, Xiaoming, Na, Qiang, Jing... I could not complete my work without their invaluable friendship and assistance.

Finally, my warmest appreciation is sent to my family – thank you for your endless support and love! It means everything that you always believe in me!

Abstract

LSCF ($La_{1-x}Sr_xCo_{1-y}Fe_yO_{3-\delta}$) is a promising cathode material for intermediate temperature SOFCs (Solid Oxide Fuel Cells). However, the LSCF cathode degrades over an extended period of time. The processes that play a dominant role for the degradation and their relation to cell durability have not been fully understood at the moment. With the developments of computer software and thermodynamic databases, advances have been made in calculating complex phase equilibria and predicting thermodynamic properties of the materials. In order to identify physicochemical degradation mechanisms of LSCF cathodes, investigation of the La-Sr-Co-Fe-O system using computational thermodynamics and designed key experiments was carried out in this work.

The first part of the research work was devoted to establish a self-consistent thermodynamic database of relevant components (La-Sr-Co-Fe-O) using the CALPHAD (CALculation of PHAse Diagrams) approach. Published thermodynamic databases and experimental data related to the La-Sr-Co-Fe-O system were critically reviewed. The thermodynamic descriptions of the La-Co-O, Sr-Co-O and La-Sr-Co-O systems were further improved in order to construct the present thermodynamic database for LSCF, while new thermodynamic modeling of the Co-Fe-O, Sr-Co-Fe-O and La-Sr-Co-Fe-O systems was performed in this work. Calculated phase equilibria in LSCF as functions of composition, temperature, oxygen partial pressure are discussed by comparing with experimental data. Based on the developed thermodynamic database, the "stability windows" of LSC ($La_{1-x}Sr_xCoO_{3-\delta}$) and LSCF are predicted and presented in *Chapter 5* and *Chapter 6*, respectively. Calculations show that the perovskite phase is stable at high La and Fe content and high oxygen partial pressure. The stability of the perovskite phase is in the trend of LSC<LSCF<LSF. Outside its "stability window", decomposition or partial decomposition of the perovskite phase takes place. Different secondary phases form under different conditions (temperature, oxygen partial pressure, composition). Taking LSC as an example, the decomposition of the perovskite phase is accompanied with formation of $(La,Sr)_2CoO_4$ at low oxygen partial pressure, or $Sr_6Co_5O_{15}$ at low temperature, or $Sr_2Co_2O_5$ at high Sr content at around 1000°C. With the thermodynamic database, capability of calculating other properties of

the LSCF perovskite, such as oxygen non-stoichiometry and cation distribution was also demonstrated.

Experimental investigations on phase stability of LSC, LSCF and LSCF/CGO composites, and applications of the thermodynamic database on analyzing the phase stability are described in the second part of this thesis. An inter-diffusion between LSCF and CGO was detected. The inter-diffusion of La and Ce/Gd between the two phases was further observed to be accompanied by a formation of a halite secondary phase in N_2. In addition, it was found that Sr diffuses out of LSCF (i.e. surface segregation), and further reacts with impurities. This phenomenon was observed even at 700°C.

In the last part of this thesis, characterization techniques including Scanning Electron Microscopy (SEM), Secondary ion mass spectroscopy (SIMS) and Transmission Electron Microscopy (TEM) were applied on a tested as well as an "as prepared" LSCF/CGO ($Ce_{1-x}Gd_xO_{2-\delta}$) composite cathode, in order to reveal the origins of the cell degradation. Issues including LSCF stability, Sr diffusion, LSCF−CGO interaction and impurity segregation were examined. The results show that partial phase separation of LSCF happens mainly at the interface with the CGO barrier layer. The inter-diffusion across the LSCF/CGO cathode – CGO barrier layer interface and the CGO barrier layer – YSZ electrolyte interface happened mainly during sintering, and only to little degree while long-term SOFC testing, and therefore shall not be counted as a major degradation mechanism. The observed Cr enrichment is a likely contributor to the observed electrical degradation whereas the consequences of the increasing sub-micron inhomogeneity are not yet known. The diffusion of Sr through the CGO barrier layer and formation of Sr-Zr phases at the CGO−YSZ interface further contribute to the long term degradation.

Dansk resumé

LSCF ($LA_{1-x}Sr_xCo_{1-y}Fe_yO_{3-\delta}$) er et lovende katodemateriale til lavtemperatur SOFC (Solid Oxide Fuel Cells). Imidlertid nedbrydes LSCF katoden over en længere periode. Indtil videre er nedbrydningsmekanismerne tvetydige. De processer, der spiller en dominerende rolle for nedbrydningen i forhold til stabel holdbarhed er ikke fuldt ud forstået i øjeblikket. Med udviklingen af computer-programmer og termodynamiske databaser, er der sket fremskridt indenfor beregning af komplekse faseligevægte og forudsigelse af materialernes termodynamiske egenskaber. For at identificere de fysisk-kemiske nedbrydningsmekanismer af LSCF, er undersøgelse af La-Sr-Co-Fe-O systemet ved hjælp af beregningsmæssig termodynamik samt design af nøgleeksperimenter blevet udført i denne afhandling.

Den første del af forskningsarbejdet var afsat til at etablere en selvkonsistent termodynamisk database af relevante komponenter (La-Sr-Co-Fe-O) ved hjælp af CALPHAD (beregning af fasediagrammer) tilgang. Offentliggjorte termodynamiske databaser og eksperimentelle data relateret til La-Sr-Co-Fe-O-systemet blev kritisk gennemgået. Den termodynamiske beskrivelse af La-CO-O, Sr-Co-O-og La-Sr-Co-O-systemer blev yderligere forbedret for at konstruere den foreliggende termodynamiske database for LSCF, mens ny termodynamisk modellering af Co-Fe-O, Sr-Co-Fe-O-og La-Sr-Co-Fe-O-systemer blev udført i dette arbejde. Beregnede faseligevægte af LSCF som funktioner af komposition, temperatur, partialtryk af ilt blev drøftet ved sammenligning med eksperimentelle data. Baseret på den udviklede termodynamiske database, blev "stabilitets vinduer" for LSC ($LA_{1-x}Sr_xCoO_{3-\delta}$) og LSCF forudsagt og præsenteret i henholdsvis kapitel 5 og kapitel 6. Beregninger viser, at perovskit fasen er stabil ved højt La og Fe-indhold samt højt partialtryk af oxygen. Stabiliteten af perovskit fasen følger tendensen i LSC <LSCF <LSF. Udenfor sit "stabilitets vindue", finder nedbrydning eller delvis nedbrydning af perovskit fasen sted. Forskellige sekundære faser dannes under forskellige betingelser (temperatur, partialtryk af oxygen, sammensætning). Med LSC som eksempel, er nedbrydningen af perovskit fasen ledsaget af dannelse af $(La, Sr)_2CoO_4$ ved lavt oxygenpartialtryk, eller $Sr_6Co_5O_{15}$ ved lav temperatur, eller $Sr_2Co_2O_5$ ved højt Sr indhold ved omkring 1000 °C. Med den

termodynamiske database, blev evnen til at beregne andre egenskaber af LSCF perovskite, såsom ikke-støkiometri af oxygen og kation fordeling, også vist.

I anden del af denne afhandling beskrives eksperimentelle undersøgelser af fasestabilitet for LSC, LSCF og LSCF / CGO kompositer, samt anvendelse af den termodynamiske database til at analysere fasestabilitet. Inter-diffusionen mellem LSCF og CGO blev opdaget. Udtyndingen af La fra LSCF forårsagede dannelse af en Co rig fase med lavt oxygenpartialtryk, hvilket er i overensstemmelse med beregningsresultatet. Desuden blev det konstateret, at Sr diffunderer ud af LSCF (dvs. overfladeadskillelse), som yderligere reagerer med urenheder fra atmosfæren. Dette fænomen blev observeret selv ved 700 °C.

I den sidste del af denne afhandling, blev hybridteknikker, inkluderende Scanning Electron Microscopy (SEM), sekundær ion-massespektroskopi (SIMS) og Transmission Electron Microscopy (TEM), anvendt på både en afprøvet samt en reference LSCF / CGO ($CE_{1-x}Gd_xO_{2-\delta}$) sammensat katode, for at finde oprindelsen af cellens nedbrydning. Emner indenfor, LSCF stabilitet, Sr diffusion, LSCF-CGO interaktion og urenheds adskillelse blev undersøgt. Resultaterne viser, at delvis nedbrydning (eller faseadskillelse) af LSCF hovedsageligt sker ved grænsefladen med CGO barrierelaget. Inter-diffusionen gennem LSCF / CGO katode - CGO barrierelag interface og CGO barrierelaget - YSZ elektrolytgrænseflade, skete hovedsagelig under sintring, og til en meget lille grad, under SOFC tests over længere tid, og skal derfor ikke anses som en betydelig nedbrydningsmekanisme. Nedbrydningen af LSCF / CGO komposit SOFC katoden kan tilskrives manglende stabilitet af LSCF, som er forårsaget af flere aspekter, bl.a. sammensætningsmæssige ændringer under sintring med CGO, Sr udtømning, faseadskillelse induceret af reduktion af lokalt oxygenpartialtryk grundet overpotential. Diffusionen af Sr gennem CGO barrierelaget og dannelse af Sr-Zr faser ved CGO-YSZ-grænsefladen bidrager yderligere til den langsigtede nedbrydning.

Contents

Chapter 1

Introduction

In this chapter, the research background including the concepts of solid oxide fuel cells (SOFCs) and LSCF-based cathodes are introduced. The motivation for the present PhD project is presented together with a critical literature survey. A hybrid method of CALPHAD modeling combined with experimental validation, which was used in the present thesis, is introduced. Finally the structure of this PhD thesis is presented in the last section of this chapter.

1.1 Research Background

Solid oxide fuel cell (SOFC) is an electrochemical device that converts chemical energy (in the form of, e.g., natural gas, hydrogen, biogas, ammonia or methanol) into electricity and heat by electrochemical reactions on the two electrodes separated by an oxide ion conducting electrolyte [1]. As compared to the traditional ways of generating electrical power, SOFC has several advantages such as high efficiency, clean and low noise operation *etc*. An SOFC comprises at least three layers (as shown in Fig. 1.1): a porous anode and a porous cathode, with a dense electrolyte in between. During operation, an oxidant (oxygen or air) is fed to the cathode where a reduction reaction takes place, forming O^{2-} which can migrate through the electrolyte to the anode side, while fuel (e.g. hydrogen) is fed to the anode side and is oxidized by O^{2-}. In addition to these three functional layers, an SOFC may also contain a support layer and contact layer(s) [3].

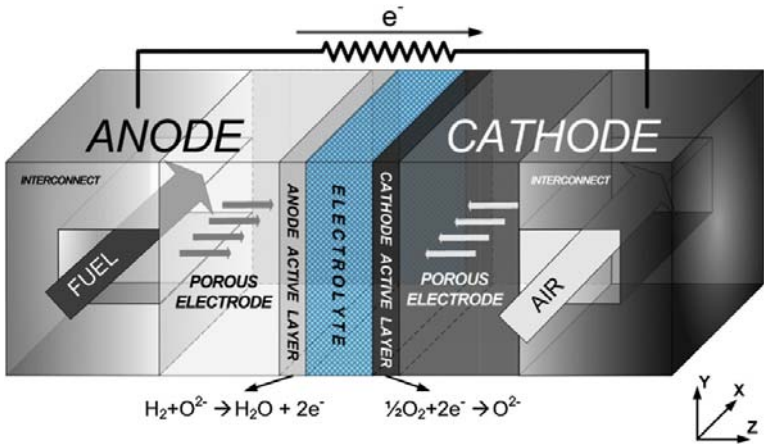

Fig. 1.1 An illustration of SOFC by Tseronis *et al.* [2].

Single SOFCs need to be stacked in series connected by interconnects to achieve practically useful voltages [3]. Normally, SOFCs operate at temperatures from 600°C to 1000°C, where the electrochemical reactions are sufficiently fast and the ionic or electronic transport is high enough in the layers. To compete with other electricity generation technologies, the main research interests in SOFC technology are [3]: 1) Cost reduction. 2) Lowering operating temperature, but still maintaining high performance (power density, efficiency *etc.*). 3) Increasing durability and reliability. If the operation temperature can be lowered, less expensive material can be used in the SOFC stack increasing likelihood of commercialization of the SOFC technology. However, with reducing temperature, the electrochemical activity of the cathode is severely decreased for

conventional LSM ($La_{1-x}Sr_xMnO_3$) cathodes [4, 5]. Strontium and iron co-doped lanthanum cobaltite (LSCF, $La_{1-x}Sr_xCo_{1-y}Fe_yO_{3-\delta}$) cathode material was developed to enable SOFC applications at intermediate temperature (600−800°C) [4, 6].

LSCF with the perovskite structure is a mixed oxide ion and electron conductor. It has attracted a lot of research interests and is currently being developed by many SOFC consortia around the world. It shows good conductivity and electro-catalytic activity at T < 700 °C (temperatures where cheap metallic interconnects can be safely used) and is recognized as one of the promising cathode materials for intermediate temperature SOFCs. Compared to pure LSCF, LSCF/CGO (gadolinium doped ceria) composite exhibits higher oxygen diffusion and surface exchange rates [7, 8, 9] and is therefore a preferred cathode currently [5].

The use of LSCF cathodes is however problematic when it is applied on the state of the art YSZ (Yittria Stabilized Zirconia) electrolyte. It has been reported in many studies that a direct contact between the LSCF cathode and the YSZ electrolyte leads to formation of insulating strontium zirconate [10, 11], resulting in failure of SOFCs. Ceria based material has been proven to be compatible with LSCF [12]. Introducing a CGO barrier layer between the YSZ electrolyte and the LSCF (or LSCF/CGO) cathode was suggested in many publications [13−14] in order to prevent or suppress the undesired reactions. The type of SOFC, which has a Ni/YSZ anode, a YSZ electrolyte, a LSCF cathode, and a CGO barrier layer between the electrolyte and the cathode and which is often referred as IT-SOFC (intermediate temperature-SOFC), has attracted a great deal of interests recently, due to its excellent initial performance at intermediate temperature [4−6]. Fig. 1.2 [15] shows a SEM image on the cross-section of such typical IT-SOFC.

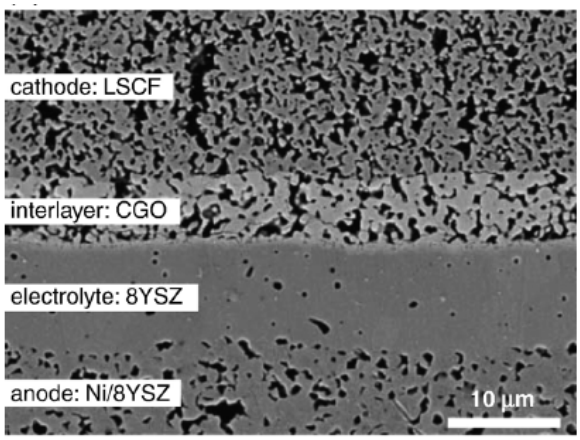

Fig. 1.2 SEM image on the cross-section of a typical IT-SOFC by Mai *et al.* [15].

1.2 Motivation

Durability is one of the critical issues in commercializing the SOFC technology. A lifetime of at least 40000 h is required for commercial SOFCs [16], corresponding to a degradation rate of less than 1% per 1000h. The IT-SOFCs show great initial performance at intermediate temperature [4−6]. However, the cells are not sufficiently stable and they degrade over extended periods of time [15−18]. Degradation originated from the cathode side has been reported as one of the major degradation mechanisms for IT-SOFCs by various groups [15−18]. Knibbe *et al.* [19] reviewed degradation of SOFCs with LSCF or LSCF/CGO cathodes from both their own studies and those from literature. The degradation rate in mΩ·cm^2/1000 h was evaluated from polarization or impedance measurements, assuming that the cell OCV (open circuit voltage) remained constant during long term testing. All the reported degradation rates are much higher than the commercially desired one of 4 mΩ·cm^2/1000 h. It was found that the reported cell voltage degradation rate (mV/1000 h) is strongly dependent on the cell operating conditions (temperature, atmosphere, current density and fuel utilization *etc.*). However, no clear relation between the degradation rate and the test conditions can be concluded. Instead, contradictory findings exist in the literature. Mai *et al.* [15] and Becker [20] showed that the cells degraded more severely at higher temperature (800°C) and pointed this to thermally activated degradation. In a recent study by Endler *et al.* [21], carried out at OCV and 600, 750, and 900 °C, an increased LSCF degradation with decreasing temperature was reported. Mai *et al.* [15] and Becker [20] also reported that a decreased oxygen partial pressure (from P_{O_2} = 0.21 atm to 0.05 atm) resulted in a slightly lower degradation rate, but current density did not have a clear influence on the cell degradation.

As discussed above, the degradation of IT-SOFCs with LSCF or LSCF/CGO cathodes has been extensively studied in various different conditions. The mechanism or the origin of the degradation is unclear at the moment, even though a few assumptions have been proposed [18−58]. Below various fundamental issues associated with durability of the IT-SOFCs are reviewed, focusing on the oxygen electrode side.

1) Decomposition of the cathode material

Phase stability of LSCF is an important issue for its application in SOFC and is also a complex issue to clarify, due to complexity of phase relationship in La-Sr-Co-Fe-O. The stability of the

LSCF perovskite depends strongly on its composition, temperature, oxygen partial pressure, steam partial pressure (humidity) *etc.*

Hashimoto and Kuhn *et al.* [22, 23] studied oxygen non-stoichiometry and phase stability of $La_{0.6}Sr_{0.4}Co_{1-y}Fe_yO_{3-\delta}$ (y=0.2, 0.4, 0.5, 0.6 and 0.8). They found $La_{0.6}Sr_{0.4}Co_{0.8}Fe_{0.2}O_{3-\delta}$ decomposed completely at low oxygen partial pressure (ca. 10^{-6} bar at 1073K), forming the A_2BO_4 phase and CoO. They concluded that the stability of $La_{0.6}Sr_{0.4}Co_{1-y}Fe_yO_{3-\delta}$ decreases with increasing the Co content. Natile *et al.* [24] reported formation of La_2CoO_4 and Co metal after reduction of LSCF in H_2 at 800 °C. Lein *et al.* [25] studied the stability of the $La_{0.5}Sr_{0.5}Fe_{1-x}Co_xO_{3-\delta}$ membranes with O_2 on the primary side and N_2 on the secondary side at 1150˚C for 1 month. On the N_2 side, no phase change to the original perovskite phase was detected. On the O_2 side, formation of new secondary phases was observed: cobalt oxide for LSC and LSCF membranes and $SrFe_{12}O_{19}$ for LSF membranes. Iguchi *et al.* [26] analyzed the cross sections of tested LSCF membranes using in-situ Raman scattering techniques together with SEM/EDX. They reported decomposition on the air side. SrO and $CoFe_2O_4$ porous layer, and La_2O_3- or SrO-rich regions were observed. As no structure (e.g. XRD) analysis was performed on the reference (as-produced) sample, it is difficult to conclude whether formation of secondary phases was caused by testing or actually due to material inhomogeneity already in the as-produced sample.

LSC is much less stable than LSCF. Morin *et al.* [27] found that the $La_{0.5}Sr_{0.5}CoO_{3-\delta}$ (LSC50) perovskite already decomposed at oxygen partial pressure of 10^{-2} atm at 1360 °C by forming $(La,Sr)_2CoO_4$ and a Co rich phase (halite). The decomposition temperature of LSC50 at low oxygen pressure was determined using High-temperature X-ray diffraction (HT-XRD). Saal [28] studied stability of LSC at 900°C, 1100°C and 1300°C under various PO_2 (10^{-4}–10^{-1} atm). The result shows that LSC is not stable at high Sr content and low PO_2. At 1100°C, the perovskite phase decompose at PO_2<10^{-3} atm. Different secondary phases formed at different temperatures. Ovenstone *et al.* [29] investigated phase transition/decomposition of $La_{1-x}Sr_xCoO_{3-\delta}$ (x=0.7, 0.4, 0.2) at low oxygen partial pressure using HT-XRD. Decomposition of perovskite into $(La,Sr)_2CoO_4$, CoO and $Sr_2Co_2O_5$ was detected when held in PO_2 as low as 10^{-5} atm at 1000°C.

It was reported in the above studies that the decomposition of LSCF or formation of secondary phases results in a significant decrease in the oxygen deficiency of the perovskite phase, which obviously affects its transport and thermo-expansion properties. In this thesis, the following questions will be addressed:

a. Can the above experimental results be explained by thermodynamic calculations?

b. What is the stable region (T, PO_2) for the pure LSCF perovskite phase with a specific composition under various temperatures and oxygen partial pressures?

c. Which are the phases that form when LSCF partially decomposes?

d. How does the oxygen non-stoichiometry in the perovskite change with changing temperature or oxygen partial pressure?

2) Surface segregation and kinetic-demixing

Surface segregation in LSCF has been reported by a few groups [31−34]. Doorn *et al.* [31] found Sr enrichment on the oxygen-lean side surface in an oxygen membrane tested for oxygen permeation (i.e. exposed to an oxygen pressure gradient) at 900°C for 500h. Oh *et al.* [32] examined surface morphological changes of LSCF pellets using SEM after heat treatment in a temperature range of 600–900°C. Submicron-sized precipitates were observed on the surface after heat treatment. AES (Auger Electron Spectroscopy) and TEM (Transmission Electron Microscopy) characterizations revealed that the precipitates were strontium (Sr)-oxygen (O) based phase. The amount of Sr–O precipitates was found to increase with increasing temperature or oxygen partial pressure. The composition and crystal structure of these precipitates were not determined. Different opinions exist in the literature on the effect of surface enrichment on the surface exchange coefficient and electrochemical activity of LSCF. Baumann *et al.* attributed strong activation of the LSCF oxygen electrode to surface enrichment of Sr and Co caused by high cathodic polarisation [33]. On the contrary, Simner *et al.* [34] concluded that Sr enrichment is actually one of the reasons for cell degradation. They reported significant Sr surface enrichment on both sides of a tested LSCF cathode (at the LSCF-SDC and LSCF-Au interfaces) after 500h testing at 750°C using XPS.

Kinetic demixing is related to cation diffusion and segregation under a chemical or electrical potential gradient. Lein *et al.* found kinetic demixing in a LSCF oxygen membrane exposed to an oxygen potential gradient [25]. An enrichment of 1 at.% La and Fe and a deficiency of 1% Sr was found on the surface of the LSCF membrane exposed to the N_2 side, while an enrichment of 1% Sr and a deficiency of 1% La was found on the O_2 side. The reliability of these result is however questionable, as only one sample was examined and a 1% change in composition is beyond the detection limit of the microscope they used.

Surface segregation or kinetic demixing in LSCF influences not only its oxygen exchange

kinetics and electrochemical activity, but also other properties. For example, the cation diffusion may be associated with formation of Kirkendall voids or micropores [35]. Besides, a change in local composition of a LSCF cathode may cause decomposition or formation of secondary phases. Thus, it will be valuable if the following questions can be answered:

a. What are the mechanisms accounting for surface segregation of Sr (or other elements) and kinetic demixing?

b. In which form (phase, crystal structure *etc.*) do Sr-rich precipitates exist?

c. How is Sr surface segregation influenced by temperature and oxygen partial pressure?

3) Sr volatilisation, diffusion and reaction

Sr is a very active element in LSCF. It tends to diffuse out (or volatilize) from bulk of the cathode onto the surface and react with YSZ forming insulating Sr zirconate phases. When a CGO interlayer is introduced between LSCF and YSZ, Sr may diffuse through the porous interlayer and reach the YSZ electrolyte surface. This can happen especially during sintering when the temperature is high and therefore the diffusion kinetics is fast [14−18, 36].

i. Volatilisation and diffusion

Becker and Tietz *et al.* [20, 37] examined LSCF oxygen electrodes by SIMS. After long-term operation, Sr-rich deposits were found on the surface of the barrier layer (in contact with the LSCF cathode) with preferential deposition in the direction of the gas flow. This observation indicates that Sr is transported by the gas stream via evaporation/condensation. The diffusion of strontium out of the cathode leads to a strontium depletion in the LSCF cathode, which was supposed to significantly lower the performance of the LSCF cathode and was regarded as the major degradation mechanism. Measurements on cells with slightly less strontium in the cathode ($La_{0.58}Sr_{0.38}Co_{0.2}Fe_{0.8}O_{3-\delta}$) showed lower performance than the one with $La_{0.58}Sr_{0.4}Co_{0.2}Fe_{0.8}O_{3-\delta}$ [38]. Hjalmarsson *et al.* [39] studied degradation of $(La_{0.6}Sr_{0.4})_{0.99}CoO_{3-\delta}$ in dry and moisturised air. Increased degradation was found in moisturised air. It seems that Sr is more active in moisture, resulting in degradation by forming strontium hydroxide at the electrode surface.

ii. Diffusion across CGO barrier layers

CGO was introduced as a barrier layer between the LSCF cathode and the YSZ electrolyte to prevent direct reaction between these two functional layers [14−18]. However, the CGO barrier layer seems difficult to prepare in a form where it fully stops Sr diffusing through and reaching the electrolyte surface, no matter what kind of processing route is applied for the barrier layer

(spraying, screen printing, PVD). Jordan *et al.* [14] investigated cation diffusion in the CGO layer produced by two different routes, screen printing and magnetron sputtering. $SrZrO_3$ was observed for both cases. Formation of $SrZrO_3$ takes place in a minor degree in the CGO layer prepared by magnetron sputtering. This type of cell was further characterized via long-term durability test. It was found that parts of the cathode layer along the edge were peeled off after testing, as the smooth CGO layer resulted in poor adhesion to the YSZ electrolyte. Similar studies have been carried out by Uhlenbruck *et al.* [11] on screen printed and PVD (physical vapor deposition) CGO layers and by Knibbe *et al.* [36] on sprayed and PLD (pulse laser deposition) CGO layers. Even with dense barrier layer, Sr (and other metal ion) migration through the barrier layer can still proceed via grain boundaries.

iii. Reaction with YSZ

It has been reported in many studies that direct contact between the LSCF cathode and the YSZ electrolyte led to formation of insulating strontium zirconate [10, 11, 40−42]. Kindermann *et al.* [40] investigated compatibility of $La_{1-x}Sr_xFe_{1-y}M_yO_{3-\delta}$ (M=Cr, Mn, Co, Ni) with YSZ at 1000°C. $SrZrO_3$ is always formed. For $La_{0.6}Sr_{0.4}Fe_{0.8}Co_{0.2}O_{3-\delta}$, up to 40 mol.% $SrZrO_3$ was observed after long-term heat treatment. In addition, small amount of $La_2Zr_2O_7$ and spinel were also detected. Similar reactions happen also between LSC and YSZ. Dieterle *et al.* [43] studied the reaction of nanocrystalline LSC thin film with YSZ substrate at 700−1000°C. Beside $SrZrO_3$, a Co-rich phase was also detected. It was shown that formation of $SrZrO_3$ is a rapid process, which happened even after 15min at 900°C. Martinez-Amesti *et al.* [44] reported formation of $SrZrO_3$ in a mixture of LSF+YSZ at high temperatures (T>925°C).

It was found that the amount of formed $SrZrO_3$ depends on sintering temperature, operating temperature, LSCF composition and oxygen partial pressure [15, 45-48]. Reactions between LSCF and YSZ forming unwanted phases like $SrZrO_3$ have been detected at 1210 °C or at 700°C for a few hundred hours [15]. Similar reactions were also found for a dense LSC film deposited on YSZ single crystal after long-term (3800h) operation at 700°C [45]. It was found that high temperature sintering promotes formation of $SrZrO_3$ [15, 43]. Kostogloudis *et al.* studied LSCF-YSZ reactions with varying the Sr content [46]. $La_{1-x}Sr_xCo_{0.2}Fe_{0.8}O_{3-\delta}$ (x = 0, 0.15, 0.2, 0.3, 0.4 and 0.5) was mixed with YSZ and heat treated at 1100°C for 120h. Formation of $La_2Zr_2O_7$ was found at x<0.2, while $SrZrO_3$ formed in all cases when x>0. The amount of $SrZrO_3$ increases with increasing Sr content in the LSCF. Simner *et al.* [47] investigated the influence of the LSCF

composition on its reaction with YSZ. No La- or Sr-zirconate formation was found in a mixture of $La_{0.2}Sr_{0.8}FeO_3$ and YSZ heat treated at 1200 °C for 2 hours, which is in agreement with the findings by Ralph *et al.* [48]. Further studies were carried out on full cells with a $La_{0.1}Sr_{0.9}Co_xFe_{1-x}O_{3-\delta}$ (x = 0, 0.2 and 0.5) cathode and a SDC barrier layer. Formation of a Sr-Zr-O layer was found in all cases after testing and the thickness of the Sr-Zr-O layer increases with increasing the Co content in the LSCF cathode. Mai *et al.* [4] reported more $SrZrO_3$ formation in a cell with a $La_{0.58}Sr_{0.4}Co_{0.2}Fe_{0.8}O_{3-\delta}$ cathode than the one with $La_{0.8}Sr_{0.2}Co_{0.2}Fe_{0.8}O_{3-\delta}$. It can be concluded from the above that formation of $SrZrO_3$ is promoted by increasing Sr or Co content in the LSCF cathode.

By introducing a CGO barrier layer, the formation of strontium zirconate is restrained to some extent, and formation of $La_2Zr_2O_7$ can be prevented [14−18]. The type and thickness of the CGO barrier layer influence the amount of formed $SrZrO_3$. Studies on different fabrication methods for the CGO layer [11, 14, 36] show that formation of $SrZrO_3$ can be suppressed to a minimum by applying dense, thick CGO (>10μm) layer at low temperature.

Yokokawa *et al.* discussed the relation between activity of SrO in LSC or LSF cathodes and its reaction with rare earth doped ceria or YSZ [49]. They concluded that formation of $SrZrO_3$ at the ceria−YSZ interface depends on the Sr diffusion kinetics and also on the thermodynamic driving force. The driving force, which is the SrO chemical potential at the cathode/doped ceria interface, is stronger in LSC than in LSF due to difference in the valence stability of Fe and Co.

A few groups [17, 20] have attributed cell degradation to mainly formation of $SrZrO_3$, since presence of $SrZrO_3$ may lead to an increase in the interface resistivity. On the contrary, Mai *et al.* [13, 15] and Knibbe *et al.* [36] reported similar cell degradation rates in cells with different types of CGO barrier layers (PVD or PLD), i.e. the cell degradation rate is independent of the amount of formed $SrZrO_3$. Formation of $SrZrO_3$ can not be treated as the main mechanism accounting for cell degradation. It is one among several mechanisms contributing to the cell degradation. Further research of the influence of $SrZrO_3$ on cell degradation is needed. In addition, it is of great importance to reveal how the $SrZrO_3$ formation is influenced by composition, temperature and oxygen partial pressure. Hopefully, this can be done by analyzing the SrO activity in LSCF.

4) Cathode microstructure change during sintering

Microstructure related aspects such as porosity and grain size have a great influence on transport properties and cell performance. A coarser structure improves factors like ionic and

electronic conductivity and gas permeability of the cathode, while a finer structure leads to a higher specific surface area of the cathode and therefore to a greater number of reaction sites [4]. Wang *et al.* [5] studied the degradation of LSCF in symmetric cells, which were prepared by spraying LSCF/CGO on both sides of the YSZ electrolyte substrate and sintered between 800 and 1200 ˚C for 2−4h. The symmetric cells were tested at 800 ˚C for 180h and showed a modest increase in Rp. After testing the samples were examined by SEM. In contradiction to many previous investigations [14−18, 40−45], no reaction product was found at the electrode−electrolyte interface. The authors attributed the degradation to the densification of the LSCF/CGO cathode rather than reactions with YSZ. The densification can be suppressed by lowering the operating temperature. For example, Mai *et al.* [15] reported no microstructure change in their cells operated at 700°C. However from several studies discussed in *section 3)* above, it is clear that for long term operation Sr diffusion through grain boundaries or porosities in the barrier layer and subsequent zirconate formation is indeed a mechanism to consider for long term operation.

5) Interaction between LSCF and CGO

It has been reported that LSCF is chemically compatible with CGO and no reaction takes place [12]. However, inter-diffusion may still take place due to mutual solubility between LSCF and CGO. Du *et al.* reported a La solubility of around 40 mol.% in CeO_2 at 700°C [50]. The inter-diffusion between LSCF and CGO can be accelerated by increasing temperature.

The inter-diffusion between LSCF and CGO has been studied only by a few groups [11, 44] via powder mixture, diffusion couple, or real SOFCs and different results have been obtained. Martínez-Amesti *et al.* [44] examined the solid-state reaction and inter-diffusion phenomena between doped ceria and LSF by XRD, SEM and electrochemical impedance spectroscopy. No reaction product was found. But a significant shift in the XRD peak position for LSF was observed, which points to the diffusion of Ce into LSF perovskite resulting in a change in the lattice parameters. Sakai *et al.* [51, 52] carried out similar studies on diffusion couples of doped ceria in contact with LSCF (or LSC) using SIMS. Depletion of La, Sr, Co, Fe in LSCF and that of Ce, Gd in doped ceria were found. Uhlenbruck *et al.* [11] investigated element migration between various adjacent layers in SOFCs by TEM. They observed Sr depletion and a slight enrichment of Gd (coming from the barrier layer) in the LSCF electrode after sintering. It was found that incorporation of Ce and Gd into LSCF or depletion of Sr and La will not only reduce the ionic conductivity [47] but also affect the LSCF stability. They [11] further prepared

$La_{0.58}Sr_{0.4}Gd_{0.01}Fe_{0.8}$-$Co_{0.2}O_{3-\delta}$ powder and calcined at 900°C for 5h. Formation of $(La,Sr)_2(Co,Fe)O_4$ and spinel was confirmed by XRD. It can therefore be concluded that inter-diffusion across the LSCF−CGO interface may lead to phase decomposition or secondary phase formation in LSCF. The above processes can happen both during cell fabrication and during cell operation. Due to the highly thermally activated character of solid state diffusion, the inter-diffusion during sintering is much more pronounced than during test. In addition, when the cell is under operation, the cathode over-potential may result in a decrease of the local oxygen partial pressure, which may also result in phase decomposition or secondary phase formation.

It should also be mentioned that cation redistribution changes also thermal expansion of the various functional layers and therefore reduces the mechanical stability of the LSCF−CGO interface, which finally may result in spallation of the cathode layer [30]. Thermal expansion coefficients (TEC) for several relevant compositions can be found in the literature [4, 32, 53].

6) Inter-diffusion between CGO and YSZ

Several groups of authors investigated phase composition of CGO_xYSZ_{1-x} (x=0−1) mixtures which were sintered at temperatures from 950˚C to 1600˚C for 2 to 10h. XRD and/or Raman Spectroscopy were used to characterize the phase information [12, 44, 54, 55]. All the compositions were determined as single-phase solid solution with the fluorite structure. It can therefore be expected that no secondary phase forms at the CGO−YSZ interface during cell fabrication, which can be explained thermodynamically. According to the ZrO_2−CeO_2 phase diagram published by Li *et al.* [56], a continuous cubic fluorite solid solution exists in a composition range from pure ZrO_2 to pure CeO_2.

Results on the inter-diffusion between YSZ and CGO have been reported in the previous work [57−60]. The inter-diffusion results in formation of a solid solution phase [12, 61], which possess the cubic fluorite structure with a concentration gradient and an ionic conductivity lower than that of YSZ or CGO [12]. Tompsett *et al.* [57] observed cation inter-diffusion between the polished ceramic pellets in intimate contact after heat treatment at 1300˚C for 72h. Horita [58] reported a solid solution phase formed at the CGO−YSZ interface after sintering at 1550˚C. Jan Van herle *et al.* [59] observed serious inter-diffusion occurring at the YSZ−CGO interface at temperatures above 1400˚C. Tsoga *et al.* [60, 62] found that CGO and YSZ already diffuse into each other during sintering at 1200˚C. A diffusion zone at the CGO−YSZ interface was detected even at 1000˚C by Zhou *et al.* [63].

Difference in the cation diffusivity may lead to formation of Kirkendahl holes close to the CGO−YSZ interface. Due to higher diffusivities of Ce and Gd in YSZ (higher than those of Zr and Y in CGO), pores were formed on the CGO-side of the interface region [62]. These defects in the interface region obviously influence the cell performance in a negative way. The CGO−YSZ solution phase was determined to possess lower conductivity (10^{-3} S/cm, 700°C) than pure CGO ($10^{-1.6}$ S/cm, 700°C) or pure YSZ ($10^{-1.4}$ S/cm, 700°C) [12, 63]. The inter-diffusion between CGO and YSZ will therefore lower the conductivity of the CGO−YSZ couple [12, 58]. Zhou *et al.* measured thermal expansion and chemical expansion of the CGO_xYSZ_{1-x} solid solution and reported that the chemical expansion of the solid solutions was larger (0.5%) than that of CGO or YSZ [63].

Various methods to suppress the CGO−YSZ inter-diffusion have been proposed in the literature, which include preparing the CGO layer by a low temperature process like PVD [11, 13, 14] or introducing a diffusion barrier between CGO and YSZ [12, 64]. It was found that applying a PVD CGO layer effectively suppressed the CGO−YSZ inter-diffusion, simply due to the low deposition temperature. On the other hand, the cell performance with a diffusion barrier between CGO and YSZ (CGO_xYSZ_{1-x}) was poor [12, 64], which was attributed to lower conductivity and still diffusion at high temperature.

As discussed above, the CGO−YSZ inter-diffusion happens mainly during sintering, simply due to the high sintering temperature. The long-term inter-diffusion behavior during operation and its influence on the cell performance have not been well studied. Bekale *et al.* [65] studied diffusion of Ce and Gd in YSZ. At 700°C, the bulk and grain boundary diffusion coefficient of Ce and Gd in YSZ was determined to be around 10^{-25} and 10^{-22} cm^2s^{-1}, respectively. This indicates that it may take a few years for Ce and Gd to diffuse 10nm at 700°C. Therefore inter-diffusion may not affect the long term stability of a fuel cell operating at 700°C to a significant degree.

7) Impact of impurities

In addition to the above mentioned aspects, the impact of impurities on cell degradation must also be taken into consideration. The impurities may come from raw material, furnace, gases, interconnect material (in a stack level) *etc.* The deposition of Cr (evaporated from interconnect material) in LSCF cathodes has been reported by many groups and has recently been reviewed by Fergus [66]. The Cr_2O_3 deposition in LSCF is more evenly distributed and less localized at the three-phase boundary, resulting in a much lower overpotential increase than that for LSM.

$SrCrO_4$ has been observed near the interconnect, which indicates that the chromium deposit reacts with the cathode. The long term contribution to the degradation of LSCF by Cr deposition was studied by Bentzen *et al.* [67]. They reported that both LSM/YSZ and LSCF/CGO cathodes were sensitive to chromium poisoning, with the LSCF/CGO cathode to a less extent than the LSM/YSZ cathode. Post-mortem investigations revealed several Cr-containing compounds filling up the cathode microstructure. Besides Cr-containing compounds, $SrCO_3$ and $SrSO_4$ were observed by Elshof *et al.* [68] when using LSCF in a methane coupling reactor. The presence of B was observed in the LSCF cathodes by Zhou *et al.* [69] using SIMS. However, the effect of boron on the electrochemical performance of the LSCF cathode was not investigated. Si and B were also observed in the cathode by Komatsu *et al.* [70].

The above literature review gives a short summary of various possible mechanisms accounting for degradation of LSCF-based cathodes in IT-SOFCs. Among the different mechanisms, decomposition of the LSCF perovskite is of great importance.

The overall aim of this PhD project was to investigate the origins of the degradation occuring in the advanced LSCF-based SOFC cathodes, and to provide suggestions to mitigate the degradation or point to the direction where the future research/development shall focus. The focus in this work is on the phase stability of LSCF itself and its chemical compatibility with other SOFC components. They will be evaluated by theoretically thermodynamic calculations and experimental verifications. As the first step a thermodynamic database of La-Sr-Co-Fe-O will be established based on assessments of low-order subsystems. Thermodynamic calculations on stability of LSCF or other relevant phases and thermodynamic properties will then be carried out. Finally, the interactions of LSCF−CGO and CGO−YSZ will be examined by both model experiments and post-mortem analyses of tested IT-SOFCs.

It should be mentioned that the materials investigated in this thesis (LSCF *etc.*) also find their use as material for oxygen separation membrane [71], high temperature sensors [72], and as catalysts [73] *etc.* The results will therefore also be of interest to these scientific communities.

1.3 Methodology

In this thesis, a hybrid method of CALPHAD modeling combined with experimental validation was applied to study the origins of degradation for LSCF cathode materials. Thermodynamic modeling and calculation were taken as the major research effort.

1.3.1 CALPHAD

The CALPHAD method, based on a scrupulous evaluation, is a fundamental technique in phase equilibrium studies and is nowadays a powerful tool for material development [74]. This method is to define appropriate thermodynamic models for all the phases in a system and to describe the Gibbs energy of each phase based on the model as a function of temperature, composition and pressure. The derived Gibbs energy functions should not only consistently reproduce the thermodynamic properties, but also allow calculation of phase diagrams that resemble the experimentally determined ones. To do so, all available thermodynamic and phase-equilibrium data are evaluated simultaneously in order to obtain one set of model equations for the Gibbs energies of all phases as functions of temperature and composition. All the data are rendered self-consistent and consistent with thermodynamic principles. Discrepancies in the available data can often be resolved, and interpolations and extrapolations can be made in a thermodynamically correct manner. Based on the databases, the properties of multicomponent systems can be calculated and predicted, to improve understanding of various industrial and technological processes.

The most important virtue of the CALPHAD method is probably that extrapolation from lower order systems allows accurate predictions of phase equilibria in higher order systems, which very often can be so complex that it is impossible to be understood by using experimental methods alone. Assuming that the lower order systems are well described using appropriate models, a limited number of carefully chosen key experiments are adequate to allow optimization of the complete higher order system over a wide temperature, pressure and composition range.

Fig. 1.3 presents a flow chart for the principle of CALPHAD approach. The input to the CALPHAD modeling consists of thermodynamic and phase diagram data and properly selected thermodynamic models. These input data can be obtained from both experimental studies and theoretical calculations such as first principle calculations.

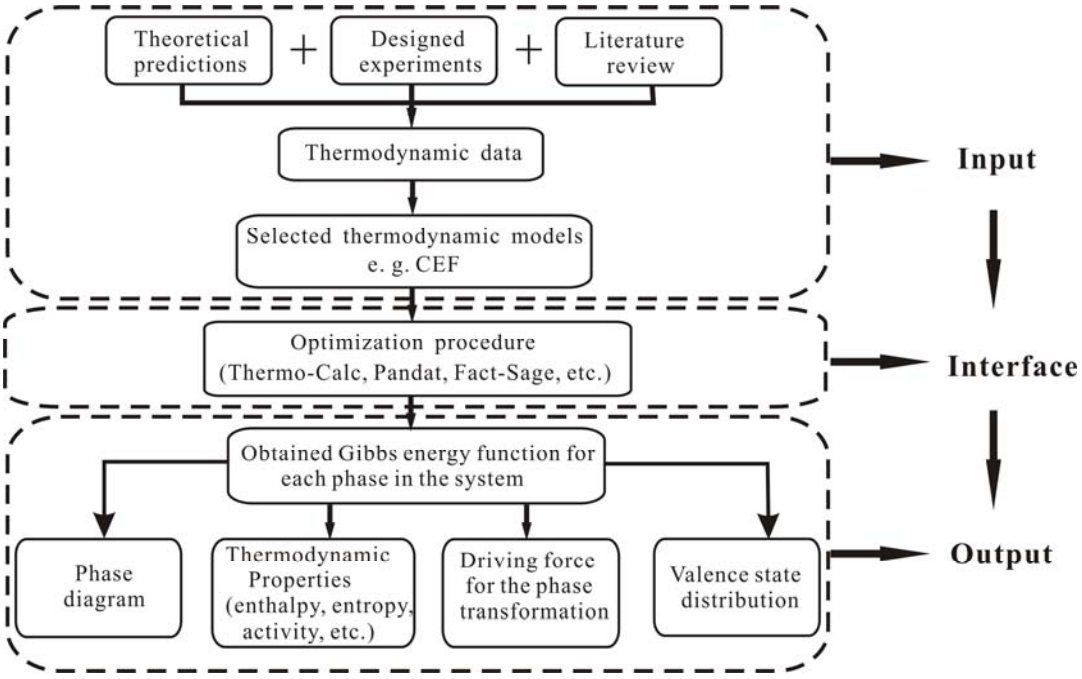

Fig. 1. 3. Schematic flow chart of the CALPHAD approach for multicomponent systems.

The thermodynamic models [75] are the core of the CALPHAD approach. In CALPHAD modeling, the Gibbs energy for a phase is given by:

$$G = {}^{srf}G - T\,{}^{conf}S + {}^{phys}G + {}^{ex}G \tag{1.1}$$

where ${}^{srf}G$ represents the Gibbs energy contribution relative to its "surface of reference" state, ${}^{conf}S$ is the configurational entropy which describes the ideal mixing and can be extended to include random arrangements in various sublattices, ${}^{phys}G$ denotes the contribution to the Gibbs energy due to physical contributions other than electronic and vibrational effects, such as magnetic contributions, and ${}^{ex}G$ describes the contributions due to non-ideal interaction between components.

For pure elements or stoichiometric compounds, only the first (${}^{srf}G$) and third (${}^{phys}G$) terms on the right hand side of *Eq. 1.1* are considered, and the non-magnetic part of the Gibbs energy can be described using an empirical formula as:

$$G - H^{SER} = a + bT + cT\ln T + dT^2 + eT^3 + fT^{-1} + \ldots \tag{1.2}$$

where SER (Stable Element Reference) denotes the reference state for pure elements at 298.15K and 1 atm.

For a solution phase, the second and fourth terms on the right hand side of *Eq. 1.1* are also needed. The ${}^{srf}G$ and ${}^{conf}S$ for the Gibbs energy of a phase is given by:

$${}^{srf}G = \sum_{i=1}^{n} y_i \, {}^{o}G_i \tag{1.3}$$

and

$${}^{conf}S = -R\sum_{i=1}^{n} y_i \ln(y_i) \tag{1.4}$$

, respectively,

where ${}^{o}G_i$ is the Gibbs energy of the component i, while y_i is the constituent fractions.

The magnetic contribution to the Gibbs energy (*Eq. 1.5*) is described using a magnetic ordering model proposed by Inden [76] and simplified by Hillert and Jarl [77].

$${}^{mag}G = RT\ln(\beta+1)f(\tau) \tag{1.5}$$

where β is the Bohr magneton number, and $\tau = T/Tc$. Tc is the critical temperature for magnetic ordering. Tc and β are model parameters. They are both dependent on the composition, and are described in the same way as for the Gibbs energy in thermodynamic databases. The function $f(\tau)$ is given as below:

For $\tau < 1$,

$$f(\tau) = 1 - \frac{1}{A}\left[\frac{79\tau^{-1}}{140p} + \frac{158}{497}\left(\frac{1}{p}-1\right)\left(\frac{\tau^3}{2} + \frac{\tau^9}{45} + \frac{\tau^{15}}{200}\right)\right] \tag{1.6}$$

For $\tau > 1$,

$$f(\tau) = -\frac{1}{A}\left[\frac{\tau^{-5}}{10} + \frac{\tau^{-15}}{315} + \frac{\tau^{-25}}{1500}\right)\right] \tag{1.7}$$

and

$$A = \frac{518}{1125} + \frac{11692}{15975}\left(\frac{1}{p}-1\right) \tag{1.8}$$

The parameter p is dependent on crystal structure. For example, it is 0.28 for a HCP or FCC structure.

The compound energy formalism (CEF) [78], which is constructed to describe phase with sublattices and is widely used in CALPHAD assessments, was used to model all the solution phases in the La-Sr-Co-Fe-O system. The ionic two-sublattice model [79, 80], which was developed within the framework of CEF, was introduced for the liquid phase in this thesis

(*Chapter 2*). All the models used for the La-Sr-Co-Fe-O system can be found in Table 6.2 (*Chapter 6)*. The choice and derivation of parameters for some of the important phases including spinel, perovskite and A_2BO_4 can be found in *Section 2.3, 3.3* and *4.3*.

Using commercial softwares, such as Thermo-Calc [81] used in this work, Pandat [82] or FactSage [83], an optimal set of thermodynamic parameters can be obtained to describe the Gibbs energy for each phase in the system. Eventually, predictions can be made from the modeling by extending the system into regions where experimental data are unavailable, e.g., phase equilibria of a high-order system, thermodynamic properties and the concentration of defects at arbitrary conditions, which are the ultimate outputs of the modeling.

The CALPHAD approach has been successfully employed in steel industry [84] and for lead-free solder materials [85]. CALPHAD modeling has also been applied to complex oxide systems, such as the ZrO_2–Nd_2O_3–Y_2O_3–Al_2O_3 pseudo-quaternary system [86]. Application of CALPHAD modeling to SOFC materials has also been carried out, for example on the $La_{1-x}Sr_xMnO_3$ (LSM) perovskite system [87] and for understanding the thermodynamics at the LSM−YSZ interface [88]. Indeed, with continuous efforts on perovskite-based compounds, theoretical modeling techniques including CALPHAD have become necessary components for studying and designing perovskites. In this thesis, based on the developed La-Sr-Co-Fe-O database, advances have been made in calculating complex phase equilibria in order to understand various degradation phenomena related to LSCF-based cathodes for SOFCs. Specifically, the thermodynamic database of La-Sr-Fe-Co-O enables predictions on

a. stability of LSC, LSF and LSCF;

b. oxygen non-stoichiometry;

c. component activity and chemical potential;

d. cation distribution and average cation valence at any specific composition, temperature, and PO_2.

1.3.2 Experimental studies

Experimental studies are indispensable in order to verify the results obtained from CALPHAD modeling and to explore degradation phenomena in tested SOFCs. In this thesis, several types of experimental studies were carried out. Experimental investigations on stability of LSC, LSCF, and LSCF/CGO composite were carried out on pressed pellets heat treated at different temperatures and oxygen partial pressures. After heat treatment, the pellets were examined with

XRD and SEM/EDS. Detail on the experimental procedures and analytical techniques are presented in *Section 5.2* and *7.2*.

Beside model experiments, degradation phenomena in tested SOFCs were investigated via post-mortem analyses of an SOFC tested at 700 °C for 2000h using techniques including SEM SIMS and TEM. Similar studies were also carried out on a reference non-tested cell. The analyses were focused on the LSCF/CGO cathode and the CGO barrier layer, as various investigations [15-18] have pointed the degradation of this type of IT-SOFC to the cathode side. In these studies, SEM/EDS and SIMS were used to investigation inter-diffusion at the CGO−YSZ interface and the CGO barrier layer−LSCF/CGO cathode interface. SIMS was further employed to investigate the distribution of impurities. Finally TEM/EDS alone was employed to examine phase stability of LSCF and phase separation or secondary phase formation in a nano-meter scale. Details of the experimental procedures and analytical techniques are described in *Section 8.2*.

1.4 Overview of the thesis

In this chapter (*Chapter 1*) a short introduction on solid oxide fuel cells and a summary of literature findings on degradation of LSCF-based cathodes are presented. The theoretical background of the CALPHAD methodology is further explained. The structure for the remaining part of the thesis is illustrated in Fig. 1. 4.

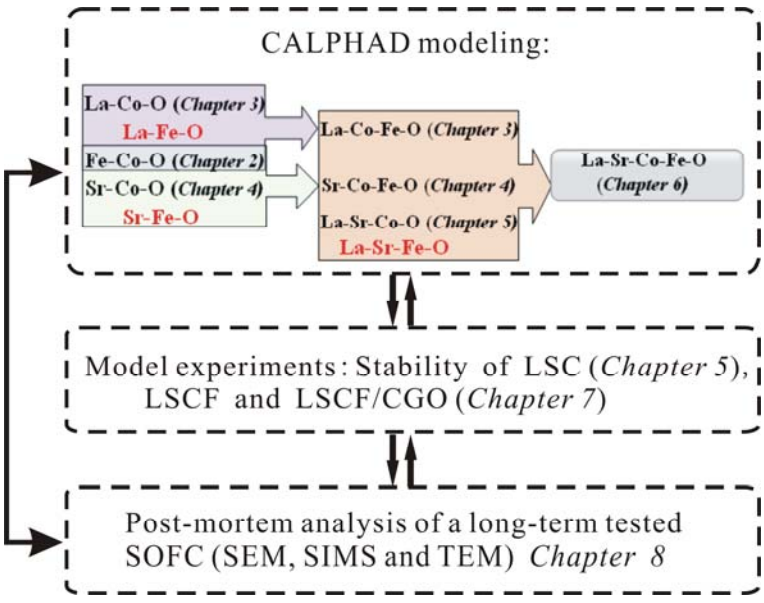

Fig.1.4 Structure of the thesis.

The main part of the thesis is organized the same way as how the PhD project proceeded. It started with establishing a thermodynamic database of La-Sr-Co-Fe-O. Published thermodynamic databases of the sub-systems in La-Sr-Co-Fe-O and relevant experimental data were reviewed and summarized. Previous assessments of the La-Fe-O [89], Sr-Fe-O and La-Sr-Fe-O [90] subsystems were adopted directly in this work. The Co-Fe-O (*Chapter 2*), La-Co-O (*Chapter 3*), Sr-Co-O (*Chapter 4*), Sr-Co-Fe-O (*Chapter 4*) and La-Sr-Co-O (*Chapter 5*) systems were modeled in this work, following the order from ternary to quaternary and to the final quinary La-Sr-Co-Fe-O (*Chapter 6*). The thermodynamic description of the La-Co-Fe-O system (*Chapter 3*) is obtained by an ideal extrapolation of the descriptions of the sub-systems. Experimental investigations on phase stability of LSCF and LSCF−CGO interactions are described in *Chapter 7*. *Chapter 8* is dedicated to post-mortem analyses of a tested and a reference intermediate temperature solid oxide fuel cell (IT-SOFC) with a focus on the cathode side. Most of these chapters have either been submitted [91] or will be submitted for publication in scientific journals. The final chapter presents conclusions of this PhD thesis and an outlook for possible future work. In the appendix, the complete thermodynamic database of La-Sr-Co-Fe-O and additional calculation results are presented.

References

[1] S.C. Singhal, K. Kendall, High Temperature Solid Oxide Fuel Cells Fundamentals, Design and Applications. Elsevier Advanced Technology, The Boulevard, Langford Lane, Kidlington Oxford, UK, (2003).

[2] K. Tseronis, I. Bonis, I.K. Kookos, C. Theodoropoulos, Int. J. Hydrogen Energy 37 (2012) 530–547.

[3] N.H. Menzler, F. Tietz, S. Uhlenbruck, H.P. Buchkremer, D. Stöver, J. Mater. Sci. 45 (2010) 3109–3135.

[4] A. Mai, V.A.C. Haanappel, S. Uhlenbruck, F. Tietz, D. Stöver, Solid Sate Ionics 176 (2005) 1341–1350.

[5] W. G. Wang, M. Mogensen, Solid Sate Ionics 176 (2005) 457–462

[6] B.C.H. Steele, Solid State Ionics 134 (2000) 3–20.

[7] A. Esquirol, J. Kilner, N. Brandon, Solid State Ionics 175 (2004) 63–67.

[8] H.J. Hwang, J.W. Moon, S. Lee, E.A. Lee, J. Power Sorces 145 (2005) 243–248.

[9] T.J. Huang, C.L. Chou, Fuel Cells 10 (2010) 718–725.

[10] J.Y. Kim, V.L. Sprenkle, N.L. Canfield, K.D. Meinhardt, L.A. Chick, J. Electrochem. Soc. 153 (2006) A880–A886.

[11] S. Uhlenbruck, T. Moskalewicz, N. Jordan, H.J. Penkalla, H.P. Buchkremer, Solid Sate Ionics, 180 (2009) 418–423.

[12] A. Tsoga, A. Naoumidis, D. Stöver, Solid State Ionics 135 (2000) 403–409.

[13] A. Mai, V.A.C. Haanappel, F. Tietz, D. Stöver, Solid State Ionics 177 (2006) 2103 – 2107.

[14] N. Jordan, W. Assenmacher, S. Uhlenbruck, V.A.C. Haanappel, H.P. Buchkremer, D. Stöver, W. Mader, Solid State Ionics 179 (2008) 919–923.

[15] A. Mai, M. Becker, W. Assenmacher, F. Tietz, D. Hathiramani, E. Ivers-Tiffée, D. Stöver, W. Mader, Solid Sate Ionics 177 (2006) 1965–1968.

[16] H. Tu, U. Stimming, J. Power Sources 127 (2004) 284–293.

[17] S.P. Simner, M.D. Anderson, M.H. Engelhard, J.W. Stevenson, Electrochem. Solid-State Lett. 9 (2006) A478–A481.

[18] F. Tietz, V.A.C. Haanappel, A. Mai, J. Mertens, D. Stöver, J. Power Sources 156 (2006) 20–22.

[19] R. Knibbe, A. Hauch, J. Hjelm, S.D. Ebbesen, M.B. Mogensen. Green 16 (2011) 141–169.

[20] M. Becker, Parameterstudie zur Langzeitbeständigkeit von Hochtemperatur-Brennstoffzellen (SOFC), Ph.D. Thesis, University Karlsruhe, Germany, (2006).

[21] C. Endler, A. Leonide, A. Weber, F. Tietz, E. Ivers-Tiffee. J. Electrochem. Soc. 157 (2010) B292–B298.

[22] S. Hashimoto, Y. Fukuda, M. Kuhn, K. Sato, K. Yashiro, J. Mizusaki, Solid State Ionics 181 (2010) 1713–1719.

[23] M. Kuhn, Y. Fukuda, S. Hashimoto, K. Sato, K. Yashiro, J. Mizusaki, ECS Trans. 35 (2011) 1881–1890.

[24] M.M. Natile, F. Poletto, A. Galenda, A. Glisenti, T. Montini, L.D. Rogatis, P. Fornasiero, Chem. Mater. 20 (2008) 2314–2327.

[25] H.L. Lein, K. Wiik, T. Grande, Solid State Ionics 177 (2006) 1587–1590.

[26] F. Iguchi, N. Sata, H. Yugami, H. Takamura, Solid State Ionics 177 (2006) 2281–2284.

[27] F. Morin, G. Trudel, Y. Denos, Solid State Ionics 96 (1997) 129–139.

[28] J.E. Saal, Thermodynamic modeling of phase transformations and defects: From Cobalt to Doped Cobaltate Perovskites (PhD thesis), The Pennsylvania State University, (2010).

[29] J. Ovenstone, J.S. White, S.T. Misture, J. Power Sources 181 (2008) 56–61.

[30] H. Yokokawa, H. Tu, B. Iwanschitz, A. Mai, J. Power Sources 182 (2008) 400–412.

[31] R.H.E. van Doorn, H.J.M. Bouwmeester, A.J. Burggraaf, Solid State Ionics 111 (1998) 263–272.

[32] D. Oh, D. Gostovic, E.D. Wachsman, J. Mater. Res. 27 (2012) 1992–1999.

[33] F.S. Baumann, J. Fleig, M. Konuma, U. Starke, H.U. Habermeier, J. Maier, J. Electrochem. Soc., 152 (2005) A2074–A2079.

[34] S.P. Simner, J.F. Bonnett, N.L. Canfield, K.D. Meinhardt, V.L. Sprenkle, J.W. Stevenson, Solid State Lett. 5 (2002) A173–A175.

[35] M. Kuznecov, P. Otschik, P. Obenaus, K. Eichler and W. Schaffrath, Solid State Ionics 157 (2003) 371–378.

[36] R. Knibbe, J. Hjelm, M. Menon, N. Pryds, M. Søgaard, H.J Wang, K. Neufeld, J. Am. Ceram. Soc. 93 (2010) 2877–2883.

[37] F. Tietz, A. Mai, D. Stover, Solid State Ionics 179 (2008) 1509–1515.

[38] J.C. Rao, Y. Zhou, D.X. Li, J. Mater. Res. 16 (2001) 1806–1813.

[39] P. Hjalmarsson, M. Søgaard, M. Mogensen, Solid State Ionics 179 (2008) 1422–1426.

[40] L. Kindermann, D. Das, H. Nickel, K. Hilpert, Solid State Ionics 89 (1996) 215–220.

[41] H. Yokokawa, N. Sakai, T. Kawada, M. Dokiya, Denki Kagaku, 57 (1989) 821–828.

[42] H. Kamata, A. Hosaka, J. Mizusaki, H. Tagawa, Mater. Res. Bull. 30 (1995) 679–687.

[43] L. Dieterle, D. Bach, R. Schneider, H. Stormer, D. Gerthsen, U. Guntow, E. Ivers-Tiffee, A. Weber, C. Peters, H. Yokokawa, J. Mater. Sci. 43 (2008) 3135–3143.

[44] A. Martínez-Amesti, A. Larraňaga, L.M. Rodríguez-Martínez, A.T. Aguayo, J.L. Pizarro, M.L. Nó, A. Laresgoiti, M.I. Arriortuaa, J. Power Sources 185 (2008) 401–410.

[45] M. Sase, D. Ueno, K. Yashiro, A. Kaimai, T. Kawada, J. Mizusaki, J. Phys. Chem. Solids 66 (2005) 343–348.

[46] G.C. Kostogloudis, G. Tsiniarakis, C. Ftikos, Solid State Ionics 135 (2000) 529–535.

[47] S.P. Simner, J.F. Bonnett, N.L. Canfield, K.D. Meinhardt, J.P. Shelton, V.L. Sprenkle, J.W. Stevenson, J. Power Sources 113 (2003) 1–10.

[48] J.M. Ralph, J.T. Vaughey, M. Krumpelt, Solid oxide fuel cells, vol. VII, in: H. Yokokawa, S.C. Singhal (Eds.), The Electrochemical Society Proceedings Series, Pennington, NJ, (2001).

[49] H. Yokokawa, N. Sakai, T. Horita, K. Yamaji, M.E. Brito, H. Kishimoto, J. Alloys Compd. 452 (2008) 41–47.

[50] Y. Du, M. Yashima, T. Koura, M. Kakihana, M. Yoshimura, CALPHAD 20 (1996) 95–l08.

[51] N. Sakai, H. Kishimoto, K. Yamaji, T. Horita, M.E. Brito, H. Yokokawa, J. Electrochem. Soc. 154 (2007) B1331–B1337.

[52] N. Sakai, H. Kishimoto, K. Yamaji, T. Horita, M.E. Brito, H. Yokokawa, ECS Transactions 7 (2007) 389–398.

[53] S. Hashimoto, Y. Fukuda, M. Kuhn, K. Sato, K. Yashiro, J. Mizusaki, Solid State Ionics 186 (2011) 37–43.

[54] B. Cale´s, J.F. Baumard, J. Electrochem. Soc. 131 (1984) 2407–2413.

[55] J.J. Bentzen, H. Schwartzbach, Solid State lonics 40/41 (1990) 942–946.

[56] L. Li, O.V.D. Biest, P.L. Wang, J. Vleugels, W.W. Chen, S.G. Huang, J. Eur. Ceram. Soc. 21 (2001) 2903–2929.

[57] G.A. Tompsett, N.M. Sammes, O.Yamamoto, J. Am. Ceram. Soc. 80 (1997) 3181–3186.

[58] T. Horita, N. Sakai, H. Yokokawa, M. Dokiya, T. Kawada, J. Van herle, K. Sasaki, J. Electroceram. 1 (1997) 155–164.

[59] J. Van herle, T. Horita, T. Kawada, N. Sakai, H. Yokokawa, M. Dokiya, Solid State Ionics 86 (1996) 1255–1258.

[60] A. Tsoga, A. Naoumidis, A. Gupta, D. Stöver, Mater. Sci. Forum 308–311 (1999) 794–799.

[61] N.M. Sammes, G.A. Tompsett, Z. Cai. Solid State Ionics 121 (1999) 121–125.

[62] A. Tsoga, A. Gupta, A. Naoumidis, D. Skarmoutsos, P. Nikolopoulos, Ionics 4 (1998) 234–240.

[63] X.D. Zhou, B. Scarfino, H.U. Anderson, Solid State Ionics 175 (2004) 19–22.

[64] A. Tsoga, A. Gupta, A. Naoumidis, P. Nikolopoulso, Acta mater. 48 (2000) 4709–4714.

[65] V.M. Bekale, A.M. Huntz, C. Legros, G. Sattonnay, F. Jomard, Philos. Mag. & Philos. Mag. Lett. 88 (2007) 1–19.

[66] J.W. Fergus, Int. J. Hydrogen Energy 32 (2007) 3664 –3671.

[67] J.J. Bentzen, J.V.T. Høgh, R. Barfod, A. Hagen, Fuel Cells 9 (2009) 823–832.

[68] J.E. ten Elshof, H.J.M. Bouwmeester, H. Verweij, Appl. Catal., A 130 (1995) 195–212.

[69] X.D. Zhou, J.W. Templeton, Z. Zhu, Y.S. Chou, G.D. Maupin, Z. Lu, R.K. Brow, J.W. Stevenson, J. Electrochem. Soc. 157 (2010) B1019–B1023.

[70] T. Komatsu, K.Watanabe, M. Arakawa, H. Arai, J. Power Sources 193 (2009) 585–588.

[71] H.J.M. Bouwmeester, Catal. Today 82 (2003) 141–150.

[72] P. Ravindran, P.A. Korzhavyi, H. Fjellvag, A. Kjekshus, Phys. Rev. B 60 (1999) 16423–16434.

[73] R.J.H. Voorhoeve, Advanced Materials in Catalysis, J. J. Burton and R. L. Garten, Eds., New York, (1977).

[74] H.L. Lukas, S.G. Fries, B. Sundman, Computational Thermodynamics, the Calphad Method, Cambridge University Press (2007).

[75] M. Hillert, Phase Equilibria, Phase Diagrams and Phase Transformations-Their Thermodynamic Basis, Cambridge University Press (1998).

[76] G. Inden, Z. Metallkd. 66 (1975) 577–582.

[77] M. Hillert, M. Jarl, CALPHAD 2 (1978) 227–238.

[78] M. Hillert, J. Alloys Compd. 320 (2001) 161–176.

[79] M. Hillert, B. Jansson, B. Sundman, J. Ågren, Metall. Trans. 16A (1985) 261–266.

[80] B. Sundman, CALPHAD 15 (1991) 109–119.

[81] B. Sundman, B. Jansson, J.O. Andersson, CALPHAD 9 (1985) 153–190.

[82] W. Cao, S.L. Chen, F. Zhang, K. Wu, Y. Yang, Y.A. Chang, R. Schmid-Fetzer, W. A. Oates, CALPHAD 33 (2009) 328–342.

[83] C.W. Bale, P. Chartrand, S.A. Decterov, G. Eriksson, K. Hack, R.B. Mahfoud, J. Melançon, A.D. Pelton, S. Petersen, CALPHAD 26 (2002) 189–228.

[84] A. Costa E Silva, J. Mining Metall. 35 (1999) 85–112.

[85] B. Brunetti, D. Gozzi, M. Iervolino, V. Piacente, G. Zanicchi, N. Parodi, G. Borzone, CALPHAD 30 (2006) 431–442.

[86] O. Fabrichnaya, G. Savinykh, G. Schreiber, H.J. Seifert, J. Eur. Ceram. Soc. 32 (2012) 3171–3185.

[87] A. N. Grundy, Ph.D. Thesis, Swiss Institute of Technology Zurich, Swiss, (2003).

[88] M. Chen, Ph.D. Thesis, Swiss Institute of Technology Zurich, Swiss, (2005).

[89] E. Povoden-Karadeniz, A.N. Grundy, M. Chen, T. Ivas, L.J. Gauckler, J. Phase Equilib. Diff. 30 (2009) 351–366.

[90] E. Povoden-Karadeniz, Thermodynamic modeling of La-Sr-Fe-O system, unpublished results.

[91] W. Zhang, M. Chen, Thermodynamic modeling of Co-Fe-O system, paper submitted.

Chapter 2

Thermodynamic modeling of the Co-Fe-O system

Abstract

As a part of the research project aimed at developing a thermodynamic database of the La-Sr-Co-Fe-O system for applications in Solid Oxide Fuel Cells (SOFCs), the Co-Fe-O subsystem was thermodynamically re-modeled in the present work using the CALPHAD methodology. The solid phases were described using the Compound Energy Formalism (CEF) and the ionized liquid was modeled with the ionic two-sublattice model based on CEF. A set of self-consistent thermodynamic parameters was obtained eventually. Calculated phase diagrams and thermodynamic properties are presented and compared with experimental data. The modeling covers a temperature range from 298K to 3000K and oxygen partial pressure from 10^{-16} to 10^{2} bar. A good agreement with the experimental data was shown.

2.1 Introduction

LSCF ($La_{1-x}Sr_xCo_{1-y}Fe_yO_{3-\delta}$) is a mixed oxide ion and electron conductor. LSCF shows good conductivity and electro-catalytic activity at temperatures lower than 1000K and is recognized as a promising cathode material for solid oxide fuel cells (SOFCs) [1]. The phase relations in La-Sr-Co-Fe-O and the stability of the perovskite material are however unclear, which complicates further material development and application in SOFCs. To clarify these issues, we are currently developing a thermodynamic database of La-Sr-Co-Fe-O. Here, we present our work on thermodynamic modeling of the Co-Fe-O subsystem.

Oxide phases in the Co-Fe-O system, such as spinel and halite (cobaltowustite), also find their own applications. The spinel phase shows both ferromagnetic and electronic properties. It has attracted a great deal of research efforts due to its importance in metal oxides [2], in oxygen separation membranes [3] and in soft magnetic material [4]. Knowledge of accurate thermodynamic information on the Co-Fe-O system is therefore important.

The Co-Fe-O system has previously been modeled by a few groups. Pelton *et al.* [5] modeled parts of the Co-Fe-O system where the spinel solid solution Co_3O_4-Fe_3O_4 and the halite phase $(Co, Fe)O_{1+\delta}$ were considered. The calculated phase equilibria show deviation from experimentally determined ones [6−10]. Later, Subramanian *et al.* [11] modeled the Co-Fe-Mn-O system at 1473K. The isothermal $\log P_{O_2}$-composition phase diagram and cation distribution in the spinel phase were calculated.

Recently, this system was modeled by Jung *et al.* [12], who used the Quasichemical model to describe the liquid phase, and by Weiland [13], who used the two-sublattice model for the liquid phase and a neutral species $FeO_{1.5}$ was introduced into the second sublattice for anions, vacancies and neutral species. These two liquid phase models are unfortunately incompatible with the liquid phase model used for other subsystems within La-Sr-Co-Fe-O, in which the ionic two-sublattice model was used and no neutral species $FeO_{1.5}$ was included [14−17]. Besides, the works by Jung *et al.* [12] and by Weiland [13] both show that the $CoFe_2O_4$ spinel is unstable at $T < 700$ K in air, in contradiction with experimental findings [4, 18, 19]. In the present work, we have remodeled the Co-Fe-O system as part of the project for developing a thermodynamic database of La-Sr-Co-Fe-O with a focus on ternary oxide solution phases (spinel and halite).

2.2 Literature review

The present study started with critical evaluation of available thermodynamic and phase diagram data from literature for the Co-Fe-O system. Table 2.1 gives an overview of the experimental data reported in the literature. Beside the oxide liquid phase, two ternary oxide solid phases also exist in the Co-Fe-O system: spinel-structured (Co, Fe)$_3$O$_4$ solution phase and rock salt structured (Co, Fe) $_{1-\delta}$O solution phase (Halite).

2.2.1. Solid solution phases

I. Spinel

The spinel is a type of minerals with a general formula of AB_2O_4. It crystallises in a cubic crystal lattice, with oxide anions arranged in a close-packed face-centered cubic (FCC) lattice and cations filling one-eighth of the tetrahedral interstitial sites and one half of the octahedral interstitial sites. If the B cations are most abundant on the octahedral sites, the spinel is called normal; if the B cations distribute evenly between the tetrahedral and octahedral sites, the spinel is called inverse [18]. In the Co-Fe-O system, the spinel phase covers the composition range from pure Co_3O_4 to pure Fe_3O_4. The most well studied is the one with a composition of $CoFe_2O_4$. It is a complete inverse type at room temperature, which means half of the Fe^{3+} ions occupy the tetrahedral-sites and the rest, together with Co^{2+} ions, occupy the octahedral-sites [4]. With increasing temperature, cation redistribution takes place in $CoFe_2O_4$ [4, 19−27].

Groups of authors have investigated the cation distribution in the (Co, Fe)$_3$O$_4$ spinel and its temperature dependence using Mössbauer spectroscopy or other methods in order to clarify the influence of cation distribution on magnetic, electrical or photochemical properties [4, 19−27]. The experimental results show a large scatter, which is most probably due to various thermal treatment conditions used in these studies.

The cation distribution in the $CoFe_2O_4$ spinel was investigated by a number of groups [4, 19−22]. Sawatzky *et al.* [20] heat treated $CoFe_2O_4$ powders at 1473K for 48h and afterwards cooled to room temperature. Two cooling approaches were employed: furnace cooling and quenching in water. The cation distribution was then determined at room temperature using Mössbauer spectroscopy. They reported that the furnace cooled sample has 4 at.% Co^{2+} cation on tetrahedral site, which is less than a fifth of what is observed on the water quenched one (21 at.%). Later [21], they made corrections on the previous results and reported 24 at.% Co^{2+} on the

Table 2.1 Summary of the experimental data from literatures

Reference	Type of data	Experimental methods	Temperature (K)	Remark [a]
	I. Cation distribution and other thermodynamic properties			
[4]	Cation distribution in $CoFe_2O_4$	Mössbauer spectroscopy (MS)	298−1473	+
[20, 21]	Cation distribution in $CoFe_2O_4$	MS	1473	+
[21]	Cation distribution in $CoFe_2O_4$	MS	1173 and 1523	−
[19]	Cation distribution in $CoFe_2O_4$	XRD	1673	−
[22]	Cation distribution in $CoFe_2O_4$	Synchrotron radiation (SR)	X [b]	−
[23]	Cation distribution in $CoFe_2O_4$	MS and infrared spectroscopy (IS)	1473	−
[25]	Cation distribution in $CoFe_2O_4$, $Co_{1.5}Fe_{1.5}O_4$, $FeCo_2O_4$ and $Co_{0.5}Fe_{0.5}O_4$	MS	1320, 1193, 1152	+
[26]	Cation distribution in Fe_3O_4-$CoFe_2O_4$	*In situ* high temperature thermo-power measurements	873 to 1573	−
[27]	Cation distribution in $CoFe_2O_4$ and $FeCo_2O_4$	XRD and MS	1170	−
[18]	Cation distribution in $CoFe_2O_4$	MS	1473	+
[28]	Cation distribution in $Co_{0.68}Fe_{2.32}O_4$ and $Co_{0.5}Fe_{2.5}O_4$	MS	1473	−
[29]	Heat capacity of $CoFe_2O_4$	Resistance measurement	473−973	+
[30]	Heat capacity of $CoFe_2O_4$ and $FeCo_2O_4$	Calorimetry	51−298	+
[31]	Heat capacity, enthalpy and Curie point for $CoFe_2O_4$	Calorimetry	673−1173	+
[32]	Enthalpy of formation of $CoFe_2O_4$	Calorimetry	973	+
[33]	Heat capacity and enthalpy of $CoFe_2O_4$	Calorimetry	400−1300	+
[34]	Enthalpy of formation and entropy of $CoFe_2O_4$	Calorimetry	298.15	+
[35]	Heat capacity of $CoFe_2O_4$	Calorimetry	298−940	+
[36]	Activity of Fe_3O_4 in spinel coexisting with Fe_2O_3	Electromotive force (EMF)	1100−1300	−
[8]	1. Activity of Co oxide and Fe_3O_4 in the spinel. 2. Gibbs energy of formation of $CoFe_2O_4$ from CoO and Fe_2O_3	Thermogravimetry (TG) and XRD	1473	+
[8]	Cation deficiency in $(Co_xFe_{1-x})_{1-\delta}O$	TG	1473	+
[37]	Cation deficiency in $(Co_xFe_{1-x})_{1-\delta}O$	TG	1273−1373	+
[41]	Cation deficiency in $(Co_xFe_{1-x})_{1-\delta}O$ x>0.6	TG	1473	+
[38]	Cation deficiency in $(Co_xFe_{1-x})_{1-\delta}O$	EMF	1473	+
[38]	CoO and FeO activity in halite	EMF	1173−1473	+
[42]	Activity of CoO in halite in equilibrium with FCC	XRD	1473	+
[43]	Activity of CoO in halite in equilibrium with the metal phases	EMF	1073, 1173, 1273	−
	II. Phase diagram data			
[44]	Phase diagram in air	XRD	Up to 1273	+
[10]	Phase equilibria between the solid phases and the oxide melt in air	SEM and XRD	1800−2000	−
[45]	Phase diagram in air on the Co rich side	XRD	773−1773	+
[6]	Isothermal section at 1473K (Fe-rich part)	XRD	1473	−
[12]	Phase boundary between halite and halite+spinel in air	SEM and EPMA	1473	+
[46]	Isothermal PO_2-composition phase diagrams from Fe_3O_4 to $(Fe_3O_4)_{0.4}(CoFe_2O_4)_{0.6}$	EMF	1173−1473	+
[47]	Isothermal PO_2-composition phase diagrams	EMF	1173−1573	+
[36]	Isothermal PO_2-composition phase diagrams (Fe-rich side)	EMF	1123−1323	+
[2]	Isothermal PO_2-composition phase diagrams	EMF, XRD, SEM&EDS	1300	+
[48][49]	Lattice parameter and isothermal PO_2-composition phase diagrams	High temperature XRD	973−1273	−
[9, 40, 50]	Isothermal PO_2-composition phase diagrams	TG	1473	+
[8]	Isothermal PO_2-composition phase diagrams	TG	1473	+
[7]	Isothermal PO_2-composition phase diagrams	TG	1273−1373	−

[a] This column indicates whether the data were used (+) in the optimization or not (−).
[b] X means that the samples might not be in equilibrium state.

tetrahedral site in the water quenched sample. Popescu & Chizdeanu [19] determined the cation distribution in samples annealed at 1673K with furnace cooling, using X-ray diffraction (XRD), but without differentiating cations with different valence states. Yakel [22] determined the Co site fraction on the octahedral site in a single crystal $CoFe_2O_4$ using energy-tuned synchrotron radiation. The $CoFe_2O_4$ single crystal was culled from an ingot, which was made by induction melting of CoO and Fe_2O_3 under CO_2 flow at 1823K and rapidly cooled to room temperature. The valence state of cobalt ion was not verfied in this study. Van Noort *et al.* [23] measured cation distribution in $CoFe_{2-x}Al_xO_4$ (x=0.1−1). The powder samples were first annealed at 1523K for 24h in oxygen. Some of the powder samples were further annealed at 1173K in oxygen for 1 hour. All the samples were furnace cooled. They found that further annealing at 1173K resulted in almost no change in the Co^{2+} concentration on the tetrahedral site, which was determined as 18 at.% by extrapolating to x=0. Na *et al.* [4] measured the magnetic properties of $CoFe_2O_4$ at various temperatures, and the results were correlated to the Co content in the spinel lattice sites. The samples were first sintered at 1573K for 5h and furnace cooled. The samples were re-heated at different temperatures and cooled in compressed Ar to room temperature. The duration of the second heat treatment was not stated in the paper. Amer and Hemeda [24] studied spinel ferrite system $Co_{1-x}Cd_xFe_2O_4$ using Mössbauer spectroscopy and infrared spectroscopy. The pellet samples were sintered at 1473K for 6h and cooled slowly to room temperature.

The cation distribution in spinel of compositions other than $CoFe_2O_4$ has also been investigated. Murray and Linnett [25] measured the distribution of Fe ions between octahedral and tetrahedral sites in four spinels having the general formula $Co_xFe_{3-x}O_4$. Samples were heat treated at different temperatures for different periods before being quenched in water. The atmosphere was not specified. Erickson and Mason [26] reported cation distributions in the system Fe_3O_4-$CoFe_2O_4$ from 873 to 1573K based on *in situ* high temperature thermopower measurements. The samples were sintered at 1573K for 5h. Ferreira *et al.* [27] measured cation distribution in $CoFe_2O_4$ and $FeCo_2O_4$ spinels using XRD, Mössbauer spectroscopy, SEM&EDS, Atomic Absorption Spectroscopy, and Inductively Coupled Plasma Emission Spectroscopy. The site fraction of Co^{2+} on the tetrahedral site was reported to be 0.24 for $CoFe_2O_4$. For $FeCo_2O_4$, pure single phase was observed at 1170K, and the cation distribution was proposed as $(0.46Co^{2+}, 0.54Fe^{3+})_1$ $[0.27Co^{2+}, 0.23Fe^{3+}, 0.5Co^{3+}]_2$ O_4. Here in this paper, we use round parentheses and square brackets to denote the tetrahedral and octahedral sites in the spinel, respectively.

DeGuire *et al.* [18] investigated the influence of cooling rate on cation distribution in spinel. The samples were heat treated in air at 1573K for 10−13h and cooled at rates between 10^{-2} and 10^{3}°C/s. The cation distribution in bulk $CoFe_2O_4$ was then determined at room temperature using Mössbauer spectroscopy. The degree of departure from the inverse distribution observed at room temperature (to normal type distribution) increased with increasing cooling rate. The results indicate that it is hard to maintain the high temperature cation distribution at room temperature with furnace cooling. The more rapidly cooled sample exhibited the smaller departure from the equilibrium condition. Later, they [28] determined the cation distributions in two rapidly solidified samples with composition of $Co_{0.68}Fe_{2.32}O_4$ and $Co_{0.5}Fe_{2.5}O_4$ at 1473K. The samples were obtained by gas atomization of CoO-Fe_2O_3-P_2O_5 melts.

The thermodynamic properties of $CoFe_2O_4$ are well studied in literature [29−35]. Bochirol [29] first reported the heat capacity of $CoFe_2O_4$ at temperatures between 473 and 973K. Experimental details regarding sample preparation and phase identification were not mentioned. King [30] conducted calorimetry measurements to determine heat capacity of $CoFe_2O_4$ and of $FeCo_2O_4$ at low temperature (50−300K). Their samples were prepared by solid state reactions of cobaltous and ferric oxides. The entropy of $CoFe_2O_4$ and $FeCo_2O_4$ at 298.15 K was reported as 134.6±2 J/mol K and 125.5±1 J/mol K, respectively. Aukrust and Muan [8] determined the Gibbs energy of formation of $CoFe_2O_4$ from CoO and Fe_2O_3 to be −34.3 kJ/mol at 1473K. Landiya *et al.* [31] carried out calorimetry, thermogravimetry and ballistic measurements on $CoFe_2O_4$ and reported its enthalpy at temperatures between 400 and 900°C and its ferromagnetic transition temperature as 773K. The heat capacity of $CoFe_2O_4$ was then derived based on these measurements. Navrotsky and Kleppa [32] determined the enthalpy of formation for $CoFe_2O_4$ from CoO and Fe_2O_3 by solution calorimetry measurements in molten oxide solvents. The enthalpy of formation for $CoFe_2O_4$ was reported as −24.64±0.88 kJ/mol at 970K and the entropy of formation (lattice entropy) was reported as 0.84 kJ/(mol K). Chachanidze [33] measured heat capacity and enthalpy of $CoFe_2O_4$ calorimetrically at temperature up to 1300 K. The magnetic contribution to the heat capacity was also determined. Kubaschewski *et al.* [34] reported the standard enthalpy and entropy of formation for $CoFe_2O_4$ at 298.15 K, as −1088.7 ± 4.6 kJ/mol and 142.7 ± 8.4 J/mol K, respectively. Reznitskii *et al.* [35] conducted adiabatic calorimetry measurements to determine heat capacity of $CoFe_2O_4$ at 298−940K. Their measured Cp shows a maximum at 784K, lower than the determined Curie temperature (810K). The heat content,

standard enthalpy of formation and entropy were then derived. Katayama *et al.* [36] carried out EMF measurements to determine the Fe_3O_4 activity in the $Co_xFe_{3-x}O_4$ (x=0−1) spinel solid solution in coexistence with Fe_2O_3 at temperatures between 1100K and 1300K. The Fe_3O_4 activity shows a small negative deviation from Raoult's law in the entire composition range and obeys Henry's law at x= 0−0.4.

II. Halite

Both CoO and FeO are of rock salt (Halite) structured phases, and they form a solid solution in the Co-Fe-O system called *Cobaltowustite* (denoted as the halite phase in this paper). In the halite structure, oxygen ions form an FCC sublattice, nearly dense packed, and octahedral interstices are filled with cations. The cation to anion ratio in halite structured oxides containing transition metal ions is in general smaller than one, i.e. a cation deficiency exists.

The cation deficiency in the halite phase was determined by various groups [8, 37, 38]. Aukrust and Muan [8] carried out a thermogravimetry study on $(Co_xFe_{1-x})_{1-\delta}O$ ($0<x<1$) at 1473K. A similar study was made by Raeder *et al.* [37] on a number of selected compositions. The phases of the samples were however not characterized, and some of the investigated compositions were actually located outside the halite single phase region. Besides, in both studies [8, 37], the samples were in contact with platinum during the thermogravimetry measurements. Dieckmann [39] reported that non-stoichiometry data for transition metal oxides may be inaccurate if the samples were in contact with platinum during the measurements, especially at low oxygen activities. The data from Aukrust and Muan [8] and from Raeder *et al.* [37] were therefore not used in the optimization. Thermogravimetry measurements on cation deficiency in $(Co_xFe_{1-x})_{1-\delta}O$, have also been carried out by Maksutov [40] at temperatures between 1273 and 1473K and by Subramanian *et al.* [41] at 1473K and $x\geq0.6$. Lykasov *et al.* [38] determined the oxygen content in $(Co_xFe_{1-x})_{1-\delta}O$ as a function of external oxygen activity and the Fe/Co ratio at 1273 K and 1473 K.

Activity measurements on halite were conducted by a few groups using EMF. Lykasov *et al.* [38] measured activity of CoO and FeO in the halite phase at 1173 K−1473K. The temperature dependence of the CoO activity is negligible according to their results. Aukrust and Muan [42] determined the CoO activity in the halite phase coexisting with FCC at 1473K. A small positive deviation from the ideal solution was detected. Seetharaman and Abraham [43] measured the CoO activity in the halite phase coexisting with metallic phases at 1073, 1173, and 1273K. A

large positive deviation from Raoult's law was detected and the extent of deviation decreases with increasing temperature, which is in conflict with the results from Lykasov *et al.* [38].

2.2.2 Phase diagrams

The phase equilibria in the Co-Fe-O system have been investigated by a large number of groups and various types of phase diagrams have been published in the literature, which includes phase diagrams in air or at a fixed oxygen partial pressure, and isothermal P_{O_2}-composition phase diagrams *etc.*

Robin and Benard [44] first investigated phase eqilibria in CoO_x-FeO_y in air. A series of iron and cobalt oxide mixtures were heat treated at temperatures up to 1273K in air and characterized using XRD. A miscibility gap was reported for the spinel phase. However, insufficient information was given on the phase boundaries. Masse and Muan [10] studied phase equilibria between the solid phases and the oxide melt in air using microscopy and XRD, as part of their study on FeO-CoO-SiO. Takahashi and Morris [45] determined the phase diagram of CoO_x-FeO_y in air for the Co rich side, with a major focus on the spinel miscibility gap. Their samples were prepared by co-precipitation. The phase boundaries were determined based on XRD results. Smiltens [6] studied the Fe-rich region in Co-Fe-O using XRD and published an incomplete isothermal section at 1473K.

A number of isothermal P_{O_2}-composition phase diagrams at different temperatures, determined mainly from Electromotive force (EMF) measurements, have been published in the literature [2, 36, 46−50]. Carter [46] determined the phase boundary between the spinel single phase region and the spinel+halite two-phase region in a composition range from Fe_3O_4 to $0.4Fe_3O_4$-$0.6CoFe_2O_4$. Four temperatures between 1173 and 1473K were selected in his study. Schmalzried and Tretjakow [47] determined equilibrium oxygen partial pressure of spinel coexisting with halite between 1173−1573K, while Katayama *et al.* [36] studied the one of corundum (Fe_2O_3) coexisting with spinel (Fe_3O_4-$CoFe_2O_4$) at 1123, 1223 and 1323K. Lundberg and Rosén [2] carried out EMF measurements in a temperature range of 970 to 1370K. The equilibrium phases were identified by XRD and the compositions were determined by SEM&WDS for samples equilibrated at 1300K. The FeO activity in the halite phase at 1300K was derived. Roiter and Paladina [7] reported equilibrium oxygen pressure in the Co_3O_4-$CoFe_2O_4$ region at temperatures between 1273 and 1573K. The results were carefully verified by chemical analysis, XRD, weight-loss determination, and pressure measurements. Touzelin carried out high

temperature XRD measurements under controlled atmosphere at 1173K [48], 973K and 1273K [49]. The phase boundaries were determined based on measured lattice parameters. A few groups [8−9, 40, 50] conducted thermogravimetry measurements to measure weight change associated with phase transition at controlled oxygen activity. The equilibrium oxygen partial pressures of the relevant phase transformations were then estimated. Inconsistency exists between the phase boundaries determined by Roiter and Paladino [7] and those by Aukrust and Muan [8]. Later Jung *et al.* [12] re-determined the phase boundaries by SEM and Electron Probe Micro-analyzer (EPMA) and their new data are in good agreement with those from Roiter and Paladino [7]. In the present work, the data from Aukrust and Muan [8] were not included in the optimization.

2.3 Thermodynamic modeling

In the present work, the thermodynamic description of the Co-Fe-O system is based on the descriptions of recently reassessed subsystems: Co-O by Chen *et al.* [51], Fe-O by Sundman [52] and Kjellqvist *et al.* [53], and Co-Fe by Ohnuma *et al.* [54]. The lattice stabilities of pure elements were adopted from Dinsdale [55]. The magnetic contribution to the Gibbs energy is given by the "Hillert–Jarl–Inden" model proposed by Inden [56] and further revised by Hillert and Jarl [57]. The compound energy formalism (CEF) [58], which is widely used in CALPHAD assessments, was used to model all the phases in Co-Fe-O.

2.3.1 Liquid

The liquid phase was modeled using the ionic two–sublattice model [59, 60], which was developed within the framework of the CEF, with one sublattice containing charged cations and the other containing charged anions and vacancies. The liquid phase in Fe-O was modeled as $(Fe^{2+}, Fe^{3+})_p(O^{2-},Va^{q-})_q$ by Sundman [52] and in Co-O as $(Co^{2+}, Co^{3+})_p(O^{2-},Va^{q-})_q$ by Chen *et al.* [51]. In the present work, the model for the liquid phase in Co-Fe-O is as the following:

$(Co^{2+}, Co^{3+}, Fe^{2+}, Fe^{3+})_p(O^{2-},Va^{q-})_q$

Where $p=2y_{O^{2-}}+qy_{Va}$ (2.1)

$q=2y_{Co^{2+}}+3y_{Co^{3+}}+2y_{Fe^{2+}}+3y_{Fe^{3+}}$ (2.2)

The Gibbs energy of the liquid phase is expressed as:

$$G_m^L = q\sum_i y_i y_{Va}\,{}^0G_{i:Va}^L + \sum_i y_i y_{O^{2-}}\,{}^0G_{i:O^{2-}}^L + pRT\sum_i y_i \ln y_i + qRT\sum_j y_j \ln y_j + {}^EG_m^L \quad (2.3)$$

Where i represents the constituents in the first sublattice, and j represents the constituents in the second sublattice. The excess Gibbs energy ${}^{E}G_m^L$ is formulated as the following:

$${}^{E}G_m^L = \sum_{i_m}\sum_{i_n \neq i_m} y_{i_m} y_{i_n} (y_{O^{2-}} L^L_{i_m,i_n:O^{2-}} + q y_{Va}{}^2 L^L_{i_m,i_n:Va}) + \sum_{i_m} y_{i_m} y_{O^{2-}} y_{Va} L^L_{i_m:O^{2-},Va} \quad (2.4)$$

where i_m and i_n represents the constituents in the first sublattice. In the above expressions, colons were used to separate species on different sublattices and commas to separate species on the same sublattice. The Gibbs energy expressions for the eight end-members were taken from the binary subsystems: ${}^{o}G^L_{Co^{2+}:VA}$, ${}^{o}G^L_{Co^{2+}:O^{2-}}$, ${}^{o}G^L_{Co^{3+}:O^{2-}}$, ${}^{o}G^L_{Co^{3+}:VA}$ from Co-O [51] and ${}^{o}G^L_{Fe^{2+}:VA}$, ${}^{o}G^L_{Fe^{2+}:O^{2-}}$, ${}^{o}G^L_{Fe^{3+}:O^{2-}}$, ${}^{o}G^L_{Fe^{3+}:VA}$ from Fe-O [52]. Interaction parameters $L^L_{m:O^{2-},Va}$ were taken also from Co-O [51] and Fe-O [52].

2.3.2 Halite (Cobaltowustite solution, $(Co,Fe)_{1-\delta}O$)

Due to the fact that wustite in Fe-O has a considerable cation deficiency, Sundman [52] modeled it as $(Fe^{2+}, Fe^{3+}, Va)_1(O^{2-})_1$. On the contrary, CoO was treated as a stoichiometric compound in Chen *et al.*'s work [51], due to its negligible cation deficiency. In the present work, the halite solid solution was modeled as $(Co^{2+}, Fe^{2+}, Fe^{3+}, Va)_1(O^{2-})_1$. Its Gibbs energy can be expressed as

$$G_m^{Halite} = \sum_i y_i \, {}^{0}G^{Halite}_{i:O^{2-}} + RT\sum_i y_i \ln y_i + {}^{E}G_m^{Halite} \quad , \quad (2.5)$$

where i represents the constituents in the first sublattice. The excess Gibbs energy ${}^{E}G_m^{Halite}$ is expressed as below:

$${}^{E}G_m^{Halite} = \sum_{i_m}\sum_{i_n \neq i_m} y_{i_m} y_{i_n} y_{O^{2-}} L^{Halite}_{i_m,i_n:O^{2-}} \quad (2.6)$$

where m and n represents the constituents in the first sublattice. The parameters for the binary Co-O and Fe-O subsystems were taken from Chen *et al.* [51] and Sundman [52].

2.3.3 Hematite (Corundum, Fe_2O_3)

Due to the fact that Co has no solubility in Fe_2O_3, in the present work, the Gibbs energy expression for the Hematite phase (Fe_2O_3) was taken from Fe-O without modification. Selleby and coworkers [61, 62] first modeled Fe_2O_3 as stoichiometric compound. Later Kjellqvist *et al.* [53]

remodeled Fe_2O_3 as $(Fe^{2+}, Fe^{3+})_2(Fe^{3+},Va)_1(O^{2-})_3$. An interstitial sublattice containing Fe^{3+} and Va was introduced in order to describe diffusivity of ionic species. To maintain charge neutrality, Fe^{2+} was introduced to the first sublattice. The description from Kjellqvist *et al.* [53] was employed in the present work.

2.3.4 Spinel

Among all the phases in Co-Fe-O, spinel is the most complicate one. The spinel solid solution spans from pure Co_3O_4 to pure Fe_3O_4 and can be treated as based on three major components: Co_3O_4, Fe_3O_4 and $CoFe_2O_4$. The Co_3O_4 spinel is a normal spinel at room temperature and with cation redistribution at high temperatures. Fe_3O_4 and $CoFe_2O_4$ are of the inverse type. Different models were used for the spinel phase in Co-O and Fe-O [51, 52]. Chen *et al.* [51] used a 3-sublattice model for Co_3O_4: $(Co^{2+},Co^{3+})_1[Co^{2+},Co^{3+}]_2\ (O^{2-})_4$. The first sublattice is for tetrahedral site, the second for octahedral sites and the third for oxygen anions. In the thermodynamic description of the Fe-O system [52, 53], an extra sublattice containing Fe^{2+} was introduced to allow for deviation from stoichiometric Fe_3O_4 towards an excess of Fe in equilibrium with wustite and liquid at high temperature. Additionally, cation vacancy was introduced into the conventional octahedral sites to allow for deviation from stoichiometry to oxygen rich (i.e. cation deficiency) at higher oxygen partial pressure. The model reads as $(Fe^{2+},Fe^{3+})_1[Fe^{2+},Fe^{3+},Va]_2\{Fe^{2+},Va\}_2(O^{2-})_4$. Furthermore, the thermodynamic model for spinel phase is still under development and the discussion never stops [63]. To simplify the modeling effort in the present work, the spinel phase in Co-Fe-O was modeled as

$(Co^{2+},Co^{3+},Fe^{2+},Fe^{3+})_{1tet}[Co^{2+},Co^{3+},Fe^{2+},Fe^{3+},Va]_{2oct}\ (O^{2-})_4$

The Gibbs energy of the spinel phase is given by the following expression:

$$G_m^{spinel} = \sum_i \sum_j y_i^T y_j^O\, {}^0G_{i:j:O^{2-}}^{spinel} + RT\sum_i y_i^T \ln y_i^T + 2RT\sum_j y_j^O \ln y_j^O + {}^EG_m^{spinel} \qquad (2.7)$$

Where i represents the constituents in the first sublattice, and j represents the constituents in the second sublattice.

According to the current model, there are 20 end-members which need to be assigned with a Gibbs energy term and should be thermodynamically reasonable. In order to make the boundary systems correct, one parameter for Co-O was taken from Chen *et al.* [51], while another six for Fe-O were taken from Sundman [52]. In order to incorporate this set of parameters into the

descriptions of spinel phase in higher ordered systems, the reference ${}^{o}G^{Spinel}_{Fe^{3+}:Fe^{2+}:O^{2-}} = {}^{o}G^{Spinel}_{Fe^{2+}:Fe^{3+}:O^{2-}}$ used for spinel phase in the Fe-O system was chosen [63]. The Gibbs energy terms for the remaining 13 end-members were defined and determined in the present work. Most of these end-members have a net charge and cannot physically exist or can be present only in neutral combinations. Thus, the number of independent parameters should be much less than this. Our strategy is to model the spinel phase by choosing appropriate neutral end-members or their combinations as model parameters, which can be optimized using experimental data. The most important end-members and combinations chosen in the present work are $(Co^{2+})_1[Fe^{3+}]_2(O^{2-})_4$ and $(Fe^{3+})_1[Co^{2+}{}_{1/2},\ Fe^{3+}{}_{1/2}]_2(O^{2-})_4$. They are schematically illustrated in Fig. 2.1, together with the description for Co_3O_4.

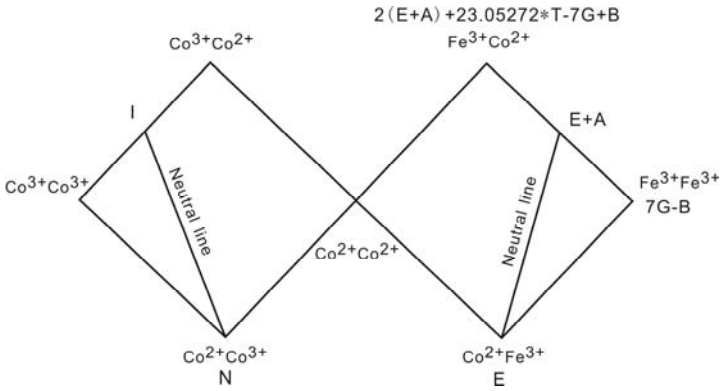

Fig. 2.1. Schematic illustration of Gibbs energy terms for some of the end-members in the Co_3O_4 –$CoFe_2O_4$ system. The overall composition will lie on the plane connected by the two neutral lines as indicated in the figure.

$(Co^{2+})_1[Fe^{3+}]_2(O^{2-})_4$ corresponds to $CoFe_2O_4$ of the normal type. In the present work, its Gibbs energy is formulated as:

$${}^{o}G^{Normal-Spinel}_{CoFe_2O_4} = {}^{o}G^{Spinel}_{Co^{2+}:Fe^{3+}:O^{2-}} = a_1 + b_1 * T + c_1 * T * \ln(T) + d_1 * T^2 + e_1 * T^{-1} = E \qquad (2.8)$$

$(Fe^{3+})_1[Co^{2+}{}_{1/2},\ Fe^{3+}{}_{1/2}]_2(O^{2-})_4$ corresponds to $CoFe_2O_4$ of the inverse type. As Fig. 1 shows, its Gibbs energy is given by:

$${}^{o}G^{Invers-Spinel}_{CoFe_2O_4} = \frac{1}{2}\,{}^{o}G^{Spinel}_{Fe^{3+}:Co^{2+}:O^{2-}} + \frac{1}{2}\,{}^{o}G^{Spinel}_{Fe^{3+}:Fe^{3+}:O^{2-}} - 2RT\ln 2 = E + A \qquad (2.9)$$

$A = a_2 + b_2 * T$ (2.10), a_1, b_1, c_1, d_1, e_1, a_2 and b_2 are variables to be optimized in the present work. According to Fig. 1, the end-members ${}^{o}G^{Spinel}_{Co^{2+}:Co^{2+}:O^{2-}}$ ${}^{o}G^{Spinel}_{Co^{3+}:Co^{2+}:O^{2-}}$ and ${}^{o}G^{Spinel}_{Co^{3+}:Co^{3+}:O^{2-}}$ can be solved by the reciprocal relations:

$$ {}^{o}G^{Spinel}_{Fe^{3+}:Fe^{3+}:O^{2-}} + {}^{o}G^{Spinel}_{Co^{2+}:Co^{2+}:O^{2-}} - {}^{o}G^{Spinel}_{Co^{2+}:Fe^{3+}:O^{2-}} - {}^{o}G^{Spinel}_{Fe^{3+}:Co^{2+}:O^{2-}} = \Delta G_1 \quad (2.11) $$

$$ {}^{o}G^{Spinel}_{Co^{2+}:Co^{2+}:O^{2-}} + {}^{o}G^{Spinel}_{Co^{3+}:Co^{3+}:O^{2-}} - {}^{o}G^{Spinel}_{Co^{3+}:Co^{2+}:O^{2-}} - {}^{o}G^{Spinel}_{Co^{2+}:Co^{3+}:O^{2-}} = \Delta G_2 \quad (2.12) $$

and description for the Gibbs energy of the inverse Co_3O_4 spinel [51],

$$ {}^{o}G^{Invers-Spinel}_{Co_3O_4} = \frac{1}{2}\,{}^{o}G^{Spinel}_{Co^{3+}:Co^{3+}:O^{2-}} + \frac{1}{2}\,{}^{o}G^{Spinel}_{Co^{3+}:Co^{2+}:O^{2-}} - 2RT\ln 2 = I \quad (2.13) $$

All the other unknown end-members are correlated in the following reciprocal relations:

$$ {}^{o}G^{Spinel}_{Fe^{2+}:Fe^{3+}:O^{2-}} + {}^{o}G^{Spinel}_{Co^{2+}:Co^{3+}:O^{2-}} - {}^{o}G^{Spinel}_{Co^{2+}:Fe^{3+}:O^{2-}} - {}^{o}G^{Spinel}_{Fe^{2+}:Co^{3+}:O^{2-}} = \Delta G_3 \quad (2.14) $$

$$ {}^{o}G^{Spinel}_{Fe^{3+}:Fe^{3+}:O^{2-}} + {}^{o}G^{Spinel}_{Co^{2+}:Co^{3+}:O^{2-}} - {}^{o}G^{Spinel}_{Co^{2+}:Fe^{3+}:O^{2-}} - {}^{o}G^{Spinel}_{Fe^{3+}:Co^{3+}:O^{2-}} = \Delta G_4 \quad (2.15) $$

$$ {}^{o}G^{Spinel}_{Co^{2+}:Fe^{3+}:O^{2-}} + {}^{o}G^{Spinel}_{Fe^{3+}:Fe^{2+}:O^{2-}} - {}^{o}G^{Spinel}_{Fe^{3+}:Fe^{3+}:O^{2-}} - {}^{o}G^{Spinel}_{Co^{2+}:Fe^{2+}:O^{2-}} = \Delta G_5 \quad (2.16) $$

$$ {}^{o}G^{Spinel}_{Co^{3+}:Co^{3+}:O^{2-}} + {}^{o}G^{Spinel}_{Fe^{3+}:Fe^{2+}:O^{2-}} - {}^{o}G^{Spinel}_{Fe^{3+}:Co^{3+}:O^{2-}} - {}^{o}G^{Spinel}_{Co^{3+}:Fe^{2+}:O^{2-}} = \Delta G_6 \quad (2.17) $$

$$ {}^{o}G^{Spinel}_{Co^{3+}:Co^{3+}:O^{2-}} + {}^{o}G^{Spinel}_{Fe^{3+}:Fe^{3+}:O^{2-}} - {}^{o}G^{Spinel}_{Fe^{3+}:Co^{3+}:O^{2-}} - {}^{o}G^{Spinel}_{Co^{3+}:Fe^{3+}:O^{2-}} = \Delta G_7 \quad (2.18) $$

$$ {}^{o}G^{Spinel}_{Fe^{2+}:Fe^{3+}:O^{2-}} + {}^{o}G^{Spinel}_{Fe^{3+}:Co^{2+}:O^{2-}} - {}^{o}G^{Spinel}_{Fe^{3+}:Fe^{3+}:O^{2-}} - {}^{o}G^{Spinel}_{Fe^{2+}:Co^{2+}:O^{2-}} = \Delta G_8 \quad (2.19) $$

$$ {}^{o}G^{Spinel}_{Co^{2+}:Fe^{2+}:O^{2-}} + {}^{o}G^{Spinel}_{Fe^{3+}:Va:O^{2-}} - {}^{o}G^{Spinel}_{Fe^{3+}:Fe^{2+}:O^{2-}} - {}^{o}G^{Spinel}_{Co^{2+}:Va:O^{2-}} = \Delta G_9 \quad (2.20) $$

$$ {}^{o}G^{Spinel}_{Co^{3+}:Fe^{2+}:O^{2-}} + {}^{o}G^{Spinel}_{Fe^{3+}:Va:O^{2-}} - {}^{o}G^{Spinel}_{Fe^{3+}:Fe^{2+}:O^{2-}} - {}^{o}G^{Spinel}_{Co^{3+}:Va:O^{2-}} = \Delta G_{10} \quad (2.21) $$

In this work, $\Delta G_x = 0\,(x{=}1{-}10)$ was chosen for convenience. The Gibbs energy terms for the 13 end-members can be obtained by solving Equations 2.8 to 2.21.

The excess Gibbs energy ${}^{E}G^{spinel}_{m}$ is formulated as the following:

$$ {}^{E}G^{spinel}_{m} = \sum_{i_l}\sum_{i_k \neq i_l}\sum_{j_m} y_{i_k} y_{i_l} y_{j_m} L^{spinel}_{i_k, i_l : j_m : O^{2-}} + \sum_{i_l}\sum_{j_m}\sum_{j_n \neq j_m} y_{i_l} y_{j_m} y_{j_n} L^{spinel}_{i_l : j_m, j_n : O^{2-}} \quad (2.22) $$

Where i_k, i_l represents the constituents in the first sublattice (tetrahedral), and j_m, j_n represents the constituents in the second sublattice (octahedral).

2.3.5 FCC_A1, BCC_A2 & HCP_A3

In the present work, the descriptions for the metallic phases, FCC_A1, BCC_A2, and HCP_A3, were taken from binary subsystems [51, 53, 54] with ideal extrapolation. No additional parameter was optimized.

2.3.6 Optimization

The experimental data utilized in the thermodynamic optimization were listed in Table 2.1. The evaluation of the model parameters was attained by recurrent runs of the PARROT program [64] in the Thermo-Calc software, which works by minimizing the square sum of the differences between experimental values and computed ones. In the optimization, each experimental datapoint was given with certain weight. The weights were adjusted during the assessment until most of the experimental data were accounted for within the claimed uncertainty limits.

During optimization, the parameters c_1, d_1, e_1 in Eq. 2.8 were first optimized using the heat capacity data. The parameters β and T_c were optimized with reported magnetic properties. The parameters a_1, a_2, b_1, b_2 in Eq. 2.8 and 2.10 were then optimized using the enthalpy and entropy data. In the end, the interaction parameters were optimized to achieve a good agreement with experimental phase diagram and cation distribution data.

For the halite phase, the interaction parameters $L^{Halite}_{Co^{2+},Fe^{3+}:O^{2-}}$ and $L^{Halite}_{Co^{2+},Fe^{2+}:O^{2-}}$ were optimized in the present work using mainly the phase boundary data. For the liquid phase, no ternary interaction parameter was optimized.

2.4 Results and discussion

After optimization, a set of self-consistent thermodynamic parameters were obtained eventually. Due to modifications in the thermodynamic descriptions of the Co_3O_4 and Fe_3O_4 phases, the Co-O and Fe-O phase diagrams and other thermodynamic properties were checked and they were similar to those in the original work [51, 52]. During this assessment, most extensive literature data (more than 500 datapoints) were used (as shown in Table 2.1). The complete set of thermodynamic parameters describing the Co-Fe-O system obtained in the present work is given in Table 2.2. The calculated thermodynamic properties and phase diagrams are shown in Fig. 2.2−2.9 and Table 2.3.

Table 2.2 Summary of the thermodynamic parameters in the Co-Fe-O system [a]

Liquid	Reference
$(Co^{2+}, Co^{3+}, Fe^{2+}, Fe^{3+})p(O^{2-}, Va^{q-})q$	

$p=2y_{O}^{2-}+qy_{Va}$ $\quad q=2y_{Co}^{2+}+3y_{Co}^{3+}+2y_{Fe}^{2+}+3y_{Fe}^{3+}$	
${}^{o}G^{L}_{Co^{2+}:Va}-H^{SER}_{Co}=GCOLIQ$	[51]
${}^{o}G^{L}_{Co^{3+}:Va}-H^{SER}_{Co}=2GCOLIQ+2GCOOS+GHSEROO-76314+103.63T-3GCOOLIQ$	[51]
${}^{o}G^{L}_{Co^{2+}:O^{-2}}-2H^{SER}_{Co}-2H^{SER}_{O}=2GCOOLIQ$	[51]
${}^{o}G^{L}_{Co^{3+}:O^{2-}}-2H^{SER}_{Co}-3H^{SER}_{O}=2GCOOS+GHSEROO-76314+103.63T$	[51]
$L^{L}_{Co^{2+}:O^{2-},Va}=182675-30.556T+(54226-20T)(y_{O^{2-}}-y_{Va})^{2}$	[51]
${}^{o}G^{L}_{Fe^{2+}:Va}-H^{SER}_{Fe}=GFELIQ$	[52]
${}^{o}G^{L}_{Fe^{3+}:Va}-H^{SER}_{Fe}=2GFELIQ-GFEOLIQ-179638+79.923T$	[52]
${}^{o}G^{L}_{Fe^{2+}:O^{2-}}-2H^{SER}_{Fe}-2H^{SER}_{O}=4GFEOLIQ$	[52]
${}^{o}G^{L}_{Fe^{3+}:O^{2-}}-2H^{SER}_{Fe}-3H^{SER}_{O}=5GFEOLIQ-179638+79.923T$	[52]
$L^{L}_{Fe^{2+},Fe^{3+}:O^{2-}}=-26362+13353(y_{Fe^{2+}}-y_{Fe^{3+}})$	[52]
$L^{L}_{Fe^{2+}:O^{2-},Va}=176681-16.368T+(-65655+30.869T)(y_{O^{2-}}-y_{Va})$	[52]
$L^{L}_{Co^{2+},Fe^{2+}:Va}=-9753.82+2757.96(y_{Co^{2+}}-y_{Fe^{2+}})^{2}$	[54]
Halite	
$(Co^{2+}, Fe^{2+}, Fe^{3+}, Va)_1(O^{2-})_1$	
$p=0.28$	[51]
${}^{0}T^{Halite}_{CCo^{2+}:O^{2-}}=-870 \quad {}^{0}\beta^{Halite}_{Co^{2+}:O^{2-}}=2.0$	[51]
${}^{o}G^{Halite}_{Co^{2+}:O^{2-}}-H^{SER}_{Co}-H^{SER}_{O}=GCOOS$	[51]
${}^{o}G^{Halite}_{Fe^{2+}:O^{2-}}-H^{SER}_{Fe}-H^{SER}_{O}=GFEO$	[52]
${}^{o}G^{Halite}_{Fe^{3+}:O^{2-}}-H^{SER}_{Fe}-H^{SER}_{O}=+1.25GFEO+1.25GAFEO$	[52]
${}^{o}G^{Halite}_{Va:O^{2-}}-H^{SER}_{O}=0$	[52]
$L^{Halite}_{Fe^{2+},Fe^{3+}:O^{2-}}=-12324+20070(y_{Fe^{2+}}-y_{Fe^{3+}})$	[52]
${}^{0}L^{Halite}_{Co^{2+},Fe^{2+}:O^{2-}}=3441.85$	This work
${}^{0}L^{Halite}_{Co^{2+},Fe^{3+}:O^{2-}}=-3766.51+9.868T$	This work
Hematite (Corundum)	
$(Fe^{2+},Fe^{3+})_2(Fe^{3+},Va)_1(O^{2-})_3$	
$p=0.28$	[53]
${}^{0}T^{Hematite}_{CFe^{2+}:Va:O^{2-}}={}^{0}T^{Hematite}_{CFe^{3+}:Va:O^{2-}}={}^{0}T^{Hematite}_{CFe^{2+}:Fe^{3+}:O^{2-}}={}^{0}T^{Hematite}_{CFe^{3+}:Fe^{3+}:O^{2-}}=-2867$	[53]
${}^{0}\beta^{Hematite}_{Fe^{2+}:Va:O^{2-}}={}^{0}\beta^{Hematite}_{Fe^{3+}:Va:O^{2-}}={}^{0}\beta^{Hematite}_{Fe^{2+}:Fe^{3+}:O^{2-}}={}^{0}\beta^{Hematite}_{Fe^{3+}:Fe^{3+}:O^{2-}}=-25.1$	[53]
${}^{o}G^{Hematite}_{Fe^{2+}:Fe^{3+}:O^{2-}}-3H^{SER}_{Fe}-3H^{SER}_{O}=GFE2O3+85000$	[53]
${}^{o}G^{Hematite}_{Fe^{3+}:Fe^{3+}:O^{2-}}-3H^{SER}_{Fe}-3H^{SER}_{O}=GFE2O3+85000$	[53]
${}^{o}G^{Hematite}_{Fe^{2+}:Va:O^{2-}}-2H^{SER}_{Fe}-3H^{SER}_{O}=GFE2O3$	[53]
${}^{o}G^{Hematite}_{Fe^{3+}:Va:O^{2-}}-2H^{SER}_{Fe}-3H^{SER}_{O}=GFE2O3$	[53]
Spinel	

$(Co^{2+},Co^{3+},Fe^{2+},Fe^{3+})_1[Co^{2+},Co^{3+},Fe^{2+},Fe^{3+},Va]_2\ (O^{2-})_4$	
${}^oG^{Spinel}_{Co^{2+}:Co^{3+}:O^{2-}} - 3H^{SER}_{Co} - 4H^{SER}_{O} = NCO3O4$	[51]
${}^oG^{Spinel}_{Co^{2+}:Co^{2+}:O^{2-}} - 3H^{SER}_{Co} - 4H^{SER}_{O} = 3ECOFE2O4 - 14GFE3O4 + 2BFE3O4 + 2ACOFE$ $+23.05272T$	This work
${}^oG^{Spinel}_{Co^{3+}:Co^{2+}:O^{2-}} - 3H^{SER}_{Co} - 4H^{SER}_{O} = ICO3O4 + 23.05272T - 0.5NCO3O4 + 1.5ECOFE2O4$ $-7GFE3O4 + BFE3O4 + ACOFE2O4$	This work
${}^oG^{Spinel}_{Co^{3+}:Co^{3+}:O^{2-}} - 3H^{SER}_{Co} - 4H^{SER}_{O} = ICO3O4 + 0.5NCO3O4 - 1.5ECOFE2O4$ $+7GFE3O4 - BFE3O4 - ACOFE2O4$	This work
${}^0L^{Spinel}_{Co^{2+},Co^{3+}:Co^{2+}:O^{2-}} = {}^0L^{Spinel}_{Co^{2+},Co^{3+}:Co^{3+}:O^{2-}} = -30847 + 44.249T$	[51]
$p = 0.28$	[52]
${}^0T^{Spinel}_{CFe^{2+}:Fe^{2+}:O^{2-}} = {}^0T^{Spinel}_{CFe^{3+}:Fe^{2+}:O^{2-}} = {}^0T^{Spinel}_{CFe^{2+}:Fe^{3+}:O^{2-}} = {}^0T^{Spinel}_{CFe^{3+}:Fe^{3+}:O^{2-}} = {}^0T^{Spinel}_{CFe^{2+}:Va:O^{2-}} = {}^0T^{Spinel}_{CFe^{3+}:Va:O^{2-}} = 848$	[52]
${}^0\beta^{Spinel}_{Fe^{2+}:Fe^{2+}:O^{2-}} = {}^0\beta^{Spinel}_{Fe^{3+}:Fe^{2+}:O^{2-}} = {}^0\beta^{Spinel}_{Fe^{2+}:Fe^{3+}:O^{2-}} = {}^0\beta^{Spinel}_{Fe^{3+}:Fe^{3+}:O^{2-}} = {}^0\beta^{Spinel}_{Fe^{2+}:Va:O^{2-}} = {}^0\beta^{Spinel}_{Fe^{3+}:Va:O^{2-}} = 44.54$	[52]
${}^oG^{Spinel}_{Fe^{2+}:Fe^{3+}:O^{2-}} - 3H^{SER}_{Fe} - 4H^{SER}_{O} = 7GFE3O4$	[52]
${}^oG^{Spinel}_{Fe^{2+}:Fe^{2+}:O^{2-}} - 3H^{SER}_{Fe} - 4H^{SER}_{O} = 7GFE3O4 + BFE3O4$	[52]
${}^oG^{Spinel}_{Fe^{3+}:Fe^{2+}:O^{2-}} - 3H^{SER}_{Fe} - 4H^{SER}_{O} = 7GFE3O4$	[52]
${}^oG^{Spinel}_{Fe^{3+}:Fe^{3+}:O^{2-}} - 3H^{SER}_{Fe} - 4H^{SER}_{O} = 7GFE3O4 - BFE3O4$	[52]
${}^oG^{Spinel}_{Fe^{2+}:Va:O^{2-}} - H^{SER}_{Fe} - 4H^{SER}_{O} = 5GFE3O4 + CFE3O4$	[52]
${}^oG^{Spinel}_{Fe^{3+}:Va:O^{2-}} - H^{SER}_{Fe} - 4H^{SER}_{O} = 5GFE3O4 + CFE3O4 - BFE3O4$	[52]
${}^oG^{Spinel}_{Fe^{2+}:Co^{2+}:O^{2-}} - H^{SER}_{Fe} - 2H^{SER}_{Co} - 4H^{SER}_{O} = 2ECOFE2O4 - 7GFE3O4 + 2BFE3O4 + 2ACOFE2O4$ $+23.05272T$	This work
${}^oG^{Spinel}_{Fe^{3+}:Co^{2+}:O^{2-}} - H^{SER}_{Fe} - 2H^{SER}_{Co} - 4H^{SER}_{O} = 2ECOFE2O4 - 7GFE3O4 + BFE3O4 + 2ACOFE2O4$ $+23.05272T$	This work
${}^oG^{Spinel}_{Fe^{2+}:Co^{3+}:O^{2-}} - H^{SER}_{Fe} - 2H^{SER}_{Co} - 4H^{SER}_{O} = 7GFE3O4 - ECOFE2O4 + NCO3O4$	This work
${}^oG^{Spinel}_{Fe^{3+}:Co^{3+}:O^{2-}} - H^{SER}_{Fe} - 2H^{SER}_{Co} - 4H^{SER}_{O} = 7GFE3O4 - BFE3O4 - ECOFE2O4 + NCO3O4$	This work
${}^oG^{Spinel}_{Co^{2+}:Fe^{2+}:O^{2-}} - H^{SER}_{Co} - 2H^{SER}_{Fe} - 4H^{SER}_{O} = BFE3O4 + ECOFE2O4$	This work
${}^oG^{Spinel}_{Co^{3+}:Fe^{2+}:O^{2-}} - H^{SER}_{Co} - 2H^{SER}_{Fe} - 4H^{SER}_{O} = ICO3O4 - 0.5NCO3O4 - 0.5ECOFE2O4 + 7GFE3O4$ $-ACOFE2O4$	This work
${}^oG^{Spinel}_{Co^{2+}:Fe^{3+}:O^{2-}} - H^{SER}_{Co} - 2H^{SER}_{Fe} - 4H^{SER}_{O} = ECOFE2O4$	This work
${}^oG^{Spinel}_{Co^{3+}:Fe^{3+}:O^{2-}} - H^{SER}_{Co} - 2H^{SER}_{Fe} - 4H^{SER}_{O} = ICO3O4 - 0.5NCO3O4 - 0.5ECOFE2O4$ $+7GFE3O4 - BFE3O4 - ACOFE2O4$	This work
${}^oG^{Spinel}_{Co^{2+}:Va:O^{2-}} - H^{SER}_{Co} - 4H^{SER}_{O} = CFE3O4 + ECOFE2O4 - 2GFE3O4$	This work
${}^oG^{Spinel}_{Co^{3+}:Va:O^{2-}} - H^{SER}_{Co} - 4H^{SER}_{O} = ICO3O4 - 0.5NCO3O4 - 0.5ECOFE2O4$ $+5GFE3O4 - BFE3O4 - ACOFE2O4 + CFE3O4$	This work
${}^0L^{Spinel}_{Fe^{3+}:Co^{2+},Fe^{3+}:O^{2-}} = -53273.3 + 21.753T$	This work

${}^0L^{Spinel}_{Co^{2+}:Co^{3+},Fe^{3+}:O^{2-}} = +56428.3 - 8.917T$	This work
${}^0L^{Spinel}_{Fe^{3+}:Co^{3+},Fe^{3+}:O^{2-}} = -72504.3 - 5.878T$	This work
${}^0L^{Spinel}_{Fe^{3+}:Co^{2+},Co^{3+}:O^{2-}} = {}^0L^{Spinel}_{Fe^{2+}:Co^{2+},Co^{3+}:O^{2-}} = +205608.0$	This work
${}^0T^{Spinel}_{CCo^{2+}:Fe^{3+}:O^{2-}} = {}^0T^{Spinel}_{CFe^{3+}:Co^{2+}:O^{2-}} = 775.15$	This work
${}^0\beta^{Spinel}_{Co^{2+}:Fe^{3+}:O^{2-}} = {}^0\beta^{Spinel}_{Fe^{3+}:Co^{2+}:O^{2-}} = -23.0$	This work
Function-Spinel	
$ECOFE2O4 = -1139700.8 + 1110.508T - 184.804T\ln(T) - 0.00764T^2 + 1597245.15T^{-1}$	This work
$ACOFE2O4 = -24439.656 + 20.610T$	This work
HCP_A3	
$(Co, Fe)_1 (Va,O)_{0.5}$	
$p = 0.28$	[51]
${}^0T^{hcp}_{CCo:Va} = 1396 \quad {}^0\beta^{hcp}_{Co:Va} = 1.35$	[51]
${}^oG^{hcp}_{Co:Va} - H^{SER}_{Co} = GHSERCO$	[51]
${}^oG^{hcp}_{Co:O} - H^{SER}_{Co} - 0.5H^{SER}_{O} = GHSERCO + 0.5GHSEROO - 122309 + 66.269T$	[51]
${}^oG^{hcp}_{Fe:Va} - H^{SER}_{Fe} = GFEHCP$	[53]
${}^oG^{hcp}_{Fe:O} - H^{SER}_{Fe} - 0.5H^{SER}_{O} = GFEHCP + 0.5GHSEROO$	[53]
${}^0L^{hcp}_{Co,Fe:Va} = +5000$	[54]
$T^{hcp}_{CCo,Fe:Va} = -253 + 1494(y_{Co} - y_{Fe}) \quad \beta^{hcp}_{Co,Fe:Va} = 5.41 - 0.24(y_{Co} - y_{Fe})$	[54]
FCC_A1	
$(Co, Fe)_1 (Va,O)_1$	
$p = 0.28$	[51]
${}^0T^{fcc}_{CCo:Va} = 1396 \quad {}^0\beta^{fcc}_{Co:Va} = 1.35$	[51]
${}^oG^{fcc}_{Co:Va} - H^{SER}_{Co} = GFCCCO$	[51]
${}^oG^{fcc}_{Co:O} - H^{SER}_{Co} - H^{SER}_{O} = GFCCCO + GHSEROO - 213318 + 107.071T$	[51]
${}^oG^{fcc}_{Fe:Va} - H^{SER}_{Fe} = GFEFCC$	[53]
${}^oG^{fcc}_{Fe:O} - H^{SER}_{Fe} - H^{SER}_{O} = GFEFCC + GHSEROO + 65T$	[53]
${}^0T^{fcc}_{CFe:Va} = -201 \quad {}^0\beta^{fcc}_{Fe:Va} = -2.1$	[53]
$L^{fcc}_{Fe:O,Va} = +168758 + 19.17T$	[54]
$L^{fcc}_{Co,Fe:Va} = -8968.75 + 3528.8(y_{Co} - y_{Fe})^2$	[54]
$T^{fcc}_{CCo,Fe:Va} = +283 + 879(y_{Co} - y_{Fe}) \quad \beta^{fcc}_{Co,Fe:Va} = +8.407 - 3.644(y_{Co} - y_{Fe})$	[54]
Bcc_A2	
$(Co, Fe)_1 (Va,O)_3$	
${}^oG^{bcc}_{Co:Va} - H^{SER}_{Co} = GCOBCC$	[51]
${}^oG^{bcc}_{Fe:Va} - H^{SER}_{Fe} = GHSERFE$	[53]

${}^{o}G_{Co:O}^{bcc} - H_{Co}^{SER} - 3H_{O}^{SER} = GCOBCC + 3GSHEOO$	[51]
${}^{o}G_{Fe:O}^{bcc} - H_{Fe}^{SER} - 3H_{O}^{SER} = GHSERFE + 3GHSEROO + 195T$	[53]
$p = 0.4$	[51]
${}^{0}T_{Co:Va}^{bcc} = 1450 \quad {}^{0}\beta_{Co:Va}^{bcc} = 1.35$	[51]
${}^{0}T_{Fe:Va}^{bcc} = 1043 \quad {}^{0}\beta_{Fe:Va}^{bcc} = 2.22$	[53]
${}^{0}L_{Fe:O,Va}^{bcc} = -517549 + 71.83T$	[53]
${}^{0}L_{Co,Fe:Va}^{bcc} = -26222.7 + 125T - 15.502T\ln T - 632250T^{-1} + (2686.79 + 632250T^{-1})(y_{Co} - y_{Fe})^2$	[54]
${}^{0}T_{Co,Fe:Va}^{bcc} = 590 \quad {}^{0}\beta_{Co,Fe:Va}^{bcc} = 1.406 \; {}^{1}\beta_{Co,Fe:Va}^{bcc} = -0.6617$	[54]
O_2 gas	
${}^{o}G_{O_2}^{gas} - 2H_{O}^{SER} = 2GHSEROO + RT\ln P$	[51]

[a] All parameters are in SI units: J, mol, K and Pa. Values for β are given in μB (Bohr magnetons).

2.4.1 Spinel phase

Fig. 2.2 presents calculated site fraction of Fe^{3+} on the tetrahedral site of $CoFe_2O_4$ in comparison with experimental data. The experimental data showed a large scatter, which may due to different sample preparation methods, thermal treatment conditions and cooling procedures (described in detail in Section 2.1.1). During the optimization a compromise had to be made between a good fit of cation distribution data and a good fit of thermodynamic and phase diagram data. As we believe the latter are more reliable, we exclude most of the cation distribution data in the optimization. As shown in Fig. 2.2, with increasing temperature, the site fraction of Fe^{3+} on the tetrahedral site decreases. The calculation agrees with the experimental results in the general trend.

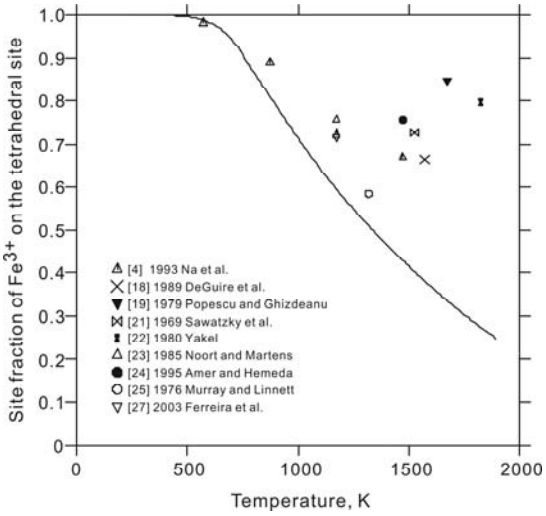

Fig. 2.2. Calculated site fraction of Fe^{3+} in the tetrahedral sublattice of $CoFe_2O_4$ in air in comparison with experimental data.

The valence state and distribution of transition metal cations in spinel is known to govern the magnetic and electrical properties. Fig. 2.3 plots cation distribution in the spinel phase as a function of cation composition from Fe_3O_4 to $CoFe_2O_4$ (along the phase boundary between spinel/spinel+halite with varying oxygen partial pressure) at three different temperatures together with the experimental results from Erickson and Mason [26]. The calculated cation distribution agrees with the experimental results reasonably well at all three temperatures (873, 1173, 1473 K).

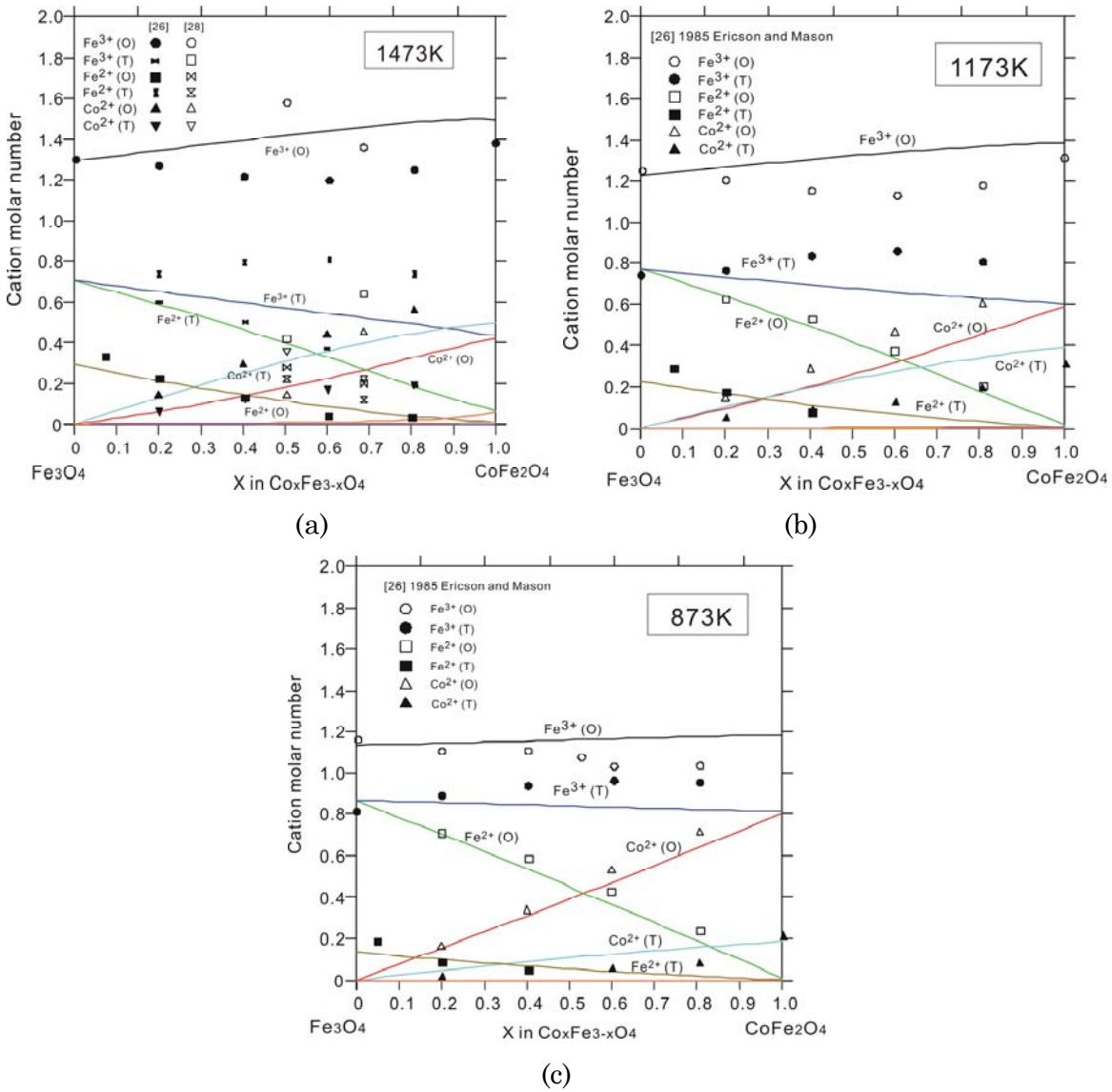

Fig. 2.3. Cation distribution in Fe_3O_4–$CoFe_2O_4$ spinel solutions saturated with halite (a) at 1473K, (b) at 1173K, (c) at 873K. "O" and "T" represent octahedral and tetrahedral sites, respectively. The lines represent calculated results from the present work.

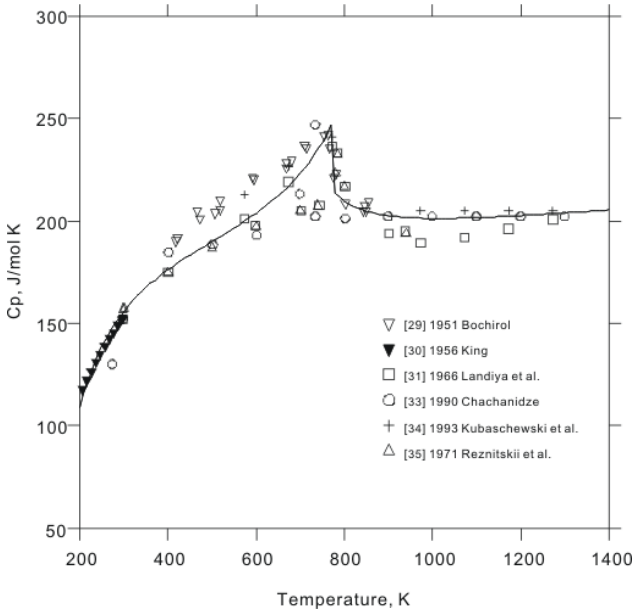

Fig. 2.4. Calculated heat capacity of $CoFe_2O_4$ as a function of temperature compared with experimental data.

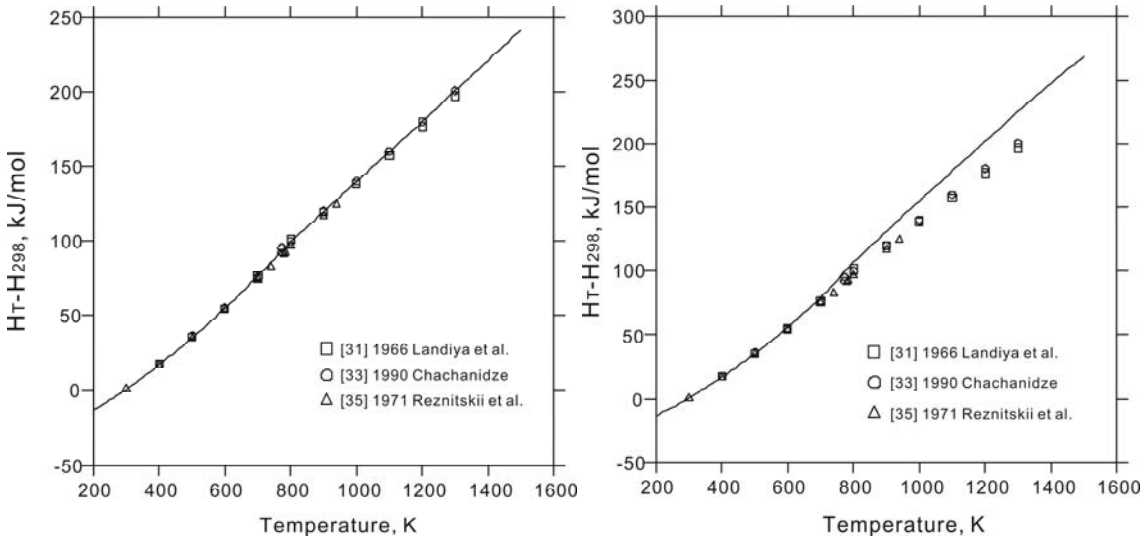

(a) (b)

Fig. 2.5. Calculated heat content of $CoFe_2O_4$ as a function of temperature compared with experimental data. (a) Without considering cation redistribution in the calculation; (b) Considering cation redistribution.

Table 2.3 summarizes enthalpy and entropy of $CoFe_2O_4$ calculated using the present optimized thermodynamic database, together with experimental data from literature. The enthalpy of formation from oxides (CoO and Fe_2O_3) reported by Navrotsky and Kleppa [32] was used in the optimization. Our calculated enthalpy of formation (from elements) is in good agreement with the value from Kubaschewski *et al.* [34]. The calculated enthalpy of formation from CoO and Fe_2O_3 at

298.15K is slightly higher than the value reported by Reznitskii *et al.* [35]. The standard entropy of formation for $CoFe_2O_4$ at 298.15K was calculated as 132.5 J/mol K, in good agreement with the value reported by Kubaschewski *et al.* (142.7 ± 8.4 J/mol K) [34]. The heat capacity of the $CoFe_2O_4$ spinel is plotted in Fig. 2.4, together with experimental data [29−35]. During the adiabatic calorimetric measurements at these relatively low temperatures, there was probably insufficient time for cations to re-equilibrate. Our calculated heat capacity was hence under the assumption that there was no contribution to the measured values from cation re-distribution. As shown in Fig. 2.4, the $CoFe_2O_4$ spinel experiences a magnetic order-disorder transition at temperature around 780K, resulting in some scatters in the measured heat capacity data around the transition region. Still the current calculation can represent most of the measured heat capacity data reasonably well. Fig. 2.5 plots the heat content for $CoFe_2O_4$. Two calculations were included: one considering cation redistribution and the other without. As can be seen the cation redistribution will influence the enthalpy at high temperatures. The one without considering cation redistribution fits experimental data better.

Table 2.3 Thermodynamic properties of $CoFe_2O_4$

Enthalpy	Reference
$\Delta^0 H_{f,elements}^{CoFe_2O_4}(298.15K) = -1088.7 \pm 4.6$ kJ/mol	[34]
$\Delta^0 H_{f,elements}^{CoFe_2O_4}(298.15K) = -1085.0$ kJ/mol	This work, calculated
$\Delta^0 H_{f,oxides}^{CoFe_2O_4}(298.15K) = -23.47$ kJ/mol	[35]
$\Delta^0 H_{f,oxides}^{CoFe_2O_4}(298.15K) = -24.88$ kJ/mol	This work, calculated
$\Delta^0 H_{f,oxides}^{CoFe_2O_4}(970K) = -24.6 \pm 0.9$ kJ/mol	[32]
$\Delta^0 H_{f,oxides}^{CoFe_2O_4}(970K) = -23.57$ kJ/mol	This work, calculated
Entropy	
${}^0S_{298.15K}^{CoFe_2O_4} = 134.6 \pm 2$ J/molK	[30]
${}^0S_{298.15K}^{CoFe_2O_4} = 142.7 \pm 8.4$ J/molK	[34]
${}^0S_{298.15K}^{CoFe_2O_4} = 132.5$ J/molK	This work, calculated
Curie temperature	
${}^0T_c^{CoFe_2O_4} = 773$ K	[31]
${}^0T_c^{CoFe_2O_4} = 810$ K	[35]
${}^0T_c^{CoFe_2O_4} = 778$ K	This work, calculated

2.4.2 Halite phase

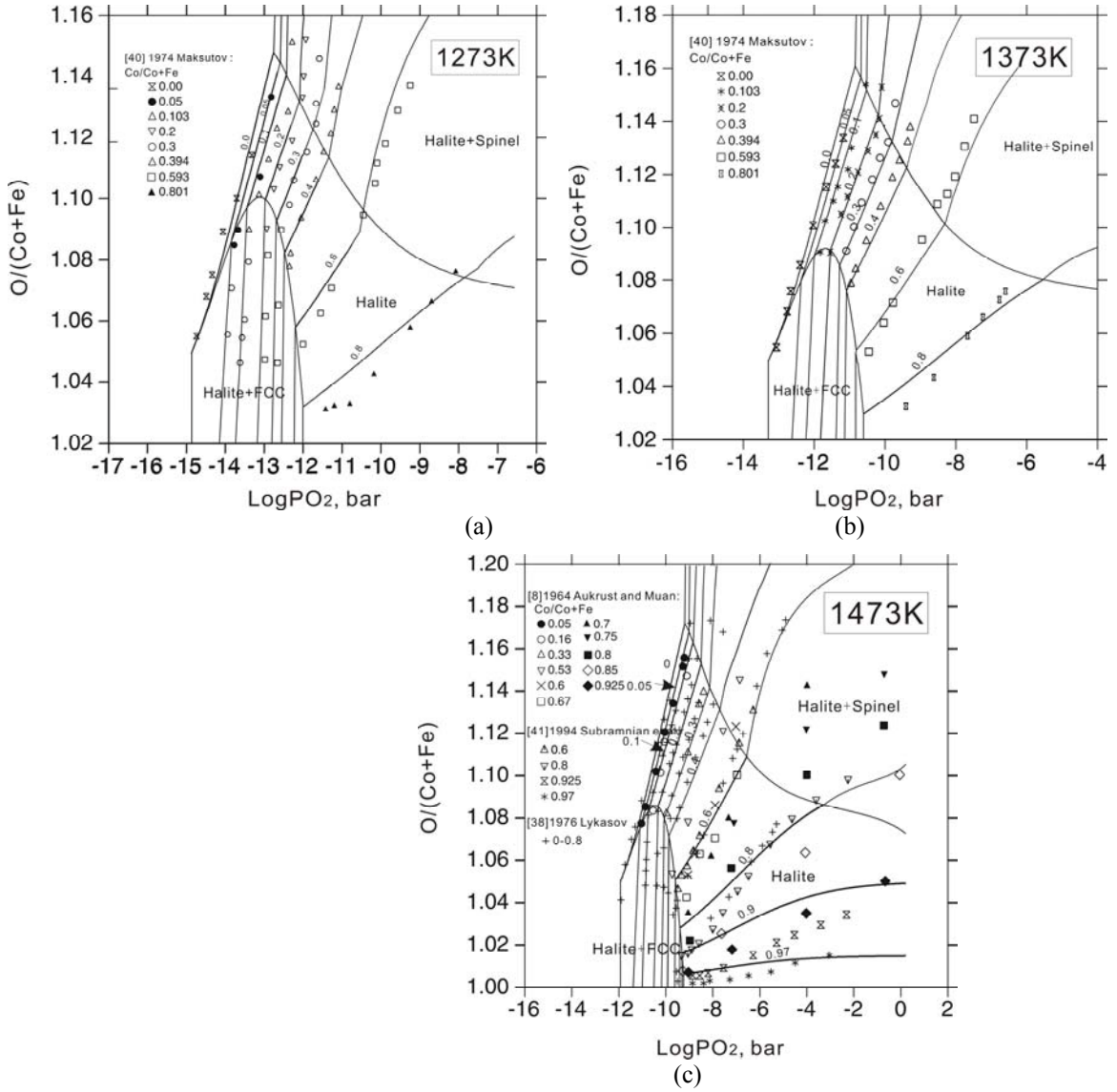

Fig. 2.6. Calculated cation deficiency (in term of O/(Co+Fe) molar ratio) as a function of oxygen partial pressure at chosen Co/(Co+Fe) content (indicated as numbers inside the figure). The variation of O/(Co+Fe) in the FCC+Halite and Spinel+Halite two-phase regions were also calculated. (a) at 1273K, (b) at 1373K, (c) at 1473K.

The cation deficiency (in term of O/(Co+Fe) ratio) of the halite phase at various cobalt content and PO_2 is illustrated in Fig. 2.6. At fixed cobalt content, the O/(Co+Fe) ratio of the halite phase is almost independent of oxygen partial pressure for the halite+FCC two-phase region, while for the halite single phase region and the halite+spinel two-phase region, the oxygen content increases with increasing oxygen partial pressure. The slope decreases with increasing the Co

content. The slopes fit well with experimental results at low Co content at all temperatures, however, show small off at high Co content. This is because the halite (CoO) in Co-O system was treated as a stoichiometric compound.

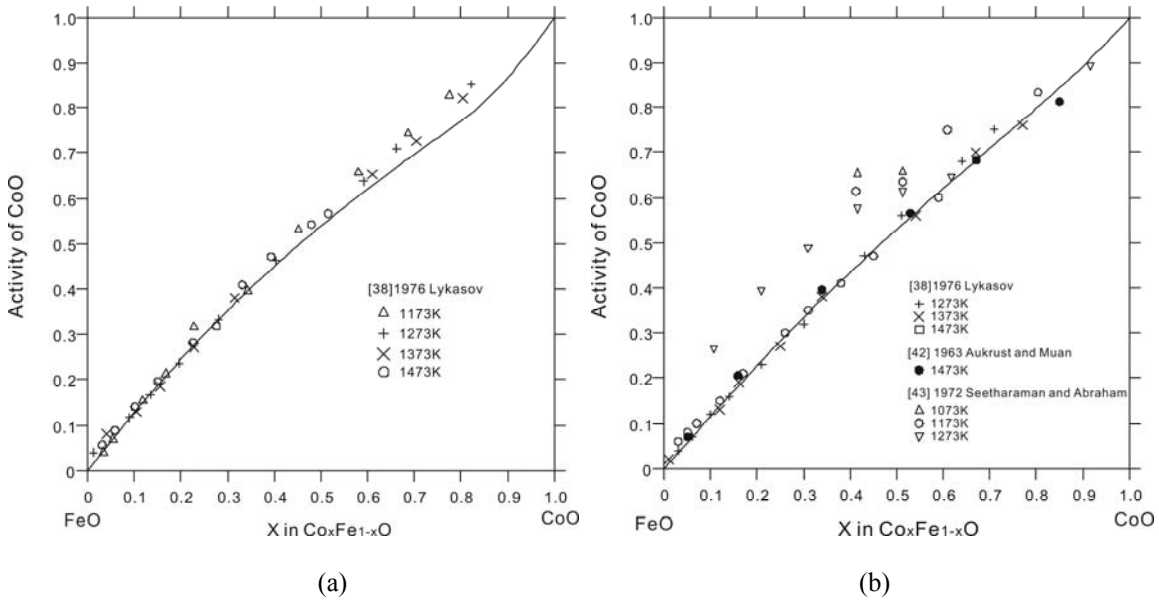

Fig. 2.7. Calculated activity of CoO in halite phase in equilibrium with spinel or FCC at 1473K. (a) in equilibrium with spinel, (b) in equilibrium with FCC.

Fig. 2.7 plots activity of CoO in the halite phase at 1473K in equilibrium with either the spinel or the FCC phase. In both cases, the CoO activity shows small positive deviation from the ideal solution at FeO rich region. Our calculations show that the temperature dependence of the CoO activity is negligible at the temperature range 1173−1473K when the halite phase is in equilibrium with FCC, in agreement with Lykasov *et al.*'s findings [38]. The deviation from ideality may be attributed to the non-stoichiometry of halite at different FeO content.

2.4.3 Phase diagrams

The calculated phase diagram of Co-Fe-O in air is presented in Fig. 2.8. The calculated phase boundaries are in good agreement with most of the experimental data. The spinel single phase region extends from pure Co_3O_4 to pure Fe_3O_4. A miscibility gap exists at temperature below 1000 K, with one close to $CoFe_2O_4$ of the inverse type spinel and the other close to Co_3O_4 of the normal type. The $CoFe_2O_4$ spinel is stable down to room temperature, in agreement with the experiment results [4, 18, 19]. In the phase diagrams calculated by Jung *et al.* [12] and Weiland [13], the

$CoFe_2O_4$ spinel decomposes at T<700K. For the liquidus part, the $CoFe_2O_4$ spinel melts congruently at 1930K in air. Additionally, an eutectic reaction of Liquid ↔ Spinel + Halite takes place at 1886K in air, with the following compositions $Co_{0.883}Fe_{2.117}O_{4-\delta}$, $Co_{0.585}Fe_{0.415}O_{1+\delta}$, and $Co_{0.433}Fe_{0.567}O_x$ for spinel, halite, and liquid, respectively. As mentioned earlier, no ternary interaction parameter for the liquid phase was optimized in the present work. The liquidus part should therefore be treated with cautiousness.

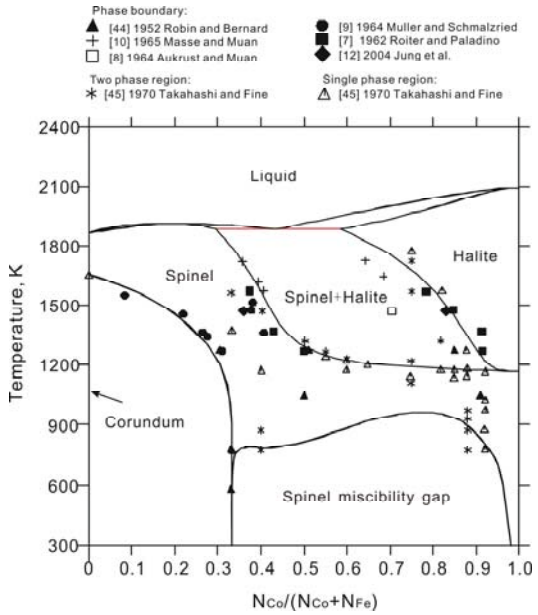

Fig. 2.8. Calculated phase diagram of Co-Fe-O in air based on the parameters obtained in the present work.

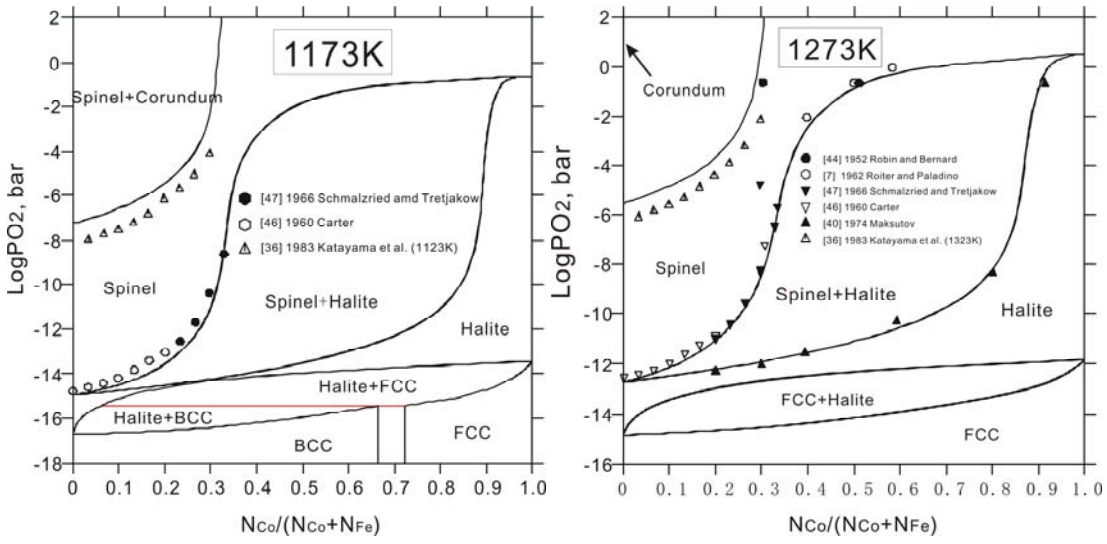

(a) (b)

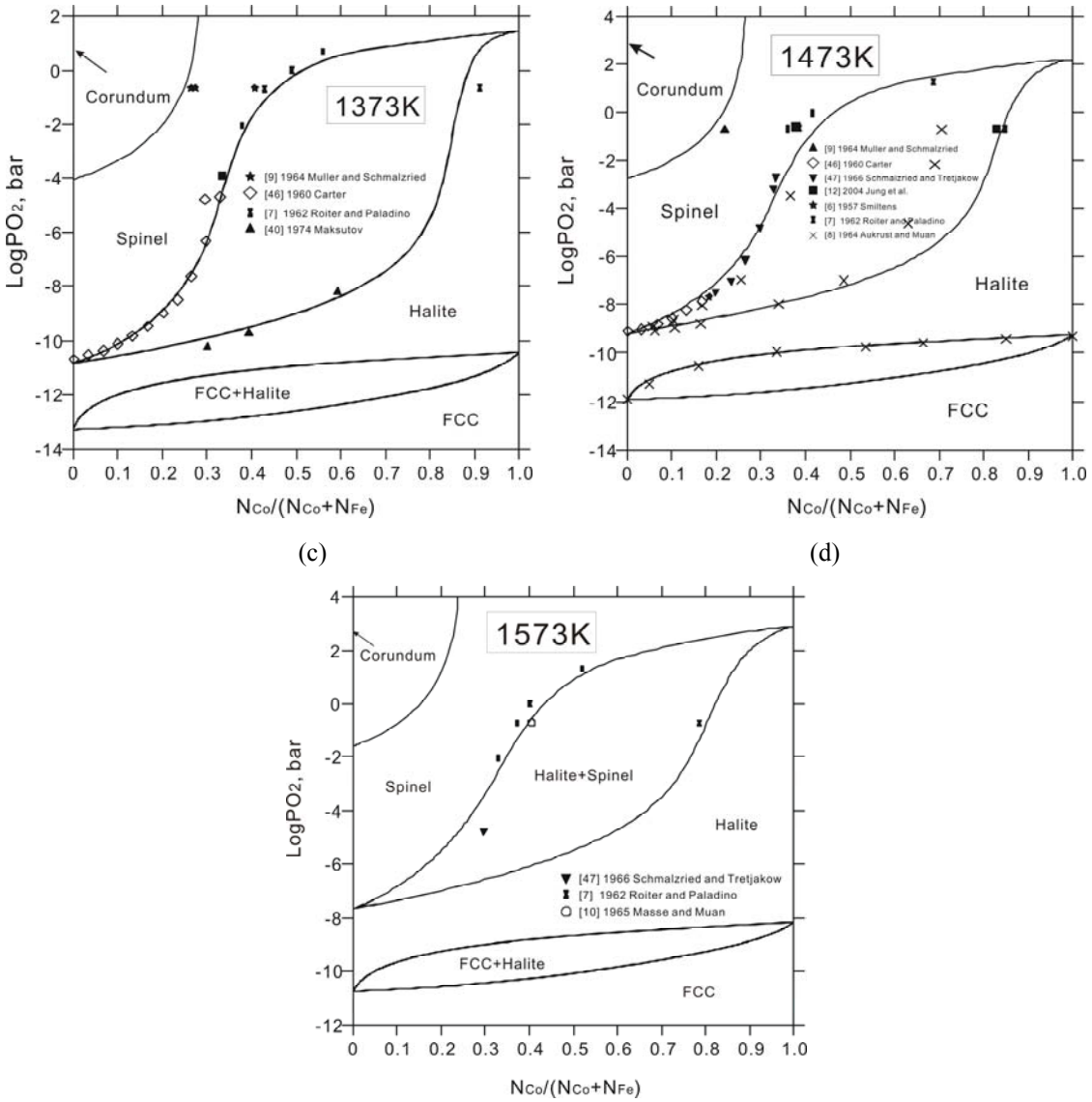

Fig. 2.9. Calculated isothermal PO_2-composition phase diagrams at: (a) 1123K, (b) 1273K, (c) 1373K, (d) 1473K, (e) 1573K.

The calculated isothermal PO_2-composition phase diagrams at different temperatures are plotted in Fig. 2.9. The computed phase diagrams were compared with the experimental data from literature [2, 7–9, 40, 46–50] at a temperature range of 900–1373K and oxygen partial pressure from 10^{-16} to 100 bar. These diagrams can be used to explore the stable region for the desired spinel phase under certain temperature and oxygen partial pressure for industrial applications.

2.5 Conclusions

In the present work, the thermodynamic and phase diagram data for the Co-Fe-O system were carefully reviewed and a thermodynamic assessment was performed. A complete set of parameters was obtained. To achieve a good agreement with most of the experimental data, a number of interaction parameters were optimized for the spinel and halite phases. The description for the ternary liquid phase was obtained by ideal extrapolation. Calculated thermodynamic properties and phase diagrams are presented and compared with experimental data, and a good agreement with most of the experimental data was achieved. Improvements were made as compared to previous modeling efforts. Our modeling covers a temperature range from 298K to 3000K and oxygen partial pressure from 10^{-16} to 10^{2} bar.

References

[1] E. Bucher, W. Sitte, Solid State Ionics 192 (2011) 480–482.

[2] M. Lundberg, E. Rosén, J. Am. Ceram. Soc. 75 (1992) 1452–1457.

[3] Y. Li, E.R. Maxey, J.W. Richardson Jr., B. Ma, Mater. Sci. Eng. B 106 (2004) 6–26.

[4] J.G. Na, T.D. Lee, S.J. Park, J. Mater. Sci. Lett. 12 (1993) 961–962.

[5] A.D. Pelton, H. Schmalzried, J. Sticher, Ber. Bunsen-Ges. Phys. Chem. 83 (1979) 241–252.

[6] J. Smiltens, J. Am. Chem. Soc. 79 (1957) 4881–4884.

[7] B.D. Roiter, A.E. Paladino, J. Am. Ceram. Soc. 45 (1962) 128–133.

[8] E. Aukrust, A. Muan, Trans. Met. Soc. AIME 230 (1964) 1395–1399.

[9] W. Müller, H. Schmalzried, Ber. Bunsen-Ges. Phys. Chem. 68 (1964) 270–276.

[10] D.P. Masse, A. Muan, J. Am. Ceram. Soc. 48 (1965) 466–469.

[11] R. Subramanian, R. Dieckmann, J. Phys. Chem. Solids 55 (1994) 391–404.

[12] I.-H. Jung, S.A. Decterov, A.D. Pelton, H.-M. Kim, Y.-B. Kang, Acta Mater. 52 (2004) 507–519.

[13] R. Weiland, Studies on the thermodynamics of oxide solution phases in the system Co-Fe-Mn-O, Max-Planck-Institut für Metallforschung, Stuttgart, 2002.

[14] E. Povoden-Karadeniz, A.N. Grundy, M. Chen, T. Ivas, L.J. Gauckler, J. Phase Equilib. Diffus. 30 (2009) 351–366.

[15] A.N. Grundy, B. Hallstedt, L.J. Gauckler, Acta Mater. 50 (2002) 2209–2222.

[16] J.E. Saal, Thermodynamic modeling of phase transformation and defects: from cobalt to doped cobaltite perovskite, Pennsylvania State Universiry, 2010.

[17] E. Povoden-Karadeniz, Unpublished results.

[18] M.R. De Guire, R.C. O'Handley, G. Kalonji, J. Appl. Phys. 65 (1989) 3167–3172.

[19] M. Popescu, C. Ghizdeanu, Phys. Stat. Sol. A 52 (1979) 169–172.

[20] G.A. Sawatzky, F. Van Der Woude, A.H. Morrish, J. Appl. Phys. 39 (1968), 1204–1206.

[21] G. A. Sawatzky, F. Van Der Woude, A.H. Morrish, Phys. Rev. 187 (1969) 747–755.

[22] H.L. Yakel, J. Phys. Chem. Solids 41 (1980) 1097–1104.

[23] H.M. Van Noort, J.W.D. Martens, W.L. Peeters, Mater. Res. Bull. 20 (1985) 41–47.

[24] M.A. Amer, O.M. Hemeda, Hyperfine Interact. 96 (1995) 99–109.

[25] P.J. Murray, J.W. Linnett, J. Phys. Chem. Solids 37 (1976) 1041–1042.

[26] D.S. Erickson, T.O. Mason, J. Solid State Chem. 59 (1985) 42–53.

[27] T.A.S. Ferreira, J.C. Waerenborgh, M.H.R.M. Mendonça, M.R. Nunes, F.M. Costa, Solid State Sci. 5 (2003) 383–392.

[28] M.R. De Guire, G. Kalonji, R.C. O'Handley, J. Am. Ceram. Soc. 73 (1990) 3002–3006.

[29] M.L. Bochirol, Compt. Rend. 232 (1951) 1474–1477.

[30] E.G. King, J. Phys. Chem. 60 (1956) 410–412.

[31] N.A. Landiya, G.D. Chachanidze, A.A. Chuprin, T.A. Pavlenishvili, N.G. Lezhava, V.S.

[32] A. Navrotsky, O.J. Kleppa, J. Inorg. Nucl. Chem. 30 (1968) 479–498.

[33] G.D. Chachanidze, Izv. Akad. Nauk SSSR, Neorg. Mater. 26 (1990) 376–379.

[34] O. Kubaschewski, C.B. Alcock, P.J. Spencer, Materials Thermochemistry, Pergamon Press, New York, 1993.

[35] L.A. Reznitskii, S.E. Filippova, N.G. Korzhukov, Russ. J. Phys. Chem. 45 (1971) 529–530.

[36] I. Katayama, T. Matsuda, Z. Kozuka, J. Jpn. Inst. Metals 47 (1983) 858–862.

[37] J.H. Raeder, J.L. Holm, O.T. Sorensen, Solid State Ionics 12 (1984) 155–159.

[38] A. A. Lykasov, Izv. Vyssh. Uchebn. Zaved. Chern. Metall. 4 (1976) 13–16.

[39] R. Dieckmann, Solid State Ionics 45 (1991) 271–276.

[40] I.A. Maksutov, Study of thermodynamic properties of solid wustite solutions in system Fe–Co–O, University of Chelyabinsk, 1974.

[41] R. Subramanian, S. Tinkler, R. Dieckmann, J. Phys. Chem. Solids 55 (1994) 69–75.

[42] E. Aukrust, A. Muan, Trans. Met. Soc. AIME 227 (1963) 1378–1380.

[43] S. Seetharaman, K.P. Abraham, Trans. Indian Inst. Met. 25 (1972) 16–19.

[44] M.M.J Robin, J. Benard, Compt. Rend. 234 (1952) 734–735.

[45] M. Takahashi, M.E. Fine, J. Am. Ceram. Soc. 53 (1970) 633–634.

[46] R.E. Carter, J. Am. Ceram. Soc. 43 (1960) 448–452.

[47] H. Schmalzried, J.D. Tretjakow, Ber. Bunsen-Ges. Phys. Chem. 70 (1966) 180–188.

[48] B. Touzelin, J. Less-Common Met. 77 (1981) 11–27.

[49] B. Touzelin, J. Less-Common Met. 114 (1985) 379–386.

[50] R. Subramanian, R. Dieckmann, J. Phys. Chem. Solids 55 (1994) 59–67.

[51] M. Chen, B. Hallstedt, and L. J. Gauckler, J. Phase Equilib. 24 (2003) 212–227.

[52] B. Sundman, J. Phase equilib. 12 (1991) 127–140.

[53] L. Kjellqvist, M. Selleby, B. Sundman, CALPHAD 32 (2008) 577–592.

[54] I. Ohnuma, H. Enokia, O. Ikeda, R. Kainuma, H. Ohtani, B. Sundman *et al.*, Acta Mater. 50 (2002) 379–393.

[55] A.T. Dinsdale, CALPHAD 15 (1991) 317–425.

[56] G. Inden, Z. Metallkd. 66 (1975) 577–582.

[57] M. Hillert, M. Jarl, CALPHAD 2 (1978) 227–238.

[58] M. Hillert, J. Alloys Compd. 320 (2001) 161–176.

[59] M. Hillert, B. Jansson, B. Sundman, J. Ågren, Metall. Trans. 16A (1985) 261−266.

[60] Sundman, Calphad 15 (1991) 109−119

[61] M. Hillert, M. Selleby, B. Sundman, Metall. Trans. A 21A (1990) 2759–2776.

[62] M. Selleby, B. Sundman, CALPHAD 20 (1996) 381–392.

[63] T.I. Barry, A.T. Dinsdale, J.A. Gisby, B. Hallstedt, M. Hillert, B. Jansson *et al.*, J. Phase Equilib. 13 (1992) 459–475.

[64] B. Sundman, B. Jansson, J.-O. Andersson, CALPHAD 9 (1985) 153–190.

Chapter 3

Thermodynamic modeling of the La-Co-O and La-Co-Fe-O systems

Abstract

A thermodynamic modeling of phase diagrams and thermodynamic properties of the La-Co-O and La-Co-Fe-O systems was presented. Special attention was given to the perovskite $LaCoO_{3-\delta}$ phase, due to its outstanding practical importance. In addition to phase equilibria, defect chemistry and charge disproportionation of lanthanum cobaltite were considered during the modeling and discussed with respect to their thermo-chemical and electrochemical applications. Two sets of optimized parameters were obtained, one for high charge disproportionation ($2Co^{3+} \rightarrow Co^{2+} + Co^{4+}$) and one for low charge disproportionation. It was decided that the parameters for low charge disproportionation will be used in the extensions to the La-Co-Fe-O database. Calculations with the presented thermodynamic database deliver fundamental materials properties for the optimization of technological materials for industrial applications, including SOFC and oxygen membrane.

3.1 Introduction

Perovskite oxides with rare earth or alkaline earth metal on the A site and with 3d transition metal on the B site have drawn a lot of research attentions due to their high catalytic activity and useful electrical and magnetic properties. $LaCoO_{3-\delta}$ is one of those perovskite oxides. It has been shown that lanthanum cobaltite offers high electronic and ionic conductivity, excellent catalytic activity and magnetic property which allow it to be widely used as hydrogenation oxidation catalyst [1], as SOFC cathode [2], as oxygen separation membrane and as magneto-hydrodynamic (MHD) electrode [3].

For most of the above mentioned applications, a successful use of lanthanum cobaltite was however limited by lack of knowledge on phase stability of oxide phases under various operating conditions (temperature and oxygen partial pressure). The La-Co-O system has been investigated previously, with efforts on either experimental determination of thermodynamic or thermochemical properties [4−11] or thermodynamic modeling [12, 13]. However, large inconsistency exists between different investigations which makes prediction of materials stability and thermochemical properties in a wide temperature and oxygen partial pressure range difficult.

In order to solve these inconsistencies, the La-Co-O system was critically reviewed and remolded focusing especially on phase equilibria. In the present work, thermodynamic database of La-Co-Fe-O was also developed as part of a project for developing a thermodynamic database of La-Sr-Co-Fe-O. In our modeling, the $LaCoO_3$ phase was originally modeled as, considering low charge disproportionation. Later, high charge disproportionation was also tested in the modeling. Two sets of parameters with different cation distribution schemes were thus obtained. Both sets of the parameters can describe phase equilibria and thermodynamic data reasonably well. In addition, attention was given to cation distribution and defect chemistry of the $LaCoO_{3-\delta}$ perovskite phase and a good agreement between experimental data and our model-predicted results was achieved. The thermodynamic database of La-Co-Fe-O was derived based on an ideal extrapolation from sub-systems.

3.2 Literature review

Previously reported experimental data on La-Co-O and La-Co-Fe-O were collected and evaluated. The experimental data include phase diagram data, thermodynamic data and oxgen-

non-stoichiometry, to name a few. These are discussed in the following. Consistent experimental findings among the various types of data were used to optimize the thermodynamic parameters, which will be described in *section 3.3*.

3.2.1. Phase equilibria and invariant reactions

La-Co-O was studied first by Sis *et al.* [4]. They investigated valence state, crystallographic and electronic structure of $LaCoO_3$ in reducing atmosphere using thermogravimetry (TG), calorimetry, X-ray diffraction (XRD) and magnetic measurements. They observed that reduction of $LaCoO_3$ proceeds through formation of a series of oxygen-deficient compounds. Janecek and Wirtz [5] investigated the La-Co-O system at 1403K using XRD. In addition to previously described La_2CoO_4 and $LaCoO_{3-\delta}$, these authors reported another equilibrium compound, $La_4Co_3O_{10}$ to be present in an isothermal section of 1403K, together with six invariant reactions. $La_4Co_3O_{10}$ is stable at $T > 1600$K in air [13]. It can also be obtained at lower temperature but with decreased PO_2. Nakamura *et al.* [6] studied the stability of $LaCoO_3$ and La_2CoO_4 at 1273 K in a PO_2-controlled atmosphere using TG. They determined the Gibbs energy change at 1273 K for the reactions: $LaCoO_3$ (s) = 1/2La_2CoO_4 (s) + 1/2CoO (s) + 1/4O_2 (gas, 1bar) and La_2CoO_4 (s) = La_2O_3 (s) + Co (s) + 1/2O_2 (gas, 1bar) as 42.7 and 162.0 kJ/mol, respectively. The first reaction was however incorrect, as $LaCoO_3$ will first decompose into $La_4Co_3O_{10}$ with decreasing oxygen partial pressure. Seppänen *et al.* [7] investigated the stability of $La_4Co_3O_{10}$, La_2CoO_4 and $LaCoO_3$ in a temperature range of 1175−1325K by means of electromotive force (EMF) measurements and presented an isothermal stability diagram at 1273K. The Gibbs energy of formation for these three compounds was then evaluated based on their own EMF data and the Gibbs energy functions of binary oxides (La and Co oxides) from the literature. Petrov *et al.* [8] studied phase equilibria in La-Co-O as a part of their study on Ln-M-O systems (Ln = La, Pr, Nd; M = Co, Ni, Cu) in a temperature range of 937−1573 K and an oxygen partial pressure range of 10^{-15} to 1 atm. The phase stability was determined by EMF measurements. Based on these data, they calculated Gibbs energy of "potential-forming" reactions and presented several isothermal PO_2-composition phase diagrams. Kitayama [9, 10] investigated phase equilibria in La-Co-O at 1473, 1423 and 1373 K in an oxygen partial pressure range of 10^{-12} to 1 atm. The standard Gibbs energy change for a number of reactions was determined using TG measurements. Based on the literature data, the following five invariant reactions exist in the La-Co-O system:

$2La_4Co_3O_{10} + 1/2O_2 = 6LaCoO_3 + La_2O_3$ (3.1)

$La_4Co_3O_{10} + CoO + 1/2O_2 = 4LaCoO_3$ (3.2)

$3La_2CoO_4 + 1/2O_2 = La_4Co_3O_{10} + La_2O_3$ (3.3)

$2La_2CoO_4 + CoO + 1/2O_2 = La_4Co_3O_{10}$ (3.4)

$La_2O_3 + Co + 1/2O_2 = La_2CoO_4$ (3.5)

Little information exists on the quaternary La-Co-Fe-O system. Proskurina *et al.* studied phase equilibria in the La-Co-Fe-O system at 1100°C in air [11]. The samples prepared by different techniques were heat treated at 1100°C in air for 24−400h and were further characterized using XRD. An isotherm section of La_2O_3-CoO-Fe_2O_3 at 1100°C in air was constructed based on the XRD results.

3.2.2. Solid oxide phases

In the present work the focus was put on oxide phases. Experimental information on the gas phase and the metallic phases will therefore not be discussed here. The following binary oxides exist in the La-Co-Fe-O system: La_2O_3 (hexagonal, partially ordered hexagonal, cubic), CoO, Co_3O_4, FeO, Fe_3O_4, and Fe_2O_3. Details on the binary oxides can be found in previous modeling work [15−17]. Three stable ternary oxides were reported in La-Co-O: $La_4Co_3O_{10}$, La_2CoO_4 and $LaCoO_{3-\delta}$. Two ternary oxides exist in La-Fe-O: $LaFeO_{3-\delta}$ perovskite and $LaFe_{12}O_{19}$ hexaferrite [18]. In Co-Fe-O, CoO and FeO form halite solid solution, while Co_3O_4 and Fe_3O_4 form spinel solid solution. $LaCoO_{3-\delta}$ and $LaFeO_{3-\delta}$ form a perovskite solid solution phase, which is the only quaternary solid oxide phase reported in La-Co-Fe-O.

I. $La_4Co_3O_{10}$

$La_4Co_3O_{10}$ was first reported by Janecek and Wirtz [19], and was later investigated also by other groups [20, 21]. It is a Ruddlesden-Popper-type phase with an orthorhombic structure. Parida *et al.* [1] determined the standard molar Gibbs energy of formation of $La_4Co_3O_{10}$ at 1002−1204K through EMF measurements.

II. La_2CoO_4

La_2CoO_4 is orthorhombically distorted relative to the tetragonal K_2NiF_4-type structure [22]. Lewandowski *et al.* [23] reported that La_2CoO_4 does not exist at the stoichiometric composition. Instead, they proposed a lanthanum-deficient composition, $La_{1.83}CoO_4$. This was however denied

by other groups [8−10]. Sreedharan and Pankajavalli [24] determined the Gibbs energy of reaction for La_2O_3 (s) + Co (s) + $1/2O_2$ (gas, 1bar) = La_2CoO_4 (s) via EMF measurements on a galvanic cell of Pt, La_2CoO_4, La_2O_3, Co/YSZ/O_2. They further derived the Gibbs energy of formation of La_2CoO_4 from oxides (La_2O_3 and CoO) in a temperature range of 973–1375 K. Parida *et al.* [1] determined thermodynamic properties of La_2CoO_4 at 1002−1204K, also via EMF measurements on a galvanic cell of Pt, La_2CoO_4, La_2O_3, $La_4Co_3O_{10}$/CSZ/Ni, NiO/Pt.

III. Perovskite ($LaCo_xFe_{1-x}O_{3-\delta}$)

The $LaCoO_{3-\delta}$ perovskite phase has a cubic structure at T > 1610 K and a rhombohedral structure at T < 1610K [12, 25]. The cubic-rhombohedral transformation is of second order, as determined by TG-DTA (differential thermal analysis) and XRD measurements. At low oxygen partial pressure, oxygen vacancies form, resulting in a further distortion of the perovskite structure to orthorhombic. The crystal structure of the $LaFeO_3$ perovskite has been reviewed by Povoden-Karadeniz [18]. It is orthorhombic at temperatures up to 1278±5 K, where it transforms to the rhombohedral structure. In the La-Co-Fe-O system, the $LaCo_xFe_{1-x}O_{3-\delta}$ pervoskite phase covers a composition range from $LaCoO_{3-\delta}$ to $LaFeO_3$. Wold and Croft [26] investigated the crystal structure of $LaFe_xCo_{1-x}O_3$ at 1100°C and 1300°C in air using XRD. It was found that the perovskite phase changes from orthorhombic to rhombohedral with increasing Fe content. Vyshatko *et al.* [27] determined the crystal structure of $LaFe_{0.5}Co_{0.5}O_3$ at around 1200°C in air to be rhombohedral.

The thermodynamic properties of $LaCoO_{3-\delta}$ have been well investigated [6, 8, 28−31]. Sreedharan and Chandrasekharaiah [28] determined the Gibbs energy of formation and phase transformation of $LaCoO_3$ between 1100 and 1325 K via EMF measurements. They used two types of galvanic cells: Pt/Ni, NiO/CSZ/Co, La_2O_3, $LaCoO_3$/Pt and Pt/Ni, NiO/CSZ/CoO, La_2O_3, $LaCoO_3$/Pt. However, both cells did not reach equilibrium and therefore their derived phase relations were wrong [6, 8, 29]. Stølen *et al.* [30] measured the heat capacity of $LaCoO_3$ from 13 to 1000K by adiabatic calorimetry. Parida *et al.* [1] determined the standard molar Gibbs energy of formation for $LaCoO_3$ at 1002−1204 K via EMF measurements. They chose same galvanic cell configuration as Sreedharan and Chandrasekharaiah [28] and their reported Gibbs energy of formation for $LaCoO_3$ is higher than the value reported by Nakamura *et al.* from [6] and Kitayama[10]. Cheng *et al.* [31] determined the enthalpy of formation for $LaCoO_3$ from

constituent oxides at 298 K as –107.64 ± 1.77 kJ/mol by high-temperature oxide melt solution calorimetry.

Oxygen deficiency in $LaCoO_{3-\delta}$ was measured by a number of groups [32–35]. Seppänen *et al.* [32] determined oxygen deficiency in $LaCoO_{3-\delta}$ as a function of oxygen partial pressure at temperatures between 1178 and 1311 K using the coulometric titration method. They measured oxygen deficiency of $LaCoO_{3-\delta}$ in equilibrium with either La_2O_3 or CoO at 1200, 1255 and 1288 K and derived partial molar enthalpy and entropy of oxygen in $LaCoO_{3-\delta}$. Mizusaki *et al.* [33] used TG to determine oxygen non-stoichiometry in $LaCoO_{3-\delta}$ at 1123, 1173, 1223 and 1273 K and PO_2 = 10^{-5} – l atm. Petrov *et al.* [34] studied oxygen non-stoichiometry of $LaCoO_{3-\delta}$ at 1273–1773 K as a function of PO_2 using TG. Recently, Zuev *et al.* [35] measured oxygen non-stoichiometry of lanthanum cobaltite as a function of oxygen partial pressure at 1173–1323 K by coulometric titration. Their results were also in agreement with those from Seppänen *et al.* [32].

Beside thermodynamic properties and oxygen non-stoichiometry, the electronic structure of $LaCoO_{3-\delta}$ has drawn special interest, as it influences magnetic properties, electronic conductivity and thermal conductivity. Goodenough [36] investigated the transition in $LaCoO_{3-\delta}$ from localized electron to collective electron by XRD, DTA and TG measurements and constructed a model for cobalt cation configuration in $LaCoO_{3-\delta}$ at various temperature intervals. It was found that Co^{2+} (high spin) and Co^{4+} (low spin) formed only at T > 673K, and there is a first order transition at 1210K from localized electron to collective electron. Bhide [37] *et al.* investigated this transition but using Mössbauer spectroscopy. They concluded that Co^{2+} (low spin) and Co^{4+} (high spin) already formed at T > 200K and Co^{3+} disappeared completely at 1210K. Abbate *et al.* [38] re-determined electronic structure of $LaCoO_{3-\delta}$ and found no evidence of charge disproportionation at a temperature range of 80–630K. The electronic structure of $LaCoO_{3-\delta}$ was recently reviewed by Petrov [14]. Despite tremendous interests and intensive research activities over the past decades, the electronic structure of $LaCoO_{3-\delta}$ and the conduction mechanism are still topics of controversial discussions.

3.3 Thermodynamic modeling

Several efforts have been carried out on thermodynamic modeling of the La-Co-O system. Yokokawa *et al.* [39] modeled the thermodynamic properties of the three ternary oxides ($LaCoO_3$, La_2CoO_4 and $La_4Co_3O_{10}$) in order to construct a chemical potential diagram for La-Co-O. All these

oxides were treated as stoichiometric compounds, and no defects were considered. Yang *et al.* [12] and Saal [13] modeled La-Co-O using the CALPHAD methodology. Their focus was the defect chemistry of the perovskite phase. Using their parameters for phase equilibrium calculation, we observed large deviations from the experiments. In our assessment we thus put effort to obtain both correct phase boundaries as well as reliable descriptions of the defect chemistry and cation disproportionation of the lanthanum cobaltite. No modeling work has been carried out on La-Co-Fe-O.

In the present work, the thermodynamic description of La-Co-O was based on those of the subsystems, La-O by Grundy *et al.* [15, 40], Co-O by Chen *et al.* [16], and La-Co by Wang *et al.* [41]. The parameters for the ternary La-Co-O system were optimized using the experimental data as described in *Section 3.2*. The description of La-Co-Fe-O was based on those of La-Fe-O by Povoden-Karadeniz [18], Co-Fe-O by Zhang and Chen [42] and La-Co-O from this work. The Compound Energy Formalism (CEF) [43], which is widely used in CALPHAD assessments, was employed to describe Gibbs energy for all the phases in La-Co-O. The lattice stability for pure elements was adopted from Dinsdale [44]. The magnetic contribution to the Gibbs energy was modeled using the "Hillert–Jarl–Inden" model proposed by Inden [45] and further modified by Hillert and Jarl [46].

3.3.1 Liquid

In the present work, the liquid phase was treated as an ideal extrapolation of the liquid from the subsystems La-O [15], Co-O [16] and Fe-O [17], where the liquid phase was modeled all using the ionic two–sublattice model [47, 48]. This model was developed within the framework of CEF, with one sublattice containing charged cations and the other containing charged anions and vacancies. The liquid phase in La-Co-Fe-O is described as:

$(Co^{2+}, Co^{3+}, La^{3+}, Fe^{2+}, Fe^{3+})_p(O^{2-}, Va^{q-})_q$

Where $p=2y_{O^{2-}}+qy_{Va}$ (3.6)

$$q=2y_{Co^{2+}}+3y_{Co^{3+}}+2y_{Fe^{2+}}+3y_{Fe^{3+}}+3y_{La^{3+}} \quad (3.7)$$

The Gibbs energy of the liquid phase is expressed as:

$$G_m^L = q\sum_i y_i y_{Va}\,{}^0G_{i:Va}^L + \sum_i y_i y_{O^{2-}}\,{}^0G_{i:O^{2-}}^L + pRT\sum_i y_i \ln y_i + qRT\sum_j y_j \ln y_j + {}^EG_m^L \quad (3.8)$$

Where i represents the constituents in the first sublattice, and j represents the constituents in the second sublattice. The excess Gibbs energy ${}^{E}G_m^L$ is formulated as the following:

$${}^{E}G_m^L = \sum_{i_m} \sum_{i_n \neq i_m} y_{i_m} y_{i_n} (y_{O^{2-}} L^L_{i_m,i_n:O^{2-}} + q y_{Va}{}^3 L^L_{i_m,i_n:Va}) + \sum_{i_m} y_{i_m} y_{O^{2-}} y_{Va} L^L_{i_m:O^{2-},Va} \quad (3.9)$$

where i_m and i_n represents the constituents in the first sublattice. In the above expressions, colons were used to separate species on different sublattices and commas to separate species on the same sublattice. In the present work, no ternary (La-Co-O) or quaternary (La-Co-Fe-O) parameter was optimized for the liquid phase due to lack of experimental data. The calculated liquidus shall therefore be treated with caution.

3.3.2 *Metallic phases*

In the present work, the thermodynamic descriptions for the metallic phases were taken from binary sub-systems with ideal extrapolation. No ternary or quaternary parameter was used. Oxygen solubility in pure metal (BCC, FCC, HCP and DHCP) was modeled using the two-sublattice model with metal atoms on the first sublattice and oxygen and vacancies on the second sublattice. In La-Co-Fe-O, the models read as the following:

BCC: (La, Co, Fe)$_1$(O, Va)$_3$

FCC: (La, Co, Fe)$_1$(O, Va)$_1$

HCP: (Co, Fe)$_1$(O, Va)$_{0.5}$

DHCP: (La)$_1$(O, Va)$_{0.5}$

The binary parameters were taken from literatures [15, 16, 41, 49], except for the BCC phase. In Co-Fe-O, the BCC phase was modeled using the model (Co, Fe)$_1$(O, Va)$_3$, while in La-O the BCC-La was modeled as (La)$_1$(O, Va)$_{1.5}$. In the present work, the BCC-La phase was remodeled as (La)$_1$(O, Va)$_3$ in accordance with the BCC-Co, Fe phase. The thermodynamic descriptions of the inter-metallic compounds in La-Co were taken from literature [41].

3.3.3 Binary oxides

The following binary oxides exist in La-Co-Fe-O: CoO, Co_3O_4, FeO, Fe_2O_3, Fe_3O_4, A-, H-, and X-La_2O_3. The Gibbs energy functions for CoO and Co_3O_4 were taken from Chen *et al.* [16] and those for Fe oxides were from Sundman [17]. For La-O, Grundy *et al.* [15] modeled the polymorphic-

La_2O_3 as non-stoichiometric. In their calculated phase diagram of La-O, solid La_2O_3 appears too stable when interacting with the liquid phase. Later, they revised the thermodynamic description of the solid La_2O_3 phases where the deviation from stochiometry was ignored [40]. It was shown that the calculated melting temperature of La_2O_3 fits better with the experimental results. Zinkevich *et al.* [50] also modeled the La-O system, but their assessment was based on a limited amount of experimental data. In the present work, we adopted the revised thermodynamic descriptions for La_2O_3 from Grundy *et al.* [40].

No mutual solubility was found between La and Co or La and Fe binary oxides and was therefore not considered in the present work. The solubility between Co and Fe oxides was modeled by Zhang and Chen [42] and the thermodynamic description of Co-Fe-O was included without modification.

3.3.4 $La_4Co_3O_{10}$ and La_2CoO_4

In the present work, $La_4Co_3O_{10}$ and La_2CoO_4 were treated also as stoichiometric compound. The Gibbs energy functions were taken from Yokokawa *et al.* [39], which were adopted by the SGTE SSUB database [51]. The Gibbs energy function for $La_4Co_3O_{10}$ was further adjusted in the present work in order to reproduce recently reported thermodynamic data and phase diagram data.

3.3.5 Perovskite ($LaCo_xFe_{1-x}O_{3-\delta}$)

We modeled the perovskite phase as one single phase without differentiating the cubic distortion structures (orthorhombic, and rhombohedral). A 3-sublattice model was used, with the first sublattice (A site) for La cations and vacancies, the second sublattice (B site) for Co, Fe cations and vacancies, and the third sublattice (O site) for oxide ions and oxygen vacancies. For La-Co-O, beside Co^{3+}, Co^{2+} and Co^{4+} were also introduced into the B site in order to model charge disproportionation ($2Co^{3+} \rightarrow Co^{2+}+Co^{4+}$). Cation vacancies were introduced into the A and B sites and oxygen vacancies to the O site, respectively, to model the perovskite non-stoichiometry, and the model reads

$(La^{3+},Va)_1(Co^{2+},Co^{3+}, Co^{4+},Va)_1 (O^{2-}, Va)_3$.

A similar model was used for the perovskite phase in La-Fe-O ($(La^{3+},Va)_1(Fe^{2+},Fe^{3+}, Fe^{4+},Va)_1 (O^{2-}, Va)_3$): [18]. For La-Co-Fe-O, the model for the perovskite phase can be expressed as:

$(La^{3+}, Va)_1[Co^{2+}, Co^{3+}, Co^{4+}, Fe^{2+},Fe^{3+}, Fe^{4+}, Va]_1 (O^{2-}, Va)_3$

The Gibbs energy function of the perovskite phase (the non-magnetic part) is given by the following expression:

$$G_m^{perovskite} = \sum_i \sum_j \sum_k y_i y_j y_k {}^oG_{i:j:k}^{perovskite} + RT\sum_i y_i \ln y_i + RT\sum_j y_j \ln y_j + 3RT\sum_k y_k \ln y_k + {}^EG_m^{perovskite} \quad (3.10)$$

Where i, j, k represent the constituents in the first, second and third sublattice, respectively.

According to the current model, 28 end-members (${}^oG_{i:j:k}^{perovskite}$ terms) need to be assigned with a Gibbs energy term. 16 of them were taken from La-Fe-O [18], including 4 end-members ${}^oG_{La^{3+}:Va:O^{-2}}^{perovskite}$, ${}^oG_{Va:Va:O^{2-}}^{perovskite}$, ${}^oG_{La^{3+}:Va:Va}^{perovskite}$, ${}^oG_{Va:Va:Va}^{perovskite}$ which were originally developed by Grundy *et al.* [52]. The other 12 end-members belong to the La-Co-O system and were determined in this work. Most of these end-members have a net charge and therefore do not physically exist. The strategy to obtain the Gibbs energy terms for these 12 end-members is to choose appropriate neutral end-members or their combinations as model parameters, which can be optimized with experimental data. Similar to previous modeling of the perovskite phase [18, 52, 53], a number of the most important end-members or their combinations were chosen as model parameters and were listed below:

Stoichiometric $LaCoO_3$: $(La^{3+})_1(Co^{3+})_1(O^{2-})_3$. Its Gibbs energy function is given by:

$${}^oG_{La^{3+}:Co^{3+}:O^{2-}}^{perovskite} = GL3OSSUB + A_1 + B_1 * T \quad (3.11)$$

where GL3OSSUB was taken from Yokokawa *et al.* [39]. A_1 and B_1 are the parameters to be optimized in the present work.

Reduced $LaCoO_3$: $(La^{3+})_1(Co^{2+})_1(O^{2-}{}_{5/6}, Va_{1/6})_3$. Its Gibbs energy function is given by:

$$G_m = \frac{5}{6}{}^oG_{La^{3+}:Co^{2+}:O^{2-}}^{perovskite} + \frac{1}{6}{}^oG_{La^{3+}:Co^{2+}:Va}^{perovskite} + 3RT\left(\frac{5}{6}\ln\frac{5}{6} + \frac{1}{6}\ln\frac{1}{6}\right) = 0.5\,{}^oG^{La_2O_3} + {}^oG^{CoO} + A_2 + B_2 * T \quad (3.12)$$

where ${}^oG^{La_2O_3}$ and ${}^oG^{CoO}$ represent the Gibbs energy functions of stoichiometric A-La_2O_3 and CoO respectively and were taken from Grundy *et al.* [40] and Chen *et al.* [16]. A_2 and B_2 are the parameters to be optimized in the present work.

Oxidized Co rich $LaCoO_3$ $(La^{3+}{}_{2/3}, Va_{1/3})_1(Co^{4+})_1(O^{2-})_3$

$$G_m = \frac{2}{3}{}^{o}G^{perovskite}_{La^{3+}:Co^{4+}:O^{2-}} + \frac{1}{3}{}^{o}G^{perovskite}_{Va:Co^{4+}:O^{2-}} + RT(\frac{2}{3}\ln\frac{2}{3} + \frac{1}{3}\ln\frac{1}{3}) = \frac{1}{3}{}^{o}G^{La_2O_3} + {}^{o}G^{CoO} + \frac{1}{2}{}^{o}G^{O_2} + A_3 + B_3 * T \quad (3.13)$$

Oxidized Co deficient $LaCoO_3$ $(La^{3+})_1(Co^{4+}{}_{3/4}, Va_{1/4})_1(O^{2-})_3$.

$$G_m = \frac{3}{4}{}^{o}G^{perovskite}_{La^{3+}:Co^{4+}:O^{2-}} + \frac{1}{4}{}^{o}G^{perovskite}_{La^{3+}:Va:O^{2-}} + RT(\frac{3}{4}\ln\frac{3}{4} + \frac{1}{4}\ln\frac{1}{4}) = 0.5{}^{o}G^{La_2O_3} + 0.75{}^{o}G^{CoO} + A_4 + B_4 * T \quad (3.14)$$

where ${}^{o}G^{O_2}$ was from Dinsdale [44] and A_3, A_4, B_3, and B_4 are the parameters to be optimized in the present work.

All the other end-members are correlated by the following reciprocal relations:

$${}^{o}G^{perovskite}_{La^{3+}:Co^{3+}:O^{2-}} + {}^{o}G^{perovskite}_{Va:Co^{3+}:Va} - {}^{o}G^{perovskite}_{La^{3+}:Co^{3+}:Va} - {}^{o}G^{perovskite}_{Va:Co^{3+}:O^{2-}} = \Delta G_1 \quad (3.15)$$

$${}^{o}G^{perovskite}_{La^{3+}:Co^{3+}:O^{2-}} + {}^{o}G^{perovskite}_{La^{3+}:Co^{4+}:Va} - {}^{o}G^{perovskite}_{La^{3+}:Co^{4+}:O^{2-}} - {}^{o}G^{perovskite}_{La^{3+}:Co^{3+}:Va} = \Delta G_2 \quad (3.16)$$

$${}^{o}G^{perovskite}_{La^{3+}:Co^{2+}:O^{2-}} + {}^{o}G^{perovskite}_{Va:Co^{3+}:O^{2-}} - {}^{o}G^{perovskite}_{La^{3+}:Co^{3+}:O^{2-}} - {}^{o}G^{perovskite}_{Va:Co^{2+}:O^{2-}} = \Delta G_3 \quad (3.17)$$

$${}^{o}G^{perovskite}_{La^{3+}:Co^{3+}:O^{2-}} + {}^{o}G^{perovskite}_{Va:Co^{4+}:O^{2-}} - {}^{o}G^{perovskite}_{La^{3+}:Co^{4+}:O^{2-}} - {}^{o}G^{perovskite}_{Va:Co^{3+}:O^{2-}} = \Delta G_4 \quad (3.18)$$

$${}^{o}G^{perovskite}_{Va:Co^{3+}:O^{2-}} + {}^{o}G^{perovskite}_{Va:Co^{2+}:Va} - {}^{o}G^{perovskite}_{Va:Co^{2+}:O^{2-}} - {}^{o}G^{perovskite}_{Va:Co^{3+}:Va} = \Delta G_5 \quad (3.19)$$

$${}^{o}G^{perovskite}_{La^{3+}:Co^{2+}:Va} + {}^{o}G^{perovskite}_{Va:Co^{3+}:Va} - {}^{o}G^{perovskite}_{La^{3+}:Co^{3+}:Va} - {}^{o}G^{perovskite}_{Va:Co^{2+}:Va} = \Delta G_6 \quad (3.20)$$

$${}^{o}G^{perovskite}_{La^{3+}:Co^{3+}:Va} + {}^{o}G^{perovskite}_{Va:Co^{4+}:Va} - {}^{o}G^{perovskite}_{La^{3+}:Co^{4+}:Va} - {}^{o}G^{perovskite}_{Va:Co^{3+}:Va} = \Delta G_7 \quad (3.21)$$

$${}^{o}G^{perovskite}_{La^{3+}:Co^{2+}:O^{2-}} + {}^{o}G^{perovskite}_{La^{3+}:Co^{3+}:Va} - {}^{o}G^{perovskite}_{La^{3+}:Co^{3+}:O^{2-}} - {}^{o}G^{perovskite}_{La^{3+}:Co^{2+}:Va} = \Delta G_8 \quad (3.22)$$

In this work, the reciprocal energy $\Delta G_x = 0$ (x=1−8) was chosen [54]. The Gibbs energy functions for the 12 end-members can be derived by solving Equations 3.11 to 3.22.

The excess Gibbs energy ${}^{E}G^{perovskite}_{m}$ is formulated as the following:

$$ {}^{E}G_m^{perovskite} = \sum_{i_l}\sum_{i_k \neq i_l}\sum_{j_m} y_{i_k} y_{i_l} y_{j_m} L^{perovskite}_{i_k, i_l : j_m : O^{2-}} + \sum_{i_l}\sum_{j_m}\sum_{j_n \neq j_m} y_{i_l} y_{j_m} y_{j_n} L^{perovskite}_{i_l : j_m, j_n : O^{2-}} \quad (3.23) $$

where i_k, i_l represents the constituents in the first sublattice (A site), and j_m, j_n represents the constituents in the second sublattice (B site).

Table 3.1 Models and parameters for the ternary oxide phases in La-Co-O system [a]

Phase	Model/parameters	Reference
$La_4Co_3O_{10}$	($La_4Co_3O_{10}$)	
	${}^{o}G^{La_4Co_3O_{10}} - 4H^{SER}_{La} - 3H^{SER}_{Co} - 10H^{SER}_{O} = GLA4CO3O10$	
La_2CoO_4	$(La^{3+})_2\ (Co^{2+})_1(O^{2-})_4$	
	${}^{o}G^{La_2CoO_4}_{La^{3+}:Co^{2+}:O^{2-}} - 2H^{SER}_{La} - H^{SER}_{Co} - 4H^{SER}_{O} = GLACOO4$	
Perovskite	$(La^{3+}, Va)(Co^{2+}, Co^{3+}, Co^{4+}, Va)_1(O^{2-}, Va)_4$	
	${}^{o}G^{perovskite}_{La^{3+}:Co^{2+}:O^{2-}} - H^{SER}_{La} - H^{SER}_{Co} - 3H^{SER}_{O} = +GLC2OV + 0.5GHSEROO + 11.2379T$	
	${}^{o}G^{perovskite}_{Va:Co^{2+}:O^{2-}} - H^{SER}_{Co} - 3H^{SER}_{O} = +0.5GVVV + GLC2OV - 2GL4VO + 1.5GLV4O$ $+2GHSEROO + 11.2379T$	
	${}^{o}G^{perovskite}_{La^{3+}:Co^{3+}:O^{2-}} - H^{SER}_{La} - H^{SER}_{Co} - 3H^{SER}_{O} = +GL3CO$	
	${}^{o}G^{perovskite}_{Va:Co^{3+}:O^{2-}} - H^{SER}_{Co} - 3H^{SER}_{O} = +GL3CO + 0.5GVVV - 2GL4VO + 1.5GLV4O$ $+1.5GHSEROO - 1.41254T$	
	${}^{o}G^{perovskite}_{La^{3+}:Co^{4+}:O^{2-}} - H^{SER}_{La} - H^{SER}_{Co} - 3H^{SER}_{O} = +\frac{1}{6}GVVV + \frac{2}{3}GL4VO + 0.5GLV4O$ $-0.5GHSEROO + 5.76283T$	
	${}^{o}G^{perovskite}_{Va:Co^{4+}:O^{2-}} - H^{SER}_{Co} - 3H^{SER}_{O} = +\frac{1}{3}GVVV - \frac{4}{3}GL4VO + 2GLV4O$ $+GHSEROO + 4.35029T$	
	${}^{o}G^{perovskite}_{La^{3+}:Va:O^{2-}} - H^{SER}_{La} - 3H^{SER}_{O} = +2GL4O - 1.5GV4O + 0.5GVVV$ $+1.5GHSEROO + 1.41263T$	
	${}^{o}G^{perovskite}_{Va:Va:O^{2-}} - 3H^{SER}_{O} = +GVVV + 3GHSEROO$	
	${}^{o}G^{perovskite}_{La^{3+}:Co^{2+}:Va} - H^{SER}_{La} - H^{SER}_{Co} = +GLC2OV - 2.5GHSEROO + 11.2379T$	
	${}^{o}G^{perovskite}_{Va:Co^{2+}:Va} - H^{SER}_{Co} = +0.5GVVV + GLC2OV - 2GL4VO + 1.5GLV4O$ $-GHSEROO + 9.82536T$	
	${}^{o}G^{perovskite}_{La^{3+}:Co^{3+}:Va} - H^{SER}_{La} - H^{SER}_{Co} = +GL3CO - 3GHSEROO$	
	${}^{o}G^{perovskite}_{Va:Co^{3+}:Va} - H^{SER}_{Co} = +GL3CO + 0.5GVVV - 2GL4VO + 1.5GLV4O$ $-1.5GHSEROO - 1.41254T$	

${}^{o}G^{perovskite}_{La^{3+}:Co^{4+}:Va} - H^{SER}_{La} - H^{SER}_{Co} = -\frac{1}{6}GVVV + \frac{2}{3}GL4VO + 0.5GLV4O$ $-3.5GHSEROO + 5.76283T$	
${}^{o}G^{perovskite}_{Va:Co^{4+}:Va} - H^{SER}_{Co} = +\frac{1}{3}GVVV - \frac{4}{3}GL4VO + 2GLV4O$ $-2GHSEROO + 4.35029T$	
${}^{o}G^{perovskite}_{La^{3+}:Va:Va} - H^{SER}_{La} = +2GL4O + 0.5GVVV - 1.5GV4O$ $-1.5GHSEROO + 1.41263T$	
${}^{o}G^{perovskite}_{La^{3+}:Co^{4+}:Va} - H^{SER}_{La} - H^{SER}_{Co} = GVVV$	
Interaction parameters and functions	
Parameter set A:	
$GLA4CO3O10 = -4684982.57 + 2325.48945T - 402T\ln(T) - 0.02715T^2$ $+2566000T^{-1}$	This work
$GLACOO4 = -2095975.55 + 951.680046T - 167.49T\ln(T) - 0.010645T^2$ $+938000T^{-1}$	This work
$GLC2OV = 0.5GLA2O3D + GCOOS + 45388.14 - 14.77T$	This work
$GL4VO = 0.5GLA2O3D + 0.75GCOOS + 0.75GHSEROO - 68796.23 - 28.21T$	This work
$GLV4O = \frac{1}{3}GLA2O3D + GCOOS + GHSEROO - 85014.24 + 223.25T$	This work
$GL3CO = GL3OSSUB - 7358.08 + 9.50T$	This work
Parameter set B:	
${}^{0}L^{Prv}_{La^{3+},Va:Co^{4+}:O^{2-}} = +1,000,000$	This work
${}^{0}L^{Prv}_{La^{3+}:Co^{4+},Va:O^{2-}} = +1,000,000$	This work
$GLA4CO3O10 = -4694982.57 + 2329.48945T - 402T\ln(T) - 0.02715T^2$ $+2566000T^{-1}$	[39]
$GLACOO4 = -2095975.55 + 951.680046T - 167.49T\ln(T) - 0.010645T^2$ $+938000T^{-1}$	[39]
$GLC2OV = 0.5GLA2O3D + GCOOS - 25550.5 + 24.985T$	This work
$GL4VO = 0.5GLA2O3D + 0.75GCOOS + 0.75GHSEROO - 91523.1 - 16.7096T$	This work
$GLV4O = \frac{1}{3}GLA2O3D + GCOOS + GHSEROO - 233150.3 + 316.7797T$	This work
$GL3CO = GL3OSSUB + 5.55T$	This work

$$GL3OSSUB = -1261010.71 - 70.3237561T + 6.17T\ln(T) - 0.14132T^2 - 1179500T^{-1} \quad [39]$$
$$298.15 < T < 550K$$
$$-1301031.07 + 751.034485T - 125.1T\ln(T) - 0.009245T^2 + 958500T^{-1}$$
$$550 < T < 1220$$
$$-1288831.07 + 669.968423T - 115.1T\ln(T) - 0.009245T^2 + 958500T^{-1}$$
$$1220 < T < 3000$$
$$GVVV = 6GL2O + 4GL4O + 3GV4O - 12GL3O - 254212 \quad [52]$$

[a] All parameters are in SI units: J, mol, K and Pa.

3.3.6 Optimization

Table 3.1 lists two sets of optimized thermodynamic parameters obtained in the present work for the ternary oxide phases in La-Co-O. The thermodynamic description of La-Co-Fe-O is based on those of La-Co-O, La-Fe-O [18] and Co-Fe-O [42] with ideal extrapolation, i.e. no extra parameter was used. Due to small modifications on the thermodynamic descriptions of the BCC-La and La_2O_3 phases in the current work, the La-O phase diagram was re-calculated and it agrees reasonably well with the ones published by Grundy *et al.* [15] and Povoden-Karadeniz *et al.* [18]. During the optimization, all experimental data were carefully assessed. The evaluation of the model parameters was obtained by recurrent runs of the PARROT program [55] in the Thermo-Calc software, which works by minimizing the square sum of the differences between experimental values and computed ones. In the optimization, each piece of experimental information is given with certain weight. The weights were adjusted during the assessment until most of the experimental data were accounted for within the claimed uncertainty limits.

The optimization of model parameters of stoichiometric phases is straight-forward. As mentioned in *section 3.4*, the parameter for $La_4Co_3O_{10}$ was further optimized using the thermodynamic and phase diagram data. On the other hand, the perovskite phase is much more interesting and demanding. A_1 and B_1 in *Eq. 3.11* were optimized using relevant thermodynamic and phase diagram data. A_2 and B_2 in *Eq. 3.12* control charge disproportionation and were optimized using oxygen non-stoichiometry data. In addition, A_3 and B_3 in *Eq. 3.13* and A_4 together with B_4 in *Eq. 3.14* were optimized in order to achieve a satisfactory agreement with the oxygen non-stoichiometry data. Two sets of parameters were obtained in the end: *Parameter Set A* is suggested for low charge disproportionation (about 0% at T < 700K) and *Parameter Set B* is for high charge disproportionation (100% at low temperature). $LaCoO_{3-\delta}$ shows very narrow

composition range with respect to the La/Co ratio. To prevent any deviation from a La/Co ratio of 1 in the calculated phase diagrams, two interaction parameters ${}^{0}L^{perovskite}_{La^{3+},Va:Co^{4+}:O^{2-}}$ and ${}^{0}L^{perovskite}_{La^{3+}:Co^{4+},Va:O^{2-}}$ were assigned with a value of 1,000,000 in *Parameter Set B*.

3.4 Results and discussion

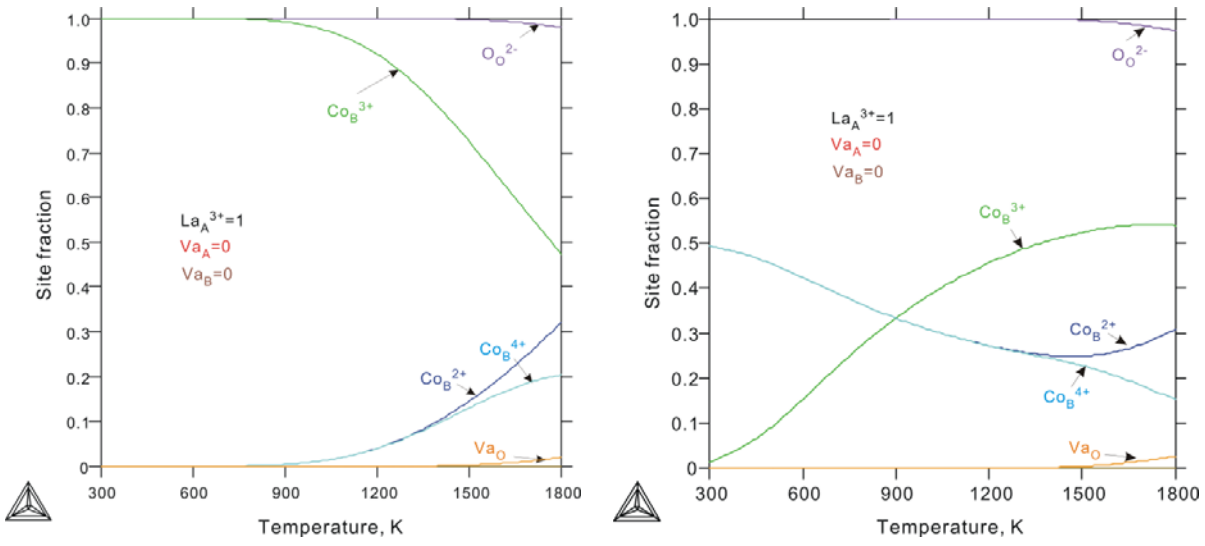

Fig. 3.1. Site fractions in $LaCoO_{3-\delta}$ in air. (a) calculated using *Parameter Set A*, (b) calculated using *Parameter Set B*.

In the present work, two sets of thermodynamic parameters were obtained representing different charge disproportionation schemes in $LaCoO_{3-\delta}$. Fig. 3.1 plots calculated site fractions in $LaCoO_{3-\delta}$ in air using these two sets of parameters. With *Parameter Set A*, $LaCoO_{3-\delta}$ shows no charge disproportionation at low temperature. Co^{2+} and Co^{4+} start forming at about 700K, which is in agreement with Goodenough and Abbate *et al.* [36, 38]. With *Parameter Set B*, $LaCoO_{3-\delta}$ shows high charge disproportionation, with Co^{2+} and Co^{4+} forming at all temperatures. Regarding thermodynamic properties and phase diagrams, both sets of the parameters represent experimental data equally well. The comparison between our calculated results and the experimental data in the following is carried out mainly for *Parameter Set A* to save space.

3.4.1 Thermodynamic properties

In the present work, the Gibbs energy functions of La_2CoO_4 and $La_4Co_3O_{10}$ were based on those from Yokokawa *et al.* [39] with minor change, and the comparison of the calculated Gibbs energy of formation with experimental data for these two phases is therefore excluded.

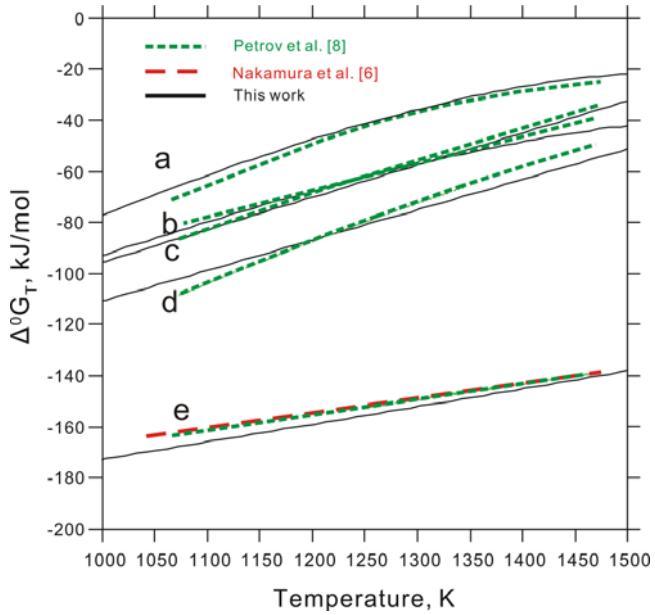

Fig. 3.2. Calculated Gibbs energy of reaction as a function of temperature using *Parameter Set A* in comparison with the experimental results [6, 8]. a) $2La_4Co_3O_{10}$ (s) $+1/2O_2$ (gas, air) = $6LaCoO_3$ (s) + La_2O_3 (s); (b) $La_4Co_3O_{10}$ (s) +CoO (s) $+1/2O_2$ (gas, air) = $4LaCoO_3$ (s); (c) $3La_2CoO_4$ (s)+ $1/2O_2$ (gas, air) = $La_4Co_3O_{10}$ (s) + La_2O_3 (s); (d) $2La_2CoO_4$ (s)+ CoO (s)+ $1/2O_2$ (gas, air) = $La_4Co_3O_{10}$ (s) and (e) La_2O_3 (s) + Co (s)+ $1/2O_2$ (gas, air) = La_2CoO_4 (s).

Using *Parameter Set A*, the enthalpy of formation for $LaCoO_3$ at 298 K from oxides (La_2O_3 and CoO) or from elements was calculated as −130 kJ/mol and −1265 kJ/mol, respectively, being more negative than those reported by Cheng *et al.* [31] (−107.42 ± 8.4 J/mol K from oxides and −1241.34 kJ/mol from elements). Fig. 3.2 plots the calculated Gibbs energy of reaction as a function of temperature using *Parameter Set A*. The reactions are (a) $2La_4Co_3O_{10}$ (s) + $1/2O_2$ (gas, air) = $6LaCoO_3$ (s) + La_2O_3 (s); (b) $La_4Co_3O_{10}$ (s) + CoO (s) + $1/2O_2$ (gas, air) = $4LaCoO_3$ (s); (c) $3La_2CoO_4$ (s) + $1/2O_2$ (gas, air) = $La_4Co_3O_{10}$ (s) + La_2O_3 (s); (d) $2La_2CoO_4$ (s) + CoO (s) + $1/2O_2$ (gas, air) = $La_4Co_3O_{10}$ (s) and (e) La_2O_3 (s) + Co (s) + $1/2O_2$ (gas, air) = La_2CoO_4 (s). A good agreement with the experimental results is achieved.

3.4.2 Phase diagrams

Figure 3.3 presents the calculated La-Co-O phase diagrams in air and Figure 3.4 shows the calculated isothermal PO_2-composition phase diagrams at 1373K, using both sets of parameters. The experimental data from Petrov *et al.* [14] were included for comparison. The calculated phase diagrams based on the two different sets of parameters agree with the experimental data equally well. Some difference can be found in the calculated temperatures for various invariant reactions

in air (Fig. 3.3) and at PO_2=1 Pa (Table 3.2). Further experimental studies on these invariant reactions are recommended in order to further narrow down the uncertainties.

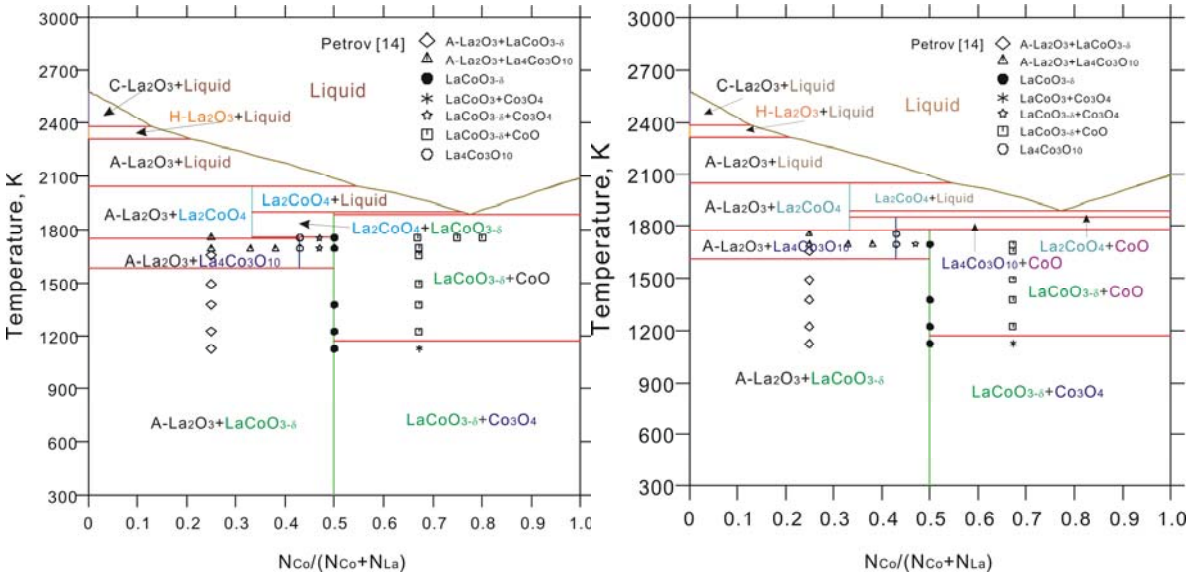

Fig. 3.3. Calculated phase diagrams of La-Co-O in air in comparison with the experimental data [14]. (a) Using *Parameter Set A* (low charge dispropostionation); b) Using *Parameter Set B* (high charge dispropostionation). *N* represents mole number.

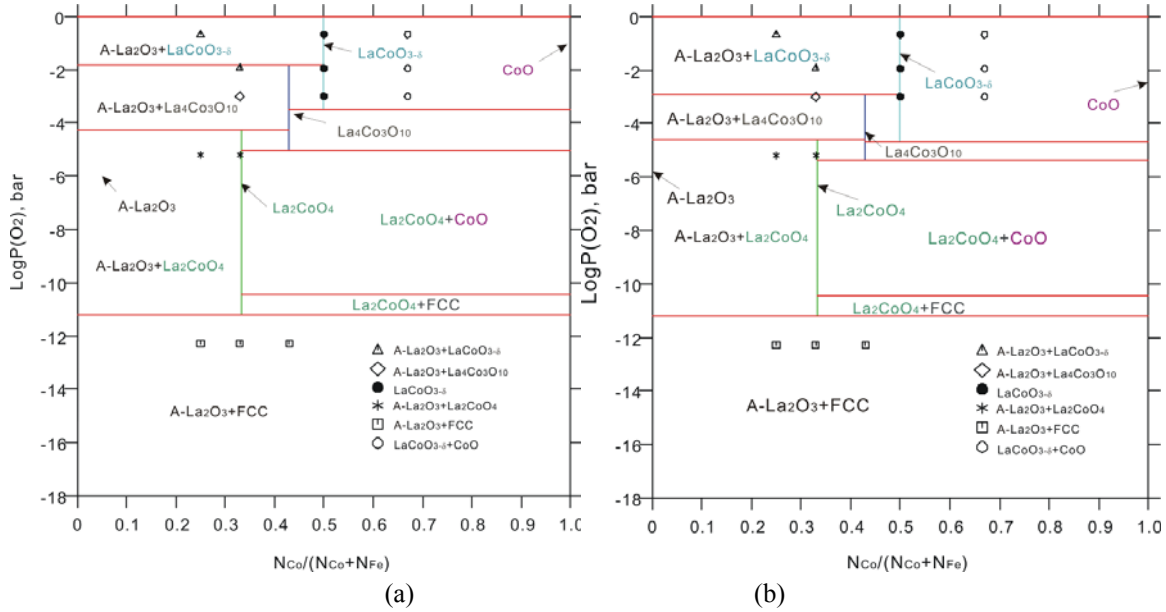

Fig. 3.4. Calculated isothermal PO_2-composition phase diagrams at 1373K in comparison with the experimental data from Petrov *et al*. [14]. (a) Using *Parameter Set A* (low charge dispropostionation); b) Using *Parameter Set B* (high charge dispropostionation).

Table 3.2 Calculated temperatures for various invariant reactions at PO_2=1Pa

Invariant Reactions	Using Parameter Set A (T, K)	Using Parameter Set B (T, K)
$2La_2CoO_4 + CoO + 1/2O_2 = La_4Co_3O_{10}$	1370	1403
$La_4Co_3O_{10} + CoO + 1/2O_2 = 4LaCoO_3$	1242	1351
$3La_2CoO_4 + 1/2O_2 = La_4Co_3O_{10} + La_2O_3$	1310	1343
$2La_4Co_3O_{10} + 1/2O_2 = 6LaCoO_3 + La_2O_3$	1116	1221

The calculated isothermal PO_2-composition phase diagrams at different temperatures are plotted in Fig. 3.5. These phase diagrams are all based on *Parameter Set A*. With decreasing temperature, the stability range for the perovskite phase extends to lower oxygen partial pressure. Fig. 3.6 shows the calculated stability phase diagrams using *Parameter Set A*. The calculations were done at different Co contents: $x(Co)/(x(Co)+x(La))$=0.3, 0.7 and 0.5. The single phase or two-phase region is labeled with phase names and the line between two neighboring regions represents a three-phase region (univariant). At high Co content (Fig. 3.6(a)) the calculation fits the experimental data very well. At low Co content (Fig. 3.6(b)), the calculated stability range for $La_4Co_3O_{10}$ is slightly larger than the experimentally determined one, with respect to both temperature and oxygen partial pressure. For SOFC applications, the La/Co ration of 1 is the most relevant, which is presented in Fig. 3.6 (c). This kind of phase diagram can be used to explore the stability range for the desired phases under certain temperature and oxygen partial pressure.

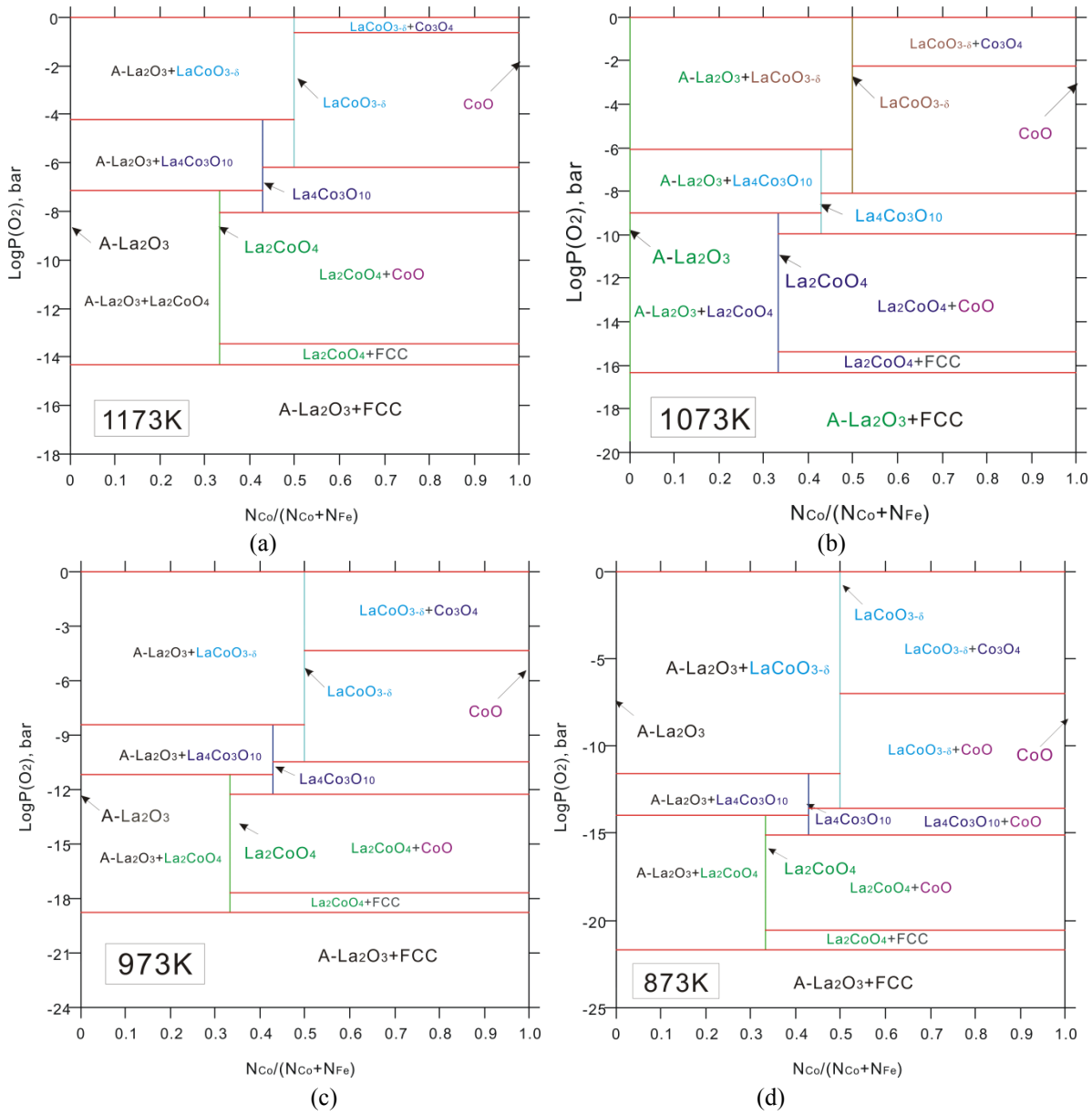

Fig. 3.5. Calculated isothermal PO_2-composition phase diagrams at different temperatures using *Parameter Set A*: (a) 1173K, (b) 1073K, (c) 973K, (d) 873K.

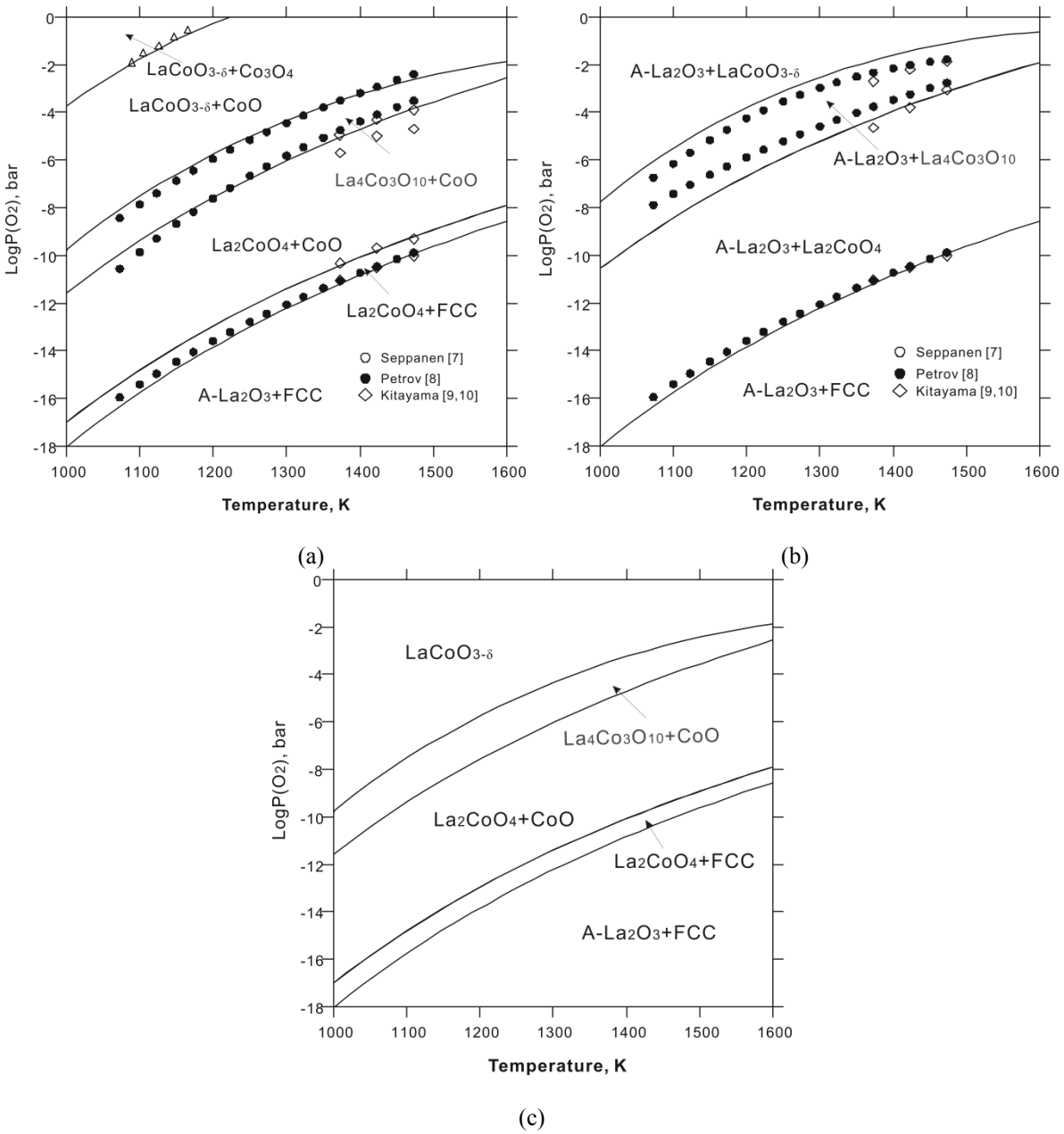

Fig. 3.6. Calculated stability diagrams of LaO_x-CoO_y using *Parameter Set A* in comparison with experimental data. (a) x(Co)/(x(Co)+x(La))=0.7; (b) x(Co)/(x(Co)+x(La))=0.3; (c) x(Co)/(x(Co)+x(La))=0.5. x represents mole fraction.

Fig. 3.7 plots calculated isothermal sections of La_2O_3-Fe_2O_3-CoO at 1373K and 973 K using *Parameter Set A*. Our calculated isothermal section at 1373K agrees with the experiment results from Proskurina *et al.* [11] in most cases, except that they treated $LaCoO_3$ and $LaFeO_3$ as different phases due to different crystal structure and this was not considered in the present

work. Fig. 3.8 presents calculated phase fraction for the composition $LaCo_{0.5}Fe_{0.5}O_3$. At 973K the $LaCo_{0.5}Fe_{0.5}O_3$ perovskite phase is stable down to $PO_2 \approx 10^{-19}$ bar.

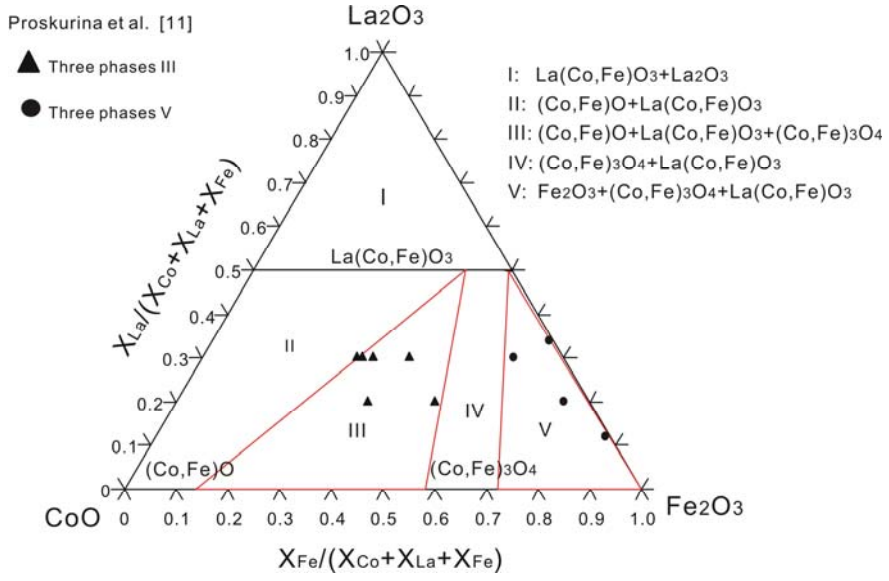

(a)

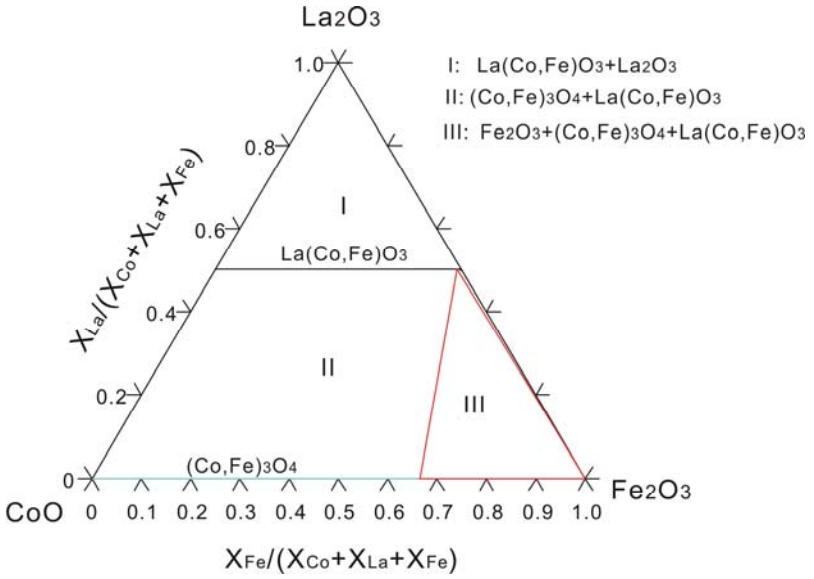

(b)

Fig. 3.7. Calculated isothermal sections of CoO-La_2O_3-Fe_2O_3 in air in comparison with the experimental data from Proskurina *et al*. [11]. (a) 1373K, (b)973K.

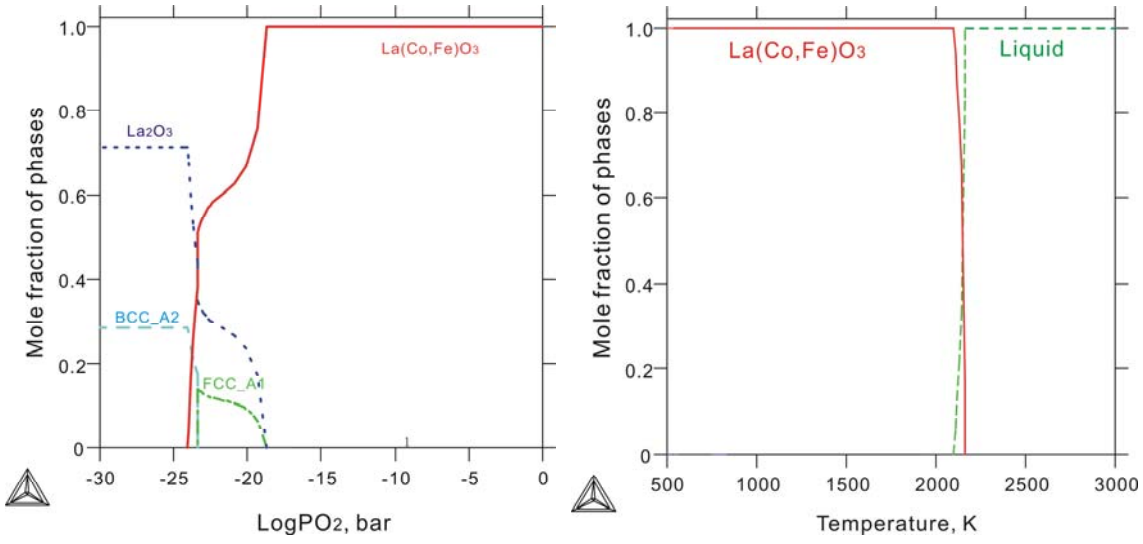

Fig. 3.8. Calculated phase fraction at the composition $LaCo_{0.5}Fe_{0.5}O_{3-\delta}$ (a) at 973K as a function of oxygen partial pressure and (b) in air (PO_2=21273 Pa) as a function of temperature.

3.4.3 Oxygen non-stoichiometry in $LaCoO_{3-\delta}$

The predominant defects in $LaCoO_{3-\delta}$ are oxygen vacancies with $\left[V_O^{\bullet\bullet}\right] \propto PO_2^{-1/2}$ [33]. Two kinds of situation may happen in $LaCoO_3$: The electronic defects are localized as valency defects, or defect electrons are delocalized in the conduction band. Petrov *et al.* [14, 34], used two different models to analyze the defect property of $LaCoO_{3-\delta}$. Model 1 is for itinerant electrons and Model 2 is for localized electrons and holes. Both models fit the experimental data equally well [14]. Based on the oxygen non-stoichiometry data, it is difficult to conclude whether the high charge disproportionation or the low charge disproportionation reflects the reality.

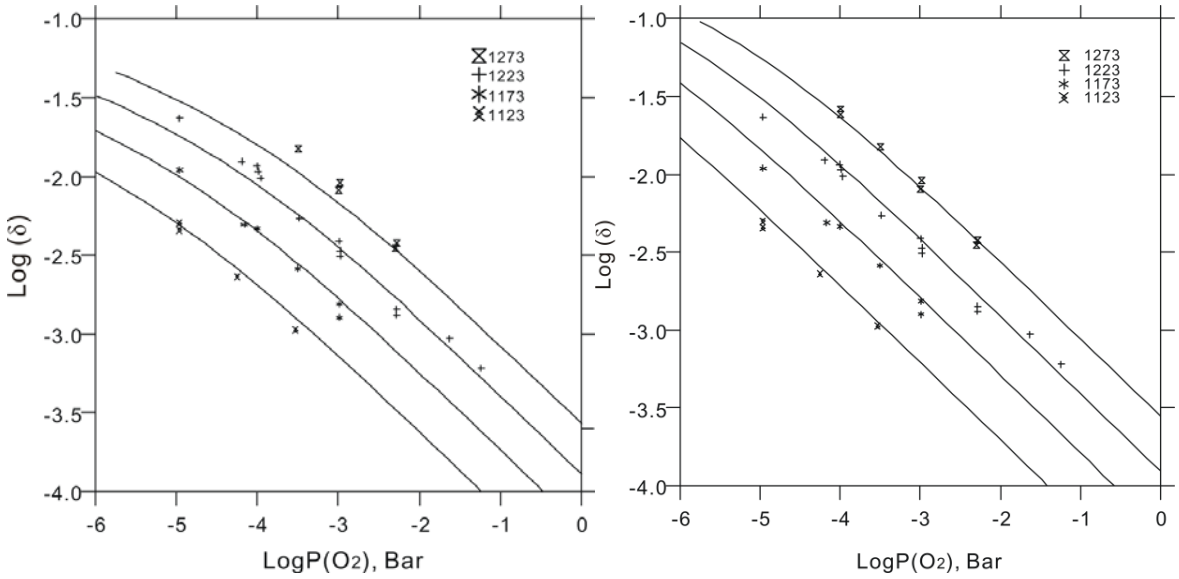

(a) (b)

Fig. 3.9. Calculated oxygen deficiency (δ) in $LaCoO_{3-\delta}$ as a function of $\log P O_2$ in comparison with experimental data [33]. (a) Using *Parameter Set A*, (b) Using *Parameter Set B*.

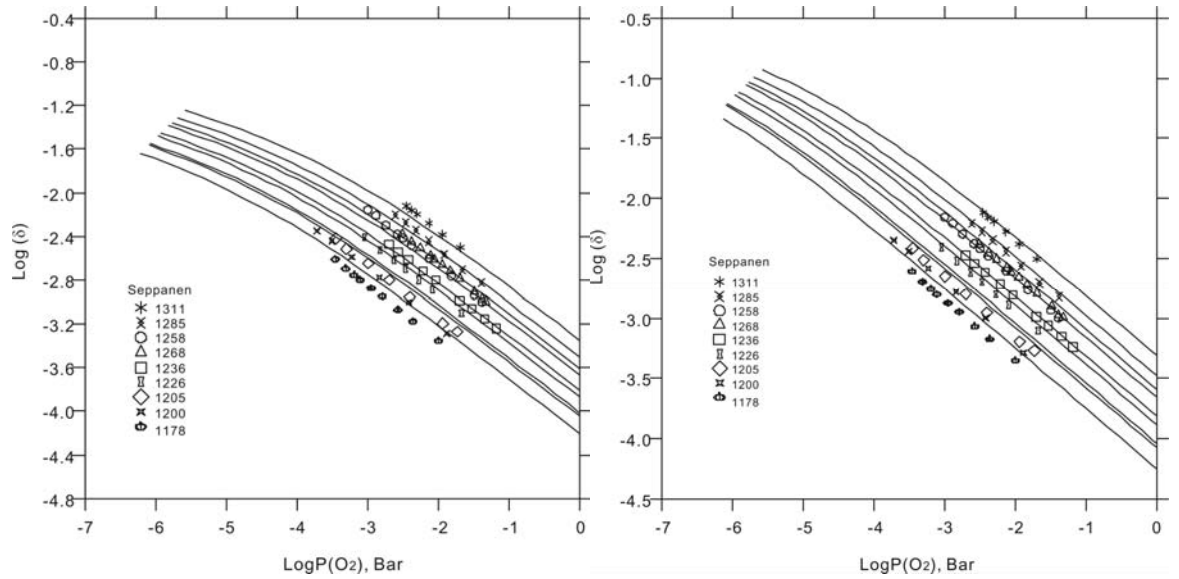

(a) (b)

Fig. 3.10. Calculated oxygen deficiency (δ) in $LaCoO_{3-\delta}$ as a function of $\log P O_2$ together with experimental data [32]. (a) Using *Parameter Set A*, (b) Using *Parameter Set B*.

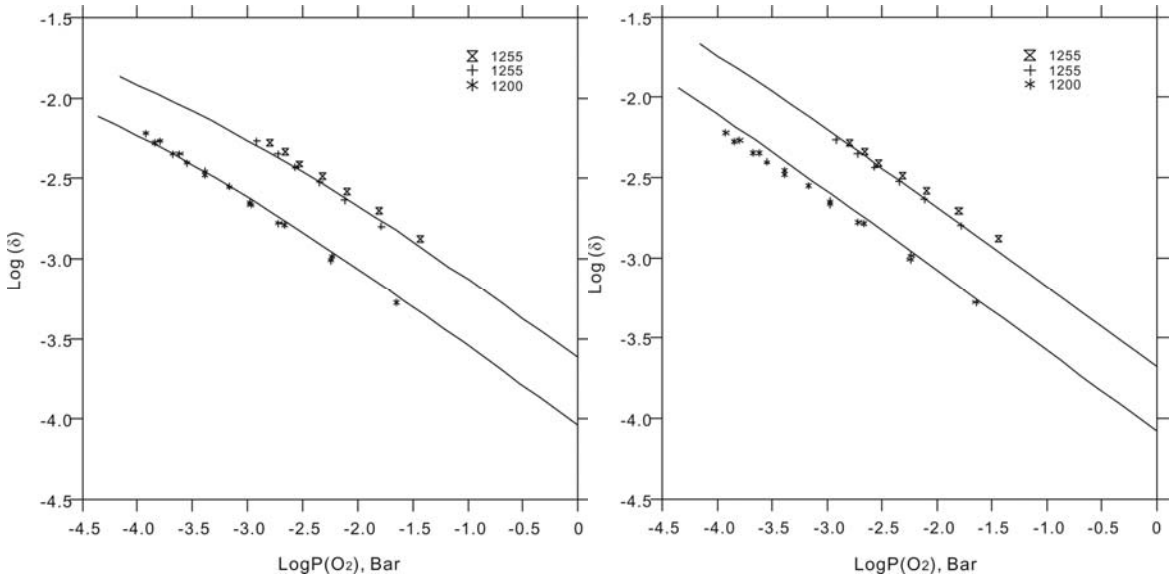

(a) (b)

Fig. 3.11. Calculated oxygen deficiency (δ) in $LaCoO_{3-\delta}$ equilibrated with CoO as a function of $\log P_{O_2}$ compared with experimental data [32]. (a) Using *Parameter Set A*, (b) Using *Parameter Set B*.

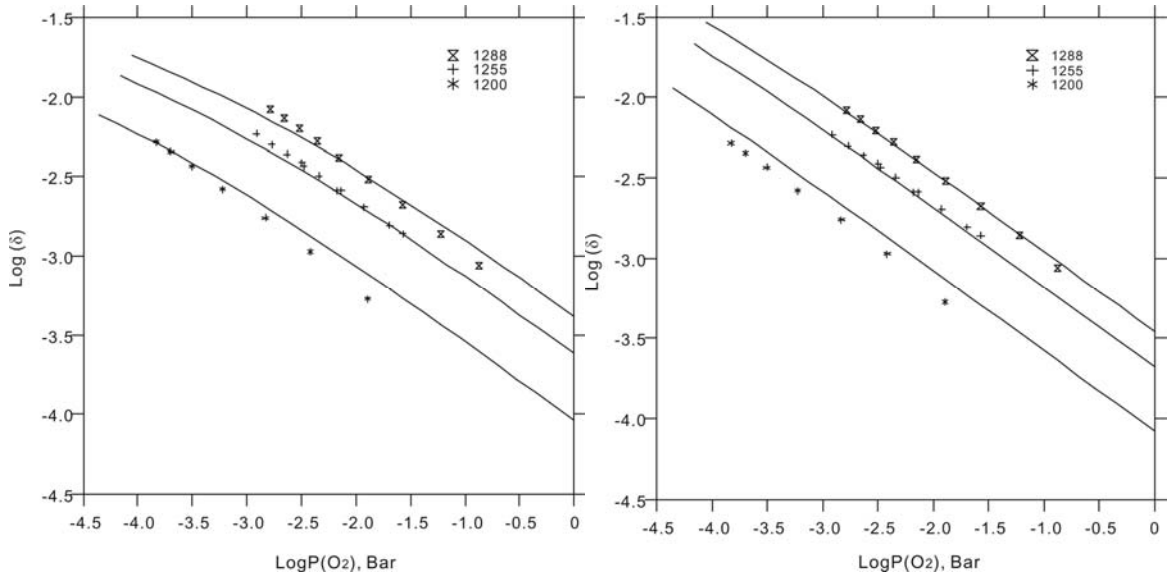

(a) (b)

Fig. 3.12. Calculated oxygen deficiency (δ) in $LaCoO_{3-\delta}$ equilibrated with La_2O_3 as a function of $\log P_{O_2}$ in comparison with experimental data [32]. (a) Using *Parameter Set A*, (b) Using *Parameter Set B*.

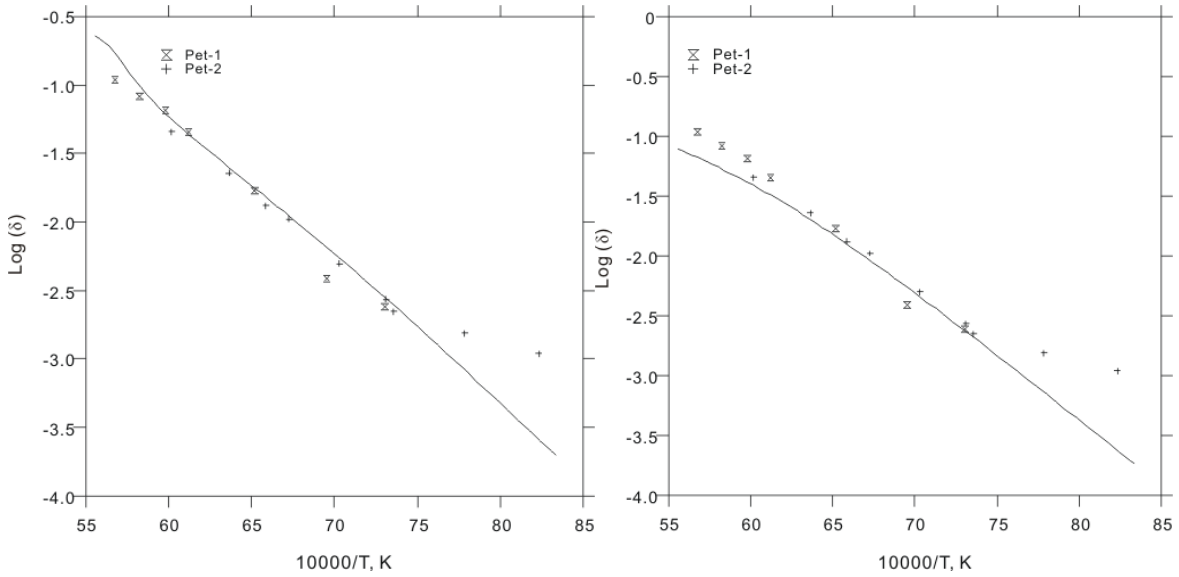

(a) (b)

Fig. 3.13. Calculated oxygen deficiency (δ) in $LaCoO_{3-\delta}$ in air as a function of temperature in comparison with experimental data [34]. (a) Using *Parameter Set A*, (b) Using *Parameter Set B*.

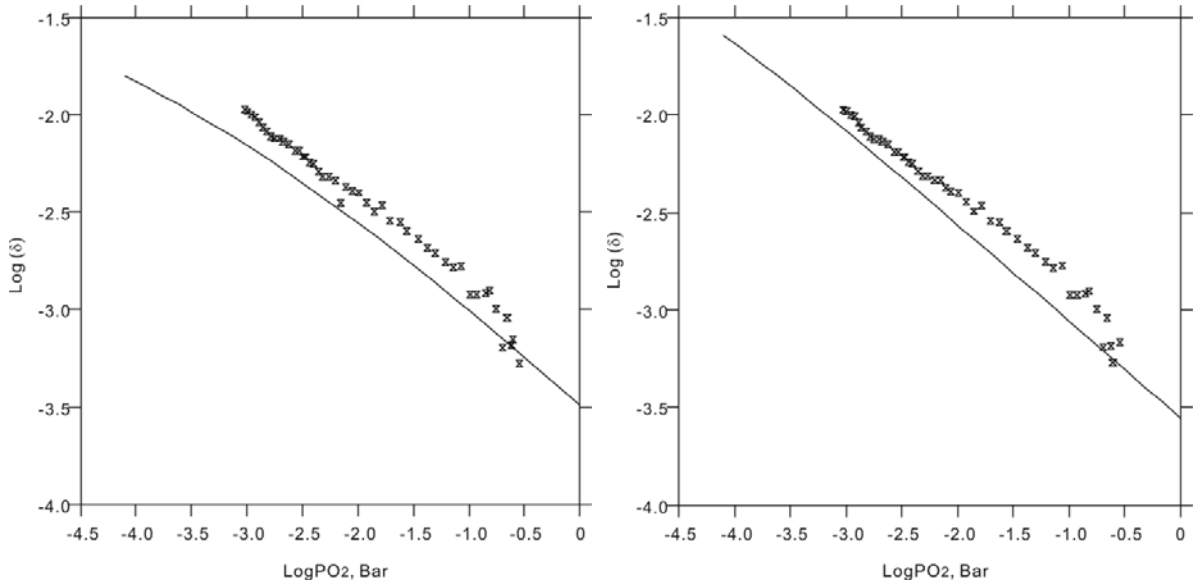

(a) (b)

Fig. 3.14. Calculated oxygen deficiency (δ) in $LaCoO_{3-\delta}$ at 1273 K in comparison with the experimental data from Zuev *et al*. [35]. (a) Using *Parameter Set A*, (b) Using *Parameter Set B*.

Figs. 3.9−3.14 present the calculated oxygen deficiency (δ) in $LaCoO_{3-\delta}$ as a function of PO_2 or temperature for single phase $LaCoO_{3-\delta}$ or equilibrated with CoO or La_2O_3. The experimental data can be reproduced equally well using any of the two sets of the parameters. It is therefore difficult to judge whether the high or the low charge disproportionation is the true picture for $LaCoO_{3-\delta}$, just based on the oxygen non-stoichiometry data. However, even though the high charge disproportionation is possible at temperatures from 1000−1300K as shown in Fig. 3.1, Co^{3+} unlikely disappears completely. In this sense, the results of Goodenough [36] and Abbate *et al*. [38] are more reliable. Thus, it was decided that *Parameter set A* with low charge disproportionation will be used for higher order systems. The charge distribution at different temperatures and PO_2 will give a sign to the magnetic properties, electronic conductivity and thermal-conductivity. Therefore, the knowledge of both the phase equilibria and the charge distribution as a function of the conditions during sample synthesis is decisive for optimization of the manufacturing process.

3.5 Conclusions

In the present work, the experimental data for the La-Co-O and La-Co-Fe-O systems were carefully reviewed. Thermodynamic modeling of the oxide phases was performed in order to reproduce experimentally determined thermodynamic and phase diagram data. Besides parameter refinements of the stoichiometric $La_4Co_3O_{10}$ phase, the chemical evolution of lanthanum cobaltite was a main issue. We found tight interrelation between oxygen non-stoichiometry and charge disproportionation between the different Co-valence states. Two distinctive sets of optimized model parameter sets can take into account both of the suggested cation schemes of the perovskite phase, i.e. negligible and high extent of the disproportionation reaction. *Parameter Set A* allows low charge disproportionation in the perovskite phase, while *Parameter Set B* allows high charge disproportionation. Both sets of parameters can reproduce most of the experimental data equally well. For higher order systems, it is recommended to use *Parameter Set A* with low charge disproportionation. The parameters for $La_4Co_3O_{10}$ phases were also optimized. The thermodynamic description of the La-Co-Fe-O system was obtained via an ideal extrapolation from the ternary subsystems. Our database can be used for calculating phase equilibria and thermodynamic properties at temperatures of 298−3000 K and oxygen partial

pressure of 10^{-20}–1 bar, and therefore enables material composition optimization for various applications, including SOFC and oxygen membrane.

References

[1] S.C. Parida, Z. Singh, S. Dash, R. Prasad, V. Venugopal. J. Alloys Compd. 285 (1999) 7–11.

[2] S. Tao, J.T.S. Irvine, J.A. Kilner, Adv. Mater. 17 (2005) 1734–1737.

[3] D.B. Meadowcroft, Energy Convers. 8 (1968) 185–190.

[4] L.B. Sis, G.P. Writz, S.C. Sornson, J. Appl. Phys. 44 (1973) 5553–5559.

[5] J.J.Janecek, G.P. Wirtz. J. Am. Ceram. Soc. 61 (1978) 242–244.

[6] T. Nakamura, G. Petzow, C.J. Gauckler, Mater. Res. Bull. 14 (1979) 649–659.

[7] M. Seppänen, M. Kyto, P. Taskinen. Scan. J. Met., 8 (1979) 199–204.

[8] A.N. Petrov, V.A. Cherepanov, A.Y. Zuyev, V.M. Zhukovsky, J. Sol. St. Chem. 77 (1988) 1–14.

[9] K. Kitayama, J. Solid State Chem. 73 (1987) 381–387.

[10] K. Kitayama, J. Solid State Chem. 131 (1997) 18–23.

[11] N.V. Proskurina, V.A. Cherepanov, O.S. Golynets, V.I. Voronin, Inorganic Materials, 40 (2004) 955–959.

[12] M. Yang, Y. Zhong, Z.K. Liu, Solid State Ionics 178 (2007) 1027–1032.

[13] J.E. Saal, Thermodynamic modeling of phase transformations and defects: From Cobalt to Doped Cobaltate Perovskites (PhD thesis), The Pennsylvania State University, (2010).

[14] A.N. Petrov . V.A. Cherepanov . A.Y. Zuev, J. Solid State Electrochem. 10 (2006) 517–537

[15] A.N. Grundy, B. Hallstedt, L.J. Gauckler, J. Phase Equilib. 22 (2001) 105–113.

[16] M. Chen, B. Hallstedt, L.J. Gauckler, J. Phase Equilib. 24 (2003) 212–227.

[17] B. Sundman, J. Phase equilib. 12 (1991) 127–140.

[18] E. Povoden-Karadeniz, A.N. Grundy, M. Chen, T. Ivas, L.J. Gauckler, J. Phase Equilib. Diff. 30 (2009) 351–366.

[19] J.J. Janecek, G.P. Wirtz. Am. Ceram. Soc. Bull. 54 (1975) 739.

[20] M. Seppänen, M.H. Tikkanen, Acta Chem. Scand. A 30 (1976) 389–390.

[21] O.H. Hansteen, H. Fjellvåg, J. Solid State Chem. 141 (1998) 212–220.

[22] U. Lehman, H. Müller-Buschbaum, Z. Anorg. Allg. Chem. 470 (1980) 59–63.

[23] J. Lewandowski, R.A. Beyerlein, J.M. Longo, R.A. McCauley, J. Am. Ceram. Soc. 69 (1986) 699–703.

[24] O.M. Sreedharan, R. Pankajavalli, J. Mater. Sci. Lett. 3 (1984) 388.

[25] Y. Kobayashi, T. Mitsunaga, G. Fujinawa, T. Arii, M. Suetake, K. Asai, J. Harada, J. Phys. Soc. Jpn. 69 (2000) 3468–3469.

[26] A. Wold, W. Croft, J. Phys. Chem. 63 (1959) 447–448.

[27] N.P. Vyshatko, V.V. Kharton, A.L. Shaula, F.M.B. Marques, Powder Diffr. 18 (2003) 159–161.

[28] O.M. Sreedharan, M.S. Chandrasekharaiah, Mater. Res. Bull. 7 (1972) 1135–1142.

[29] O.M. Sreedharan, M.S. Chandrasekharaiah, J. Mater. Sci. 21 (1986) 2581–2584.

[30] S. Stølen, F. Grønvold, H. Brinks, J. Chem. Thermodynamics 30 (1998) 365–377.

[31] J. Cheng, A. Navrotskya, X.-D Zhou, H.U. Anderson. J. Mater. Res. 20 (2005) 191–200.

[32] M. Seppänen, M. Kyto, P. Taskinen. Scan. J. Met. 9 (1980) 3–11.

[33] J. Mizusaki, Y. Mima, S. Yamauchi, K. Fueki, H. Tagawa, J. Sol. St. Chem. 80 (1989) 102–111.

[34] A.N. Petrov, V.A. Cherepanov, A.Y. Zuev, Zh. Fiz. Khim. 61 (1987) 630–637.

[35] A.Y. Zuev, A.N. Petrov, A.I. Vylkov, D.S. Tsvetkov, Russ. J. Phys. Chem. 81 (2007) 73–77.

[36] J. B. Goodenough, Czech. J. Phys. 13 (1967) 304–336.

[37] V.G. Bhide, D.S Rajoria, Y.S. Beddy, Phys. Rev. Lett. 28 (1972) 1133–1136.

[38] M. Abbate, J.C. Fuggle, A. Fujimori, L.H. Tjeng, C.T. Chen, R. Potze, G.A. Sawatzky, H. Eisaki, S. Uchida, Phys. Rev. B, 47 (1993) 16124–13130.

[39] H. Yokokawa, T. Kawada, M. Dokiya, J. Am.Ceram. Soc. 72 (1989) 2104–2110.

[40] A.N. Grundy, B. Hallstedt, L.J. Gauckler, Acta Mater. 50 (2002) 2209–2222.

[41] C.P. Wang, J. Wang, X.J. Liu, I. Ohnuma, R. Kainuma, K. Ishida, J. Alloys Compd. 453 (2008) 174–179.

[42] W.-W Zhang, M. Chen, CALPHAD, submitted.

[43] M. Hillert, J. Alloys Compd. 320 (2001) 161–176.

[44] A.T. Dinsdale, CALPHAD 15 (1991) 317–425.

[45] G. Inden, Z. Metallkd. 66 (1975) 577–582.

[46] M. Hillert, M. Jarl, CALPHAD 2 (1978) 227–238.

[47] M. Hillert, B. Jansson, B. Sundman, J. Ågren, Metall. Trans. 16A (1985) 261–266.

[48] B. Sundman, Calphad 15 (1991) 109–119.

[49] M. Kowalski, P. Spencer, CALPHAD 19 (1995) 229–243.

[50] M. Zinkevich, S. Geupel, F. Aldinger, A. Durygin, S.K. Saxena, M. Yang, Z.K. Liu, J. Phys. Chem. Solids 67 (2006) 1901–1907.

[51] S.G.T.E. Thermodynamic Properties of Inorganic Materials, volume 19 of Landolt-Börnstein New Series, Group IV. Springer, Verlag Berlin Heidelberg, (1999).

[52] A.N. Grundy, M. Chen, B. Hallstedt, L.J. Gauckler, J. Phase Equilib. Diff. 26 (2005) 131–151.

[53] E. Povoden-Karadeniz, M. Chen, A.N. Grundy, T. Ivas, L.J. Gauckler, J. Phase Equilib. Diff. 30 (2009) 12–27.

[54] E. Povoden-Karadeniz, M. Chen, T. Ivas, A.N. Grundy, L.J. Gauckler, J. Mater. Res. 27 (2012) 1915–1926.

[55] B. Sundman, B. Jansson, J.O. Andersson, CALPHAD 9 (1985) 153–190.

Chapter 4

Thermodynamic modeling of the Sr-Co-Fe-O system

Abstract

This paper reviews and reassesses phase equilibria and thermodynamic properties in the Sr-Co-Fe-O system, focusing on oxide phases, especially the $SrCo_{1-x}Fe_xO_{3-\delta}$ perovskite. The liquid phase was modeled with a two-sublattice ionic liquid model. The $SrCo_{1-x}Fe_xO_{3-\delta}$ perovskite was modeled with a three-sublattice model. The three sublattices correspond to the A, B and oxygen sites in an ABO_3 perovskite, respectively. A number of other important ternary oxide phases in Sr-Co-O and Sr-Co-Fe-O were also included. The thermodynamic and phase diagram data available were carefully assessed. A thermodynamic description of Sr-Co-O was derived using the CALPHAD approach and was further extrapolated to Sr-Co-Fe-O. The new database allows for calculating phase diagrams, thermodynamic properties, cation distribution and defect chemistry properties, and therefore enables material composition optimization for various applications, including solid oxide fuel cells (SOFCs) and oxygen membranes.

4.1 Introduction

Strontium cobaltites offer good electronic and ionic conductivities that enable their application in solid oxide fuel cells (SOFCs) and oxygen-permeating membranes [1]. $Sr_3Fe_{2-x}Co_xO_{7-\delta}$ and $SrCo_{1-x}Fe_xO_{3-\delta}$ in Sr-Co-Fe-O have also received special attention due to their magnetic properties, notably the magnetoresistance (MR) effect [2, 3]. Both the magnetic and the electrical properties of these oxides depend strongly on composition and preparation methods [4]. Though extensive studies have been carried out on the effect of composition and sample preparation on the structure and physical properties of the oxides in Sr-Co-Fe-O, the phase relationship and thermodynamic properties have not been well established.

In this research, thermodynamic databases of Sr-Co-O and Sr-Co-Fe-O were developed. This is also a part of our project to develop a thermodynamic database of La-Sr-Co-Fe-O for SOFC applications [5−7]. The literature data available on Sr-Co-O and Sr-Co-Fe-O were carefully reviewed. A thermodynamic description of Sr-Co-O was derived using the CALPHAD approach and was combined with a description of Sr-Fe-O developed by Povoden *et al.* [8] and further extrapolated to Sr-Co-Fe-O. Various phase diagrams and thermodynamic properties were calculated and then compared with experimental data reported in the literature. The potential applications of our database were also examined.

4.2 Literature review

4.2.1. Solid oxide phases

Since the focus of this research was on oxide phases, experimental information on the gas phase and the metallic phases is not discussed here. The Sr-Co-Fe-O system contains the following binary oxides: SrO, SrO_2, CoO, Co_3O_4, FeO, Fe_2O_3 and Fe_3O_4. Detailed information on the binary oxides can be found in previous modeling work [9−11]. There are five ternary oxides in Sr-Fe-O: $SrFeO_{3-\delta}$, $Sr_2FeO_{4-\delta}$, $Sr_4Fe_3O_{10-\delta}$, $Sr_3Fe_2O_{7-\delta}$, $Sr_4Fe_6O_{13-\delta}$ [8]. Two ternary oxides have been reported in Co-Fe-O: halite ($Co_xFe_{1-x}O$) and spinel ($Co_xFe_{3-x}O_4$) [12]. The reported ternary and quaternary solid oxide phases for Sr-Co-O and Sr-Co-Fe-O were reviewed in this research. Below is a short summary of results from the relevant literature.

I. $Sr_2Co_2O_5$

$Sr_2Co_2O_5$ has a brownmillerite-type structure, which is a close relative of the perovskite structure. Grenier *et al.* investigated the crystal structure of $Sr_2Co_2O_5$ at high temperatures [13] and found that, on cooling, it undergoes an exothermic reaction and transforms into a hexagonal phase. Takeda *et al.* reported [14] that $Sr_2Co_2O_5$ is stable in a narrow temperature range. It transforms into the $SrCoO_{3-\delta}$ perovskite phase with increasing temperature at about 1373K in N_2. They also found ordered oxygen vacancies in $Sr_2Co_2O_{5-\delta}$ (δ=0.04−0.16). No Fe solubility in $Sr_2Co_2O_5$ was reported. Saal reports on thermodynamic properties of $Sr_2Co_2O_5$ obtained via first-principle calculations [15].

II. $Sr_6Co_5O_{15}$

$Sr_6Co_5O_{15}$ has previously been described as a low-temperature rhombohedral/hexagonal form of $Sr_2Co_2O_5$ [13, 16, 17]. Takeda *et al.* [14] propose that this hexagonal phase is cobalt-deficient 2H-$SrCo_{1-x}O_y$, (x≈0.1). Harrison *et al.* [18] were the first to confirm the existence of $Sr_6Co_5O_{15}$ with a stoichiometric composition. $Sr_6Co_5O_{15}$ is related to the 2H-hexagonal-perovskite-type phase. When high temperature brownmillerite $Sr_2Co_2O_5$ cools in air, it decomposes into a two-phase mixture of $Sr_6Co_5O_{15}$ and CoO_x [18]. No Fe solubility in $Sr_6Co_5O_{15}$ is reported in the literature. Its crystallographic, magnetic, and electronic properties have been extensively studied by Sun *et al.* and Iwasaki *et al.* [19, 20]. No experimental study was carried out on the thermodynamic properties of $Sr_6Co_5O_{15}$. Saal *et al.* [21] report on its heat capacity and entropy up to 1300K from first-principle calculations using the Debye-Grüneisen model. They further derived the Gibbs energy function for $Sr_6Co_5O_{15}$.

A few other strontium cobaltites with a hexagonal perovskite-like structure have been reported, with a Co content of 42.8−44.5 cat.%, including $Sr_{24}Co_{19}O_{57}$, $Sr_{14}Co_{11}O_{33}$, $Sr_4Co_3O_9$ and $Sr_5Co_4O_{12}$ [22−25]. The existence of $Sr_{24}Co_{19}O_{57}$ and $Sr_{14}Co_{11}O_{33}$ has been denied by Aksenova *et al.* and Li *et al.* [23, 24]. The reported $Sr_4Co_3O_9$ and $Sr_5Co_4O_{12}$ have similar XRD patterns and stability ranges to those of $Sr_6Co_5O_{15}$ [25]. The existence of $Sr_4Co_3O_9$ and $Sr_5Co_4O_{12}$ has also been doubted.

III. $Sr_3Co_2O_{7-\delta}$

$Sr_3Co_2O_{7-\delta}$ is an oxygen-deficient Ruddlesden-Popper type phase. Its crystal structure was characterized by Dann and Weller [26] using X-ray and neutron diffraction and was reported as orthorhombic-type. They indicated that this phase can be obtained at high temperatures

(1000−1200°C) and ambient pressure. At low temperatures and/or high P_{O_2}, $Sr_3Co_2O_{7-\delta}$ decomposes into a mixture of $Sr_6Co_5O_{15}$, $SrCoO_{3-\delta}$ and SrO. The oxygen deficiency (δ in $Sr_3Co_2O_{7-\delta}$) was reported to be around 1 ± 0.2, corresponding to an average Co oxidation state of around +3 ± 0.2. The crystal structure and magnetic property of this phase have been reported in various studies [27−29]. It is possible to synthesize other Ruddlesden-Popper type phases ($Sr_{n+1}Co_nO_{3n+1}$, $n\leq4$) under 6GPa at 1000−1500°C [30]. However, they are not stable under ambient conditions.

IV. $SrCo_{1-x}Fe_xO_{3-\delta}$

$SrCoO_{3-\delta}$ is a fully disordered oxygen-deficient cubic perovskite phase with Pm3m symmetry. The stoichiometric $SrCoO_3$ can be synthesized only under high oxygen partial pressure [14, 31]. $SrCoO_{3-\delta}$ has been extensively studied due to its interesting magnetic [31, 32] and electric properties [32] and its oxygen mobility [33]. Taguchi *et al.* [31] investigated the effect of oxygen deficiency on the magnetic properties of $SrCoO_{3-\delta}$ ($0<\delta<0.5$). They found a strong dependence of the Curie temperature on the oxygen deficiency. They determined the Co^{4+} content at low temperatures (<350°C) and high oxygen pressures (50−2600 bars) assuming the presentce of Co^{4+} and Co^{3+} only. Nakatsuka *et al.* [33] prepared a single crystal $SrCoO_{3-\delta}$ at high temperature in an O_2 gas flow and reported the average Co valency as +3.28 using XRD. Co^{3+} and Co^{4+} ions co-exist in the oxygen-deficient $SrCoO_{3-x}$ cubic perovskite. Takeda *et al.* [14] investigated the stability of $SrCoO_{3-\delta}$ at a few chosen temperatures and atmospheres. Rodriguez *et al.* [34] reported the transformation temperature from $SrCoO_{3-\delta}$ to $Sr_2Co_2O_5$ as 840°C at $P_{O_2}\approx10^{-4}$ atm. Vashook *et al.* [35] determined the stability range of $SrCoO_{3-\delta}$ at various temperatures using DTA and XRD. They [36, 37] further investigated the oxygen non-stoichiometry and electrical conductivity of $SrCoO_{3-\delta}$ in a temperature range of 950−1050°C and an oxygen partial pressure range of 1−1000Pa by solid electrolyte coulometry and resistivity measurements. They reported a large decrease in resistivity accompanying with the transition from $Sr_6Co_5O_{15}$ to $SrCoO_{3-\delta}$. Federico *et al.* [38] reported the Gibbs energy of formation for $SrCoO_3$ as −163kJ/mol at 298K obtained from first-principle calculations.

$SrFeO_{3-\delta}$ has a tetragonal perovskite type structure. By substituting Fe with Co, the crystal structure changes from tetragonal to cubic [23, 39]. Aksenova *et al.* [23] determined the stability range of $SrCo_{1-x}Fe_xO_{3-\delta}$ by XRD and reported that the perovskite phase is stable within the range of $0\leq x\leq0.7$ at 1100°C in air. The oxygen non-stoichiometry and phase stability of $SrCo_{1-x}Fe_xO_{3-\delta}$

have been studied by a number of groups [40−44], focusing on the composition $SrCo_{0.8}Fe_{0.2}O_{3-\delta}$. Depending on temperature and oxygen partial pressure, $SrCo_{0.8}Fe_{0.2}O_{3-\delta}$ is either a single phase perovskite or a two-phase mixture of perovskite and brownmillerite. Liu *et al.* [41] studied the temperature range of 823−1263 K and P_{O_2} = 0.015−1 atm using TG and XRD, while Grunbaum *et al.* [42] chose a temperature interval of 823−1223 K and P_{O_2} =10^{-5}−1 atm using TG and HT-XRD. Moreover, McIntosh *et al.* [43] investigated the stability of $SrCo_{0.8}Fe_{0.2}O_{3-\delta}$ at T=873−1173 K and P_{O_2} = 5×10^{-4}−1 atm using *in situ* neutron diffraction. All these studies concluded that the cubic $SrCo_{0.8}Fe_{0.2}O_{3-\delta}$ perovskite is stable at T>1073 K in 10^{-5}−1 atm and that its stability range extends to lower temperatures with increasing oxygen partial pressure. However, the stability range determined for $SrCo_{0.8}Fe_{0.2}O_{3-\delta}$ from these studies is unreliable, because the samples used were unlikely equilibrated due to a short annealing time. Moreover, they were unable to distinguish the hexagonal $Sr_6Co_5O_{15}$ phase from the $SrCo_{1-x}Fe_xO_{3-\delta}$ and $Sr_2Co_2O_5$ phases. McIntosh *et al.* [43, 44] measured the oxygen non-stoichiometry of $SrCo_{1-x}Fe_xO_{3-\delta}$ using TG-DTA, but different results were reported from the same group which reduces the reliability of their studies.

With respect to compositions other than $SrCo_{0.8}Fe_{0.2}O_{3-\delta}$, Mitchell *et al.* [45] investigated the stability of $SrCo_{0.2}Fe_{0.8}O_{3-\delta}$ at 900°C and P_{O_2} = $10^{-0.68}$ to $10^{-13.3}$ atm, and found that it is stable for the entire P_{O_2} range. Vashuk *et al.* [46] studied the oxygen non-stoichiometry and defect chemistry of $SrCo_{0.25}Fe_{0.75}O_{3-\delta}$ using solid-electrolyte coulometry, TG, and conductivity measurements at temperatures from 300−1000°C and oxygen partial pressures from 10 to 10^5 Pa. $SrCo_{0.25}Fe_{0.75}O_{3-\delta}$ was shown to be p-type throughout the entire oxygen partial pressure and temperature range. Phase transformation at low temperatures was reported.

V. Solid solution $Sr_3Fe_{2-x}Co_xO_{7-\delta}$

The electronic, magnetic and magneto-resistance properties of $Sr_3Fe_{2-x}Co_xO_{7-\delta}$ were studied by Veith *et al.* [2]. They report that single-phase $Sr_3Fe_{2-x}Co_xO_{7-\delta}$ exists in a composition range of $0.25\leq x\leq1.75$ at 1000°C under flowing O_2. Aksenova *et al.* [23] report a single phase region of $Sr_3Fe_{2-x}Co_xO_{7-\delta}$ at 1100°C in air ($0\leq x\leq0.4$). With x>0.4, they detected formation of $Sr_3Co_2O_{7-\delta}$.

VI. Solid solution $Sr_4Fe_{6-x}Co_xO_{13-\delta}$

The $Sr_4Fe_{6-x}Co_xO_{13-\delta}$ solid solution has an orthorhombic structure (space group Iba2) [47, 48]. The phase stability of $Sr_4Fe_{6-x}Co_xO_{13-\delta}$ and its electrical conductivity and oxygen permeability

have been investigated by a number of groups. A certain amount of Co can be dissolved in $Sr_4Fe_{6-x}Co_xO_{13-\delta}$ without forming a secondary phase. Beyond the solubility limit, the $Sr_4Fe_{6-x}Co_xO_{13-\delta}$ single phase is replaced by a three-phase mixture of $Sr_4Fe_{6-x}Co_xO_{13-\delta}$, $SrCo_{1-x}Fe_xO_{3-\delta}$ and $Co_xFe_{1-x}O$ or $Co_xFe_{3-x}O_4$ [48−50]. The Co content (x in $Sr_4Fe_{6-x}Co_xO_{13-\delta}$) affects not only its phase stability but also its oxygen permeability and electrical conductivity. Both oxygen permeability and electrical conductivity increase with increasing x in either the single phase region or the three-phase region [49−51]. Various solubility limits of Co in $Sr_4Fe_{6-x}Co_xO_{13-\delta}$ have been reported. Xia *et al.* [48] report a maximum Co solubility corresponding to x=1.8 at 1000°C. The solubility decreases with increasing temperature in the range 1000–1100°C. Armstrong *et al.* [51] report a Co solubility limit of x=1.5 in $Sr_4Fe_{6-x}Co_xO_{13-\delta}$ at 1000°C. Deng *et al.* [50] determined x=1.5 in samples slowly cooled from1200°C. They also report an average valence state of Co and Fe as around 2.9~3.0. Moreover, values of x=1.4, ≈1.6, 1.6 were reported by Kim *et al.* [52] in samples sintered at 1150°C, by Ma *et al.* [49] in samples sintered at 1200°C, and by Aksenova *et al.* [23] in samples sintered at 1100°C, respectively. Fossdal *et al.* [53] systemically measured the Co solubility in $Sr_4Fe_{6-x}Co_xO_{13-\delta}$ at several temperatures. They concluded that $Sr_4Fe_{6-x}Co_xO_{13-\delta}$ is stable only in a narrow temperature range from 775 to 1220°C. The highest Co solubility was obtained in samples sintered at 900°C, and the maximum Co-content was close to $Sr_4Fe_4Co_2O_{13}$. At higher or lower sintering temperatures, Co solubility decreases. This inconsistency in the Co solubility limits reported is probably due to the slow reaction kinetics for the transition between the single phase $Sr_4Fe_{6-x}Co_xO_{13-\delta}$ and the three-phase mixture of $Sr_4Fe_{6-x}Co_xO_{13-\delta}$, $SrFe_{1-x}Co_xO_{3-\delta}$ and $Co_xFe_{1-x}O$ or $Co_xFe_{3-x}O_4$ during heating or cooling [53].

VII. Other ternary oxides

For the other ternary oxides, no solubility of a third cation has been reported, e.g. no solubility of Sr in $Co_xFe_{1-x}O_{1+\delta}$ or in $Co_xFe_{3-x}O_4$ and no Co solubility in $SrFe_{12}O_{19-\delta}$.

4.2.2 Phase diagram data

I. Sr-Co-O

Previous studies of phase equilibria in Sr-Co-O have focused on compositions related to the perovskite phase. The stability of other oxide phases, such as the Ruddlesden-Popper phase ($Sr_3Co_2O_{7-\delta}$), has not been fully studied. Takeda *et al.* [14] investigated phase relations in Sr-Co-O. They studied phase composition as a function of temperature in various atmospheres using

XRD and TG-DTA. They report the existence of cubic perovskite, brownmillerite and unknown low temperature phases, as well as their stability ranges. Rodriguez *et al.* [34] studied phase transition in $Sr_2Co_2O_5$ using neutron powder diffraction in an atmosphere of $PO_2 \approx 10^{-4}$ atm with continuously changing temperature. They were unable to identify the low temperature phases [18]. Vashook *et al.* [35, 37] explored phase transformation temperatures for strontium cobaltite ($SrCoO_x$) in a PO_2 range of 50−400Pa using XRD and TG. The stability regions for cubic perovskite, brownmillerite and low temperature phases ($Sr_6Co_5O_{15}$) at low PO_2 were mapped out. They describe the transformation from cubic perovskite to brownmillerite as second-order and the one from brownmillerite to $Sr_6Co_5O_{15}$ and Co_3O_4 as first-order.

II. Sr-Co-Fe-O

There is very little phase diagram data for the Sr-Co-Fe-O system. Aksenova *et al.* [23] studied the phase equilibria in the Sr-Co-Fe-O system at 1100°C in air using 68 samples with various compositions. They determined the stability region and crystal structure of solid solutions in the Sr-Co-Fe-O system using XRD and they constructed an 1100°C isothermal section of the pseudo-ternary system SrO-CoO-Fe_2O_3 in air. Fossdal *et al.* [53] studied the phase relations of the $Sr_4Fe_{6-x}Co_xO_{13-\delta}$ phase in the range of 775−1220°C using XRD and DTA and have provided a Fe rich part of the isothermal section of SrO-CoO-Fe_2O_3 at 900°C in air.

4.3 Thermodynamic modeling

This research was carried out to reassess the Sr-Co-O system and provide a new thermodynamic description. The thermodynamic description of the Sr-Co-O system given by Saal [15] includes only the perovskite phase and other phases in equilibrium with it, and the entropy of the perovskite phase in this description becomes unreasonably high at high temperatures. The new thermodynamic description of Sr-Co-O presented here is based on thermodynamic descriptions of the sub-systems Sr-O (by Risold *et al.* [9]) and Co-O (by Chen *et al.* [10]). A thermodynamic description of Sr-Co-Fe-O was subsequently derived from those for Sr-Fe-O by Povoden-Karadeniz [8], Co-Fe-O by Zhang and Chen [12], and Sr-Co-O in this research. Compound Energy Formalism (CEF) [54], which is widely used in CALPHAD assessments, was employed for modeling the Gibbs energy for all the phases in Sr-Co-Fe-O. The lattice stability for pure elements was adopted from Dinsdale [55]. The magnetic contribution to the Gibbs energy

was modeled using the "Hillert-Jarl-Inden" model (proposed by Inden [56] and subsequently modified by Hillert and Jarl [57]).

4.3.1 Liquid

The description for the liquid phase was ideally extrapolated from those of the subsystems (Sr-O [9], Co-O [10] and Fe-O [11]), in which the liquid phase was all modeled using the ionic two–sublattice model [58, 59]. This model was developed within the framework of the CEF, with one sublattice containing charged cations and the other containing charged anions and vacancies. The liquid phase in Sr-Co-Fe-O is described as:

$(Co^{2+}, Co^{3+}, Fe^{2+}, Fe^{3+}, Sr^{2+})_p(O^{2-},Va^{q-})_q$

where $p=2y_{O^{2-}}+qy_{Va}$ (4.1)

$$q=2y_{Co^{2+}}+3y_{Co^{3+}}+2y_{Fe^{2+}}+3y_{Fe^{3+}}+2y_{Sr^{2+}} \quad (4.2)$$

The Gibbs energy of the liquid phase is expressed as:

$$G_m^L = q\sum_i y_i y_{Va}\,{}^oG_{i:Va}^L + \sum_i y_i y_{O^{2-}}\,{}^oG_{i:O^{2-}}^L + pRT\sum_i y_i \ln y_i + qRT\sum_j y_j \ln y_j + {}^EG_m^L \quad (4.3)$$

where i represents the constituents in the first sublattice, and j represents the constituents in the second sublattice. The excess Gibbs energy ${}^EG_m^L$ is formulated as:

$${}^EG_m^L = \sum_{i_m}\sum_{i_n\neq i_m} y_{i_m}y_{i_n}(y_{O^{2-}}L_{i_m,i_n:O^{2-}}^L + qy_{Va}{}^2L_{i_m,i_n:Va}^L) + \sum_{i_m} y_{i_m}y_{O^{2-}}y_{Va}L_{i_m:O^{2-},Va}^L \quad (4.4)$$

where i_m and i_n represent the constituents in the first sublattice. In the above expressions, colons were used to separate species on different sublattices and commas to separate species on the same sublattice. No ternary or quaternary parameters were optimized for the liquid phase due to lack of experimental data, so the calculated liquidus must be treated with caution.

4.3.2 $Sr_2Co_2O_5$ and $Sr_6Co_5O_{15}$

This research treated $Sr_2Co_2O_5$ and $Sr_6Co_5O_{15}$ as stoichiometric compounds. Their Gibbs energy functions were derived from the first-principle calculation results of Saal *et al.* [15, 21], with the enthalpy and entropy terms further optimized using phase diagram data.

4.3.3 $Sr_3Co_2O_7$

$Sr_3Co_2O_7$ was modeled with a 5-sublattice model reflecting its actual crystal structure. The model reads as follows:

$(Sr^{2+})_1(Sr^{2+})_2(Co^{3+})_2(O^{2-}, Va)_6(O^{2-})_1$

The Gibbs energy for the end member $(Sr^{2+})_1(Sr^{2+})_2(Co^{3+})_2(O^{2-})_6(O^{2-})_1$ is formulated as

$$ {}^{o}G^{Sr_3Co_2O_7}_{Sr^{2+}:Sr^{2+}:Co^{3+}:O^{2-}:O^{2-}} = 3\,{}^{o}G^{SrO} + 2\,{}^{o}G^{CoO} + {}^{o}G^{O_2} + A_0 + B_0 * T \tag{4.5} $$

and for the other one $(Sr^{2+})_1(Sr^{2+})_2(Co^{3+})_2(Va)_6(O^{2-})_1$ as

$$ {}^{o}G^{Sr_3Co_2O_7}_{Sr^{2+}:Sr^{2+}:Co^{3+}:Va:O^{2-}} = 3\,{}^{o}G^{SrO} + 2\,{}^{o}G^{CoO} - 2\,{}^{o}G^{O_2} \tag{4.6} $$

where ${}^{o}G^{SrO}$, ${}^{o}G^{CoO}$ and ${}^{o}G^{O_2}$ were taken from Risold *et al.* [9], Chen *et al.* [10] and Dinsdale [55], respectively, and A_0, B_0 values were optimized using phase diagram data.

4.3.4 Perovskite $SrCo_{1-x}Fe_xO_{3-\delta}$

A three-sublattice model was used for the perovskite phase, with the first sublattice (A site) for Sr cation (Sr^{2+}) and vacancy, the second (B site) for Co cation (Co^{3+}, Co^{2+} and Co^{4+}) and vacancy, and the third (O site) for oxide ion and oxygen vacancy. Just as in the Sr-Fe-O system [8], cation and oxygen vacancies (Va) were introduced to the A/B and O site, respectively, in order to model oxygen non-stoichiometry and to maintain charge neutrality. The model reads as follows:

$(Sr^{2+},Va)_1(Co^{2+},Co^{3+}, Co^{4+}, Fe^{2+},Fe^{3+}, Fe^{4+},Va)_1 (O^{2-}, Va)_3$

The Gibbs energy of the perovskite phase (the non-magnetic part) is given by the following expression:

$$ G_m^{perovskite} = \sum_i \sum_j \sum_k y_i\, y_j y_k\, {}^{o}G^{perovskite}_{i:j:k} + RT\sum_i y_i \ln y_i + RT\sum_j y_j \ln y_j + 3RT\sum_k y_k \ln y_k + {}^{E}G_m^{perovskite} \tag{4.7} $$

where i, j, k represent the constituents in the first, second and third sublattices, respectively.

According to the current model, 28 end-members (${}^{o}G^{perovskite}_{i:j:k}$ terms) need to be assigned a Gibbs energy value. In order to be consistent with the perovskite model used in Sr-Fe-O [8] and La-Co-O (*Chapter 3*), the same Gibbs energy terms must be applied to all the common end-members. The thermodynamic descriptions of 16 common end-members were taken from Sr-Fe-O [8] while the

other six were taken from La-Co-O (*Chapter 3*). The remaining six end-members belong to the Sr-Co-O system and were determined during this research. The strategy to obtain the Gibbs energy terms for these six end-members was to choose appropriate neutral end-members or their combinations as model parameters, which could be optimized using experimental data. As in the previous modeling of the perovskite phase [8, 61−63], a number of the most important end-members or their combinations were chosen as model parameters and these are listed below:

Stoichiometric $SrCoO_3$ $(Sr^{2+})_1(Co^{4+})_1(O^{2-})_3$. Its Gibbs energy function is given by:

$$ {}^{o}G^{perovskite}_{Sr^{2+}:Co^{4+}:O^{2-}} = {}^{o}G^{SrO} + {}^{o}G^{CoO} + 0.5\,{}^{o}G^{O_2} + A_1 + B_1 * T \tag{4.8} $$

where A_1, B_1 are parameters optimized to reproduce thermodynamic and phase diagram data.

Reduced $SrCoO_{3-\delta}$ $(Sr^{2+})_1(Co^{3+})_1(O^{2-}{}_{5/6}, Va_{1/6})_3$. Its Gibbs energy function is given by:

$$ G_m = \frac{5}{6}\,{}^{o}G^{perovskite}_{Sr^{2+}:Co^{3+}:O^{-2}} + \frac{1}{6}\,{}^{o}G^{perovskite}_{Sr^{2+}:Co^{3+}:Va} + 3RT\left(\frac{5}{6}\ln\frac{5}{6} + \frac{1}{6}\ln\frac{1}{6}\right) = {}^{o}G^{SrO} + {}^{o}G^{CoO} + 0.25\,{}^{o}G^{O_2} + A_2 + B_2 * T \tag{4.9} $$

and further reduced $SrCoO_{3-\delta}$ $(Sr^{2+})_1(Co^{2+})_1(O^{2-}{}_{2/3}, Va_{1/3})_3$

$$ G_m = \frac{2}{3}\,{}^{o}G^{perovskite}_{Sr^{2+}:Co^{2+}:O^{2-}} + \frac{1}{3}\,{}^{o}G^{perovskite}_{Sr^{2+}:Co^{2+}:Va} + RT\left(\frac{2}{3}\ln\frac{2}{3} + \frac{1}{3}\ln\frac{1}{3}\right) = {}^{o}G^{SrO} + {}^{o}G^{CoO} + A_3 + B_3 * T \tag{4.10} $$

where A_2, B_2, A_3 and B_3 are parameters to be optimized.

All the other end-members were correlated by the following reciprocal relations:

$$ {}^{o}G^{perovskite}_{Sr^{2+}:Co^{4+}:O^{2-}} + {}^{o}G^{perovskite}_{Va:Co^{3+}:Va} - {}^{o}G^{perovskite}_{Sr^{2+}:Co^{4+}:Va} - {}^{o}G^{perovskite}_{Va:Co^{3+}:O^{2-}} = \Delta G_1 \tag{4.11} $$

$$ {}^{o}G^{perovskite}_{Sr^{2+}:Co^{4+}:O^{2-}} + {}^{o}G^{perovskite}_{Sr^{2+}:Co^{3+}:Va} - {}^{o}G^{perovskite}_{Sr^{2+}:Co^{4+}:Va} - {}^{o}G^{perovskite}_{Sr^{2+}:Co^{3+}:O^{2-}} = \Delta G_2 \tag{4.12} $$

$$ {}^{o}G^{perovskite}_{Sr^{2+}:Co^{4+}:O^{2-}} + {}^{o}G^{perovskite}_{Sr^{2+}:Co^{2+}:Va} - {}^{o}G^{perovskite}_{Sr^{2+}:Co^{4+}:Va} - {}^{o}G^{perovskite}_{Sr^{2+}:Co^{2+}:O^{2-}} = \Delta G_3 \tag{4.13} $$

In this research, the reciprocal energy $\Delta G_x = 0$ (x=1, 2, 3) was chosen [64]. The Gibbs energy functions for the 6 end-members can be derived by solving Equations 8 to 13.

The excess Gibbs energy ${}^{E}G_{m}^{perovskite}$ is formulated as:

$${}^{E}G_{m}^{perovskite} = \sum_{i_l}\sum_{i_k \neq i_l}\sum_{j_m} y_{i_k} y_{i_l} y_{j_m} L_{i_k,i_l:j_m:O^{2-}}^{perovskite} + \sum_{i_l}\sum_{j_m}\sum_{j_n \neq j_m} y_{i_l} y_{j_m} y_{j_n} L_{i_l:j_m,j_n:O^{2-}}^{perovskite} \qquad (4.14)$$

where i_k, i_l represent the constituents in the first sublattice (A site), and j_m, j_n represent the constituents in the second sublattice (B site).

4.3.5 $Sr_3Fe_{2-x}Co_xO_{7-\delta}$ and $Sr_4Fe_{6-x}Co_xO_{13-\delta}$

To model the Co solubility in these two phases, Co cation was introduced to the Fe site. As the average Co valence state reported is around +3, only Co^{3+} was included to keep the model simple. The Gibbs energy functions for $Sr_3Fe_{2-x}Co_xO_{7-\delta}$ and $Sr_4Fe_{6-x}Co_xO_{13-\delta}$ can be found in Table 1.

4.3.6 Other ternary oxides phases

Two more ternary oxides in Sr-Co-O were included in the present work: $Sr_4Co_3O_9$ and $Sr_5Co_4O_{12}$ were modeled as stoichiometric compounds. In Sr-Fe-O, the description for $Sr_4Fe_3O_{10}$ and $SrFe_{12}O_{19}$ was taken from Sr-Fe-O [11] without modification, because no Co solubility in these two compounds has been reported in the literature.

Table 4.1 Parameters obtained for the ternary oxide phases in the Sr-Co-O system and the quaternary solid solution phases in the Sr-Co-Fe-O system [a]

Phase	Parameters
Perovskite	$(Sr^{2+}, Va)_1(Co^{2+},Co^{3+},Co^{4+}, Fe^{2+},Fe^{3+},Fe^{4+}, Va)_1(O^{2-}, Va)_3$
	${}^{o}G_{Sr^{2+}:Co^{2+}:O^{2-}}^{perovskite} - H_{Sr}^{SER} - H_{Co}^{SER} - 3H_{O}^{SER} = +GS2OV + GHSEROO + 15.8759T$
	${}^{o}G_{Sr^{2+}:Co^{3+}:O^{2-}}^{perovskite} - H_{Sr}^{SER} - H_{Co}^{SER} - 3H_{O}^{SER} = +0.5GHSEROO + GS3OV + 11.2379T$
	${}^{o}G_{Sr^{2+}:Co^{4+}:O^{2-}}^{perovskite} - H_{Sr}^{SER} - H_{Co}^{SER} - 3H_{O}^{SER} = +GS4O$
	${}^{o}G_{Sr^{2+}:Co^{2+}:Va}^{perovskite} - H_{Sr}^{SER} - H_{Co}^{SER} = +GS2OV - 2GHSEROO + 15.8759T$
	${}^{o}G_{Sr^{2+}:Co^{3+}:Va}^{perovskite} - H_{Sr}^{SER} - H_{Co}^{SER} = +GS3OV - 2.5GHSEROO + 11.2379T$
	${}^{o}G_{Sr^{2+}:Co^{4+}:Va}^{perovskite} - H_{Sr}^{SER} - H_{Co}^{SER} = -3GHSEROO + GS4O$
	${}^{0}L_{Sr^{2+}:Co^{2+},Co^{3+}:O^{2-}}^{perovskite} = -38661.9$
	${}^{0}L_{Sr^{2+}:Co^{3+},Fe^{3+}:*}^{perovskite} = -81672.9$
	${}^{0}L_{Sr^{2+}:Co^{3+},Fe^{4+}:*}^{perovskite} = -29398.0$

	${}^{0}L^{perovskite}_{Sr^{2+}:Co^{2+},Fe^{3+}:O^{2-}} = 120086.0$
$Sr_2Co_2O_5$	$(Sr^{2+})_2(Co^{2+})_1(Co^{4+})_1(O^{2-})_5$
	${}^{o}G^{Sr_2Co_2O_5}_{Sr^{2+}:Co^{2+}:Co^{4+}:O^{-2}} - 2H^{SER}_{Sr} - 2H^{SER}_{Co} - 5H^{SER}_{O} = GSR2CO2O5$
$Sr_3Co_2O_7$	$(Sr^{2+})_1(Sr^{2+})_2\ (Co^{3+})_2(O^{2-}, Va)_6(O^{2-})_1$
	${}^{o}G^{Sr_3Co_2O_7}_{Sr^{2+}:Sr^{2+}:Co^{3+}:O^{2-}:O^{2-}} - 3H^{SER}_{Sr} - 2H^{SER}_{Co} - 7H^{SER}_{O} = 3GSROSOL + 2GCOOS$ $+2GHSEROO - 100000 + 60T$
	${}^{o}G^{Sr_3Co_2O_7}_{Sr^{2+}:Sr^{2+}:Co^{3+}:Va:O^{2-}} - 3H^{SER}_{Sr} - 2H^{SER}_{Co} - H^{SER}_{O} = 3GSROSOL + 2GCOOS$ $-4GHSEROO$
$Sr_3Fe_{2-x}Co_xO_{7-\delta}$ [b]	$(Sr^{2+})_1(Sr^{2+})_2(Co^{3+}, Fe^{3+}, Fe^{4+})_2(O^{2-}, Va)_6(O^{2-})_1$
	${}^{o}G^{Sr_3Fe_{2-x}Co_xO_7}_{Sr^{2+}:Sr^{2+}:Co^{3+}:O^{2-}:O^{2-}} - 3H^{SER}_{Sr} - 2H^{SER}_{Co} - 7H^{SER}_{O} = 3GSROSOL + 2GCOOS$ $+2GHSEROO + 15000$
	${}^{o}G^{Sr_3Fe_{2-x}Co_xO_7}_{Sr^{2+}:Sr^{2+}:Co^{3+}:Va:O^{2-}} - 3H^{SER}_{Sr} - 2H^{SER}_{Co} - H^{SER}_{O} = 3GSROSOL + 2GCOOS$ $-4GHSEROO$
	${}^{o}L^{Sr_3Fe_{2-x}Co_xO_7}_{Sr^{2+}:Sr^{2+}:Fe^{3+},Co^{3+}:O^{2-}:O^{2-}} = -165000$
	${}^{o}L^{Sr_3Fe_{2-x}Co_xO_7}_{Sr^{2+}:Sr^{2+}:Fe^{3+},Co^{3+}:Va:O^{2-}} = -100000$
$Sr_4Fe_{6-x}Co_xO_{13}$ [b]	$(Sr^{2+})_4(Fe^{3+})_4(Co^{3+}, Fe^{2+}, Fe^{3+}, Fe^{4+})_2(O^{2-})_{12}(O^{2-}, Va)_2$
	${}^{o}G^{Sr_4Fe_{6-x}Co_xO_{13}}_{Sr^{2+}:Fe^{3+}:Co^{3+}:O^{2-}:O^{2-}} - 4H^{SER}_{Sr} - 4H^{SER}_{Fe} - 2H^{SER}_{Co} - 14H^{SER}_{O} = +4GSRPRV$ $+2GHSERCO + 4GHSEROO - 478000$
	${}^{o}G^{Sr_4Fe_{6-x}Co_xO_{13}}_{Sr^{2+}:Fe^{3+}:Co^{3+}:O^{2-}:Va} - 4H^{SER}_{Sr} - 4H^{SER}_{Fe} - 2H^{SER}_{Co} - 12H^{SER}_{O} = +4GSRPRV$ $+2GHSERCO + 2GHSEROO - 170000$
$Sr_6Co_5O_{15}$	$(Sr^{2+})_6\ (Co^{4+})_4(Co^{2+})_1(O^{2-})_{15}$
	${}^{o}G^{Sr_6Co_5O_{15}}_{Sr^{2+}:Co^{4+}:Co^{2+}:O^{-2}} - 6H^{SER}_{Sr} - 5H^{SER}_{Co} - 15H^{SER}_{O} = 5899515.9 + 3806.83T$ $-602.231T\ln(T) - 0.08953T^2 + 4863524T^{-1}$
	Functions
	$GS2OV = GSROSOL + GCOOS + 28889.74 - 15.20777T$
	$GS3OV = GSROSOL + GCOOS + 0.5GHSEROO - 20754.002 + 10.997T$

$$GS4O = GSROSOL + GCOOS + GHSEROO - 86550.2 + 75.64357T$$

$$GCOOS = -252530 + 270.075 - 47.825T\ln(T) - 0.005112T^2 + 225008T^{-1}$$

$$GSROSOL = -607870 + 268.9T - 47.56T\ln(T) - 0.00307T^2 + 190000T^{-1}$$

$$GSR2CO2O5 = -1864898.9 + 1216.424 - 213.734T\ln(T) - 0.023799T^2$$
$$+1635410.1T^{-1}$$

$$GSR3FE2O7 = 2GSRPRV + GSROSOL$$

$$GSRPRV = GSROSOL + 0.5GFE2O3 - 44701 - 8.73T$$

$$GHSERCO = -310.241 + 133.36601T - 25.0861T\ln(T)$$
$$-0.002654739T^2 + 1.7348\times10^{-7}T^3 - 72527T^{-1}$$
$$298.15 < T < 1768$$

$$-17197.666 + 253.28374T - 40.5T\ln(T) + 9.3488\times10^{30}T^{-9}$$
$$1768 < T < 6000$$

$$GHSEROO = -3480.87226 - 25.5028601T - 11.1355068T\ln(T)$$
$$-0.005098873T^2 + 6.6184604\times10^{-7}T^3 - 38364.8742T^{-1}$$
$$298.15 < T < 1000$$

$$-6568.76015 + 12.6600017T - 16.8138015T\ln(T)$$
$$-5.9579637\times10^{-4}T^2 + 6.78055555\times10^{-9}T^3 + 262904.778T^{-1}$$
$$1000 < T < 3300$$

$$-13986.728 + 31.259625T - 18.9536T\ln(T) - 4.25243\times10^{-4}T^2$$
$$+1.0721\times10^{-8}T^3 + 4383200T^{-1}$$
$$3300 < T < 6000$$

[a] All parameters are in SI units: J, mol, K and Pa.

[b] The Gibbs energy terms for the end-members belonging to Sr-Fe-O can be found in Reference [8].

4.3.7 Optimization

Table 4.1 lists a set of optimized thermodynamic parameters obtained in this research for the ternary oxide phases in Sr-Co-O and for the quaternary solid solution phases in Sr-Co-Fe-O. During optimization, all experimental data were carefully assessed. The evaluation of the model parameters was carried out using recurrent runs of the PARROT program [65] in the Thermo-Calc software, which works by minimizing the square sum of the differences between experimental values and computed ones. In the optimization, each piece of experimental

information is given a certain weight. The weights were adjusted during the assessment until most of the experimental data were accounted for within the uncertainty limits stated.

The main challenge in modeling the Sr-Co-O system is the lack of experimental data, especially thermodynamic data. For the perovskite phase, A_1 in Eq.8 was optimized with enthalpy of formation from Federico *et al.* [38], while B_1 was obtained by assuming that the entropy of $SrCoO_{3-\delta}$ at 298 K is similar to that of $Sr_2Co_2O_5$, and making further adjustments using phase diagram data. A_2 and B_2 in Eq.9, A_3 and B_3 in Eq. 10, and one interaction parameter ${}^0L^{perovskite}_{Sr^{2+}:Co^{2+},Co^{3+}:O^{2-}}$ were optimized using phase diagram data and oxygen non-stoichiometry data.

As mentioned in *Section 4.3.3*, parameters for $Sr_2Co_2O_5$ and $Sr_6Co_5O_{15}$ were further adjusted using phase diagram data from Takeda *et al.* and Vashook *et al.* [35, 14]. During the optimization, a compromise had to be made between a good fit with first principle results and a good fit with phase diagram data. Due to the higher uncertainty of first principle calculations, phase diagram data were given more weight in the optimization. But still we tried to keep the deviation from both types of data within a reasonable range during modeling. For $Sr_3Co_2O_7$, A_0 and B_0 in Eq.5 were adjusted to make the phase stable at 1100°C in air in accordance with the findings of Aksenova *et al.* and Cherepanov *et al.* [23, 66].

For the Sr-Co-Fe-O system, three interaction parameters ${}^0L^{perovskite}_{Sr^{2+}:Co^{3+},Fe^{3+}:*}$, ${}^0L^{perovskite}_{Sr^{2+}:Co^{3+},Fe^{4+}:*}$, ${}^0L^{perovskite}_{Sr^{2+}:Co^{2+},Fe^{3+}:*}$ for the perovskite phase were optimized using phase diagram and oxygen non-stoichiometry data. In addition, interaction parameters for $Sr_3Fe_{2-x}Co_xO_{7-\delta}$ (${}^0L^{Sr_3Fe_{2-x}Co_xO_7}_{Sr^{2+}:Sr^{2+}:Fe^{3+},Co^{3+}:O^{2-}:O^{2-}}$ and ${}^0L^{Sr_3Fe_{2-x}Co_xO_7}_{Sr^{2+}:Sr^{2+}:Fe^{3+},Co^{3+}:Va:O^{2-}}$) and Gibbs energy terms for the end-members of $Sr_4Fe_{6-x}Co_xO_{13}$ (${}^oG^{Sr_4Fe_{6-x}Co_xO_{13}}_{Sr^{2+}:Fe^{3+}:Co^{3+}:O^{2-}:O^{2-}}$ and ${}^oG^{Sr_4Fe_{6-x}Co_xO_{13}}_{Sr^{2+}:Fe^{3+}:Co^{3+}:O^{2-}:Va}$) were optimized to account for the Co solubility in $Sr_3Fe_2O_7$ and $Sr_4Fe_6O_{13}$, respectively.

4.4 Results and discussion

4.4.1 The Sr-Co-O system

The enthalpy of formation, entropy, and Gibbs energy of formation calculated in this research for $Sr_6Co_5O_{15}$, $Sr_2Co_2O_5$ and $SrCoO_{3-\delta}$ at 298 K are listed in Table 4.2, together with references from the literature. The CALPHAD results deviate in general from those obtained via first

principle calculations. For a better determination of the Gibbs energy functions, thermodynamic measurements would be advantageous.

Table 4.2 Enthalpy of formation, entropy, and Gibbs energy of formation for $Sr_6Co_5O_{15}$, $Sr_2Co_2O_5$ and $SrCoO_{3-\delta}$ at 298 K

Phase	Results	Method	Reference
$Sr_6Co_5O_{15}$	$\Delta^o H_{f,elements}^{Sr_6Co_5O_{15}}(298K) = -206.899$ kJ/mol	First principle	[15,21]
	$\Delta^o H_{f,elements}^{Sr_6Co_5O_{15}}(298K) = -206.899$ kJ/mol	CALPHAD	[15]
	$\Delta^o H_{f,elements}^{Sr_6Co_5O_{15}}(298K) = -218.437$ kJ/mol	CALPHAD	This work
	${}^oS^{Sr_6Co_5O_{15}}(298K) = 17.348$ J/mol/K	First principle	[15,21]
	${}^oS^{Sr_6Co_5O_{15}}(298K) = 22.8$ J/mol/K	CALPHAD	[15]
	${}^oS^{Sr_6Co_5O_{15}}(298K) = 12.87$ J/mol/K	CALPHAD	This work
$Sr_2Co_2O_5$	$\Delta^o H_{f,elements}^{Sr_2Co_2O_5}(298K) = -210.112$ kJ/mol	First principle	[15]
	$\Delta^o H_{f,elements}^{Sr_2Co_2O_5}(298K) = -150.309$ kJ/mol	CALPHAD	[15]
	$\Delta^o H_{f,elements}^{Sr_2Co_2O_5}(298K) = -198.676$ kJ/mol	CALPHAD	This work
	${}^oS^{Sr_2Co_2O_5}(298K) = 18.25$ J/mol/K	First principle	[15]
	${}^oS^{Sr_2Co_2O_5}(298K) = 55.095$ J/mol/K	CALPHAD	[15]
	${}^oS^{Sr_2Co_2O_5}(298K) = 27.52$ J/mol/K	CALPHAD	This work
$SrCoO_{3-\delta}$	$\Delta^o G_{f,elements}^{SrCoO_3}(298K) = -163$ kJ/mol	First principle	[38]
	$\Delta^o G_{f,elements}^{SrCoO_3}(298K) = -171$ kJ/mol	CALPHAD	[15]
	$\Delta^o G_{f,elements}^{SrCoO_3}(298K) = -183$ kJ/mol	CALPHAD	This work
	${}^oS^{SrCoO_3}(298K) = 55.57$ J/mol/K	CALPHAD	[15]
	${}^oS^{SrCoO_3}(298K) = 27.26$ J/mol/K	CALPHAD	This work

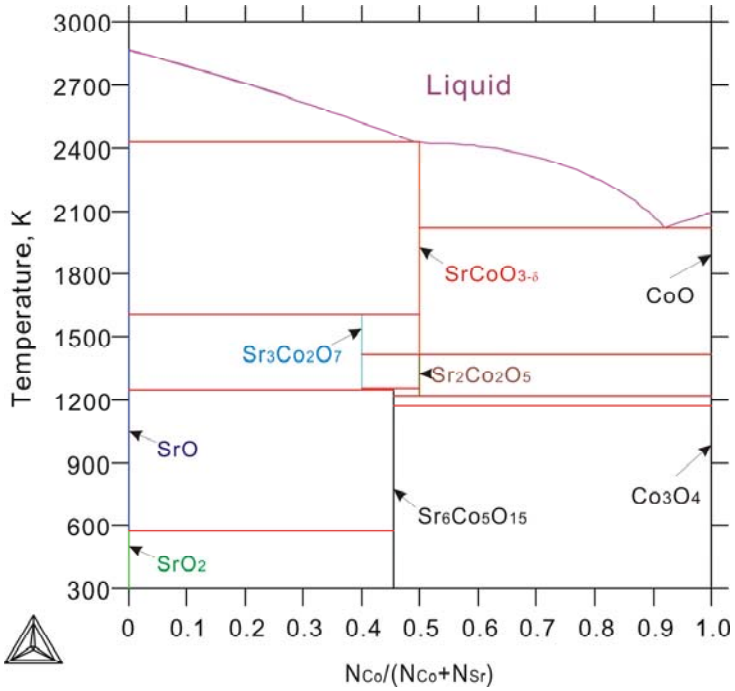

Fig. 4.1. Calculated phase diagram of SrO_x-CoO_y in air based on the parameters obtained in this research.

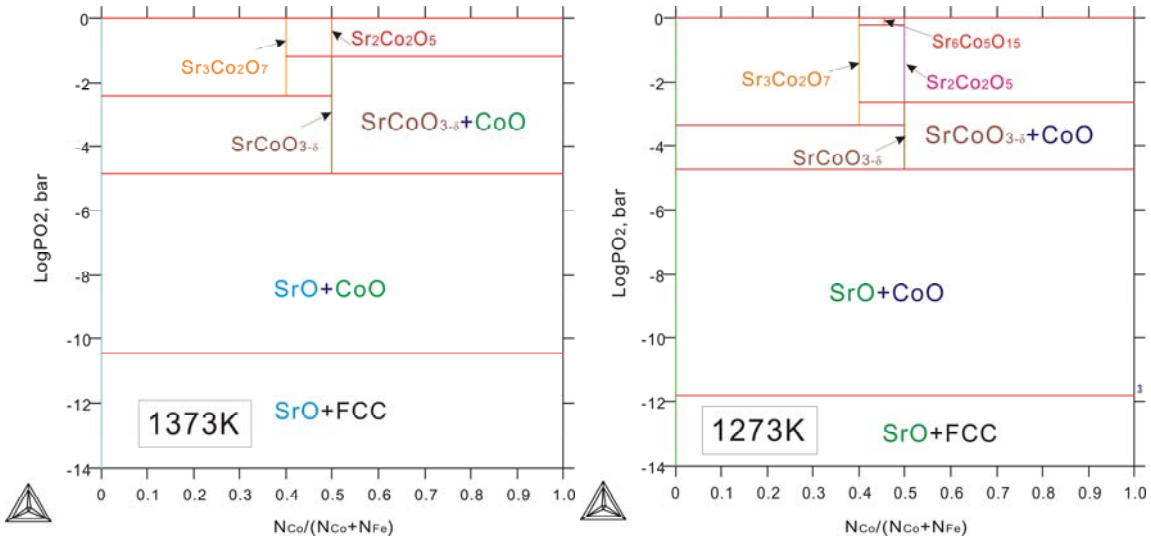

(a) (b)

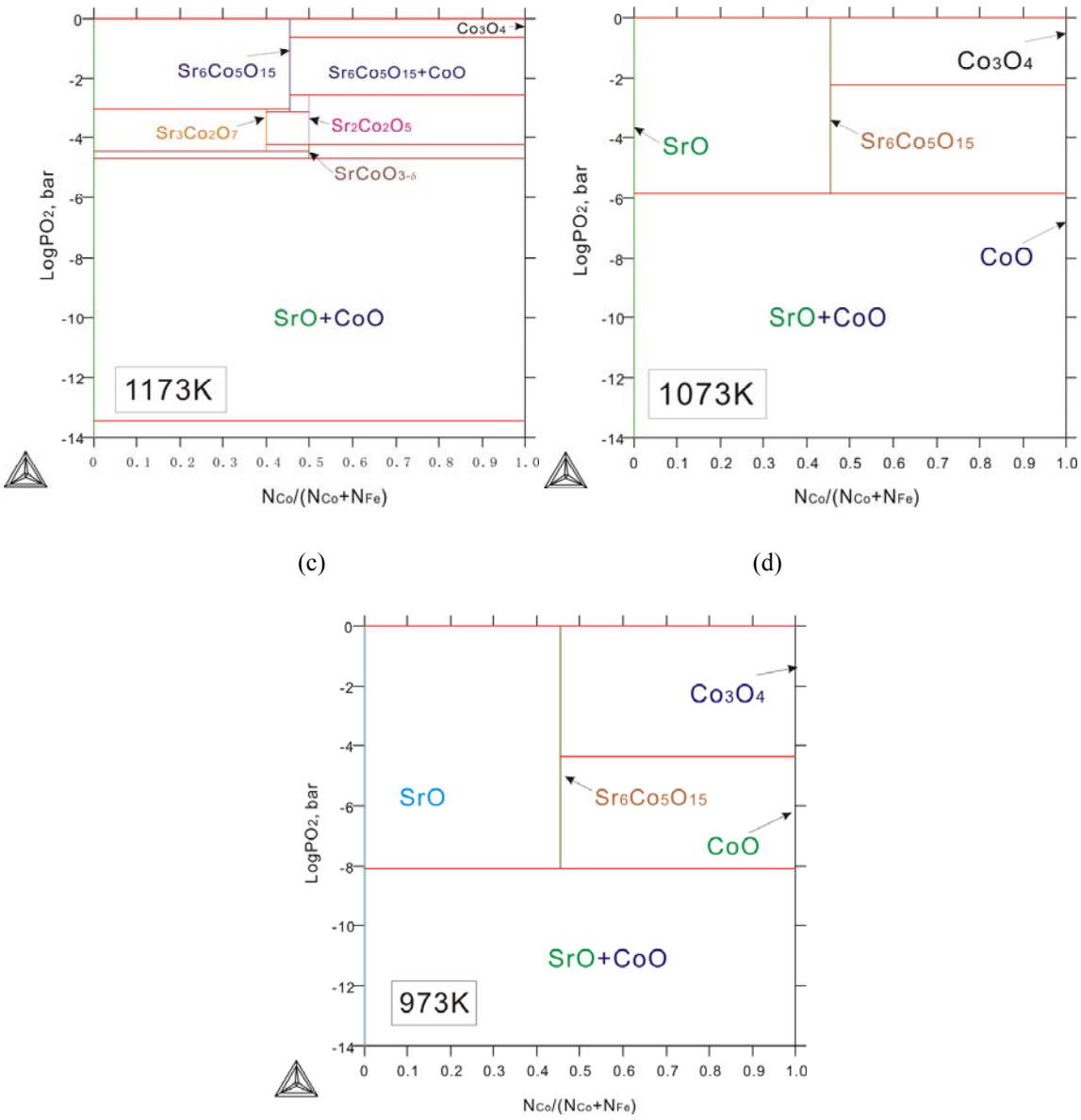

Fig. 4.2. Calculated isothermal PO_2-composition phase diagrams at different temperatures based on the parameters obtained in this research. (a) 1373K, (b) 1273K, (c) 1173K, (d) 1073K, (e) 973K.

The calculated phase diagrams for SrO_x-CoO_y from this work are shown in Figs. 4.1−4.3. Fig. 4.1 presents the calculated SrO_x-CoO_y phase diagram in air. The phase equilibrium is more complex in a composition range of $x(Co)/(x(Co)+x(Sr))$= 0.4−0.5 and a temperature range of T=1100−1500K. In addition to $Sr_6Co_5O_{15}$, Wong-Ng *et al.* [25] report also the existence of $Sr_4Co_3O_9$

and $Sr_5Co_4O_{12}$ at 1123K in air. According to the current modeling, however, $Sr_4Co_3O_9$ and $Sr_5Co_4O_{12}$ phases cannot co-exist with $Sr_6Co_5O_{15}$ at 1123 K in air. These two phases were therefore excluded in the final database. The calculated stable temperature range for $Sr_3Co_2O_{7-\delta}$ in air is from 1246 to 1610 K. Fig. 4.2 shows the calculated isothermal PO_2-composition (PO_2 from 10^{-14} to 1 bar) phase diagrams at temperatures 973−1373K. The stable phases at different conditions can be read directly from the figures.

$SrCoO_{3-\delta}$ is one of the most important oxides in Sr-Co-O and its stability depends strongly on temperature and oxygen partial pressure. Fig. 4.3 shows the calculated stability phase diagram for a composition of $x(Co)/(x(Co)+x(Sr))=0.5$ in comparison with experimental results. The single phase or two-phase region is labeled with phase names and the line between two neighboring regions represents a univariant reaction. As shown in Fig. 4.3, the deviation between the calculations and the experimental results is within a reasonable range. The $SrCoO_{3-\delta}$ perovskite phase is stable only at high temperature. In a temperature range of 1250−1423 K, $SrCoO_{3-\delta}$ is stable at PO_2 = $10^{-0.5}$−$10^{-4.8}$ bar, and its stability decreases with decreasing temperature. The type of diagram shown in Fig. 4.3 can be used to explore the stability range (temperature and oxygen partial pressure) for required phases under a given composition.

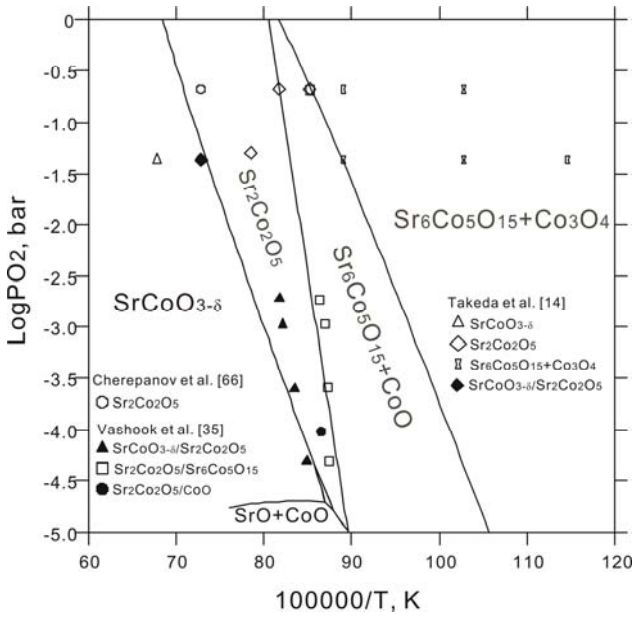

Fig. 4.3. Calculated stability diagram of Sr-Co-O based on the parameters obtained in this research for a composition of x(Co)/(x(Co)+x(Sr))=0.5 with experimental data included. The symbols represent single-phase or two-phase region or phase boundary between two neighboring regions, e.g. $Sr_2Co_2O_5/Sr_6Co_5O_{15}$.

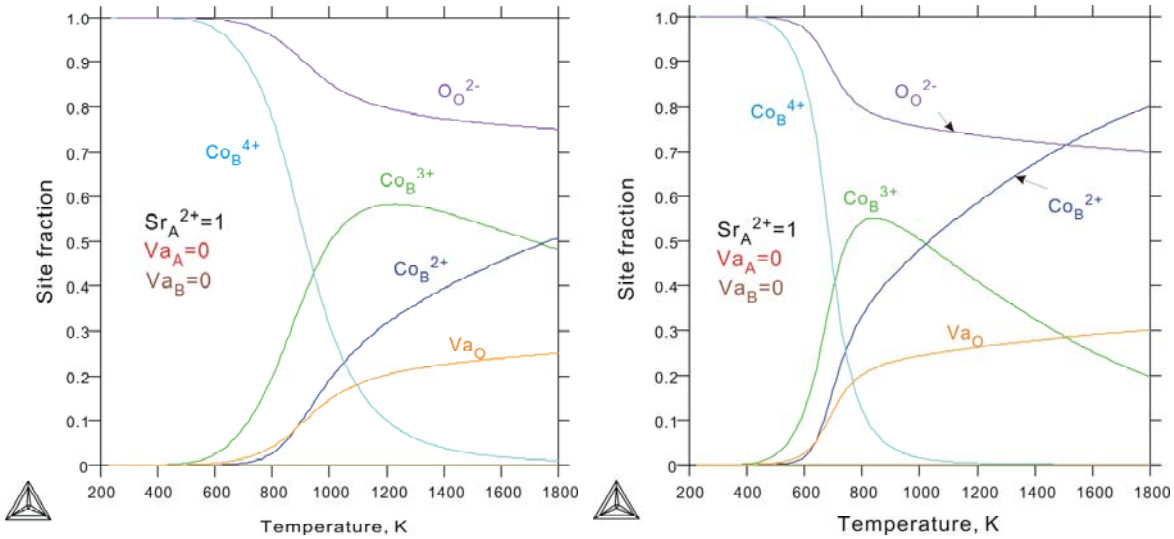

Fig. 4.4. Site fractions in $SrCoO_{3-\delta}$. (a) in air (b) at PO_2=1 Pa.

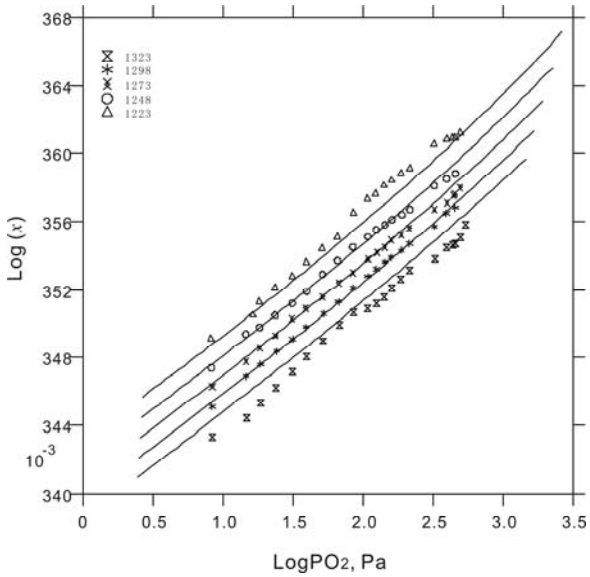

Fig. 4.5. Calculated oxygen non-stoichiometry (x) in $SrCoO_x$ as a function of logPO_2 in comparison with experimental data from Vashook *et al.* [37].

Fig. 4.4 plots site fractions in $SrCoO_{3-\delta}$ in air and at PO_2 = 1Pa calculated in this research. At low temperatures where $SrCoO_{3-\delta}$ is metastable, Co exists mainly as Co^{4+} in $SrCoO_{3-\delta}$. At high temperatures, $SrCoO_{3-\delta}$ has a large oxygen vacancy at the O site where Co^{3+} and Co^{2+} form. Fig. 4.5 shows the oxygen non-stoichiometry in $SrCoO_x$ calculated in this research, which agrees very well with the experimental results.

4.4.2. The Sr-Co-Fe-O system

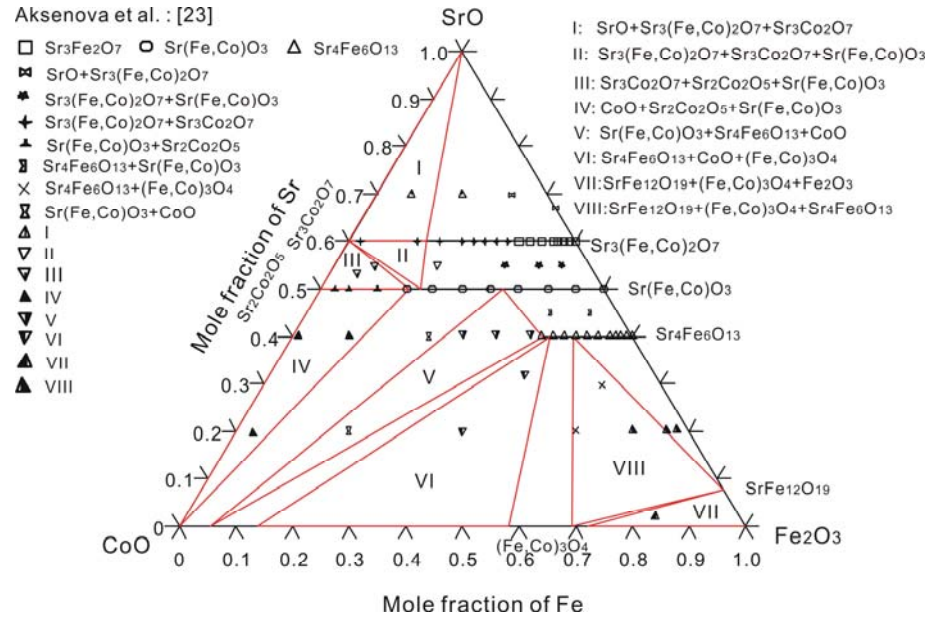

(a)

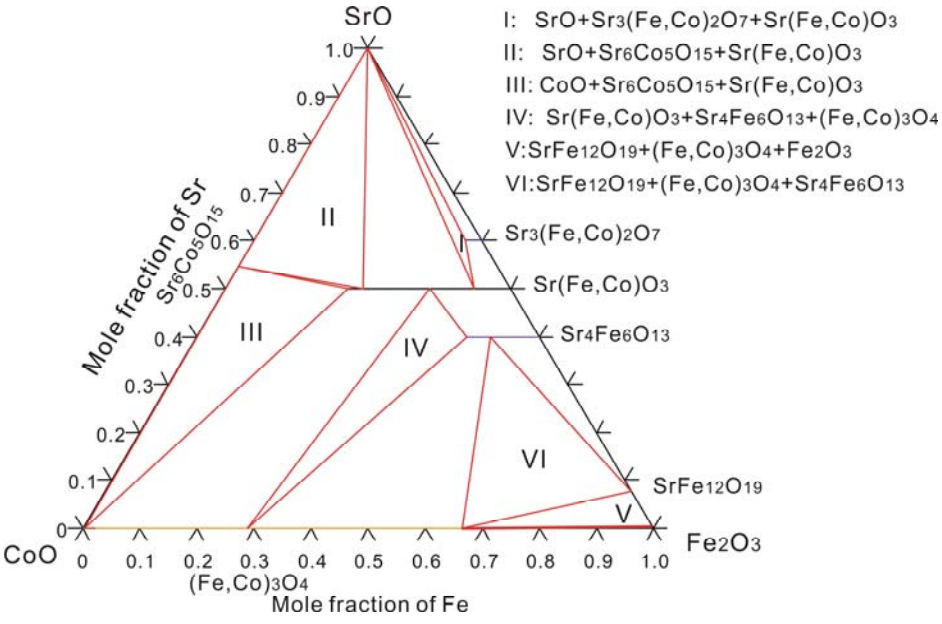

(b)

Fig. 4.6. Calculated isotheromal sections of SrO-Fe_2O_3-CoO_x in air compared with the experimental data from Aksenova *et al*. [23]. a) at 1373 K, b) at 1173 K.

Fig. 4.6 presents the calculated SrO-Fe_2O_3-CoO_x isothermal sections at 1373 K and 1173 K in air. The calculated isothermal section at 1373 K agree quite well with most of the experiment

data from Aksenova *et al.* [23], except for the Co solubility in $Sr_3Fe_{2-y}Co_yO_{7-\delta}$. The isothermal section at 1173K differs quite a lot from the one at 1373 K. Further experimental studies on phase equilibria in $SrO\text{-}Fe_2O_3\text{-}CoO_x$ at various temperatures and oxygen partial pressures would be very valuable to validate the calculations and the database of Sr-Co-Fe-O. At both temperatures, the $SrCo_{1-x}Fe_xO_{3-\delta}$ perovskite phase is more stable on the Fe-rich side (i.e. close to $SrFeO_{3-\delta}$) and forms secondary phases on the Co-rich side. Fig. 4.7 plots the phase fraction for the composition $SrFe_{1-x}Co_xO_3$ at 1273 K and 973 K in air. According to the calculation, the $SrFe_{1-x}Co_xO_3$ perovskite is stable when x<0.64 at 1273K, and when x<0.35 at 973 K. Table 4.3 lists the calculated Co solubility in $Sr_4Fe_{6-x}Co_xO_{13}$ at different temperatures in air, as compared with experimental results. It clearly shows that the Co solubility in $Sr_4Fe_{6-x}Co_xO_{13}$ decreases with decreasing temperature.

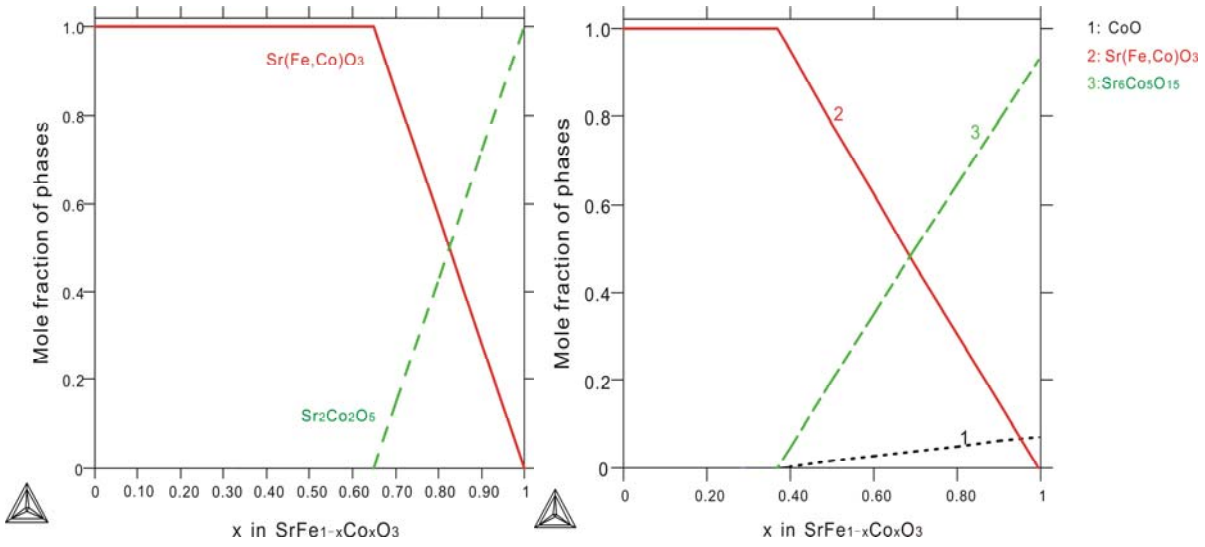

(a) (b)

Fig. 4.7. Calculated phase fraction for the composition $SrFe_{1-x}Co_xO_{3-\delta}$ in air, (a) at 1273 K and (b) 973 K.

Table 4.3 Co solubility (x) in $Sr_4Fe_{6-x}Co_xO_{13}$ at different temperatures in air

T	Calculated solubility from this research (x)	Experimentally determined solubility from the literature	
1123	1.1	1	[53]
1173	1.2	1.5	[53]
1223	1.3	2	[53]

1273	1.4	1.5	[51, 53]
		1.8	[48]
1373	1.6	1	[53]
		1.6	[23]
1423	1.6	1.4	[52]
1473	1.7	1.5	[50]

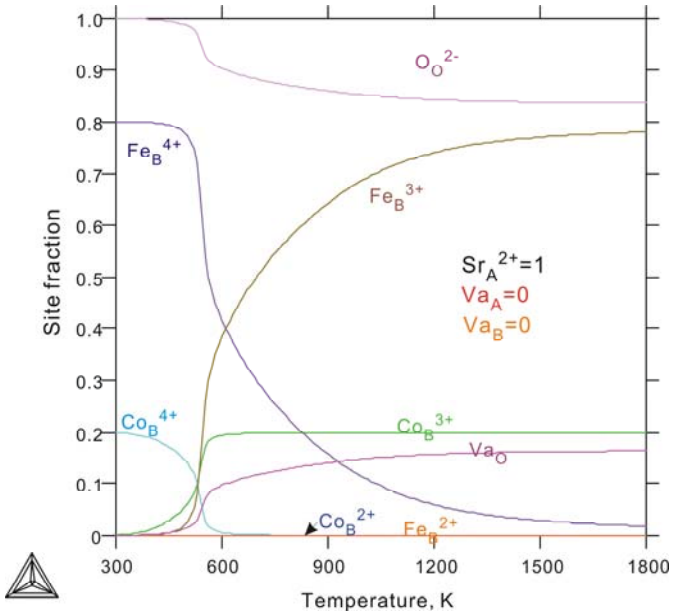

Fig. 4.8 Calculated site fractions in $SrCo_{0.2}Fe_{0.8}O_{3-\delta}$ in air as a function of temperature.

As for the $SrFe_{1-x}Co_xO_3$ perovskite, the cation valences (especially the B-site cations) have a significant influence on the magnetic property, electronic conductivity and thermal-conductivity of the perovskite. Fig. 4.8 presents the site fractions in $SrCo_{0.2}Fe_{0.8}O_{3-\delta}$ in air as a function of temperature calculated in this research. Co and Fe exist mainly as cations with a valency of 4+ or 3+ in $SrCo_{0.2}Fe_{0.8}O_{3-\delta}$ in air, which is in agreement with experimental results [31, 33]. With increasing temperature, the concentration of Co^{3+} and of Fe^{3+} increases at the expense of a decrease in the concentration of Co^{4+} and Fe^{4+}.

4.5 Conclusions

As a part of a research project aimed at developing a thermodynamic database of the La-Sr-Fe-Co-O system for applications in SOFCs and gas separation membranes, thermodynamic databases for the Sr-Co-O and Sr-Co-Fe-O systems were developed by applying the CALPHAD method. Due to the lack of experimental data, a few assumptions were made on the thermodynamic properties of the complex oxides in Sr-Co-O. This means that the calculations presented in this paper must be treated with caution, especially where the experimental study is missing. The resulting database can be used for calculating phase equilibria and thermodynamic properties at temperatures of 298−3000 K and oxygen partial pressure of 10^{-15}−1 bar using Gibbs energy minimization software. In Sr-Co-O, the perovskite phase is stable only at high temperatures. In Sr-Co-Fe-O, at $T \leq 1373$ K, the perovskite phase is stable with high Fe content and its stability decreases with decreasing temperature. New experimental studies on thermodynamic properties and the phase stability of non-perovskite phases will be valuable in validating the calculations presented in this paper and further improving the database.

References

[1] L. Qiu, T.H. Lee, L.-M. Liu, Y.L. Yang, A.J. Jacobson, Solid State Ionics 76 (1995) 321–329.

[2] G.M. Veith, R. Chen, G. Popov, M. Croft, Y. Shokh, I. Nowik, M. Greenblatt, J. Solid State Chem. 166 (2002) 292–304.

[3] S. Ghosh, P. Adler, J. Mater. Chem. 12 (2002) 511–521.

[4] M.V. Zinkevich, V.V. Vashuk, Neorg. Mater. 28 (1992) 816–821.

[5] D. Gostovic, J.R. Smith, D.P. Kundinger, K.S. Jones, E. D. Wachsman, Electrochem. Solid-State Lett. 10 (2007) B214–B217.

[6] D. Beckel, U.P. Muecke, T. Gyger, G. Florey, A. Infortuna, L.J. Gauckler, Solid State Ionics 178 (2007) 407–415.

[7] G. DiGiuseppe, L. Sun, Int. J. Hydrogen Energy, 36 (2011) 5076–5087.

[8] E. Povoden-Karadeniz, Thermodynamic modeling of Sr-Fe-O system, unpublished work. http://wwwt.tuwien.ac.at/fileadmin/t/wwwt/forschung/wt/Projekte/Erwin_Povoden-Karadeniz/databases/LSF.TDB.

[9] D. Risold, B. Hallstedt, L.J. Gauckler, CALPHAD, 20 (1996) 353–361.

[10] M. Chen, B. Hallstedt, L.J. Gauckler, J. Phase Equilib. 24 (2003) 212–227.

[11] B. Sundman, J. Phase Equilib. 12 (1991) 127–140.

[12] W.-W Zhang, M. Chen, Thermodynamic modeling of Co-Fe-O system, submitted to CALPHAD.

[13] J.-C. Grenier, S. Ghodbane, G. Demazeau, Muter. Res. Bull. 14 (1979) 831.

[14] Y. Takeda, R. Kanno, T. Takada, O. Yamamoto, M. Takano, Y. Bando, Z. Anorg. Allg. Chem. 540/541(1986) 259–270.

[15] J.E. Saal, Thermodynamic modeling of phase transformations and defects: From Cobalt to Doped Cobaltate Perovskites (PhD thesis), The Pennsylvania State university, (2010).

[16] J. Rodriguez, M. Gonzalez-Calbert, Muter. Res. Bull. 21 (1986) 429.

[17] P.D. Battle, T.C. Gibb, A.T. Steel, J. Chem. SOC. Dalton Trans. (1987) 2359.

[18] W.T.A. Harrison, S.L. Hegwood, A.J.Jacobson, J. Chem. Soc. Chem. Commun. (1995) 1953–1954.

[19] J.L. Sun, G.B.Li, Z.F. Li, L.P. You, J.H. Lin, Inorg. Chem. 45 (2006) 8394–8402.

[20] K. Iwasaki, T. Ito, T. Matsui, T. Nagasaki, S. Ohta, K. Koumoto, Mater. Res. Bull. 41 (2006) 732–739.

[21] J.E. Saal, Y. Wang, S. Shang, Z.-K. Liu, Inorg. Chem. 49 (2010) 10291–10298.

[22] O. Gourdon, V. Petricek, M. Dusek, P. Bezdicka, S. Durovic, D. Gyepesova, M. Evain, Acta Crystallogr., Sect. B: Struct. Sci. 55 (1999) 841–848.

[23] T.V. Aksenova, L.Ya. Gavrilova, V.A. Cherepanov, J. Solid State Chem. 181 (2008) 1480–1484.

[24] K. Li, D. Sheptyakov, Y. Wang, C.-K. Loong, J. Lin, J. Solid State Chem. 184 (2011) 888–892.

[25] W. Wong-Ng, G. Liu, J. Martin, E.L. Thomas, N. Lowhorn, J.A. Kaduk, J. Appl. Phys. 107 (2010) 033508.

[26] S.E. Dann, M.T. Weller, J. Solid State Chem. 115 (1995) 499–507.

[27] D. Pelloquin, N. Barrier, A. Maignan, V. Caignaert, Solid State Sciences 7 (2005) 853–860.

[28] J.M. Hill, B. Dabrowski, J.F. Mitchell, J.D. Jorgensen, Phys. Rev. B 74 (2006) 174417.

[29] L. Viciu, H.W. Zandbergen, Q. Xu, Q. Huang, M. Lee, R.J. Cava, Journal of Solid State Chemistry 179 (2006) 500–511.

[30] X.L. Wang, H. Sakurai, E. Takayama-Muromachi, J. Appl. Phys. 97 (2005) 10M519.

[31] H. Taguchi, M. Shimada, M. Koizumi, J. Solid State Chem. 29 (1979) 221–225.

[32] H. Taguchi, M. Shimada, M. Koizumi, Mater. Res. Bull. 15 (1980) 165–169.

[33] A. Nakatsuka, A. Yoshiasa, N. Nakayama, T. Mizota, H. Takei. Acta Cryst. C60 (2004) i59–i60.

[34] J. Rodriguez, J.M. Gonzalez-Calbet, J.C. Grenier, J. Pannetier, M. Anne, Solid State Commun. 62 (1987) 231–234.

[35] V.V. Vashook, M.V. Zinkevich, Y.G. Zonov, Solid State Ionics 116 (1999) 129–138.

[36] V.V. Vashuk, S.A. Prodan, M.V. Zinkevich, O. P. Ol'shevskaya. Inorg. Mat. 29 (1993) 730–734.

[37] V.V. Vashook, M.V. Zinkevich, H. Ullmann, J. Paulsen, N. Trofimenko, K. Teske, Solid State Ionics 99 (1997) 23–32.

[38] F. Calle-Vallejo, J.I. Martínez, J.M. García-Lastra, M. Mogensen, J. Rossmeisl, Angew. Chem. Int. Ed. 49 (2010) 7699–7701.

[39] L.V. Kokhanovskii, Y.G. Zonov, O.P. Ol'shevskaya, V.V. Pan'kov, Inorg. Mater. 41 (2005) 876–881.

[40] L.V. Kokhanovskii, V.V. Vashuk, O. . Ol'shevskaya, O. I. Kirilenko, Inorg. Mater. 37 (2001) 730–736.

[41] L.M. Liu, T.H. Lee, L. Qiu, Y.L. Yang, A.J. Jacobson, Mater. Res. Bull. 31 (1996) 29–35.

[42] N. Grunbaum, L. Mogni, F. Prado, A. Caneiro, Journal of Solid State Chemistry 177 (2004) 2350–2357.

[43] S. McIntosh, J.F. Vente, W.G. Haije, D.H.A. Blank, H.J.M. Bouwmeester, Solid State Ionics 177 (2006) 833–842.

[44] S. McIntosh, J.F. Vente, W.G. Haije, D.H.A. Blank, H.J.M. Bouwmeester, Solid State Ionics 177 (2006) 1737–1742.

[45] B.J. Mitchell, R.C. Rogan, J.W. Richardson Jr., B. Ma, U. Balachandran, Solid State Ionics 146 (2002) 313–321.

[46] V. V. Vashuk, L. V. Kokhanovskii, I. I. Yushkevich, Inorg. Mater. 36 (2000) 1043−1049.

[47] H. Fjellvåg, B. C. Hauback, R. Bredesen, J. Mater. Chem. 7 (1997) 2415–2419.

[48] Y. Xia, T. Armstrong, F. Prado, A. Manthiram, Solid State Ionics 130 (2000) 81–90.

[49] B. Ma, J.P. Hodges, J.D. Jorgensen, D.J. Miller, J.W. Richardson, U. Balachandran, J. Solid State Chem. 141 (1998) 576–586.

[50] Z.-Q. Deng, G.-G. Zhang, W. Liu, D.-K. Peng, C.-S. Chen, Solid State Ionics 152– 153 (2002) 735–739.

[51] T. Armstrong, E. Prado, Y. Xia, A. Manthiram, J. Electrochem. Soc. 147 (2000) 435–438.

[52] S. Kim, Y.L. Yang, R. Christoffersen, A.J. Jacobson, Solid State Ionics 109 (1998) 187–196.

[53] A. Fossdal, L.T. Sagdahl, M.A. Einarsrud, K. Wiik, T. Grande, P.H. Larsen, F.W. Poulsen, Solid State Ionics 143 (2001) 367–377.

[54] M. Hillert, J. Alloys Compd. 320 (2001) 161–176.

[55] A.T. Dinsdale, CALPHAD 15 (1991) 317–425.

[56] G. Inden, Z. Metallkd. 66 (1975) 577–582.

[57] M. Hillert, M. Jarl, CALPHAD 2 (1978) 227–238.

[58] M. Hillert, B. Jansson, B. Sundman, J. Ågren, Metall. Trans. 16A (1985) 261–266.

[59] B. Sundman, CALPHAD 15 (1991) 109–119.

[60] M. Kowalski, P. Spencer, CALPHAD 19 (1995) 229–243.

[61] A.N. Grundy, B. Hallstedt, L.J. Gauckler, J. Phase Equilib. Diff. 25 (2004) 311–319.

[62] A.N. Grundy, M. Chen, B. Hallstedt, L.J. Gauckler, J. Phase Equilib. Diff. 26 (2005) 131–151.

[63] E. Povoden, M. Chen, A.N. Grundy, T. Ivas, L.J. Gauckler, J. Phase Equilib. Diff. 30 (2009) 12–27.

[64] E. Povoden-Karadeniz, M. Chen, T. Ivas, A.N. Grundy, L.J. Gauckler, J. Mater. Res. 27 (2012) 1915–1926.

[65] B. Sundman, B. Jansson, J.-O. Andersson, CALPHAD 9 (1985) 153–190.

[66] V.A. Cherepanov, L.Ya. Gavrilova, L.Yu. Barkhatova, V.I. Voronin, M.V. Trifonova, O.A. Bukhner, Ionics 4 (1998) 309–315

Chapter 5

Phase equilibria and defect chemistry of the La-Sr-Co-O system

Abstract

LSC ($La_{1-x}Sr_xCoO_{3-\delta}$) is a promising material for intermediate temperature SOFCs (Solid Oxide Fuel Cells) and oxygen membrane. However, the thermodynamic instability of the LSC material impedes its application in service. The present work is aiming to identify phase stability of LSC by thermodynamic modeling of the La-Sr-Co-O system using the CALPHAD (CALculation of PHAse Diagrams) method coupled with key experiments. Phase stability of LSC as functions of composition, temperature and oxygen partial pressure was predicted. The calculated results were validated using experimental data from literatures, as well as experiments carried out in the present work. General agreement was achieved between model predicted and experimental results. Beside phase stability, other properties of the LSC perovskite, such as oxygen non-stoichiometry and cation distribution, were also calculated and predicted based on the developed La-Sr-Co-O database. The calculations can assist to design various related material for industrial applications, including SOFC and oxygen membrane.

5.1 Introduction

$La_{1-x}Sr_xCoO_{3-\delta}$ (LSC, lanthanum strontium cobaltite) as a versatile perovskite offers high electronic and ionic conductivity, excellent catalytic activity and interesting magnetic properties, which allow it to be widely used as oxidation and reduction catalyst [1], as cathode for solid oxide fuel cells (SOFCs) [2], as oxygen separation membrane [3], as gas sensor and as magnetoresistor [4, 5]. However, full clarify on the thermodynamic stability of LSC does not exist [6−9]. The present knowledge of the La-Sr-Co-O phase diagram is fragmentary which complicates the application of this kind of material. A comprehensive investigation of the phase equilibria in La-Sr-Co-O by obtaining accurate Gibbs energy functions for all relevant phases will facilitate understanding the thermodynamic and thermochemical properties of the LSC perovskite.

In the present work, we aim to establish a thermodynamic database of the multicomponent La-Sr-Co-O system by the CALPHAD (CALculation of PHAse Diagrams) method, in order to investigate the phase stability of LSC and specifically to predict conditions of operation in various applications where undesired phases can be avoided. The assessment of the La-Sr-Co-O system is based on the sub-systems (La-Co-O, Sr-Co-O *etc.*) which were developed in the previous chapters [10, 11]. The literature data regarding the La-Sr-Co-O system were carefully reviewed. After modeling of the La-Sr-Co-O system, phase diagrams and other properties were calculated and compared with literature data. To validate the developed La-Sr-Co-O database, model predicted results on stability of LSC under various conditions were compared with experimental results obtained in the present work.

The high oxide ion conductivity and high catalytic activity of LSC stems from its large oxygen non-stoichiometry. Extensive works [12-18] have been conducted on oxygen non-stoichiometry and transport properties of LSC. However, due to lack of phase stability information, reliability of these investigations is in some cases questionable. In this work, we have tried systematically to reproduce the equilibrium oxygen non-stoichiometry of LSC based on the developed thermodynamic database. The oxygen deficiency can be calculated and predicted at any given Sr content, temperature and oxygen partial pressure, which will be valuable in studying defect chemistry and conductivity. By obtaining a set of self-consistent Gibbs energy functions, knowledge of the cation distribution in the perovskite phase can be descried, which thus can be used for predicting magnetic properties of the material.

5.2 Methods

5.2.1. CALPHAD modeling

In the present work, the modeling of the La-Sr-Co-O system was based on the recently assessed subsystems (Table 5.1). The lattice stability for pure elements was adopted from Dinsdale [24]. The Compound Energy Formalism (CEF) [25], which is widely used in CALPHAD assessments [26, 27], was introduced to describe the Gibbs energy for all the phases in La-Sr-Co-O system. The CEF was developed to describe phases using sublattices. The CEF models for all phases in La-Sr-Co-O are listed in Table 5.2. The Gibbs energy descriptions for the perovskite phase and other relevant phases were elucidated in pervious chapters (*Section 3.3* and *Section 4.3*).

Table 5.1 References for assessed subsystems adopted in this work

System	References
La-O	Grundy *et al*. [19] [20]
Sr-O	Risold *et al*. [21]
Co-O	Chen *et al*. [22]
La-Co	Wang *et al*. [23]
La-Sr-O	Grundy *et al*. [20]
La-Co-O	Zhang *et al*. [10]
Sr-Co-O	Zhang *et al*. [11]

Table 5.2 Phases and models for the La-Sr-Co-O system

Phase	Description	Model	References
Liquid	Ionic liquid phase	$(La^{3+},Sr^{2+},Co^{2+},Co^{3+})_p(O^{2-}, Va)_q$	[19] [20] [21] [22]
$La_{1-x}Sr_xCoO_{3-\delta}$	Perovskite	$(La^{3+},Sr^{2+},Va)_1(Co^{2+},Co^{3+},Co^{4+}, Va)_1(O^{2-}, Va)_3$	This work
$(La,Sr)_2CoO_4$	La_2CoO_4 with Sr solubility	$(La^{3+},Sr^{2+})_2 (Co^{2+},Co^{4+})_1 (O^{2-})_4$	This work
A-$(La,Sr)_2O_3$	hexagonal La_2O_3 with Sr solubility	$(La^{2+},La^{3+},Sr^{2+})_2(O^{2-},Va)_3$	[19]
H-$(La,Sr)_2O_3$	partially ordered hexagonal La_2O_3 with Sr solubility	$(La^{3+},Sr^{2+})_2(O^{2-},Va)_3$	[20]
X-$(La,Sr)_2O_3$	Cubic La_2O_3 with Sr solubility	$(La^{3+},Sr^{2+})_2(O^{2-},Va)_3$	[20]
(Sr,La)O	SrO with La solubility	$(La^{3+},Sr^{2+},Va)_1 (O^{2-})_1$	[20]

SrO_2	Stoichiometric compound	$(Sr^{4+})_1(O^{2-})_2$	[21]
Co_3O_4	Spinel	$(Co^{2+},Co^{3+})_1\ (Co^{2+},Co^{3+})_2\ (O^{2-})_4$	[22]
CoO	Halite	$(Co^{2+})_1\ (O^{2-})_1$	[22]
La_4SrO_7	Beta phase	$(La^{3+},Sr^{2+})_2(O^{2-},Va)_3$	[20]
$La_4Sr_3O_9$	Stoichiometric compound	$(La^{3+})_4(\ Sr^{2+})_3(O^{2-})_9$	[20]
$La_4Co_3O_{10}$	Stoichiometric compound	$(La^{3+})_4(Co^{2+})_1(Co^{3+})_2(O^{2-})_{10}$	[10]
$Sr_6Co_5O_{15}$	Stoichiometric compound	$(Sr^{2+})_6(Co^{4+})_4(Co^{2+})_1\ (O^{2-})_{15}$	[11]
$Sr_2Co_2O_5$	Brownmillerite	$(Sr^{2+})_2(Co^{2+})_1\ (Co^{4+})_1\ (O^{2-})_5$	[11]
$Sr_3Co_2O_7$	Stoichiometric compound	$(Sr^{2+})_1(Sr^{2+})_2(Co^{3+})_2(\ O^{2-},\ Va)_6\ (O^{2-})_1$	[11]
FCC	Metallic La-Co FCC phase with Sr, O solubility	$(La,\ Sr,\ Co)_1(O,\ Va)_1$	[10, 11, 22]
BCC	Metallic La BCC phase with Sr, Co, O solubility	$(La,\ Sr,\ Co)_1(O,\ Va)_3$	[10, 11, 22]
HCP	Metallic Co HCP phase with O solubility	$(Co)_1(O,\ Va)_{0.5}$	[22]
DHCP	Metallic La DHCP phase with O solubility	$(La)_1(O,\ Va)_{0.5}$	[19]

In the present work, most phases were treated as ideal extrapolation from the subsystems. For the liquid phase, no quaternary parameter was optimized due to lack of experimental data. The calculated liquidus shall therefore be treated with caution. In the present work, the parameters for the LSC perovskite phase and $(La,Sr)_2CoO_4$ were optimized using available experimental data. After optimization, a set of thermodynamic parameters was obtained.

5.2.2 Experiments

In order to verify calculated phase diagrams and to experimentally determine phase stability of LSC, experiments were also carried out in the present work.

I. Sample preparation

Commercial LSC powder from HTAS (synthesized using the glycine–nitrate combustion route) with a composition of $(La_{0.6},Sr_{0.4})_{0.99}CoO_{3-\delta}$ (LSC396) was used as starting material. The LSC powder was pressed into pellets of 12 mm in diameter and 2−5mm in thickness. Some of the pellets were pre-sintered at 1400˚C in air for 5h. During sintering, the pellets were put on top of a Pt sheet to avoid undesired reactions with alumina crucibles. After sintering, the upper surface

of the pellets, i.e. the surface exposed to air, was further polished. A few samples were kept as reference.

II. Heat treatments

Except for the reference samples, the pre-sintered and as pressed pellets were heat treated under different conditions, as following:

1) at 1250˚C in air or in N_2 for 100h;
2) at 1000˚C in air or in N_2 for 1000h;
3) at 700˚C in air or in N_2 for 2000h.

The oxygen partial pressure in N_2 is close to 10^{-4} bar. Longer annealing time was chosen at low temperature in order to achieve equilibrium.

III. Characterization

After heat treatment, the pellets were characterized using X-Ray Diffraction (XRD) and Scanning Electron Microscopy (SEM).

The surface of the pellets was analyzed with XRD to evaluate formation of secondary phases or reaction products. The XRD data were collected with a Bruker D8 powder diffractometer equipped with a Lynx-eye detector. The XRD scan was carried out at a step size of 0.04° per 5s over a 2θ range of 10 to 90° with a Cu Kα radiation (λ=0.15406 nm). Peak position fittings were determined with the program EVA.

The surface microstructure and element distribution was determined using SEM/EDS. The sample surface was observed first using a TM-1000 electron microscope and afterwards a Zeiss Supra-35 SEM equipped with a field-emission gun and an energy-dispersive X-ray (EDS) spectrometer. EDS analysis was performed using the aforementioned miscroscope in conjunction with Noran System Six software to determine chemical composition of various phases.

5.3 Results and discussion

Table 5.3 lists a set of optimized thermodynamic parameters obtained in the present work for LSC and $(La,Sr)_2CoO_4$. The phase equilibria in the boundary systems were calculated using the present La-Sr-Co-O database. No notable change was found as compared with the result from original works.

Table 5.3 Parameters obtained in the present work for quaternary solid solution phases in La-Sr-Co-O [a]

Phases	Model/parameters
$(La,Sr)_2CoO_4$	$(La^{3+}, Sr^{2+})_2 (Co^{2+}, Co^{4+})_1(O^{2-})_4$
	${}^{o}G^{La_2CoO_4}_{La^{3+}:Co^{2+}:O^{2-}} - 2H^{SER}_{La} - H^{SER}_{Co} - 4H^{SER}_{O} = GLACOO4$
	${}^{o}G^{La_2CoO_4}_{La^{3+}:Co^{4+}:O^{2-}} - 2H^{SER}_{Sr} - H^{SER}_{Co} - 4H^{SER}_{O} = GSRCOO4 - 2GSROSOL + GLA2O3D$
	${}^{o}G^{La_2CoO_4}_{Sr^{2+}:Co^{2+}:O^{2-}} - 2H^{SER}_{Sr} - H^{SER}_{Co} - 4H^{SER}_{O} = GLACOO4 + 2GSROSOL - GLA2O3D$
	${}^{o}G^{La_2CoO_4}_{Sr^{2+}:Co^{4+}:O^{2-}} - 2H^{SER}_{Sr} - H^{SER}_{Co} - 4H^{SER}_{O} = GSRCOO4$
	${}^{0}L^{La_2CoO_4}_{La^{+3},Sr^{2+}:*:O^{2-}} = -82000 - 60T$
Perovskite	$(La^{3+}, Sr^{2+}, Va)_1(Co^{2+},Co^{3+},Co^{4+}, Va)_1(O^{2-}, Va)_3$
	${}^{0}L^{Prv}_{La^{3+},Sr^{+2}:Co^{3+}:*} = -25713.4$
	${}^{1}L^{Prv}_{La^{3+},Sr^{+2}:Co^{3+}:*} = 17774.8$
	${}^{2}L^{Prv}_{La^{3+},Sr^{+2}:Co^{3+}:*} = 41090.7$
	${}^{0}L^{Prv}_{La^{3+},Sr^{+2}:Co^{4+}:*} = 13510.8$
	${}^{1}L^{Prv}_{La^{3+},Sr^{+2}:Co^{4+}:*} = -73293.2$
	${}^{0}L^{Prv}_{La^{3+},Sr^{+2}:Co^{3+}:O^{2-},Va} = 11792.1$
	${}^{0}L^{Prv}_{La^{3+},Sr^{+2}:Co^{4+}:O^{2-},Va} = -823830.6$
Functions	$GLACOO4 = -2095975.55 + 951.680046T - 167.49T\ln(T) - 0.010645T^2 + 938000T^{-1}$
	$GSRCOO4 = -1591501.7 + 876.17T - 149.513T\ln(T) - 0.031876T^2 + 386659.81T^{-1}$
	$GSROSOL = -607870 + 268.9T - 47.56T\ln(T) - 0.00307T^2 + 190000T^{-1}$
	$GLA2O3D = -1835600 + 674.72T - 118T\ln(T) - 0.008T^2 + 620000T^{-1}$

[a] All parameters are in SI units: J, mol, K and Pa.

5.3.1 Thermodynamic properties

Based on the thermodynamic database obtained in this work, thermodynamic properties for various phases in La-Sr-Co-O can be calculated. Fig. 5.1a illustrated the calculated Gibbs energy of formation for $La_{1-x}Sr_xCoO_{3-\delta}$ in comparison with the result from Calle-Vallejo *et al.* [28], who reported the Gibbs energy of formation from the elements at 298 K for $La_{1-x}Sr_xCoO_{3-\delta}$ (x=0.25, 0.5, 0.75) from first-principle calculations. The CALPHAD calculated values from this work are lower than those reported by Vallejo *et al.*, but the difference is within the uncertainty range for first

principle calculations [28]. Fig. 5.1b shows the calculated enthalpy of formation for $La_{1-x}Sr_xCoO_{3-\delta}$ at 298 K from elements. It can be concluded from Fig. 5.1 that the stability of LSC decreases with increasing Sr content.

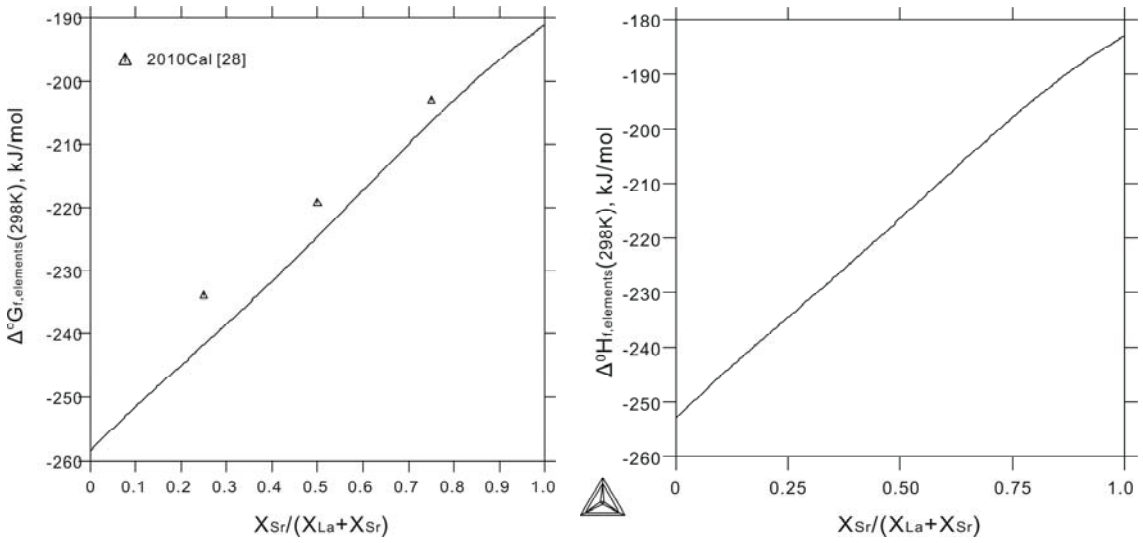

(a) (b)

Fig. 5.1. Calculated a) Gibbs energy of formation and b) enthalpy of formation for $La_{1-x}Sr_xCoO_{3-\delta}$ from elements at 298K from the present work. The results from Calle-Vallejo *et al.* [28] from first principle calculations were included for comparison.

5.*3.2* *Phase diagrams*

Petrov *et al.* [29] reviewed phase equilibria, defect structure, and charge transfer properties in doped lanthanum cobaltites. For $La_{1-x}Sr_xCoO_{3-\delta}$, the phase equilibria were reported by Cherepanov *et al.* [30] at 1100°C. An 1100°C isothermal section of the pseudoternary system La_2O_3-SrO-CoO in air was constructed [30]. Fig. 5.2 presents the calculated isothermal section of the pseudoternary system La_2O_3-SrO-CoO at 1100°C in air in comparison with the experimental data. The calculated phase diagram agrees well with most of the experimental datapoints. Cherepanov *et al.* [30] also investigated phase equilibria at low oxygen pressure. Their results were in contradiction with those reported by Saal [6]. In addition, Cherepanov *et al.* [30] were unable to distinguish the Sr_xCoO_y oxides ($Sr_6Co_5O_{15}$, $Sr_2Co_2O_5$ and $SrCoO_{3-\delta}$). Their results for low oxygen pressure are probably less reliable.

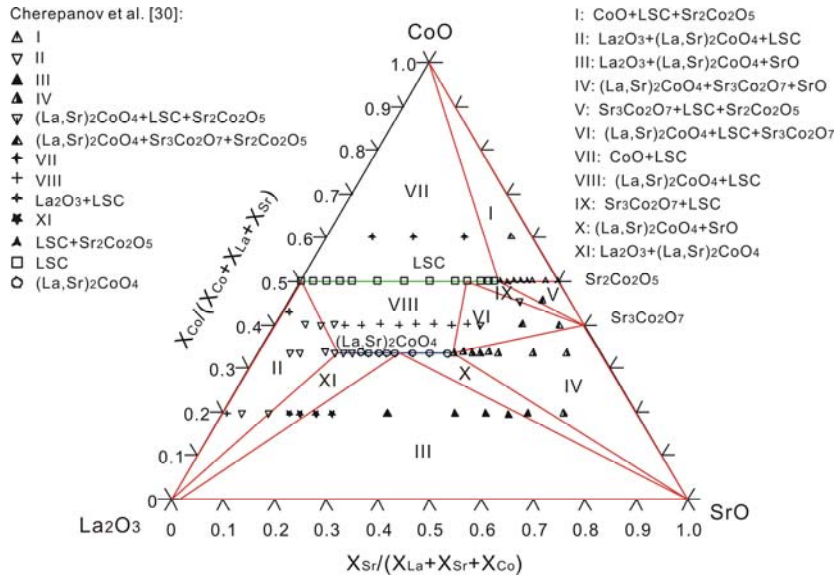

Fig. 5.2. Calculated isothermal section of La_2O_3-SrO-CoO in air at 1100°C based on the parameters obtained in the present work.

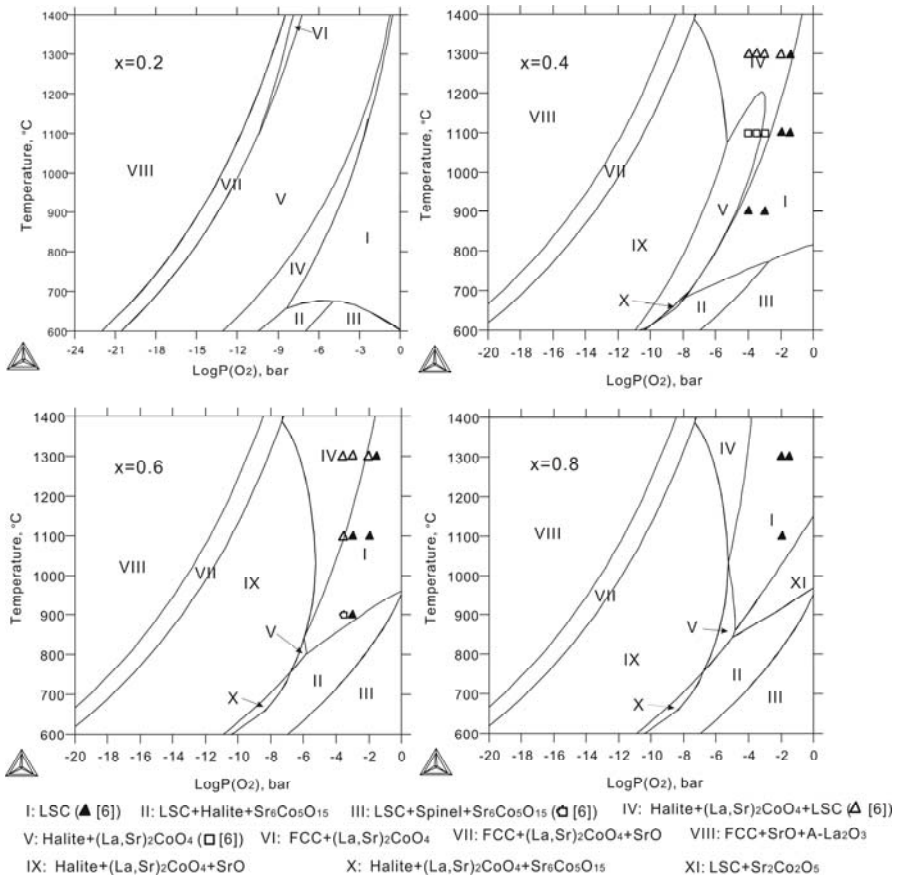

Fig. 5.3. Calculated stability phase diagrams of $La_{1-x}Sr_xCoO_y$ based on the database obtained in the present work with experimental data included.

Figs. 5.3−5.4 present the calculated phase diagrams of $La_{1-x}Sr_xCoO_y$ based on the database obtained in the present work with experimental data included. As shown in Fig. 5.3, the phase relations in La-Sr-Co-O varies with changing either temperature or oxygen partial pressure. The stability region for single-phase LSC is limited by formation of various secondary phases, $(La,Sr)_2CoO_4$ at low oxygen partial pressure, $Sr_6Co_5O_{15}$ at low temperature, or $Sr_2Co_2O_5$ at high Sr content. Several groups of authors have experimentally studied the phase stability of LSC by XRD and SEM [6−8]. Saal [6] studied stability of LSC at 900°C, 1100°C and 1300°C under various PO_2. Powder samples were heated for 3−30 days at different conditions. The result shows that LSC is not stable at high Sr content and low PO_2. Different secondary phases were observed at different temperatures. As shown in Fig. 5.3 and 5.4, the calculated phase diagrams from this work agree with most of Saal's results. Morin *et al.* [7] investigated decomposition of $La_{0.5}Sr_{0.5}CoO_{3-\delta}$ (LSC50) at 1200°C−1425°C and low oxygen pressure using high-temperature X-ray diffraction (HT-XRD). They also reported that single-phase perovskite can only be obtained at a strict A:B ratio of 1:1. As shown in Fig. 5.4, with increasing temperature, the LSC50 perovskite (Region I) decomposes into a mixture of $(La,Sr)_2CoO_4$ and halite (Region IV). The transition temperature corresponds to the boundary line between these two regions. The reported transition temperatures from Morin *et al.* [7] are about 100 °C higher than the reported by Saal [6]. The decrepancy could be caused by sluggish reaction kinetics in the HT-XRD measurements or less accuracy control of the oxygen partial pressure during experiments. Ovenstone *et al.* [8] investigated phase transition/decomposition of $La_{1-x}Sr_xCoO_{3-\delta}$ (x=0.7, 0.4, 0.2) at low oxygen partial pressure using HT-XRD. Decomposition of the perovskite into $(La,Sr)_2CoO_4$, CoO and $Sr_2Co_2O_5$ was reported.

In addition to thermodynamic modeling, experimental investigations were also carried out in this work to determine phase stability of LSC and further verify calculated phase diagrams. Three temperatures were chosen for the experimental study: 1250°C (typical sintering temperature for LSC cathodes for SOFCs), 1000°C and 700°C (the latter is a typical operating temperatures for SOFCs with LSC cathodes). The experimentally determined phase stability in comparison with the calculations is presented in Fig. 5.5 and in Table 5.4.

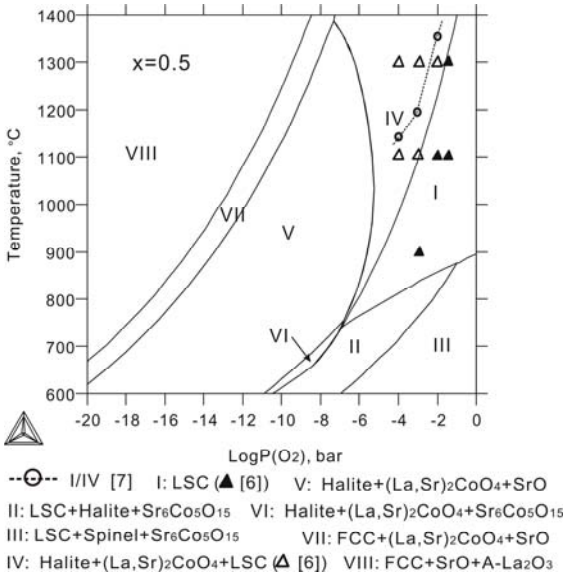

Fig. 5.4. Calculated stability phase diagram of $La_{0.5}Sr_{0.5}CoO_y$ based on the database obtained in the present work in comparison with experimental data.

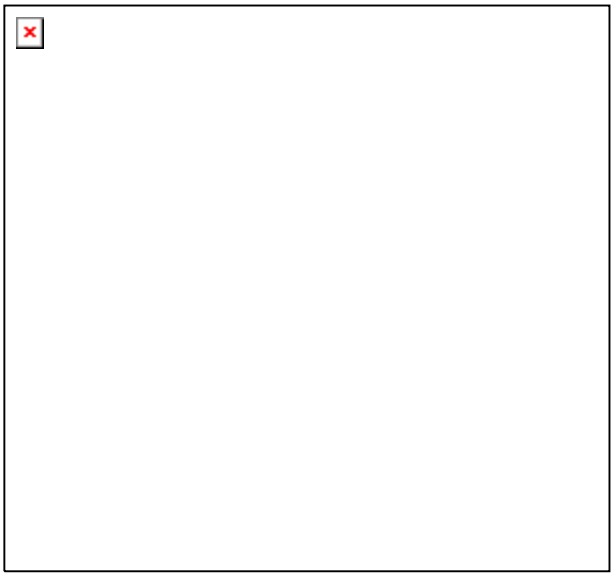

Fig. 5.5. Calculated stability phase diagram of $(La_{0.6}Sr_{0.4})_{0.99}CoO_y$ based on the database obtained in the present work in comparison with experimental data.

Table 5.4 Identified phases for the pellet samples studied in this work.

Sample name	Pre-sintering at 1400°C in air for 5 hours and polishing of the upper surface	Heat treatment	Phases identified by XRD	Phases identified by SEM&EDS
1	Yes	1250˚C in air for 100h	LSC	LSC
2	No	1250˚C in air for 100h	LSC	LSC
3	Yes	1250˚C in N_2 for 100h*	LSC+$(La,Sr)_2O_4$+halite	LSC+$(La,Sr)_2O_4$+halite
4	No	1250˚C in N_2 for 100h	LSC+$(La,Sr)_2O_4$+halite	LSC+$(La,Sr)_2O_4$+halite
5	Yes	1000˚C in air for 1000h	LSC+$Sr_3(PO_4)_2$	LSC + $Sr_3(PO_4)_2$+CoO_x
6	No	1000˚C in air for 1000h	LSC	LSC
7	Yes	1000˚C in N_2 for 1000h	LSC+$Sr_3(PO_4)_2$	LSC+$Sr_3(PO_4)_2$+ CoO_x
8	No	1000˚C in N_2 for 1000h	LSC+$(La,Sr)_2O_4$+halite	LSC+$(La,Sr)_2O_4$+halite
9	Yes	700˚C in air for 2000h	LSC	LSC
10	No	700˚C in air for 2000h	LSC+$Sr_6Co_5O_{15}$	—
11	Yes	700˚C in N_2 for 2000h	LSC	LSC
12	No	700˚C in N_2 for 2000h	LSC+$Sr_6Co_5O_{15}$	—

*: The oxygen partial pressure in N_2 is close to 10^{-4} bar.

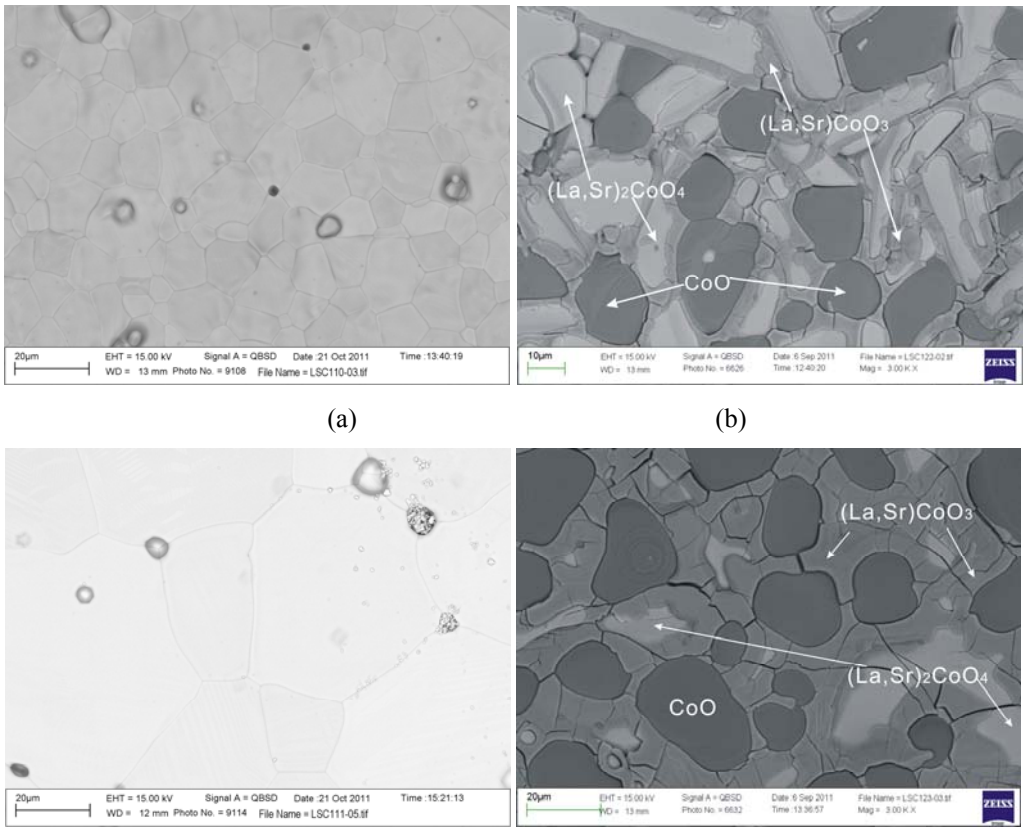

Fig. 5.6. SEM back-scattered images showing the upper surface of the LSC396 pellets anneal at 1250°C for 100 hours. For a) and b), the samples were directly heated from the as-pressed state without any pre-sintering or polishing. a) in air, b) in N_2. The phases were identified according to the EDS results (shown in Table 5.5). For c) and d), before the heat treatment at 1250°C, the pellets were pre-sintered at 1400°C for 5 hours and the upper surface was further polished. c) in air, d) in N_2.

Table 5.5 Compositions of the phases identified in the pellet annealed at 1250°C in N_2 * (Fig. 5.6b)

Phase	La cat.%	Sr cat.%	Co cat.%	Remark
LSC perovskite	16.9	44.7	37.4	EDS
	5.1	44.9	50	calculation
$(La,Sr)_2CoO_4$	42.6	28.4	29.0	EDS
	41.4	25.3	33.3	calculation
CoO			100	EDS
			100	calculation

*: The oxygen partial pressure in N_2 is close to 10^{-4} bar.

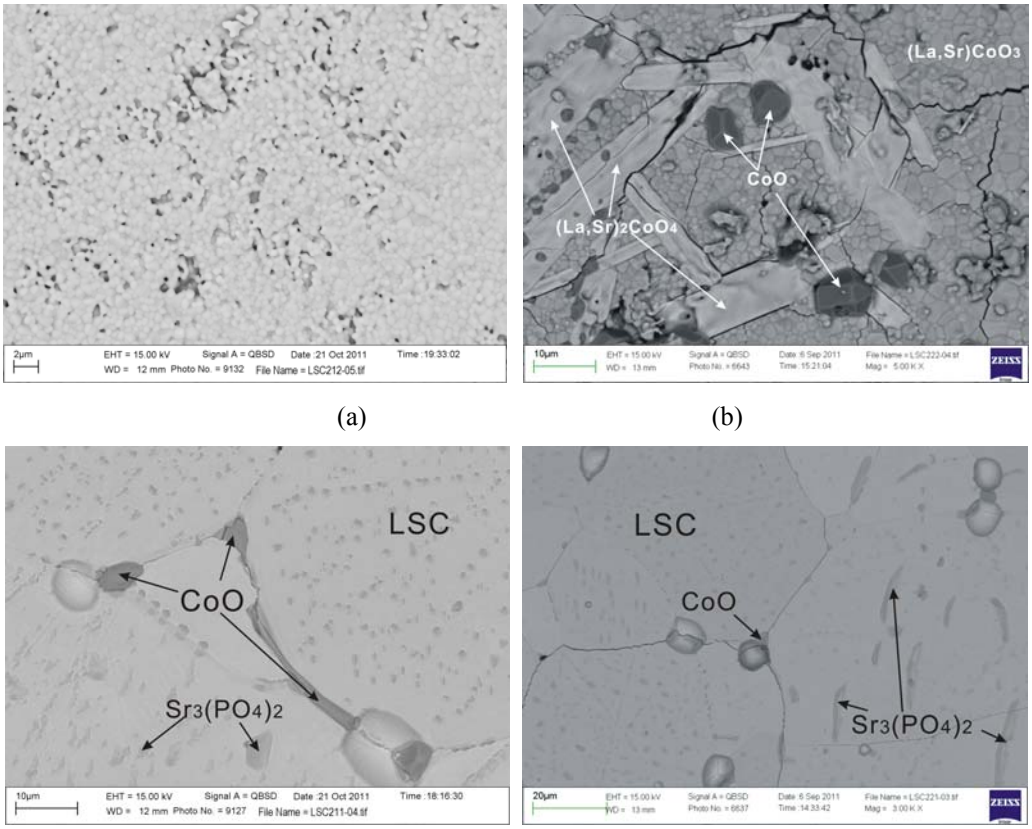

Fig. 5.7. SEM back-scattered images showing the upper surface of the LSC396 pellets anneal at 1000°C for 1000 hours. For a) and b), the samples were directly heated from the as-pressed state without any pre-sintering or polishing. a) in air, b) in N_2. The phases were identified according to the EDS results (shown in Table 5.6). For c) and d), before the heat treatment at 1000°C, the pellets were pre-sintered at 1400°C for 5 hours and the upper surface was further polished. c) in air, d) in N_2.

Table 5.6 Compositions of the phases identified in the pellet annealed at 1000°C in N_2 * (Fig. 5.7b)

Phase	La cat.%	Sr cat.%	Co cat.%	Remark
LSC perovskite	31.8	24.1	44.16	EDS
	16.7	33.3	50	calculation
$(La,Sr)_2CoO_4$	40.6	29.7	29.7	EDS
	38.4	28.3	33.3	calculation
CoO			100	EDS
			100	calculation

*: The oxygen partial pressure in N_2 is close to 10^{-4} bar.

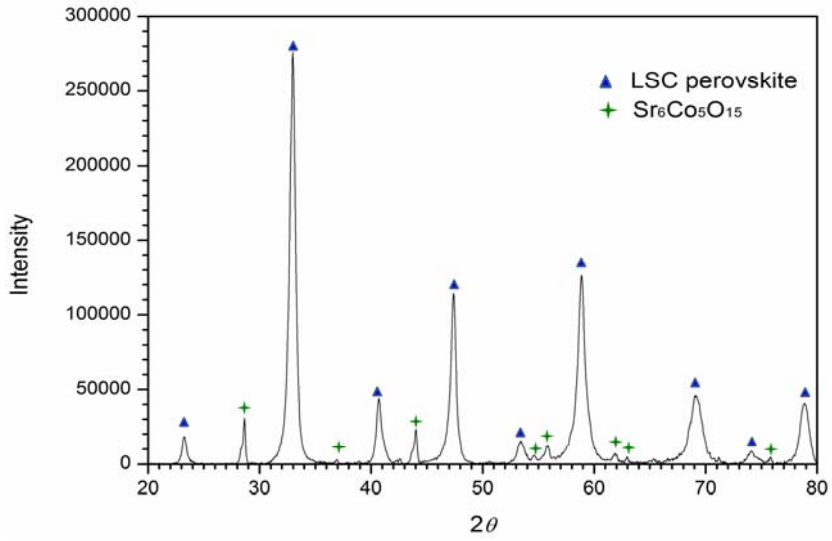

(a)

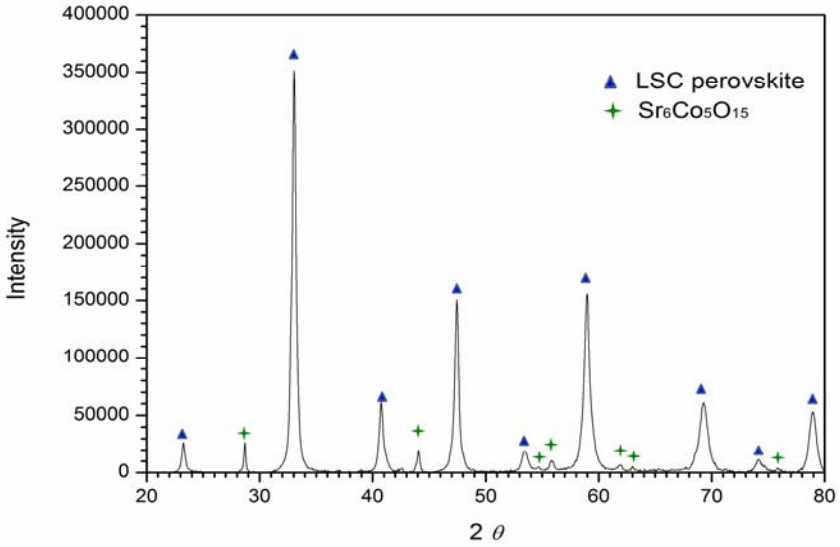

(b)

Fig. 5.8. XRD spectra of the pellets anneal at 700°C for 2000h, a) in air, b) in N_2. The samples were direct heated from the as-pressed state and without any pre-sintering or polishing.

According to the calculated stability diagram of $(La_{0.6}Sr_{0.4})_{0.99}CoO_y$ shown in Fig. 5.5, at 1250°C, LSC396 is stable in air. With lowering oxygen partial pressure, it starts partially decomposing, forming secondary phases of $(La,Sr)_2CoO_4$ and halite. Fig. 5.6 shows SEM back-scattered images on the upper surface of the pellets heat-treated at 1250°C in air or in N_2 for 100h. The compositions of the phases for the sample annealed in N_2 were determined by SEM/EDS and were presented in Table 5.5, together with the calculated ones. The experimental

results in general agree with the calculations. Interestingly, from both EDS and calculation, a significant composition change for the perovskite phase is found. A more Sr-rich perovskite forms on the partial decomposition when the $(La,Sr)_2CoO_4$ and halite phases form. The Co content in LSC perovskite determined from EDS is lower than the calculated one, while the La content is higher than calculated. As claimed by Morin *et al.* [7], the single-phase perovskite can only be obtained at a strict A:B ratio of 1:1. The EDS results are probably less accurate, which may due to the overlap of La and Co X-ray peaks in the EDS spectra. According to Fig. 5.5, LSC396 is stable in air, and starts decomposing at PO_2 around 10^{-4} bar with forming $(La,Sr)_2CoO_4$ and halite. Fig. 5.7 illustrated back-scattered images on the upper surface of the pellets heat-treated at 1000°C in air or in N_2 for 1000h. At this temperature, the decomposition can only be found on the sample directly heated from the as-pressed state and without any pre-sintering or polishing (Fig. 5.7b), but not on the pre-sintered sample (Fig. 5.7d). This is because it is difficult to achieve equilibrium from the sintered dense structure, even after heating at 1000°C for 1000h. Thus great care should be taken when doing stability experiments at low temperatures. The $Sr_3(PO_4)_2$ phase was observed on the pre-sintered sample surface (Fig. 5.7c and d). Phosphorous probably comes from the furnace used for heat treatment. The compositions of the phases for the sample annealed in N_2 were determined by SEM/EDS and are presented in Table 5.6, together with the calculated ones. At 700°C, according to the CALPHAD calculation (Fig. 5.5), the LSC is stable in neither air nor N_2 with coexistence of $Sr_6Co_5O_{15}$ and spinel (minor) phases. The phases are hard to be distinguished using SEM/EDS. Fig. 5.8 presents the XRD results for samples directly heated at 700°C in air or in N_2 for 2000h. The XRD result shows clearly existence of $Sr_6Co_5O_{15}$ phase at these conditions.

Fig. 5.8. presents the calculated "stability window" for LSC at 700°C, 900°C, 1100°C and 1300°C. The perovskite phase is stable at high La content and high oxygen partial pressure. Outside its "stability window", decomposition or partial decomposition of the perovskite phase takes place at low oxygen partial pressure due to formation of the $(La,Sr)_2CoO_4$ phase, at low temperature when $Sr_6Co_5O_{15}$ starts forming, or at high Sr content with formation of $Sr_2Co_2O_5$ at around 1000 −1100°C. (More calculation results can be found in *Appendix B*.)

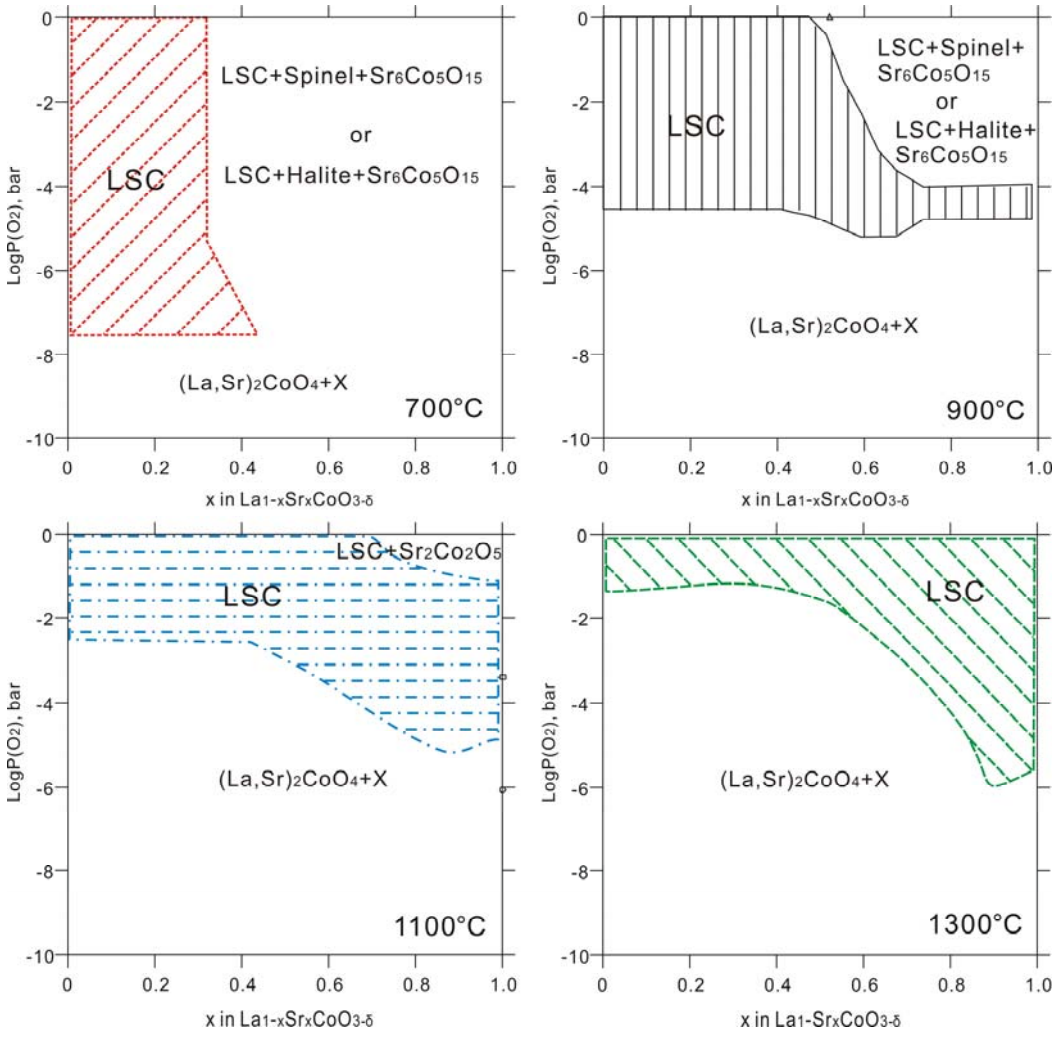

Fig. 5.8. Calculated stability diagram ("stability window") for LSC at different temperatures.

5.3.3 Oxygen non-stoichiometry and defect chemistry

The two end-members of the LSC perovskite, $LaCoO_{3-\delta}$ and $SrCoO_{3-\delta}$, have different oxygen non-stoichiometry schemes. The oxygen non-stoichiometry for the compositions in between has been investigated by many groups [12−18]. Besides composition, external conditions (e.g. T and PO_2) also influence oxygen non-stoichiometry.

Mizusaki *et al.* [12] determined oxygen non-stoichiometry in $La_{1-x}Sr_xCoO_{3-\delta}$ (x=0, 0.1, 0.2, 0.3, 0.5, 0.7) at 300−1000°C and PO_2 = 10^{-5} − 1 atm using thermogravimetry (TG). The low temperature data were not used in the optimization, as according to our calculations the corresponding compositions are outside the perovskite single-phase region. Their results are

presented in Figs. 5.9 and 5.11. Petrov *et al.* [13] studied the oxygen non-stoichiometry of $La_{1-x}Sr_xCoO_{3-\delta}$ ($0<x<0.6$) as a function of temperature (300−1400°C) and oxygen partial pressure (10^{-3} − 1 atm) using TG and coulometric titration and their results are presented in Fig. 5.9c. They also determined the boundaries for the perovskite $La_{0.7}Sr_{0.3}CoO_{3-\delta}$ (LSC30) single-phase region. Lankhorst *et al.* [14] investigated the oxygen non-stoichiometry of $La_{1-x}Sr_xCoO_{3-\delta}$ (x=0.2, 0.4 and 0.7) using high temperature coulometric titration. They further modeled the oxygen non-stoichiometry using an itinerant electron model and the effect of electronic band structure was also discussed. Their results for x=0.7 agree with those from Mizusaki *et al.* [12] at $T\geq$1073K. It should be noted that, from the present calculations, the compositions at high Sr content are located outside the perovskite single-phase region. The presence of secondary phases $Sr_2Co_2O_5$ and $Sr_6Co_5O_{15}$ therefore influences the determined oxygen deficiency. Patrakeev *et al.* [15] measured oxygen non-stoichiometry and conductivity of $La_{0.4}Sr_{0.6}CoO_{3-\delta}$ (LSC60) at 923−1173K and PO_2 of 10^{-5} − 1atm. Their results are summarized in Fig. 5.9f. Sitte *et al.* [16, 17] studied oxygen non-stoichiometry and transport properties of LSC40 and LSC60 by oxygen exchange measurements and presented ionic conductivity as a function of oxygen non-stoichiometry. Kozhevnikov *et al.* [18] measured non-stoichiometry and conductivity of LSC30. Their results differ from those reported by Mizusaki *et al.* [12] and Petrov *et al.* [13], and were not used in the optimization. Søgaard *et al.* [3] studied oxygen non-stoichiometry, structure and transport properties of $(La_{0.6}Sr_{0.4})_{0.99}CoO_{3-\delta}$ (LSC396) and $La_{0.85}Sr_{0.15}CoO_{3-\delta}$ (LSC15) by HT-XRD at various temperature and PO_2. Their results agree with those from Lankhorst *et al.* [14]. Søgaard *et al.* [3] further modeled the oxygen non-stoichiometry using the itinerant electron model. A linear correlation between the electrical conductivity and the oxygen vacancy concentration was obtained for both compositions. Saal [6] determined oxygen non-stoichiometry of $La_{1-x}Sr_xCoO_{3-\delta}$ at high Sr content, where most likely $Sr_6Co_5O_{15}$ or $Sr_2Co_2O_5$ was formed as secondary phase. Their results are illustrated in Fig. 5.10.

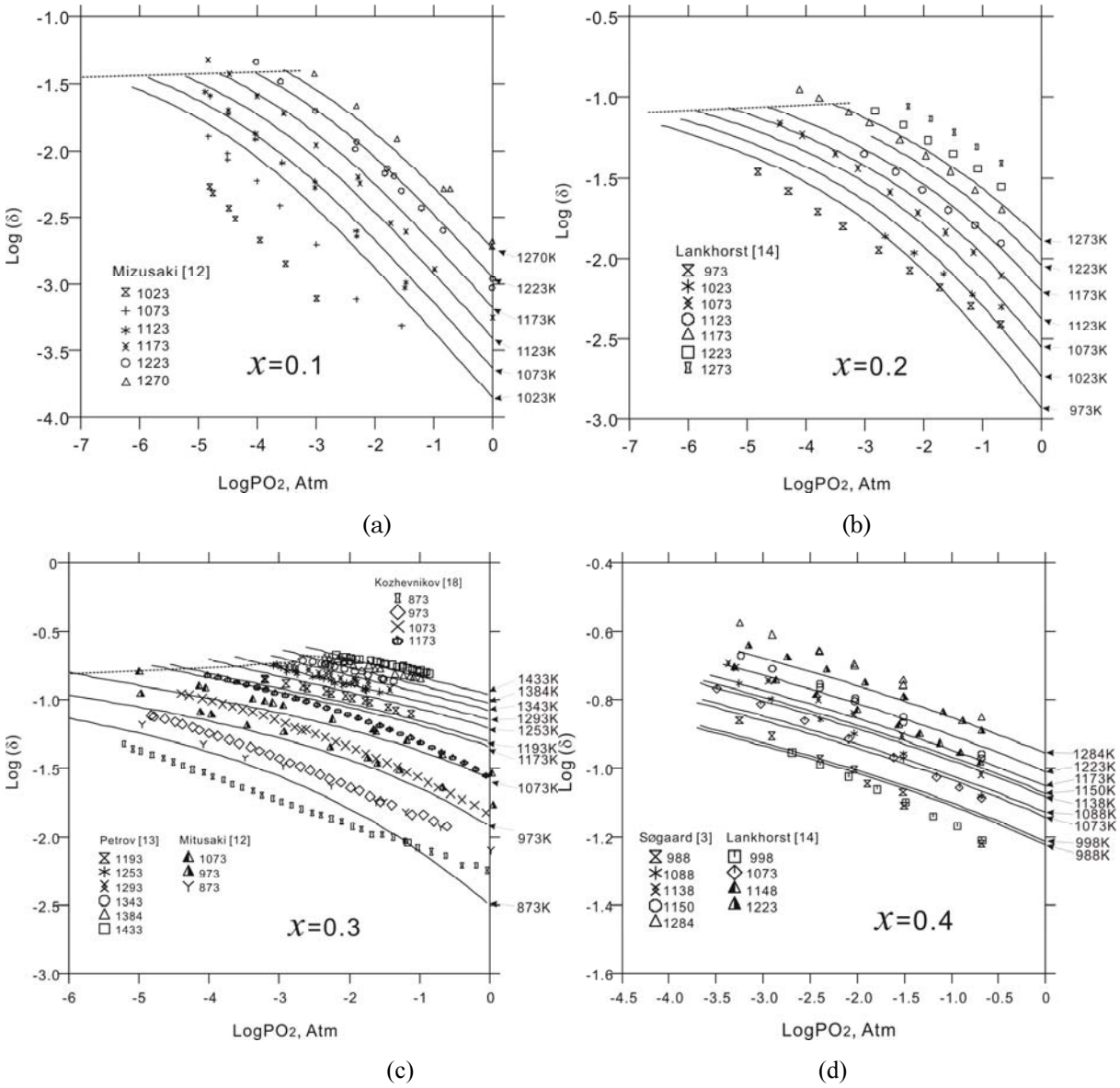
Log (δ)
LogPO2, Atm
Mizusaki [12]
1023
1073
1123
1173
1223
1270
x=0.1
1270K
1223K
1173K
1123K
1073K
1023K
(a)
Lankhorst [14]
973
1023
1073
1123
1173
1223
1273
x=0.2
1273K
1223K
1173K
1123K
1073K
1023K
973K
(b)
Kozhevnikov [18]
873
973
1073
1173
Petrov [13]
1193
1253
1293
1343
1384
1433
Mitusaki [12]
1073
973
873
x=0.3
1433K
1384K
1343K
1293K
1253K
1193K
1173K
1073K
973K
873K
(c)
Søgaard [3]
988
1088
1138
1150
1284
Lankhorst [14]
998
1073
1148
1223
x=0.4
1284K
1223K
1173K
1150K
1138K
1088K
1073K
998K
988K
(d)

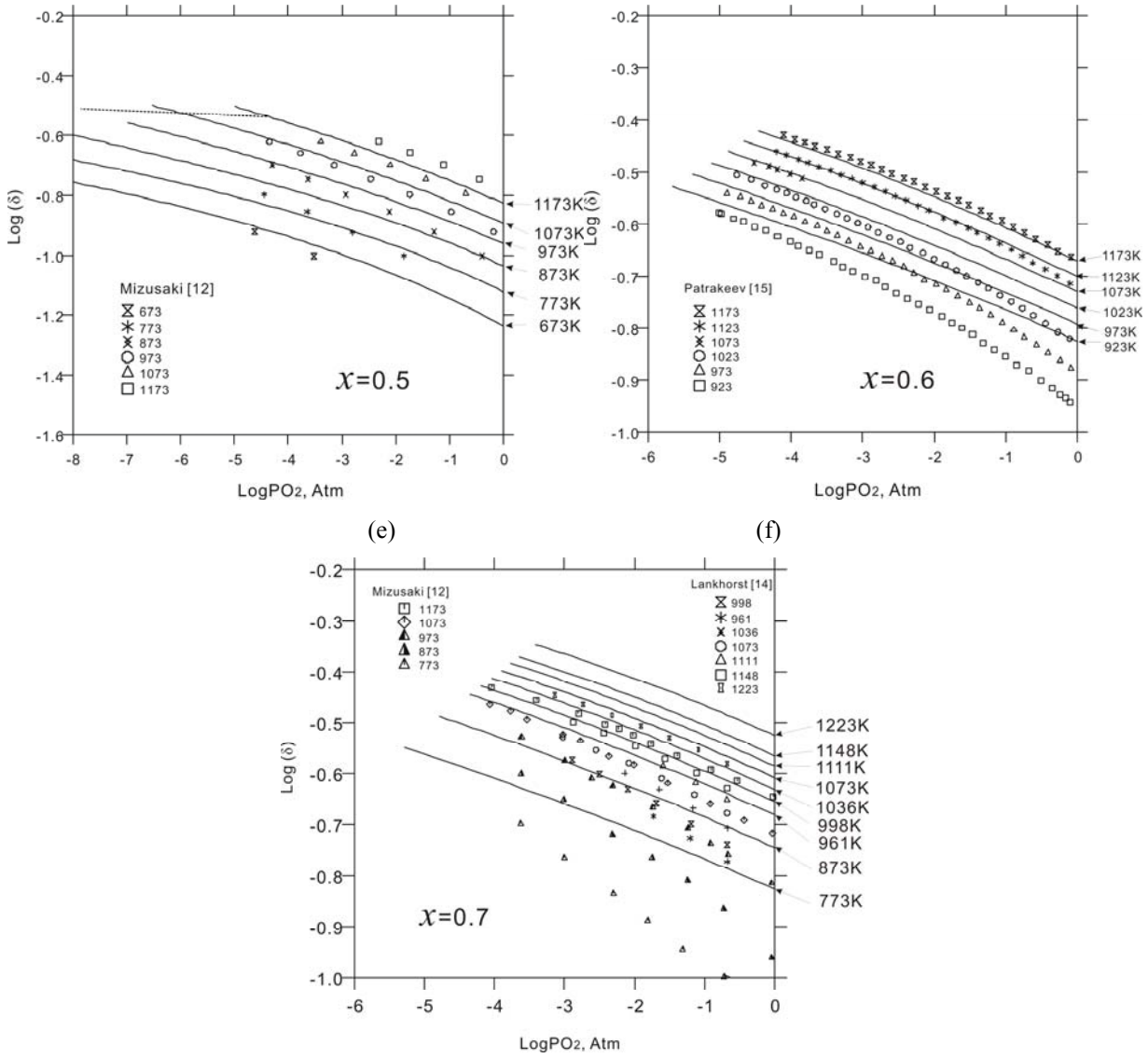

Fig. 5.9. Calculated oxygen non-stoichiometry of $La_{1-x}Sr_xCoO_{3-\delta}$ as a function of oxygen partial pressure at different temperatures in comparison with experimental data from literature. (a) x=0.1, (b) x=0.2, (c) x=0.3, (d) x=0.4, (e) x=0.5, (f) x=0.6, (g) x=0.7.

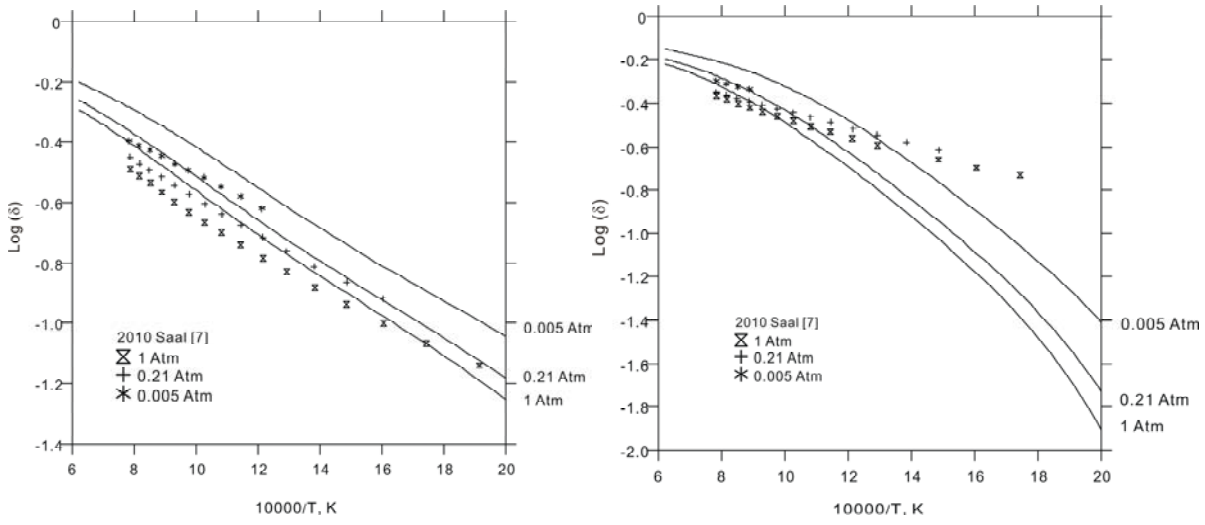

Fig. 5.10. Calculated oxygen non-stoichiometry of $La_{1-x}Sr_xCoO_{3-\delta}$ as a function of temperature at different oxygen partial pressures in comparison with experimental data from literature, (a) x=0.8, (b) x=0.9.

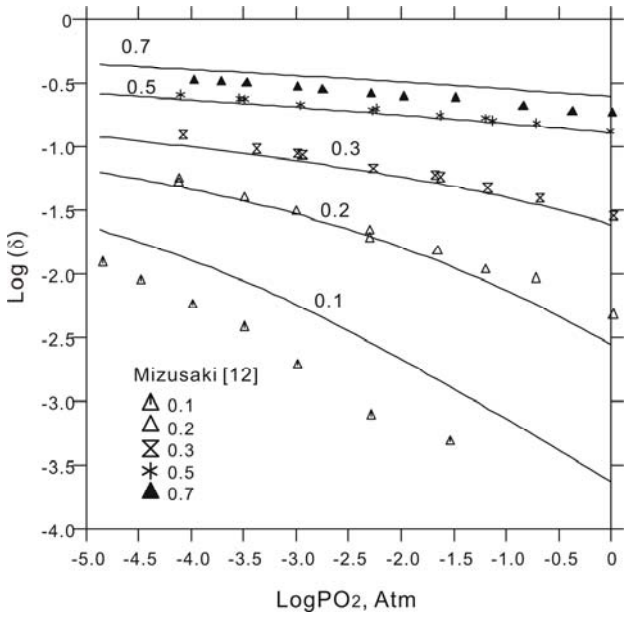

Fig. 5.11. Calculated oxygen non-stoichiometry of $La_{1-x}Sr_xCoO_{3-\delta}$ as a function of oxygen partial pressure at 1073K with different Sr contents in comparison with experimental data from Mizusaki *et al.* [12].

Fig. 5.9−5.11 illustrates the calculated oxygen non-stoichiometry of the LSC perovskite phase in comparison with experimental data from literature. General agreement was achieved between the calculations and the experimental results. It can be concluded that the oxygen deficiency in

LSC increases with increasing Sr content or temperature, or decreasing PO_2. The slope of $\log(\delta)-\log PO_2$ becomes flatter with increasing Sr content (Fig. 5.11). A phase boundary between the perovskite single-phase region and a three-phase mixture of LSC + $(La,Sr)_2CoO_4$ + halite was further implemented onto Fig. 5.9a–c. The partial decomposition reaction of LSC into LSC + $(La,Sr)_2CoO_4$ + halite takes place at $\delta \approx 0.035$ for $La_{0.9}Sr_{0.1}CoO_{3-\delta}$, at $\delta \approx 0.08$ for $La_{0.8}Sr_{0.2}CoO_{3-\delta}$, and at $\delta \approx 0.178$ for $La_{0.7}Sr_{0.3}CoO_{3-\delta}$. The boundary line was calculated to be a straight line for all three compositions.

Beside thermodynamic properties and oxygen non-stoichiometry, the electronic structure of $La_{1-x}Sr_xCoO_{3-\delta}$ perovskite has also drawn a lot of interests, as it influences magnetic properties [31, 32], electronic conductivity and ionic conductivity. Jonker and Van Santen [31] studied the magnetic properties of LSC. Ferromagnetic peroperties were observed at intermediate Sr content, which is attributed to a positive $Co^{3+}-Co^{4+}$ interaction. The Co^{4+} concentration was determined at various Sr contents. Their reported Co^{4+} concentration at high Sr content is however too high, in contradiction with those derived from oxygen non-stoichiometry results. Petrov *et al.* [32] investigated crystal structure, electrical and magnetic properties of LSC. Iodometric titration was used to determine the concentration of Co^{4+} ions.

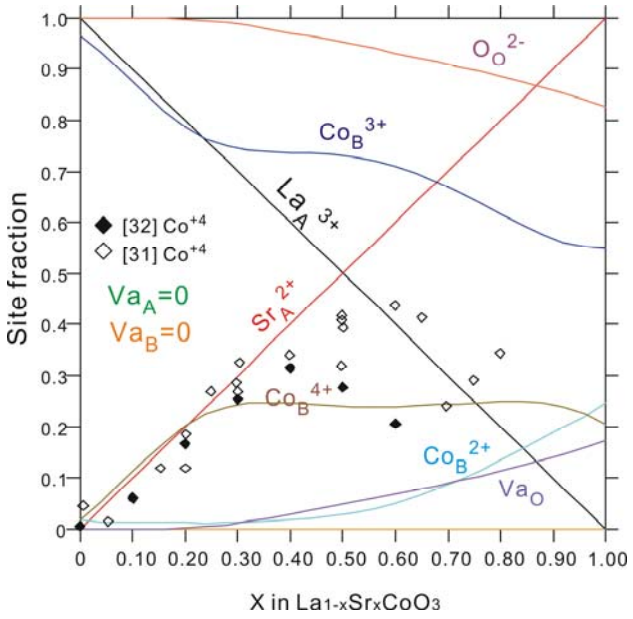

Fig. 5.12. Calculated site fraction of ions in $La_{1-x}Sr_xCoO_{3-\delta}$ at 800°C in air.

Fig. 5.12. shows the calculated site fraction of ions in LSC at 800°C in air with varying Sr content. The experimental data from literatures were not utilized in the optimization. The calculated Co^{4+} concentration agrees well with the experimental results at low Sr content. Deviation starts at x>0.4 (x in $La_{1-x}Sr_xCoO_{3-\delta}$). The experiments may be taken at a mixture-phase region as LSC starts decomposing at high Sr content. According to the calculation, the Co^{4+} concentration shows a linear increase with increasing the Sr content at x < 0.3 (x in $La_{1-x}Sr_xCoO_{3-\delta}$), remains almost constant at x = 0.3−0.9, decreases slightly afterwards. The oxygen vacancy concentration is almost zero at x < 0.2 and starts increasing linearly at x>0.3. This indicates that strontium substitution of lanthanum in $La_{1-x}Sr_xCoO_{3-\delta}$ is compensated by formation of Co^{4+} (instead of Co^{3+}) at low Sr content and further by formation of oxygen vacancies at high Sr content.

5.4 Conclusions

In the present work, the thermodynamic assessment of the La-Sr-Co-O system was performed by applying the CALPHAD method. Thermodynamic and phase diagram data for La-Sr-Co-O in the literature were carefully reviewed. A thermodynamic database of the La-Sr-Co-O system focusing on the oxide part was developed. The resulting database can be used for calculating phase equilibria and thermodynamic properties at temperatures of 298−3000 K and oxygen partial pressure of 10^{-20} − 1 atm using Gibbs energy minimization software. To validate the developed La-Sr-Co-O database, model predicted results on stability of LSC under various conditions were compared with experimental results obtained in the present work. The agreement between the selected experimental data-points and the calculated phase diagram is, in general, good. Our results show that:

1) The phase relation in La-Sr-Co-O varies with changing either temperature and or oxygen partial pressure. The stability region for single-phase LSC was limited by forming various secondary phases, $(La,Sr)_2CoO_4$ at low oxygen partial pressure, $Sr_6Co_5O_{15}$ at low temperature, or $Sr_2Co_2O_5$ at high Sr content.
2) The oxygen deficiency in LSC increases with increasing Sr content or temperature, or decreasing PO_2.
3) Strontium substitution of lanthanum in $La_{1-x}Sr_xCoO_{3-\delta}$ is compensated by formation of Co^{4+} at low Sr content and further by formation of oxygen vacancies at high Sr content.

References

[1] R.J.H. Voorhoeve, Advanced Materials in Catalysis, J. J. Burton and R. L. Garten, Eds., New York, (1977).

[2] K.T. Lee, A. Manthiram, J. Electrochem. Soc., 153 (2006) A794–A798.

[3] M. Søgaard, P.V. Hendriksen, M. Mogensen, F.W. Poulsen, E. Skou, Solid State Ionics 177 (2006) 3285–3296.

[4] P. Ravindran, P. A. Korzhavyi, H. Fjellvag, A. Kjekshus, Phys. Rev. B 60 (1999) 16423–16434.

[5] J. Wu, C. Leighton, Phys. Rev. B 67 (2003) 174408.

[6] J.E. Saal, Thermodynamic modeling of phase transformations and defects: From Cobalt to Doped Cobaltate Perovskites (PhD thesis), The Pennsylvania State University, (2010).

[7] F. Morin, G. Trudel, Y. Denos, Solid State Ionics 96 (1997) 129–139.

[8] J. Ovenstone, J.S. White, S.T. Misture, J. Power Sources 181 (2008) 56–61.

[9] R.H.E. van Doorn, H.J.M. Bouwmeester, A.J. Burggraaf, Solid State Ionics 111 (1998) 263–272.

[10] W.-W Zhang, M. Chen, E. Povoden-Karadeniz, P.V. Hendriken, Thermodynamic modeling of La-Co-O system, paper to be submitted.

[11] W.-W Zhang, M. Chen, Peter Vang Hendriken, Thermodynamic modeling of Sr-Co-O system, un-submitted paper.

[12] J. Mizusaki, Y. Mima, S. Yamauchi, K. Fueki, H. Tagawa, J. Solid State Chem. 80 (1989) 102–111.

[13] A.N. Petrov, V.A. Cherepanov, O.F. Kononchuk, L.Y. Gavrilova, J. Solid State Chem. 87 (1990) 69–76.

[14] M.H.R. Lankhorst, H.J.M. Bouwmeester, H. Verweij, J. Solid State Chem. 133 (1997) 555–567.

[15] M.V. Patrakeev, I.A. Leonidov, E.B. Mitberg, A.A. Lakhtin, V.G. Vasiliev, V.L. Kozhevnikov, K.R. Poeppelmeier, Ionics 5 (1999) 444–449.

[16] W. Sitte, E. Bucher, A. Benisek, W. Preis, Spectrochim. Acta, Part A 57 (2001) 2071–2076.

[17] W. Sitte, E. Bucher, W. Preis, Solid State Ionics 154/155 (2002) 517– 522.

[18] V.L. Kozhevnikov, I.A. Leonidov, E.B. Mitberg, M.V. Patrakeev, A.N. Petrov, K.R. Poeppelmeier, J. Solid State Chem. 172 (2003) 296–304.

[19] A.N. Grundy, B. Hallstedt, L.J. Gauckler, J. Phase Equilib. 22 (2001) 105–113.

[20] A.N. Grundy, B. Hallstedt, L.J. Gauckler, Acta Mater. 50 (2002) 2209–2222.

[21] D. Risold, B. Hallstedt, L.J. Gauckler, CALPHAD, 20 (1996) 353–361.

[22] M. Chen, B. Hallstedt, L.J. Gauckler, J. Phase Equilib. 24 (2003) 212–227.

[23] C.P. Wang, J. Wang, X.J. Liu, I. Ohnuma, R. Kainuma, K. Ishida. J. Alloys Compd. 453 (2008) 174–179.

[24] A.T. Dinsdale, CALPHAD 15 (1991) 317–425.

[25] M. Hillert, J. Alloys Compd. 320 (2001) 161–176.

[26] M. Hillert, B. Jansson, B. Sundman, J. Ågren, Metall. Trans. 16A (1985) 261-266

[27] B. Sundman, Calphad 15 (1991) 109–119.

[28] F. Calle-Vallejo, J.I. Martínez, J.M. García-Lastra, M.Mogensen, J. Rossmeisl, Angew. Chem. Int. Ed. 49 (2010) 7699–7701.

[29] A.N. Petrov, V.A. Cherepanov, A.Y. Zuev, J. Solid State Electrochem. 10 (2006) 517–537.

[30] V.A. Cherepanov, L.Ya. Gavrilova, L.Yu. Barkhatova, V.I. Voronin, M.V. Trifonova, O.A. Bukhner, Ionics 4 (1998) 309–315.

[31] G.H. Jonker, J.H. Van Santen, Physica 19 (1953) 120–130.

[32] A.N. Petrov, O.F. Kononchuk, A.V. Andreev, V.A. Cherepanov, P. Kofstad, Solid State Ionics 80 (1995) 189–199.

Chapter 6

Thermodynamic modeling of the La-Sr-Co-Fe-O system

Abstract

In this research, a thermodynamic database of the La-Sr-Co-Fe-O system was developed based on previously assessed subsystems using the CALPHAD (CALculation of PHAse Diagrams) method, in order to clarify the phase stability of the $La_{1-x}Sr_xCo_{1-y}Fe_yO_{3-\delta}$ (LSCF) perovskite. The phase stability of LSCF was predicted as a function of composition, temperature and oxygen partial pressure. The computed results indicate that the LSCF perovskite tends to decompose with high Sr or Co content, or at elevated temperatures or reduced oxygen partial pressure. In addition to phase stability, other properties of the LSCF perovskite which are crucial for various relevant technological applications, such as oxygen non-stoichiometry, were also modeled and predicted based on the La-Sr-Co-Fe-O database.

6.1 Introduction

$La_{1-x}Sr_xCo_{1-y}Fe_yO_{3-\delta}$ (LSCF) perovskite exhibits good oxide ion and electron conductivity and electro-catalytic activity at T < 800 °C [1] and is one of the most studied solid oxide fuel cell (SOFC) cathode materials today. It also exhibits high oxygen permeability and is widely used as an oxygen separation membrane material [2]. However, the stability of the LSCF material is a critical issue, which may cause degradation during long-term operation. Natile *et al.* [3] reported formation of La_2CoO_4 and Co metal after reduction of LSCF in H_2 at 800 °C. Hashimoto and Kuhn *et al.* [4, 5] studied the oxygen non-stoichiometry and phase stability of $La_{0.6}Sr_{0.4}Co_{1-y}Fe_yO_{3-\delta}$ (y=0.2, 0.4, 0.5, 0.6 and 0.8), and found that $La_{0.6}Sr_{0.4}Co_{1-y}Fe_yO_{3-\delta}$ decomposed completely at low oxygen partial pressure, forming the A_2BO_4 phase and CoO. They concluded that the stability of $La_{0.6}Sr_{0.4}Co_{1-y}Fe_yO_{3-\delta}$ decreases with increasing Co content.

Present knowledge about phase equilibria in the La-Sr-Co-Fe-O system remains very fragmentary. This research was aimed at achieving a comprehensive understanding of the phase equilibria in La-Sr-Co-Fe-O at various oxygen partial pressures (from 10^{-20} to 10^{0} bar), temperatures (from 300K to 3000K) and for various compositions. For this, a thermodynamic database of La-Sr-Co-Fe-O is needed. This research has established a thermodynamic database for the multicomponent La-Sr-Co-Fe-O system based on previously assessed subsystems [6−19] using the CALPHAD (CALculation of PHAse Diagrams) method. Based on the current database, various properties for the perovskite phase which are crucial for relevant technological applications, such as thermodynamic properties, cation distribution and oxygen non-stoichiometry, can be modeled and predicted.

6.2 CALPHAD modeling

The modeling of the La-Sr-Co-Fe-O system was based on recently assessed subsystems (Table 6.1). The lattice stability for pure elements was adopted from Dinsdale [20]. Compound Energy Formalism (CEF) [21], which is widely used in CALPHAD assessments [22, 23], was introduced to describe the Gibbs energy for all the phases in La-Sr-Co-Fe-O. CEF was developed to describe phases using sublattices. The CEF models for phases in La-Sr-Co-Fe-O are listed in Table 6.2. The Gibbs energy descriptions for the perovskite phase and other relevant phases have been discussed in previous chapters (*Sections 2.3, 3.3* and *4.3*).

Due to the lack of experimental data in La-Sr-Co-Fe-O, ideal extrapolation was applied to most of the solution phases except for the perovskite phase, where its interaction parameters were optimized using oxygen non-stoichiometry data. Table 6.3 lists the optimized interaction parameters in this research.

Table 6.1 References for assessed subsystems used in this research

System	References
La-O	Grundy *et al*. [6] [7]
Sr-O	Risold *et al*. [8]
Co-O	Chen *et al*. [9]
Fe-O	Sundman [10], Kjellqvist *et al*. [11]
La-Co	Wang *et al*. [12]
Co-Fe	Ohnuma *et al*. [13]
La-Sr-O	Grundy *et al*. [7]
La-Co-O	Zhang *et al*. [14]
La-Fe-O	Povoden-Karadeniz *et al*. [15]
Sr-Co-O and Sr-Co-Fe-O	Zhang *et al*. [16]
Sr-Fe-O and La-Sr-Fe-O	Povoden-Karadeniz *et al*. [17]
Co-Fe-O	Zhang *et al*. [18]
La-Sr-Co-O	Zhang *et al*. [19]

Table 6.2 Phases and models for the La-Sr-Co-Fe-O system

Phase	Description	Model	References
Liquid	Ionic liquid phase	$(La^{3+},Sr^{2+},Co^{2+},Co^{3+},Fe^{2+},Fe^{3+})_p(O^{2-},Va)_q$	[6−13]
$La_{1-x}Sr_xCo_{1-y}Fe_yO_{3-\delta}$	Perovskite	$(La^{3+},Sr^{2+},Va)_1(Co^{2+},Co^{3+},Co^{4+},Fe^{2+},Fe^{3+},Fe^{4+},Va)(O^{2-},Va)_3$	[14−17]
$(La,Sr)_2(Co,Fe)O_4$	La_2CoO_4-Sr_2FeO_4 solid solution phase	$(La^{3+},Sr^{2+})_2(Co^{2+},Co^{4+},Fe^{4+})_1(O^{2-})_4(O^{2-},Va)_1$	[17, 19]
A-$(La,Sr)_2O_3$	Hexagonal La_2O_3 with Sr solubility	$(La^{2+},La^{3+},Sr^{2+})_2(O^{2-},Va)_3$	[6]
H-$(La,Sr)_2O_3$	Partially ordered hexagonal La_2O_3 with Sr solubility	$(La^{3+},Sr^{2+})_2(O^{2-},Va)_3$	[7]
X-$(La,Sr)_2O_3$	Cubic La_2O_3 with Sr solubility	$(La^{3+},Sr^{2+})_2(O^{2-},Va)_3$	[7]
(Sr,La)O	SrO with La solubility	$(La^{3+},Sr^{2+},Va)_1(O^{2-})_1$	[7]
SrO_2	Stoichiometric compound	$(Sr^{4+})_1(O^{2-})_2$	[8]
$(Co,Fe)_3O_4$	Spinel	$(Co^{2+},Co^{3+},Fe^{2+},Fe^{3+})_1(Co^{2+},Co^{3+},Fe^{2+},Fe^{3+},Va)_2(O^{2-})_4$	[18]

(Co,Fe)O	Halite	$(Co^{2+}Fe^{2+},Fe^{3+},Va)_1 (O^{2-})_1$	[9,10]
Fe_2O_3	Corundum	$(Fe^{2+},Fe^{3+})_2(Fe^{3+},Va)_1 (O^{2-})_3$	[10]
La_4SrO_7	Beta phase	$(La^{3+},Sr^{2+})_2(O^{2-},Va)_3$	[6]
$La_4Sr_3O_9$	Stoichiometric compound	$(La^{3+})_4(Sr^{2+})_3(O^{2-})_9$	[7]
$La_4Co_3O_{10}$	Stoichiometric compound	$(La^{3+})_4(Co^{2+})_1(Co^{3+})_2(O^{2-})_{10}$	[14]
$Sr_6Co_5O_{15}$	Stoichiometric compound	$(Sr^{2+})_6(Co^{4+})_4(Co^{2+})_1 (O^{2-})_{15}$	[16]
$Sr_2Co_2O_5$	Brownmillerite	$(Sr^{2+})_2(Co^{2+})_1 (Co^{4+})_1 (O^{2-})_5$	[16]
$Sr_3Co_2O_7$	$Sr_3Co_2O_7$ compound	$(Sr^{2+})_1(Sr^{2+})_2(Co^{3+})_2(O^{2-}, Va)_6 (O^{2-})_1$	[16]
$(Sr,La)_3(Fe,Co)_2O_7$	$Sr_3Fe_2O_7$ with La and Co solubility	$(La^{3+},Sr^{2+})_1(La^{3+},Sr^{2+})_2(Co^{3+},Fe^{3+},Fe^{4+})_2 (O^{2-}, Va)_6 (O^{2-})_1$	[16,17]
$(La,Sr)_3Fe_2O_7$	$(La,Sr)_3Fe_2O_7$ solid solution	$(Sr^{2+})_1(La^{3+},Sr^{2+})_2(Fe^{3+},Fe^{4+})_2(O^{2-})_6 (O^{2-})_1$	[17]
$(Sr,La)_4Fe_3O_{10}$	$Sr_4Fe_3O_{10}$ with La solubility	$(La^{3+},Sr^{2+})_1(La^{3+},Sr^{2+})_3(Fe^{3+},Fe^{4+})_3(O^{2-}, Va)_9(O^{2-})_1$	[17]
$(Sr,La)_4Fe_6O_{13}$	$Sr_4Fe_6O_{13}$ with La solubility	$(La^{3+},Sr^{2+})_4(Fe^{3+})_4(Co^{3+}, Fe^{2+},Fe^{3+},Fe^{4+})_2(O^{2-})_{12} (O^{2-},Va)_2$	[17]
$(Sr,La)Fe_{12}O_{19}$	$SrFe_{12}O_{19}$ with La solubility	$(La^{3+},Sr^{2+})_1(Fe^{2+},Fe^{3+})_1(Fe^{3+})_{11}(O^{2-})_{19}$	[17]
FCC	Metallic La-Co-Fe FCC phase with Sr, O solubility	$(La, Sr,Co,Fe)_1(O, Va)_1$	[6,9,11−13, 15]
BCC	Metallic La-Fe BCC phase with Sr, Co, O solubility	$(La, Sr,Co,Fe)_1(O, Va)_3$	[9, 11, 12,14]
HCP	Metallic Co HCP phase with Fe, O solubility	$(Co,Fe)_1(O, Va)_{0.5}$	[9, 11, 13]
DHCP	Metallic La DHCP phase with O solubility	$(La)_1(O, Va)_{0.5}$	[6]

Table 6.3 Parameters obtained in the present research for the perovskite phase

Parameters	Values
${}^0L^{Perovskite}_{La^{3+},Sr^{+2}:Co^{2+},Fe^{3+}:*}$	−54643.7
${}^0L^{Perovskite}_{La^{3+},Sr^{+2}:Co^{3+},Fe^{3+}:*}$	18971.3
${}^0L^{Perovskite}_{La^{3+},Sr^{+2}:Co^{4+},Fe^{3+}:*}$	−131664.6

6.3 Results and discussion

For the CALPHAD assessment, the phase equilibria in the boundary systems were calculated using the present La-Sr-Co-Fe-O database. No notable change was found as compared with the results in the original work, which can be found in the literature listed in Table 6.1.

6.3.1 Thermodynamic properties

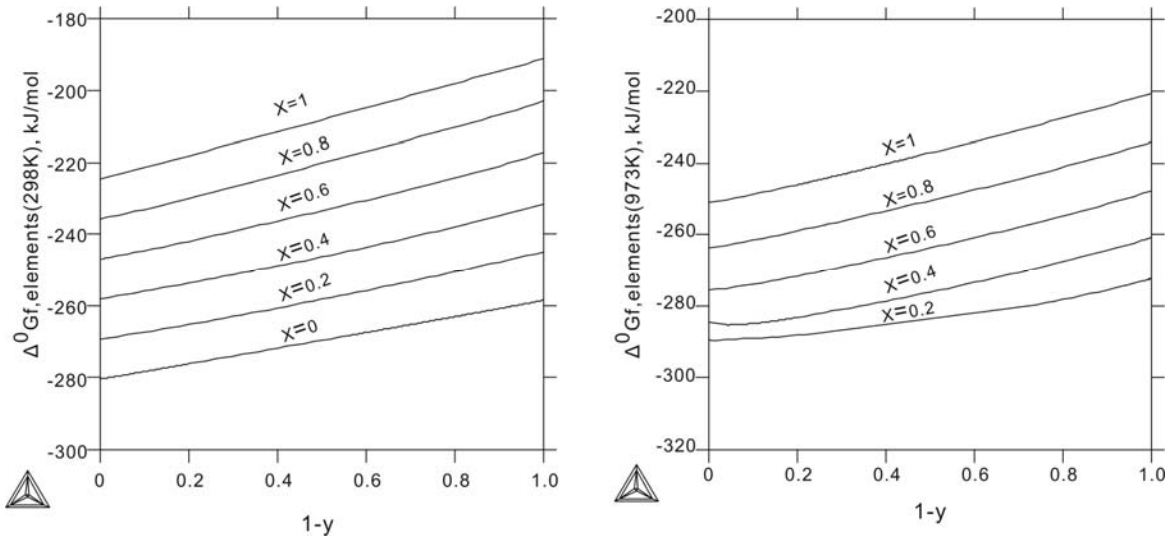

(a) (b)

Fig. 6.1. Calculated Gibbs energy of formation for the $La_{1-x}Sr_xCo_{1-y}Fe_yO_{3-\delta}$ perovskite phase from elements at a) 298K. b) 973K.

Based on the thermodynamic database obtained in this research, the thermodynamic properties can be calculated. Fig. 6.1 plots the calculated Gibbs energy of formation for the LSCF perovskite from elements at two different temperatures and various compositions. At both temperatures, the Gibbs energy of formation increases (i.e. less negative = less stable) with increasing Sr or Co content. With increasing temperature, the Gibbs energy of formation becomes more negative (= more stable) due to the entropy contribution. These results indicate that the stability of LSCF decreases with increasing Sr or Co content.

Sr is a very active element in LSCF. It tends to segregate on the surface of LSCF. When LSCF is employed as an SOFC cathode on a bi-layer CGO−YSZ electrolyte, Sr may diffuse through the porous CGO layer and reach the YSZ surface forming Sr zirconate [24]. Oh *et al.* [25] examined the surface of LSCF pellets after heat treatment in a temperature range of 600–900 °C using scanning electron microscopy (SEM), auger electron spectroscopy (AES) and transmission electro-

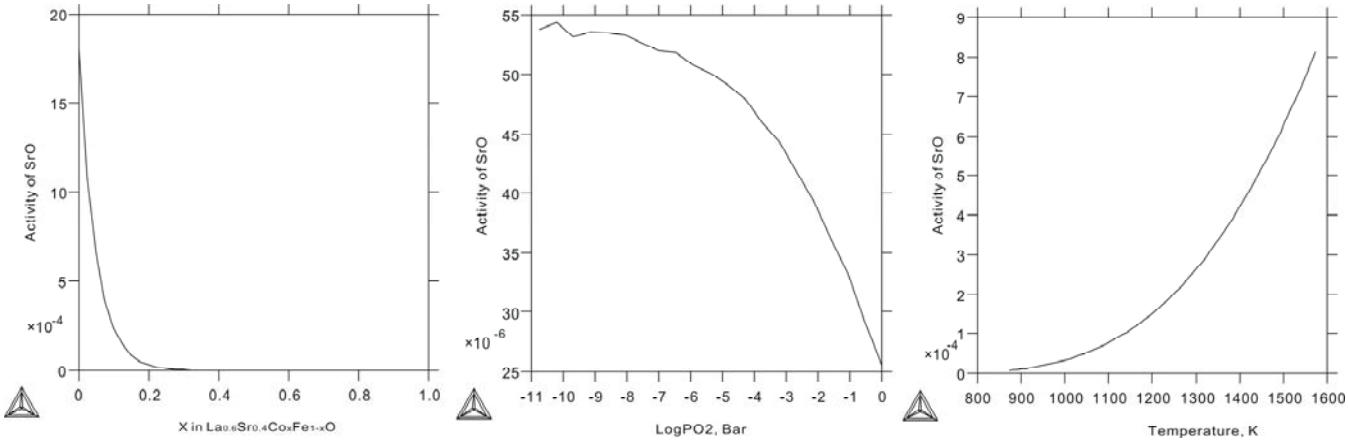

(a) (b) (c)

Fig. 6.2 Calculated activity of SrO in the perovskite phase: a) with varying the Co content in $La_{0.6}Sr_{0.4}Co_yFe_{1-y}O_{3-\delta}$ at 700°C, (b) with varying oxygen partial pressure for $La_{0.6}Sr_{0.4}Co_{0.2}Fe_{0.8}O_{3-\delta}$ at 700°C, (c) with varying temperature for $La_{0.6}Sr_{0.4}Co_{0.2}Fe_{0.8}O_{3-\delta}$ in air. The reference state was chosen as solid SrO.

n microscopy (TEM). Sr-rich precipitate was observed. The amount of Sr-rich precipitate was found to increase with increasing temperature or oxygen partial pressure. Fig. 6.2 plots the activity of SrO in the perovskite phase in different conditions. Our calculations show that the SrO activity increases with decreasing Co content or increasing temperature, or decreasing oxygen partial pressure. Fig. 6.2b disagrees with the result of Oh *et al.* [25]. This is probably because the formation of Sr-rich precipitates is directly related to the partial pressures of Sr-containing gas species, which are determined by both the SrO activity and the oxygen partial pressure.

6.*3.2* *Phase stability of LSCF*

The phase diagrams for LSCF at various temperatures and oxygen partial pressures are presented in Figs. 6.3 and 6.4. At 700°C, the perovskite phase is stable with high La and Fe content, while at the "$SrCoO_x$" corner it exists as a 3-phase mixture of "perovskite + $Sr_6Co_5O_{15}$ + halite (CoO)". In this 3-phase region, the majority is perovskite and $Sr_6Co_5O_{15}$, while the amount of Co-rich halite phase is very small (around 1 mol %). The calculation is further supported by the XRD result for the $(La_{0.6}Sr_{0.4})_{0.99}CoO_{3-\delta}$ pellet heat treated at 700°C in air (*Chapter 5*, Fig. 5.8a), which clearly shows the existence of perovskite+$Sr_6Co_5O_{15}$. The diagram at PO_2=1Pa (Fig. 3b) is similar to the one in air, except that the perovskite single-phase region enlarges slightly. This is in accordance with the stability of the perovskite phase in the Sr-Co-O system (cf. Fig. 4.3 in *Chapter 4*). At 1100°C in air (Fig. 6.4a), the perovskite phase is stable except at the "$SrCoO_x$" corner, where it coexists with $Sr_2Co_2O_5$ (brownmillerite). In this two-phase region, the amount of

the perovskite phase decreases with increasing Sr or Co content. At PO_2=1Pa (Fig. 6.4b), the perovskite phase is much less stable. Several three- and four-phase regions exist on the Co-rich part of the diagram. In these regions, the perovskite phase coexists with halite or (La, Sr)$_2$(Co, Fe)O_4 or (La, Sr)$_3$(Co, Fe)$_2O_7$. A second perovskite phase (LSCF′) may also form, which is richer in Sr and Co than LSCF. Experimental investigations on the stability of LSCF with a composition of $La_{0.58}Sr_{0.4}Co_{0.2}Fe_{0.8}O_{3-\delta}$ were also carried out and the results are presented in *Chapter 7*.

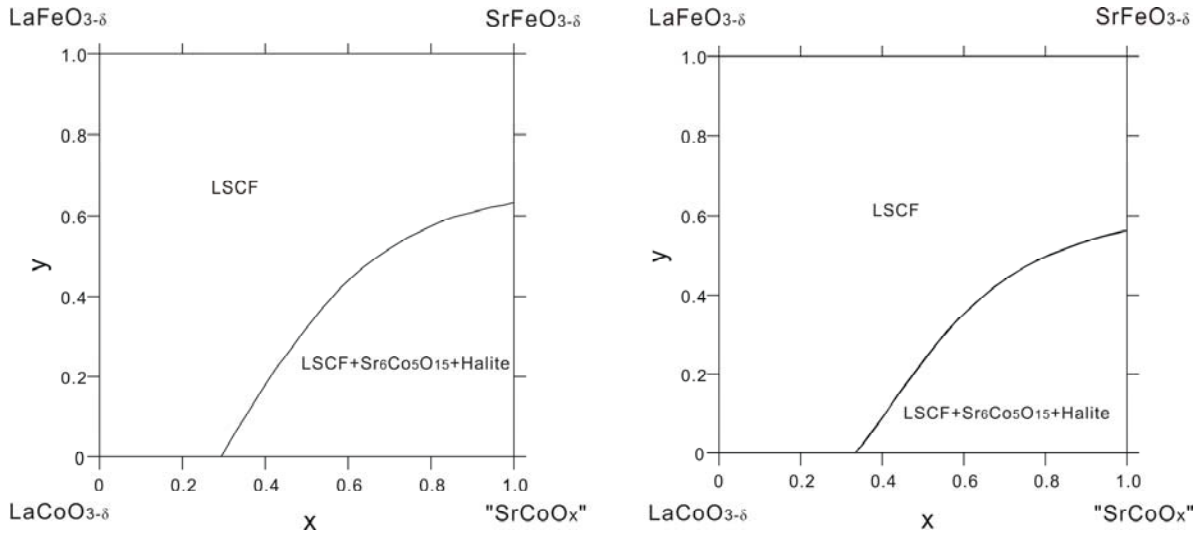

Fig. 6.3. Phase diagrams for $La_{1-x}Sr_xCo_{1-y}Fe_yO_{3-\delta}$ at 700°C calculated in this research: a) in air, b) at PO_2=1Pa.

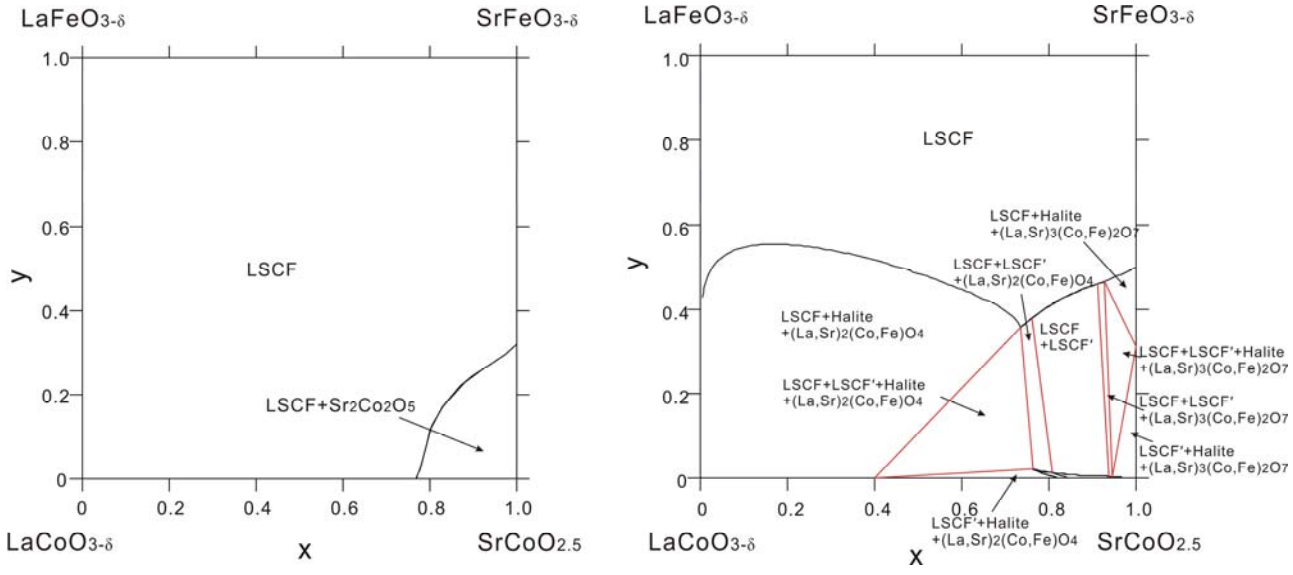

Fig. 6.4. Phase diagrams for $La_{1-x}Sr_xCo_{1-y}Fe_yO_{3-\delta}$ at 1100°C calculated in this research: a) in air, b) at PO_2=1Pa.

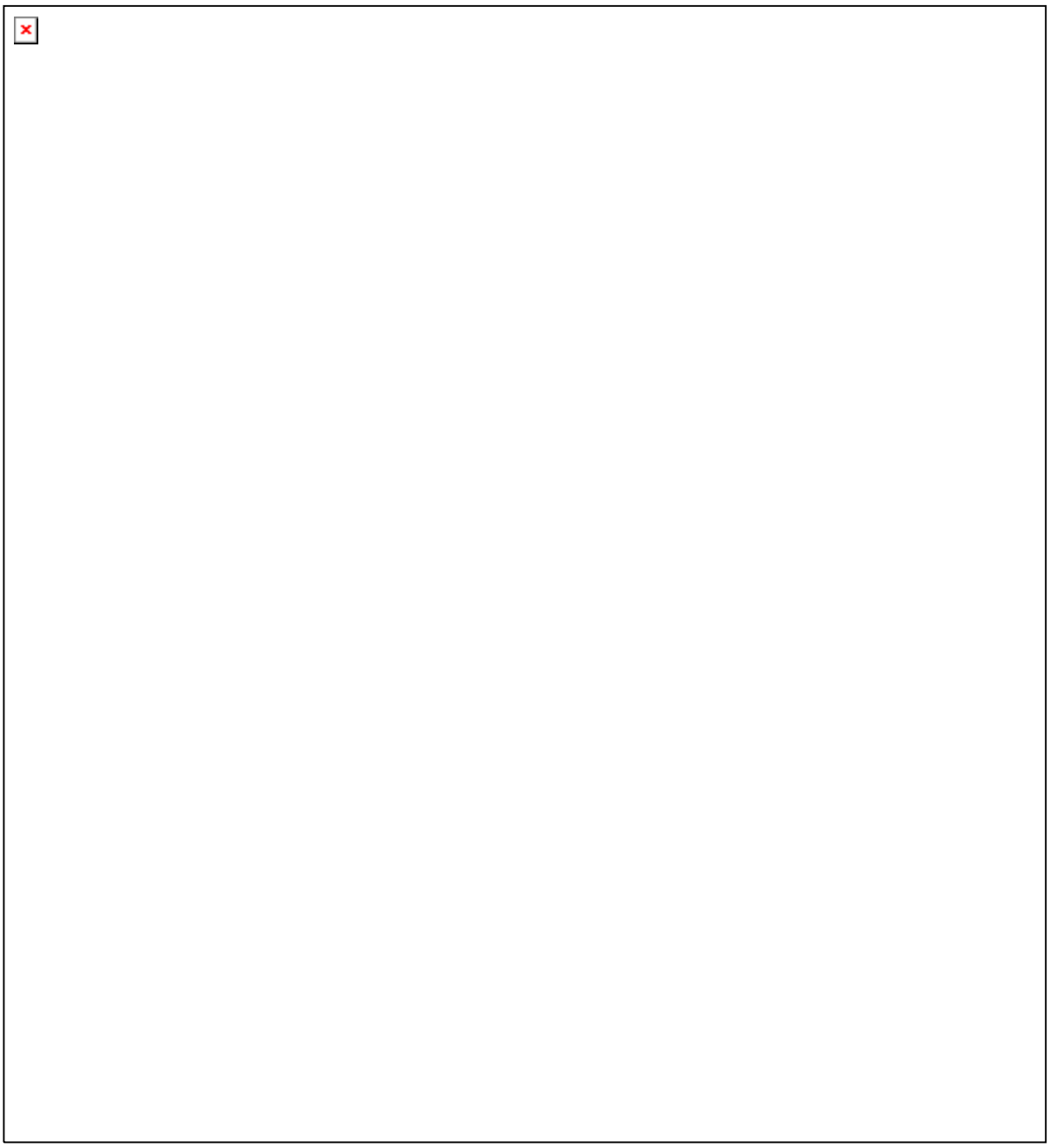

Fig. 6.5. Calculated phase diagrams for $La_{0.6}Sr_{0.4}Co_{1-y}Fe_yO_{3-\delta}$ as a function of temperature and oxygen partial pressure: a) y=0.8, b) y=0.6 c) y=0.4, and d) y=0.2.

Fig. 6.5 presents the phase diagrams for $La_{0.6}Sr_{0.4}Co_{1-y}Fe_yO_{3-\delta}$ (y = 0.2, 0.4, 0.6 and 0.8) as a function of temperature and oxygen partial pressure calculated in this research. Region I corresponds to the perovskite single-phase region. Its area shrinks with decreasing Fe content. The formation of secondary phases takes place at lower oxygen partial pressure or higher

temperature. At 700°C and starting from Region I, $(La,Sr)_2(Co,Fe)O_4$ and halite form first with decreasing oxygen partial pressure, in agreement with the experimental results from Hashimoto *et al.* [4].

Fig. 6.6 presents the calculated phase diagrams for $La_{1-x}Sr_xCo_{0.2}Fe_{0.8}O_{3-\delta}$ (x = 0.2 and 0.6). It can be concluded that at high Fe content, increasing the Sr content does not necessarily have a negative effect on LSCF stability. At high temperatures, increasing the Sr content actually has a positive effect.

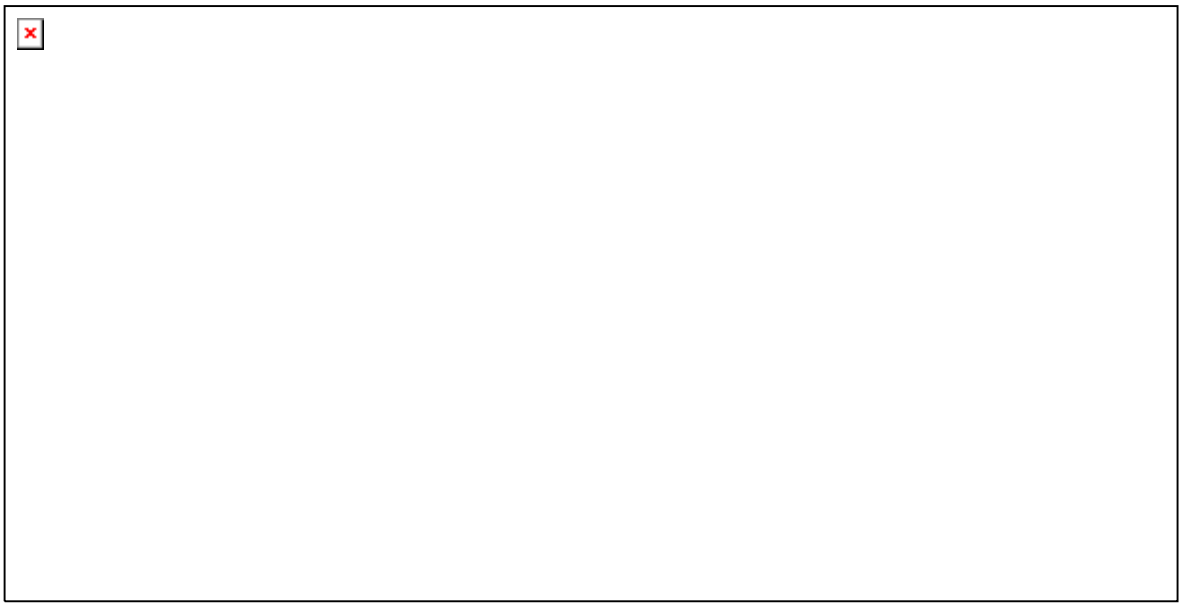

(a) (b)

Fig. 6.6. Calculated phase diagrams for $La_{1-x}Sr_xCo_{0.2}Fe_{0.8}O_{3-\delta}$ as a function of temperature and oxygen partial pressure: a) x=0.2 and b) x=0.6.

In addition to stability phase diagrams, the amount of equilibrium phases can also be calculated. Fig. 7 shows the calculated equilibrium phase fraction for $La_{0.6}Sr_{0.4}Co_{0.2}Fe_{0.8}O_{3-\delta}$ at 700 °C and 1100 °C. At 700 °C, the perovskite phase with a composition of $La_{0.6}Sr_{0.4}Co_{0.2}Fe_{0.8}O_{3-\delta}$ is stable down to logPO_2/bar of about −15. Decreasing oxygen partial pressure further results in the formation of secondary phases. At 1100 °C, the perovskite phase with a composition of $La_{0.6}Sr_{0.4}Co_{0.2}Fe_{0.8}O_{3-\delta}$ is stable down to logPO_2/bar of about −7.

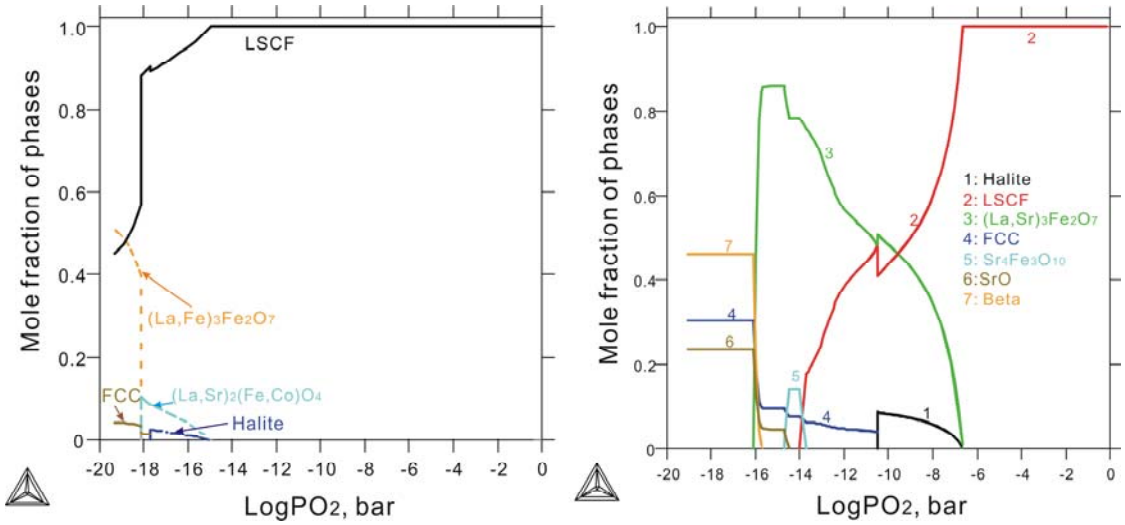

Fig. 6.7. Calculated equilibrium phase fraction for $La_{0.6}Sr_{0.4}Co_{0.2}Fe_{0.8}O_{3-\delta}$ as a function of oxygen partial pressure: a) at 700°C and b) at 1100°C.

For SOFC applications, composite LSCF/CGO cathodes are often used instead of pure LSCF cathodes. Inter-diffusion takes place across the LSCF−CGO interface, either in the LSCF/CGO composite cathode or at the cathode−barrier layer interface, which may alter the stability of the LSCF perovskite. Fig. 6.8 presents the calculated stability phase diagrams for $La_{0.6}Sr_{0.4}Co_{0.2}Fe_{0.8}O_{3-\delta}$ with 20% deficiency for each of the four cations, while the stability diagram for $La_{0.6}Sr_{0.4}Co_{0.2}Fe_{0.8}O_{3-\delta}$ is presented in Fig. 6.5a. The most noticeable change happens at the right bottom corner (high oxygen partial pressure and low temperature). Without cation deficiency (Figure 5a), $La_{0.6}Sr_{0.4}Co_{0.2}Fe_{0.8}O_{3-\delta}$ exists as a single-phase perovskite. With A-site La or Sr deficiency, spinel and halite form as secondary phases, while with B-site Co or Fe deficiency, $(La,Sr)_2(Co,Fe)O_4$ and $(La,Sr)_3Fe_2O_7$ phases form. In this corner, the perovskite phase is the majority phase. Formation of the secondary phases is due to A/B ratio deviating from 1.

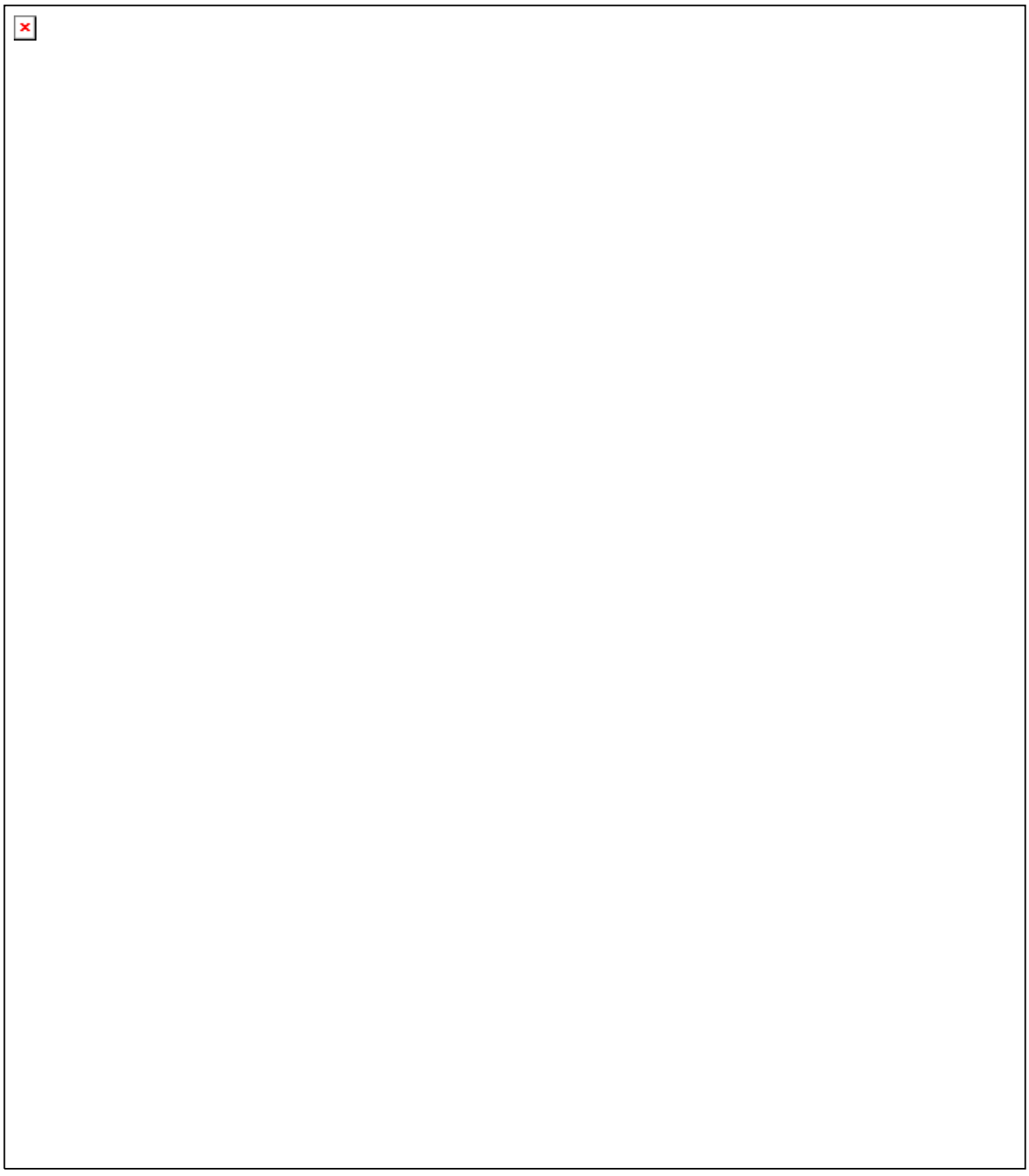

Fig. 6.8. Calculated phase diagrams for $La_{0.6}Sr_{0.4}Co_{0.2}Fe_{0.8}O_{3-\delta}$ with cation deficiency: a) $La_{0.48}Sr_{0.4}Co_{0.2}Fe_{0.8}O_{3-\delta}$, b) $La_{0.6}Sr_{0.32}Co_{0.2}Fe_{0.8}O_{3-\delta}$ c) $La_{0.6}Sr_{0.4}Co_{0.16}Fe_{0.8}O_{3-\delta}$, and d) $La_{0.6}Sr_{0.4}Co_{0.2}Fe_{0.64}O_{3-\delta}$.

6.3.3 Oxygen non-stoichiometry and defect chemistry

Groups of authors have experimentally studied the oxygen non-stoichiometry of LSCF using thermogravimetry (TG) [4, 5 26, 27] or coulometric titration techniques [4, 5, 27] at various temperatures and oxygen partial pressures. In this research, we also calculated the oxygen content of LSCF using our database and compared with the experimental data from the literature [4]. As shown in Fig. 6.9, good agreement with the experimental results was achieved at high Fe content. The oxygen content in $La_{0.6}Sr_{0.4}Co_{1-y}Fe_yO_{3-\delta}$ decreases with decreasing PO_2 or increasing temperature. The sharp decreases correspond to phase decomposition or secondary phase formation.

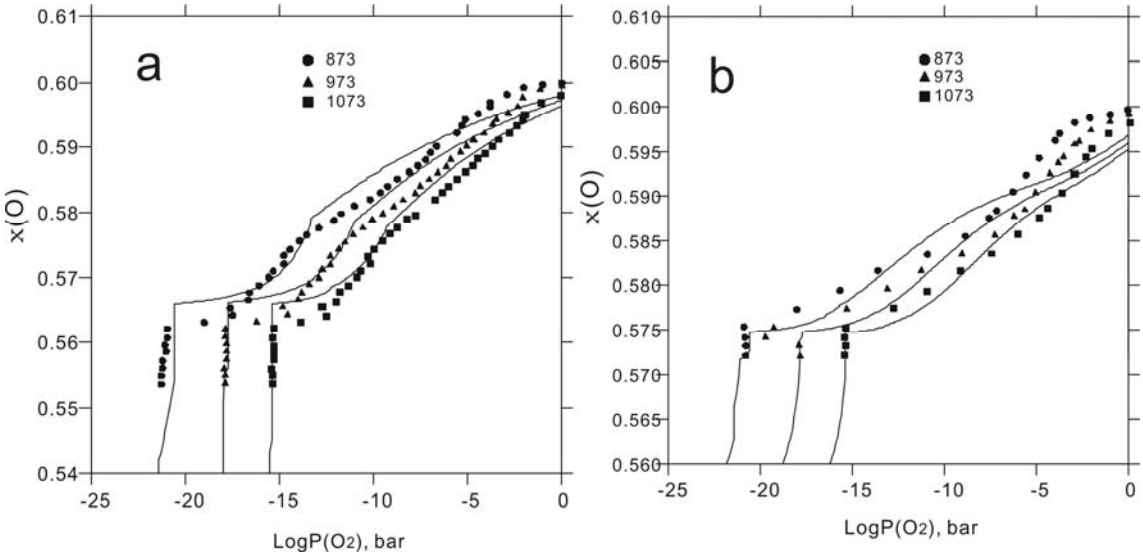

Fig. 6.9. Calculated oxygen content in $La_{0.6}Sr_{0.4}Co_{1-y}Fe_yO_{3-\delta}$ (y= 0.6 and 0.8) at different temperatures as a function of oxygen partial pressure with experimental data [4] included, (a) y=0.6, (b) y=0.8.

The distribution of transition metal cations in perovskite affects magnetic and electrical properties. Knowledge of the cation valence state will be helpful in analyzing the defect chemistry of LSCF perovskite. Fig. 6.10a plots the site fraction of ions in the $La_{0.6}Sr_{0.4}Co_{0.2}Fe_{0.8}O_{3-\delta}$ perovskite phase as a function of oxygen partial pressure at 700°C. The calculation results show that the amount of A-site or B-site cation vacancy is negligible. Fig. 10b plots the average valence state for Co and Fe cations. The average valency for Co ranges from +2.8 to +3.5, while that for Fe ranges from +3 to +3.25.

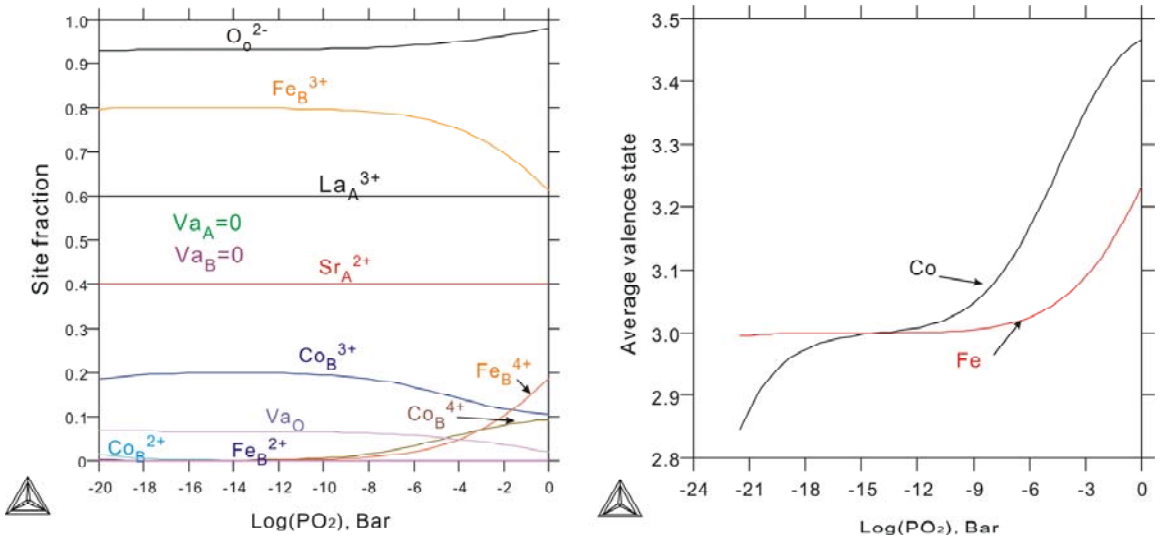

(a) (b)

Fig. 10 a) Calculated site fraction of ions in the $La_{0.6}Sr_{0.4}Co_{0.2}Fe_{0.8}O_{3-\delta}$ perovskite phase as a function of oxygen partial pressure at 700°C. b) Calculated average valence state for Co and Fe cations in the $La_{0.6}Sr_{0.4}Co_{0.2}Fe_{0.8}O_{3-\delta}$ perovskite phase as a function of oxygen partial pressure at 700°C.

6.4 Conclusions

A thermodynamic database of the La-Sr-Co-Fe-O system was developed by applying the CALPHAD method. The resulting database can be used for calculating phase equilibria and thermodynamic properties at temperatures of 298−3000 K and oxygen partial pressure of 10^{-25}−1 bar using Gibbs energy minimization software. The following can be concluded from the calculations:

1) The stability of the LSCF perovskite phase decreases with increasing Co or Sr content or increasing temperature or decreasing oxygen partial pressure. Different secondary phases form under different conditions (temperature, oxygen partial pressure, composition).

2) The oxygen content of the perovskite phase decreases with decreasing PO_2 or increasing temperature. The Co content does not affect the oxygen deficiency of the perovskite phase significantly.

References:

[1] N.H. Menzler, F. Tietz, S. Uhlenbruck, H.P. Buchkremer, D. Stöver, J. Mater Sci. 45 (2010) 3109–3135.

[2] H.J.M. Bouwmeester, Catal. Today 82 (2003) 141–150.

[3] M.M. Natile, F. Poletto, A. Galenda, A. Glisenti, T. Montini, L. De Rogatis, P. Fornasiero, Chem. Mater. 20 (2008) 2314–2327.

[4] S. Hashimoto, Y. Fukuda, M. Kuhn, K. Sato, K. Yashiro, J. Mizusaki, Solid State Ionics 181 (2010) 1713–1719.

[5] M. Kuhn, Y. Fukuda, S. Hashimoto, K. Sato, K. Yashiro, J. Mizusaki, ECS Trans. 35 (2011) 1881–1890.

[6] A.N. Grundy, B. Hallstedt, L.J. Gauckler, J. Phase Equilib. 22 (2001) 105–113.

[7] A.N. Grundy, B. Hallstedt, L.J. Gauckler, Acta Mater. 50 (2002) 2209–2222.

[8] D. Risold, B. Hallstedt, L.J. Gauckler, CALPHAD, 20 (1996) 353–361.

[9] M. Chen, B. Hallstedt, L.J. Gauckler, J. Phase Equilib. 24 (2003) 212–227.

[10] B. Sundman, J. Phase equilib. 12 (1991) 127–140.

[11] L. Kjellqvist, M. Selleby, B. Sundman, CALPHAD 32 (2008) 577–592.

[12] C.P. Wang, J. Wang, X.J. Liu, I. Ohnuma, R. Kainuma, K. Ishida, J. Alloys Compd. 453 (2008) 174–179.

[13] I. Ohnuma, H. Enokia, O. Ikeda, R. Kainuma, H. Ohtani, B. Sundman, K. Ishida, Acta Mater. 50 (2002) 379–393.

[14] W.-W. Zhang, M. Chen, E. Povoden-Karadeniz, P.V. Hendriken, Thermodynamic modeling of La-Co-O system, unpublished results.

[15] E. Povoden-Karadeniz, A.N. Grundy, M. Chen, T. Ivas, L.J. Gauckler, J. Phase Equilib. Diff. 30 (2009) 351–366.

[16] W.-W Zhang, M. Chen, P.V. Hendriken, Thermodynamic modeling of Sr-Co-Fe-O system, unpublished results.

[17] E. Povoden-Karadeniz, Thermodynamic modeling of La-Sr-Fe-O system, unpublished results.

[18] W.-W. Zhang, M. Chen, Thermodynamic modeling of Co-Fe-O system, paper submitted.

[19] W.-W. Zhang, M. Chen, E. Povoden-Karadeniz, P. V. Hendriken Thermodynamic modeling of La-Sr-Co-O system, unpublished results.

[20] A.T. Dinsdale, CALPHAD 15 (1991) 317–425.

[21] M. Hillert, J. Alloys Compd. 320 (2001) 161–176.

[22] M. Hillert, B. Jansson, B. Sundman, J. Ågren, Metall. Trans. 16A (1985) 261-266

[23] B. Sundman, Calphad 15 (1991) 109–119.

[24] A. Mai, V.A.C. Haanappel, S. Uhlenbruck, F. Tietz, D. Stöver, Solid State Ionics 176 (2005) 1341–1350.

[25] D. Oh, D. Gostovic, E.D. Wachsman, J. Mater. Res. 27 (2012) 1992–1999.

[26] H.L. Lein, K. Wiik, T. Grande, Solid State Ionics 177 (2006) 1795–1798.

[27] M.H.R. Lankhorst, J.E. ten Elshof, J. Solid State Chem. 130 (1997) 302–310.

Chapter 7

An experimental study of reactions between $La_{0.58}Sr_{0.4}Co_{0.2}Fe_{0.8}O_{3-\delta}$ and $Ce_{0.9}Gd_{0.1}O_{3-\delta}$

Abstract

$La_{0.58}Sr_{0.4}Co_{0.2}Fe_{0.8}O_{3-\delta}$ (LSCF5842) and $Ce_{0.9}Gd_{0.1}O_{2-\delta}$ (CGO10) are used as composite cathodes in SOFCs. In this work, experimental investigations on stability of LSCF5842 and inter-diffusion between LSCF5842 and CGO10 were carried out using pellets and diffusion couples under various oxygen partial pressures and temperatures. LSCF5842 powder and LSCF5842–CGO10 powder mixtures were pressed into pellets and then heat treated in air or N_2. Polished LSCF5842 pellets were also placed in contact with CGO10 pellets to establish diffusion couples. The surfaces of the pellets were examined with XRD and SEM/EDS after heat treatment. In powder mixture samples of LSCF5842+CGO10 heat treated at high temperatures (T = 1250 and 1400 °C), dissolution of La into the fluorite phase (CGO) and Ce and Gd into the LSCF perovskite phase was detected. It was further found that accompanying the incorporation of Ce and Gd into the perovskite, exsolution of a halite phase takes place when the powder mixture is treated in N_2 at 1250°C. For the diffusion couples, it was found that Sr diffused out or volatilized from LSCF5842 and enriched on the surface of CGO10 forming Sr-containing secondary phases.

Chapter 7 An experimental study of reactions between $La_{0.58}Sr_{0.4}Co_{0.2}Fe_{0.8}O_{3-\delta}$ and $Ce_{0.9}Gd_{0.1}O_{3-\delta}$

7.1 Introduction

In the previous chapters of this thesis, a thermodynamic database for the La-Sr-Co-Fe-O system was introduced. Phase stabilities of LSC ($La_{1-x}Sr_xCoO_{3-\delta}$) and LSCF were evaluated from thermodynamic calculations and were further compared with experimental results from both our own studies and those reported in the literature. A good agreement between the calculations and the experimental results in the comparable regions of phase space was observed allowing reliable phase stability predictions at various temperatures, oxygen partial pressures and compositions to be made by use of the models.

CGO (gadolinium doped ceria) has high oxide ion conductivity. It is often mixed with LSCF to form a composite cathode [1,2] to obtain high oxygen diffusivity and surface exchange rate, or used as the interlayer between the LSCF cathode and the YSZ (Yittria Stabilized Zirconia) electrolyte to prevent undesired reactions between LSCF and YSZ [3−5]. It has been reported that LSCF is chemically compatible with CGO [6] and no direct reaction was found between them at 1000-1200 °C for 30-672h [7]. However, according to the CeO_2-La_2O_3 phase diagram published by Du *et al.* [8], CeO_2 has a large La solubility (around 40 mol.% in air at 700°C). Hence, inter-diffusion may take place between LSCF and CGO [7]. A few studies have been carried out on this topic [7, 9−12]. Izuki *et al.* [7] investigated inter-diffusion across the LSCF/CGO interface at temperatures between 1000 and 1200 °C by SIMS (Secondary Ion Mass Spectrometry). A significant amount of La diffusion into CGO and Ce and Gd diffusion into LSCF was observed. The diffusion of Sr, Fe and Co into CGO was reported to be very limited. Martínez-Amesti *et al.* [9] found a significant shift in the positions of X-ray diffraction peaks for mixtures of LSF + doped ceria heat treated at 1150°C, indicating that inter-diffusion had taken place. Sakai *et al.* [10, 11] studied inter-diffusion in diffusion couples of doped ceria and LSCF (or LSC) using SIMS. The depletion of La, Sr, Co, Fe in LSCF and that of Ce and Gd in doped ceria were found. Uhlenbruck *et al.* [12] investigated element migration between adjacent layers in SOFCs by TEM (Transmission Electron Microscopy). They observed Sr depletion and a slight enrichment of Gd (coming from the CGO barrier layer) in the LSCF electrode after sintering. It was found that incorporation of Ce and Gd in the perovskite or depletion of Sr and La from it, not only reduced the ionic conductivity of the phase [13], but also affected its stability. Besides, the thermal expansion of the various functional layers is also influenced by the inter-diffusion [14]. A $La_{0.58}Sr_{0.4}Gd_{0.01}Fe_{0.8}Co_{0.2}O_{3-\delta}$ powder was further prepared by Uhlenbruck *et al.* [12]. The powder

was calcined at 900°C for 5h leading to formation of $(La,Sr)_2(Co,Fe)O_4$ and spinel as confirmed by XRD. It can therefore be speculated that inter-diffusion across the LSCF−CGO interface may lead to phase decomposition or secondary phase formation.

Most of the previous studies were conducted in air at high temperature. It is of great importance to clarify the stability of LSCF with or without the presence of CGO at operating conditions for IT-SOFCs, e.g. at 700°C and with reduced PO_2 corresponding to the case where the LSCF cathode is polarized. In this chapter, the inter-diffusion between LSCF and CGO was studied experimentally. Two types of samples were prepared including $La_{0.58}Sr_{0.4}Co_{0.2}Fe_{0.8}O_{3-\delta}$ (LSCF5842) and $Ce_{0.9}Gd_{0.1}O_{2-\delta}$ (CGO10) mixtures and LSCF5842/CGO10 diffusion couples, which were used to mimic reactions inside a LSCF/CGO composite cathode and at the LSCF cathode – CGO barrier layer interface, respectively. Two atmospheres were chosen for both types of the experiments, air and N_2, corresponding to local oxygen partial pressures in the LSCF cathode under OCV or when strongly polarized (~200 mV). After heat treatment, the samples were characterized using XRD (X-ray diffraction) and SEM/EDS (Scanning Electron Microscopy/ Energy Dispersive Spectroscopy).

7.2 Experiments

7.2.1. Sample preparation

LSCF powder ($La_{0.58}Sr_{0.4}Co_{0.2}Fe_{0.8}O_{3-\delta}$ − LSCF5842, HC Starck) and CGO powder ($Ce_{0.9}Gd_{0.1}O_{2-\delta}$ − CGO10, HATS) were used as starting materials. The powder or powder mixture of LSCF5842 and CGO10 (1/1 in weight ratio) were pressed into pellets of 12 mm in diameter and 2−5mm in thickness. Some of the LSCF5842 and LSCF5842+CGO10 pellets were pre-sintered at 1400 °C in air for 5h, while some of the CGO10 pellets were pre-sintered at 1450 °C in air for 5h. During sintering, the pellets were put on top of a Pt sheet to avoid reactions with alumina crucibles. After sintering, the upper surface of the pellets, i.e. the surface exposed to air, was further polished. A few samples were kept as reference.

Two LSCF5842/CGO10 diffusion couples were prepared by bringing the polished surfaces of the pre-sintered pellets in contact. Samples were kept in place by help of a platinum wire.

7.2.2 Heat treatment

Except for the reference samples, all the other samples were heat treated under different conditions. For the pellet samples (as-pressed and pre-sintered), they were heat treated at six

different conditions: three temperatures (1250°C, 1000°C and 700°C) and two atmospheres (air and N_2. The oxygen partial pressure in N_2 is close to 10^{-4} bar in this experimental work). For the pre-sintered pellets, the upper surface was polished before further heat treatment. This gives coarser grains as compared to the as-pressed samples, which enables more accurate EDS analyses of phase compositions. The diffusion couples were heat treated at 1200°C in air or in N_2 for 5 days. All the heat treatment conditions are listed in Table 7.1, 7.2 and 7.11. Longer annealing time was chosen at low temperature in order to get closer to equilibrium.

7.2.3 Characterization

After heat treatment, the surface of the pellets was analyzed with XRD to evaluate formation of secondary phases or reaction products. The XRD data were collected at room temperature with a Bruker D8 powder diffractometer equipped with a Lynx-eye detector. The XRD scans were carried out at a scan speed of 0.04° per 5 s over a 2θ range of 20 to 80° with Cu-Kα radiation (λ=0.15406 nm). Peak position and pattern fitting were determined with the program EVA.

The surface microstructure and element distribution was characterized using SEM/EDS. The sample surface was observed first using a TM-1000 electron microscope and afterwards a Zeiss Supra-35 SEM equipped with a field-emission gun and an energy-dispersive X-ray (EDS) spectrometer. Both back-scattered electron (BSE) detector and secondary electron (SE) detector were used for each sample. EDS analysis was performed using the aforementioned microscope in conjunction with Noran System Six software to determine chemical composition of various phases.

7.3 Results

7.3.1 LSCF and LSCF+CGO pellets

A summary of the results obtained on the pellet samples is presented in Tables 7.1−2.

Table 7.1. Summary of the results for the pellet samples heat treated in air

Samples No.	Heat treatment	Phases detected by XRD¤	SEM/EDS result¤
LSCF1400	Pre-sintered reference (1400°C for 5h), no further heat treatment	Prv	Prv + (Co, Fe)O_x
LSCF1250A-DH*	As-pressed sample directly heat treated at 1250˚C in air for 100h	Prv	Prv
LSCF1250A-PS	Pre-sintered sample heat treated at 1250˚C in air for 100h	Prv	Prv + Sr-P-O
LSCF1000A-DH	As-pressed sample directly heat treated at 1000˚C in air for 1000h	Prv	—

LSCF1000A-PS	Pre-sintered sample heat treated at 1000˚C in air for 1000h	Prv	Prv + Sr-P-O
LSCF700A-DH	As-pressed sample directly heat treated at 700˚C in air for 2000h	Prv + $SrSO_4$	—
LSCF700A-PS	Pre-sintered sample heat treated at 700˚C in air for 2000h	Prv	Prv + CoO_x +Sr-S-O
Mix1400	Pre-sintered reference (1400°C for 5h), no further heat treatment	Prv + Flu	Prv (with dissolved Ce and Gd) + Flu (with dissolved La)
Mix1250A-DH	As-pressed sample directly heat treated at 1250˚C in air for 100h	Prv + Flu	Prv (with dissolved Ce and Gd) + Flu (with dissolved La) + $Sr_{10}O(PO_4)_6$
Mix1250A-PS	Pre-sintered sample heat treated at 1250˚C in air for 100h	Prv + Flu + $Sr_{10}O(PO_4)_6$	Prv (with dissolved Ce and Gd) + Flu (with dissolved La)+ $Sr_{10}O(PO_4)_6$
Mix1000A-DH	As-pressed sample directly heat treated at 1000˚C in air for 1000h	Prv + Flu	—
Mix1000A-PS	Pre-sintered sample heat treated at 1000˚C in air for 1000h	Prv + Flu	Prv (with dissolved Ce and Gd) + Flu (with dissolved La)+ Sr-P-O phase
Mix700A-DH	As-pressed sample directly heat treated at 700˚C in air for 2000h	Prv + Flu	—
Mix700A-PS	Pre-sintered sample heat treated at 700˚C in air for 2000h	Prv + Flu	Prv+Flu

*: DH denotes the directly heat treated samples, and PS denotes the pre-sintered samples.
¤: Prv represents the perovskite phase while Flu stands for the fluorite phase.

Table 7.2. Summary of the results for the pellet samples heat treated in N_2 §

Samples No.	Heat treatment	Phaes detected by XRD¤	SEM/EDS result¤
LSCF1250N-DH	As-pressed sample directly heat treated at 1250˚C in N_2 for 100h	Prv	Prv + CoO_x
LSCF1250N-PS	Pre-sintered sample heat treated at 1250˚C in N_2 for 100h	Prv	Prv + CoO_x
LSCF1000N-DH	As-pressed sample directly heat treated at 1000˚C in N_2 for 1000h	Prv	—
LSCF1000N-PS	Pre-sintered sample heat treated at 1000˚C in N_2 for 1000h	Prv + $Sr_3(PO_4)_2$	Prv + Sr-P-O (little) + CoO_x
LSCF700N-DH	As-pressed sample directly heat treated at 700˚C in N_2 for 2000h	Prv	—
LSCF700N-PS	Pre-sintered sample heat treated at 700˚C in N_2 for 2000h	Prv	Prv + CoO_x+Sr-S-O #
Mix1250N-DH	As-pressed sample directly heat treated at 1250˚C in N_2 for 100h	Prv + Flu +Halite (<2 %)	Prv (with dissolved Ce and Gd) + Flu (with dissolved La) + Halite
Mix1250N-PS	Pre-sintered sample heat treated at 1250˚C in N_2 for 100h	Prv + Flu + Halite (≈20 %)	Prv (with dissolved Ce and Gd) + Flu (with dissolved La)+ Halite
Mix1000N-DH	As-pressed sample directly heat treated at 1000˚C in N_2 for 1000h	Prv + Flu	—
Mix1000N-PS	Pre-sintered sample heat treated at 1000˚C in N_2 for 1000h	Prv + Flu + $Sr_3(PO_4)_2$	Prv (with dissolved Ce and Gd) + Flu (with dissolved La)+ $Sr_3(PO_4)_2$
Mix700N-DH	As-pressed sample directly heat treated at 700˚C in N_2 for 2000h	Prv + Flu	—
Mix700N-PS	Pre-sintered sample heat treated at 700˚C in N_2 for 2000h	Prv + Flu +$SrSO_3$	Prv + Flu + CoO_x+Sr-S-O

*: DH denotes the directly heat treated, and PS denotes the pre-sintered samples.
¤: Prv means the perovskite phase while Flu means the fluorite phase
#: The composition of the Sr-S-O phase cannot be determined by EDS, due to too small grain.
§: The oxygen partial pressure in N_2 is close to 10^{-4} bar.

Chapter 7 An experimental study of reactions between $La_{0.58}Sr_{0.4}Co_{0.2}Fe_{0.8}O_{3-\delta}$ and $Ce_{0.9}Gd_{0.1}O_{3-\delta}$

I. Phase stability of LSCF in air with or without the presence of CGO

The XRD spectra of the LSCF pellets heat treated in air are presented in Fig. 7.1. The major phases are marked in the figure. Beside the perovskite phase, a $SrSO_4$ phase was found on the LSCF700A-DH pellet directly heat treated at 700 °C for 2000h. The other small peaks, which have an intensity lower than 1% of that of the perovskite phase, might correspond to the CoO_x phase or the Sr-impurity phase. Fig. 7.2 presents the XRD spectra for the LSCF+CGO pellets heat treated in air. No direct reaction between LSCF and CGO was detected at any of the temperatures. In addition to the perovskite and fluorite phases, $Sr_{10}O(PO_4)_6$ was found on the Mix1250A-PS pellet (pre-sintered and surface polished before heat treatment) heat treated at 1250 °C for 100h. Peak position are however observed to shift between the samples that have experienced temperatures of 1250 or 1400 °C and the samples which have only been treated at temperatures of 1000 °C or less. This is evident from Fig. 7.3: Comparing diffractograms of the two "low" temperature samples (Mix1000A-DH and MIX700A-DH, diffractograms d and f) with the 5 remaining ones (a,b,c e and g) that have all experienced either a pre-sintering at 1400 °C or aging at 1250 °C a clear shift of the fluorite peak positions to lower angles going from the low temperature samples to the high temperature ones is observed (illustrated in the Figure with vertical lines). This could indicate that La or Sr, which have larger cation radius than Ce and Gd,

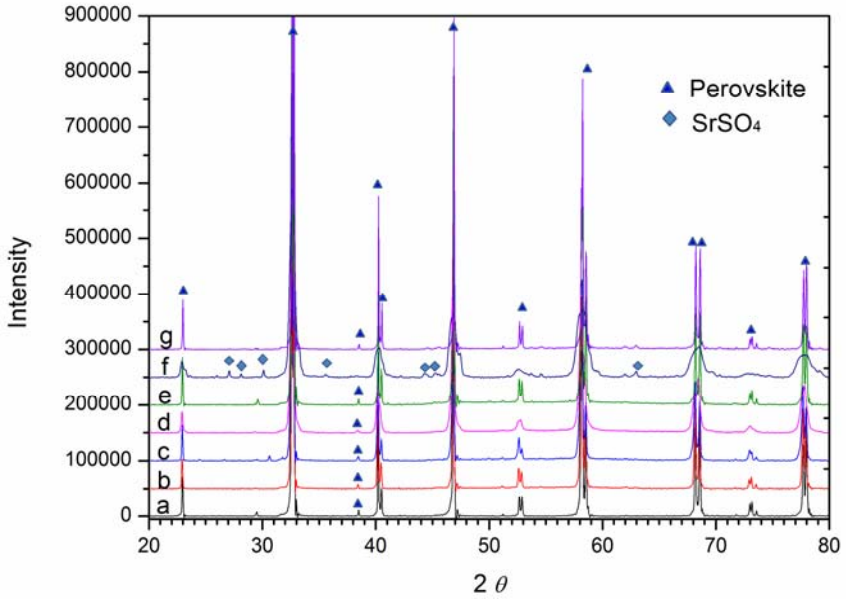

Fig. 7.1 XRD spectra of the LSCF pellets heat treated in air. (a) LSCF1400, (b) LSCF1250A-DH, (c) LSCF1250A-PS, (d) LSCF1000A-DH, (e) LSCF1000A-PS, (f) LSCF700A-DH and (g) LSCF700A-PS.

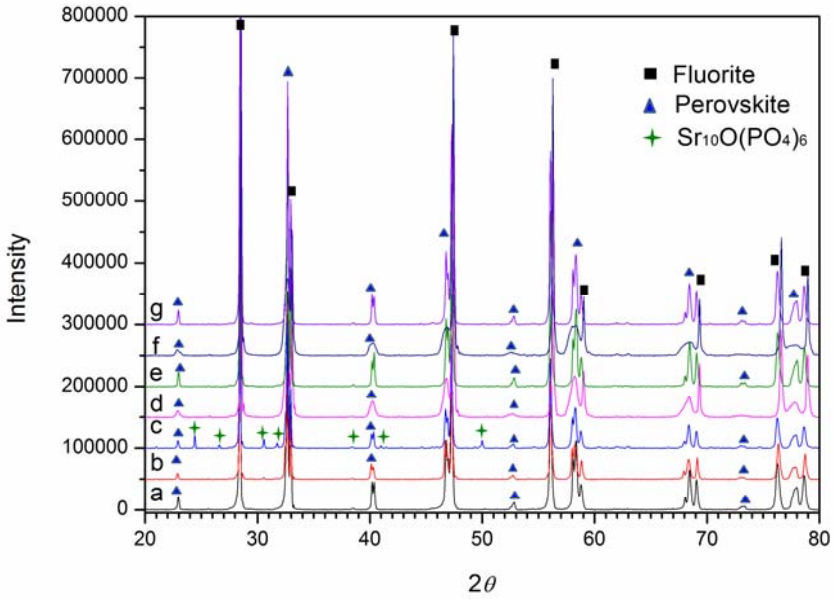

Fig. 7.2 XRD spectra of the LSCF+CGO pellets heat treated in air. (a) Mix1400, (b) Mix1250A-DH, (c) Mix1250A-PS, (d) Mix1000A-DH, (e) Mix1000A-PS, (f) Mix700A-DH and (g) Mix700A-PS.

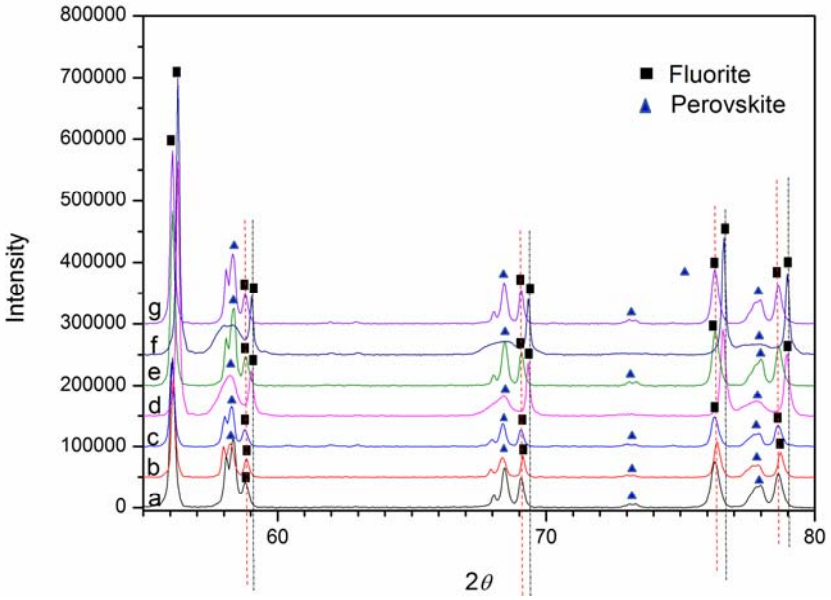

Fig. 7.3 Enlargement of Fig. 7.2 at high 2θ values (55-80°). (a) Mix1400, (b) Mix1250A-DH, (c) Mix1250A-PS, (d) Mix1000A-DH, (e) Mix1000A-PS, (f) Mix700A-DH and (g) Mix700A-PS.

has been incorporated in the CGO fluorite structure during pre-sintering at 1400 °C or heat treatment at 1250 °C. Interestingly, when comparing the peak positions of the perovskite phase, where these can be clearly determined (diffractograms a, b, c, e, g), there is a tendency that the peaks shift to higher

angles going from the diffratogram of the mixture heated at 1250 °C (Mix1250A-DH, diffractogram b) to all the pre-sintered ones that has experienced 1400 °C. This could indicate partial substitution of the larger La by the smaller Ce, Gd on the A site of the perovskite.

Fig.7.4 presents the SEM BSE images on the polished upper surface of the reference LSCF, CGO and LSCF+CGO pellets. $(Co,Fe)O_x$ secondary phase was observed on the sintered LSCF sample (Fig.7.4a). No secondary phase was detected on the CGO and LSCF+CGO pellets (Fig. 7.4b and c). Fig.7.4d and Table 7.3 shows the results of EDS point analyses on the sample Mix1400. EDS results indicate that La dissolved in CGO and Ce and Gd dissolved in the perovskite phase. EDS analyses were also carried out on the LSCF1400 and CGO1450 reference pellets and the results are presented in Table 7.4. Based on Table 7.3 and 7.4, it can be concluded that inter-diffusion between LSCF and CGO has taken place during pre-sintering at 1400 °C.

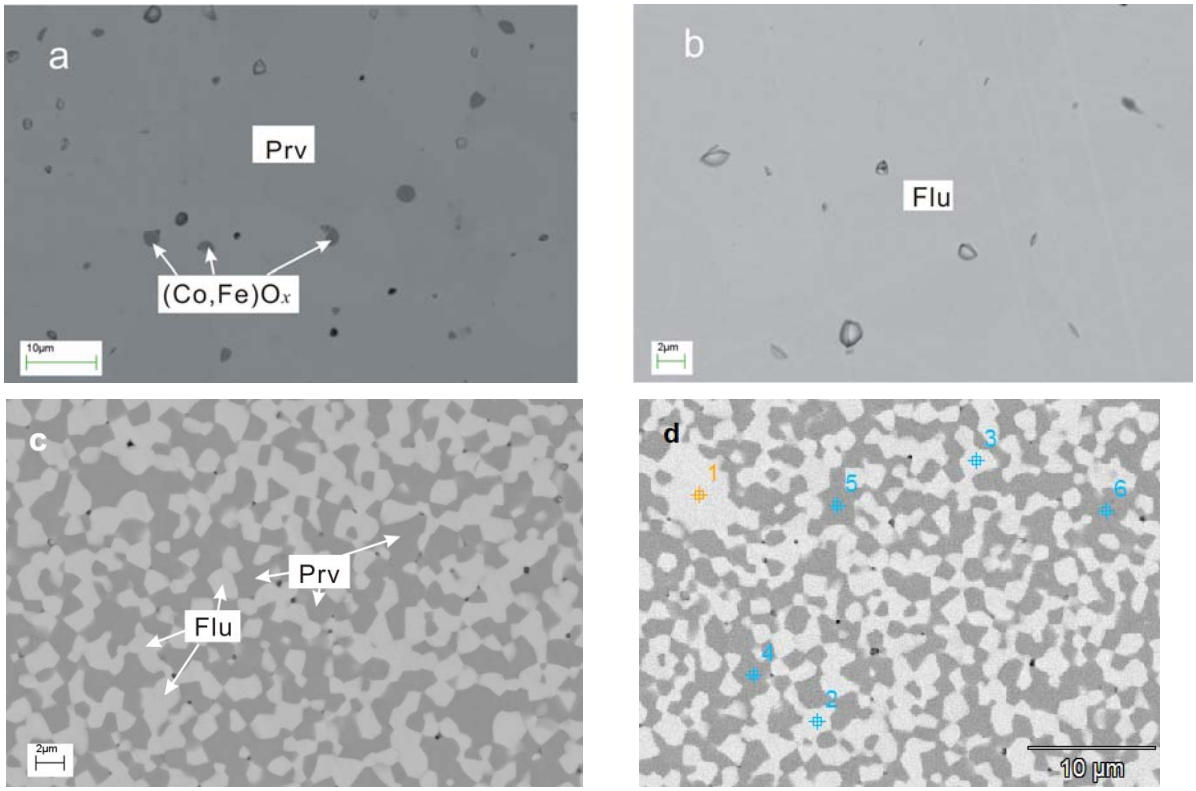

Fig. 7.4 SEM BSE images showing the upper surface of the pellet samples, (a) LSCF1400, (b) CGO1450, (c) Mix1400, (d) Mix1400 with EDS point analyses marked.

Table 7.3 Compositions of the phases in Mix1400 measured by EDS

Point	Phase	La cat.%	Sr cat.%	Co cat.%	Fe cat.%	Ce cat.%	Gd cat.%
1	Fluorite	8.66				83.93	7.41
2	Fluorite	8.61				84.50	6.89

3	Fluorite	10.18				82.16	7.66
4	Perovskite	27.56	18.95	8.29	37	5.77	2.35
5	Perovskite	27.92	18.7	9.51	36.25	5.77	1.85
6	Perovskite	26.27	18.67	10.45	35.86	6.71	2.04
Average	Fluorite	9.15				83.53	7.32
Average	Perovskite	27.25	18.77	9.42	36.37	6.08	2.08

Table 7.4 Average phase composition measured by EDS on the polished surface of the LSCF1400 and CGO1450 reference samples

Sample	Phase	La cat.%	Sr cat.%	Co cat.%	Fe cat.%	Ce cat.%	Gd cat.%
LSCF1400	$(Co,Fe)O_x$			85.07	14.93		
	Perovskite	32.82	19.27	9.01	38.9		
CGO1450	Fluorite					90.91	9.09

The SEM/EDS results for LSCF or LSCF+CGO samples heat treated at different temperatures in air are presented in Fig. 7.5-7.6 and Table 7.5-7.7. For the DH-type LSCF pellets (no pre-sintering), SEM&EDS results confirm pure perovskite for the sample heat treated at 1250 °C (Fig. 7.5a). For the samples heat treated at 1000°C (Fig. 7.5c) or 700°C (Fig. 7.5e), one cannot obtain reliable information on phase composition by SEM/EDS due to too small grain size. For the pre-sintered (PS) LSCF pellets, the grain size is big enough for EDS point analyses. Thus, in this work, the discussion on the EDS results focus on the PS-type samples aged at different temperatures. The phases and their compositions are summarized in Tables 7.5-7.7. For the sample annealed at 1000°C (LSCF1000A-PS), beside a perovskite and a S-P-O phase, a Co-rich phase was also detected. Due to too small grain size of this Co-rich phase, EDS point analysis always results in signals also from the neighboring S-P-O or LSCF phase. The phase compositions for this sample are listed in Table 7.6. For the sample LSCF700A-PS (annealed at 700°C for 2000h), precipitation of a Co-rich phase was detected (Fig. 7.5f). From BSE image (Fig. 7.5f), the sample surface is similar to the 1400°C sintered reference one (Fig. 7.4a, p156). However, by using a SE detector, formation of a Sr-S-O phase on the sample surface was also detected. The Sr-S-O phase is almost invisible in the BSE image (Fig. 7.5f) due to very small difference in the contrast in comparison with that of LSCF perovskite. Neither can XRD detect this phase due to small amount. Phosphorous or sulfur probably comes from the furnaces used for heat treatment. Further experiments are needed to verify the source of the impurities. Just based on the SEM images, it was found that the amount of the Sr-impurity phases (Sr-P-O or Sr-S-O) is higher in the PS-type samples annealed at higher temperature.

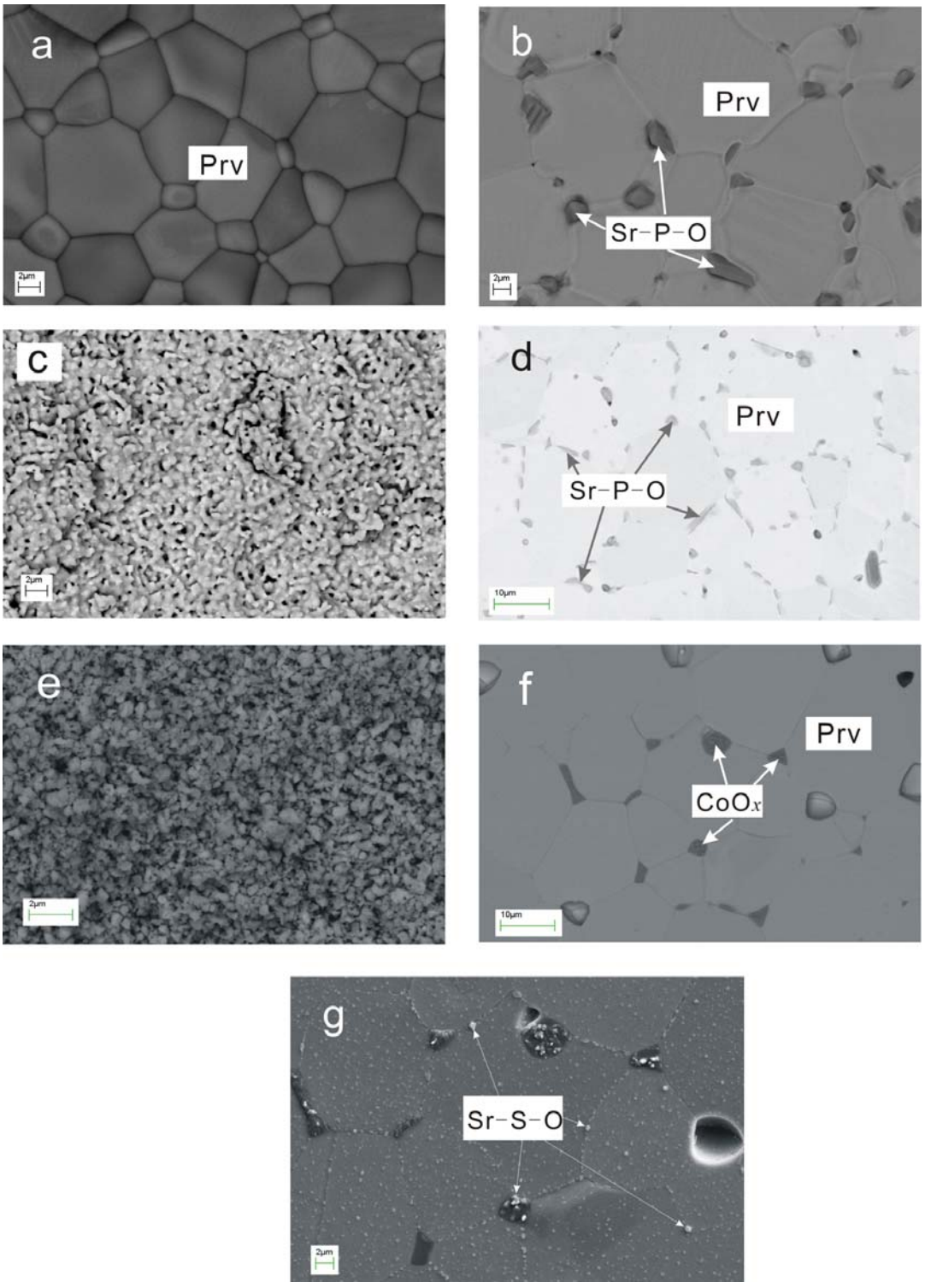

Fig. 7.5. SEM BSE images on the upper surface of the LSCF pellets heat treated in air, (a) LSCF1250A-DH; (b) LSCF1250A-PS; (c) LSCF1000A-DH; (d) LSCF1000A-PS; (e) LSCF700A-DH; (f) LSCF700A-PS; (g) SE image of the same place as (f).

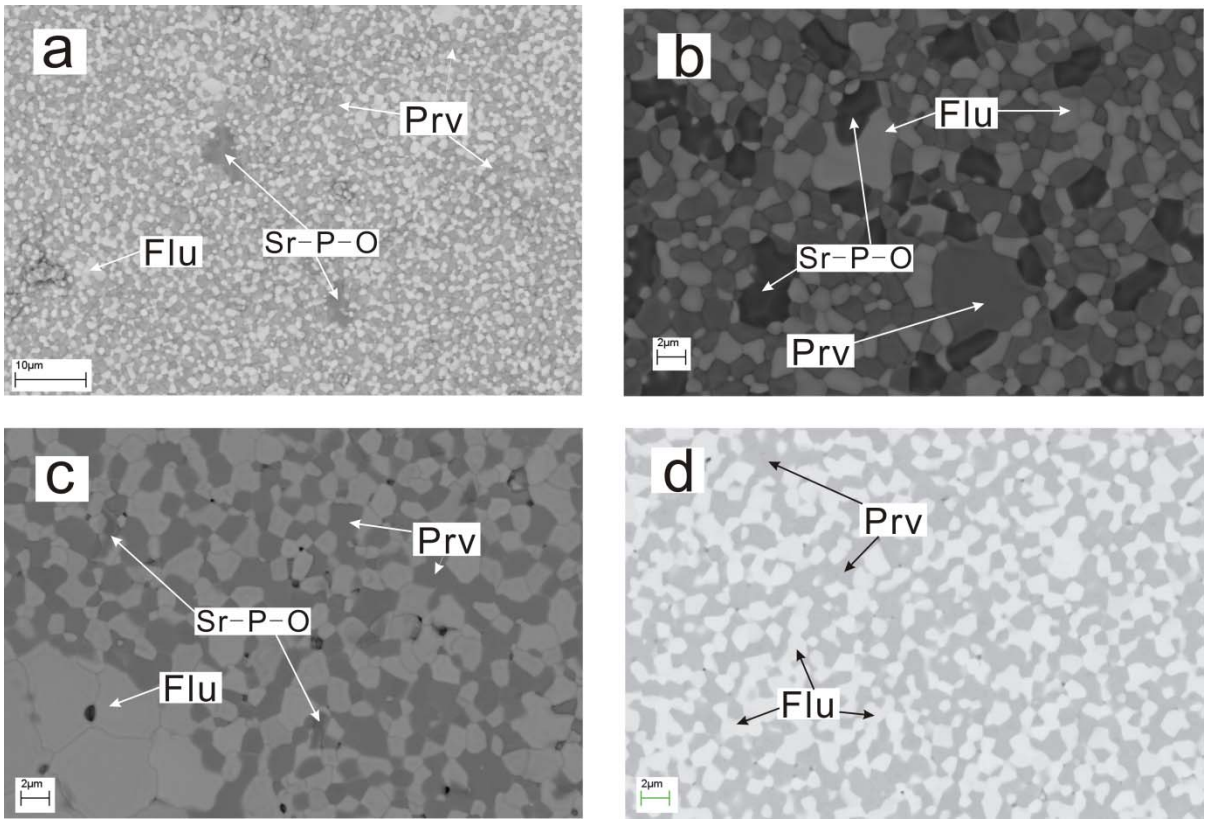

Fig.7.6. SEM BSE images showing the upper surface of the LSCF+CGO mixture samples heat treated in air. (a) Mix1250A-DH; (b) Mix1250A-PS; (c) Mix1000A-PS; (d) Mix700A-PS.

Table 7.5 Average compositions of the phases measured by EDS on the upper surface of the samples heat treated at 1250°C in air

Sample	Phase	La cat.%	Sr cat.%	Co cat.%	Fe cat.%	Ce cat.%	Gd cat.%	P cat.%
LSCF1250A-DH	Perovskite	32.36	19.42	9.64	38.58			
LSCF1250A-PS	Perovskite	32.39	19.34	9.59	38.68			
	Sr-P-O	2.31	53.98		1.05			42.66
Mix1250A-DH	Fluorite	5.64				87.14	7.22	
	Perovskite	29.84	18.87	8.09	39.84	2.70	0.66	
	Sr-P-O	3.84	54.95					41.21
Mix1250A-PS	Fluorite	10.07				82.93	7.00	
	Perovskite	28.39	18.71	8.01	38.92	4.05	1.92	
	Sr-P-O			53.45		3.24		43.31

Fig. 7.6 shows BSE images on the upper surface of the LSCF+CGO mixture pellets annealed in air at different temperatures. For the samples annealed at 1250˚C, the Sr-P-O phase appears as the black phase shown in Fig. 7.6a and b. The amount of the Sr-P-O phase is higher in Mix1250A-

PS than in Mix1250A-DH. XRD pattern fitting points it to be $Sr_{10}O(PO_4)_6$. Table 7.5 presents the EDS results on these two samples and on reference LSCF. La was detected in the CGO phase, while La deficiency and Ce and Gd dissolution were found for the LSCF phase. For the sample annealed at 1000°C (Mix1000A-PS, Fig. 7.6c), a small amount of the Sr-P-O phase was found on the surface. As mentioned previously, phosphorous may come from the furnaces used for heat treatment, deposit on the upper surface of the pellets, and react with Sr from LSCF forming $Sr_{10}O(PO_4)_6$. However, further experiments with surface re-polished samples sealed in clean crucible to verify the source of impurities are needed. The phase compositions determined by EDS are listed in Table 7.6. Fig. 7.6d shows a SEM BSE image for the sample Mix700A-PS, which was annealed at 700°C. The EDS determined compositions for the perovskite and fluorite phases are listed in Table 7.7.

Table 7.6 Average compositions of the phases measured by EDS on the upper surface of the samples heat treated at 1000°C in air

Sample	Phase	La cat.%	Sr cat.%	Co cat.%	Fe cat.%	Ce cat.%	Gd cat.%	P cat.%
LSCF1000A-PS	Perovskite	32.49	19.4	8.5	39.61			
	Sr-P-O	3.61	50.19		3.5			42.7
	CoO_x *	2.63	19.66	54.02	9.14			14.55
Mix1000A-PS	Fluorite	7.45				85.24	7.31	
	Perovskite	27.16	18.7	9.31	37.75	4.72	2.36	
	Sr-P-O	14.4	43.2	5.37	3.85	10.44		22.74

*: The measured composition of the CoO_x phase was influnced by neighboring Sr-P-O and perovskite phases.

Table 7.7 Average compositions of the phases measured by EDS on the upper surface of the samples heated at 700°C in air

Sample	Phase	La cat.%	Sr cat.%	Co cat.%	Fe cat.%	Ce cat.%	Gd cat.%	S cat.%	Mg cat.%
LSCF700A-PS	Perovskite	33.18	18.58	9.5	38.74				
	$(Co,Fe)O_x$			85.66	12.63				
	Sr-S-O		53.18					46.82	1.71
Mix700A-PS	Fluorite	5.87				86.03	8.09		
	Perovskite	27.06	18.26	9.95	36.73	5.56	2.44		

II. Phase stability of LSCF in N_2 with or without the presence of CGO

The XRD diffractions on the LSCF and LSCF+CGO pellets annealed in N_2 are presented in Fig. 7.7 and 7.8, respectively. For the LSCF pellets (Fig. 7.7), a perovskite was identified as the

predominant phase. In LSCF1000N-PS (annealed at 1000°C for 1000h), formation of $Sr_3(PO_4)_2$ was also detected by XRD. For the LSCF+CGO pellets, formation of halite was detected by XRD

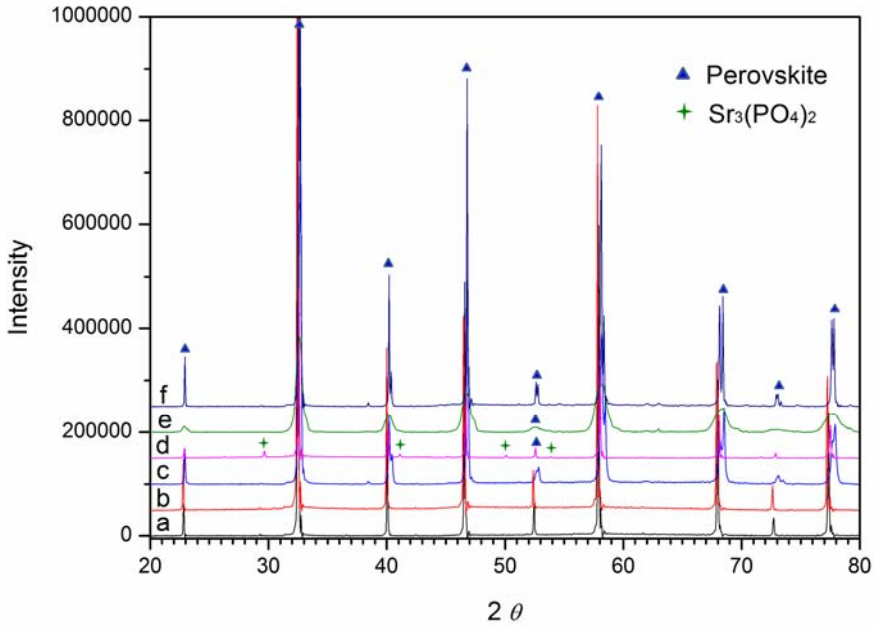

Fig. 7.7 XRD spectra of the LSCF pellets annealed in N_2. (a) LSCF1250N-DH, (b) LSCF1250N-PS, (c) LSCF1000N-DH, (d) LSCF1000N-PS, (e) LSCF700N-DH, (f) LSCF700N-PS.

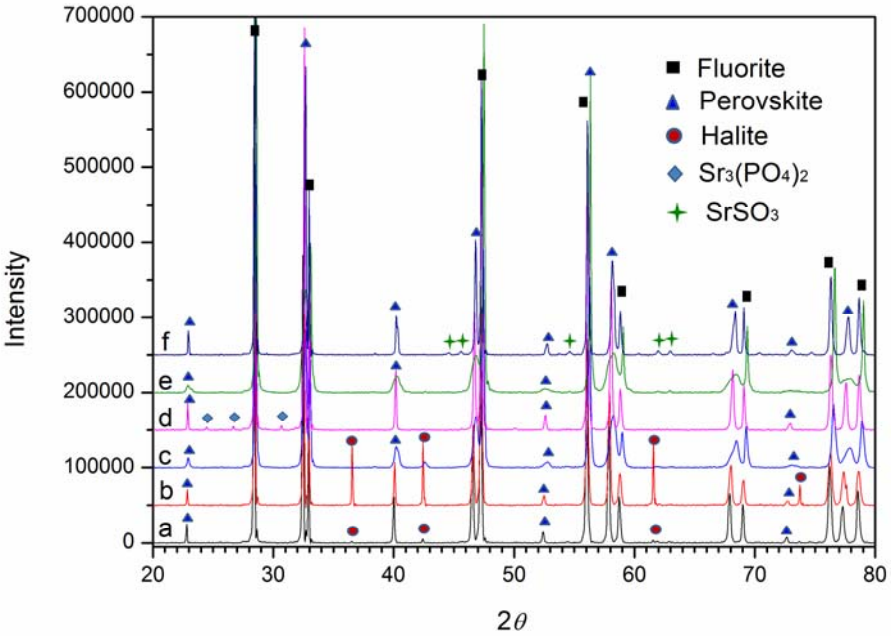

Fig. 7.8 XRD spectra of the LSCF+CGO pellets annealed in N_2. (a) Mix1250N-DH, (b) Mix1250N-PS, (c) Mix1000N-DH, (d) Mix1000N-PS, (e) Mix700N-DH, (f) Mix700N-PS.

in samples annealed at 1250°C and formation of Sr-impurity phases was detected in samples annealed at lower temperature. The amount of the halite phase was evaluated in a semi-quantitative way, using the ratio between the 100% intensity reflection of the halite phase and that of the cubic CGO phase. As shown in Table 7.2, more halite formation was observed in the pre-sintered samples as compared to the as-pressed ones.

Table 7.8 Average phase compositions determined by EDS for the samples annealed at 1250°C in N_2 [§]

Sample	Phase	La cat.%	Sr cat.%	Co cat.%	Fe cat.%	Ce cat.%	Gd cat.%	Mg cat.%
LSCF1250N-DH	Perovskite	32.31	19.49	9.99	38.21			
	CoO_x	0.79		94.92	0.76			3.53
LSCF1250N-PS	Perovskite	32.06	19.81	10.08	38.05			
	CoO_x	2.67		92.25	2.28			2.8
Mix1250N-DH	Fluorite	10.14				82.69	7.17	
	Perovskite	26.34	20.4	8.31	38.71	4.63	1.61	
	Halite			100				
Mix1250N-PS	Fluorite	7.88				85.28	6.84	
	Perovskite	27.33	18.58	7.99	38.66	4.99	2.24	
	Halite			97.49		1.24		1.27
Mix1400	Fluorite	9.15				83.53	7.32	
	Perovskite	27.25	18.77	9.42	36.37	6.08	2.08	

[§]: The oxygen partial pressure in N_2 is close to 10^{-4} bar.

The SEM/EDS results for the LSCF samples annealed at different temperatures in N_2 are presented in Fig. 7.9 and Tables 7.8-7.10. The sample annealed at 1250 °C (Fig. 7.9a) consists of perovskite plus a small amount of Co-rich phase, which is most probably formed due to the A site deficiency. The samples annealed at low temperature contain also Sr-impurity phases, which is a Sr-P-O phase for the samples annealed at 1000 °C and a Sr-S-O phase at 700 °C. Same as in the sample LSCF700A-PS, the Sr-S-O phase is only visible in a SE image (Fig. 7.9d), co-existing with the perovskite and halite phases. The phase compositions were summarized in Table 7.9−7.10.

For the LSCF+CGO mixture samples annealed in N_2 at 1250 °C, secondary phase formation is clearly seen in the SEM images (Fig. 7.10a and 7.10b), with the white phase as CGO fluorite, the grey phase as LSCF perovskite and the black phase as CoO halite. The compositions of these phases are listed in Table 7.8. The amount of the halite phase was found to be higher in the pre-sintered samples. The formation of a halite phase may be caused by inter-diffusion between CGO and LSCF, since much higher amount of halite phase was found on the LSCF+CGO pellets (Fig.7.10b) than the pure LSCF pellet under the same condition (Fig.7.9b). The amount of the

halite phase on the pure LSCF pellets is too small to be detected by XRD. The Sr-P-O phase was found in the DH-type samples annealed at 1000°C (Fig. 7.9c) and the EDS determined phase compositions are listed in Table 7.9. For the sample annealed at 700 °C, no secondary phase is visible in the BSE image (Fig. 7.10d). However, Sr-rich particles, which are in sub-micron scale, are visible from the SE image (Fig. 7.10e). The phase compositions determined by EDS are listed in Table 7.10.

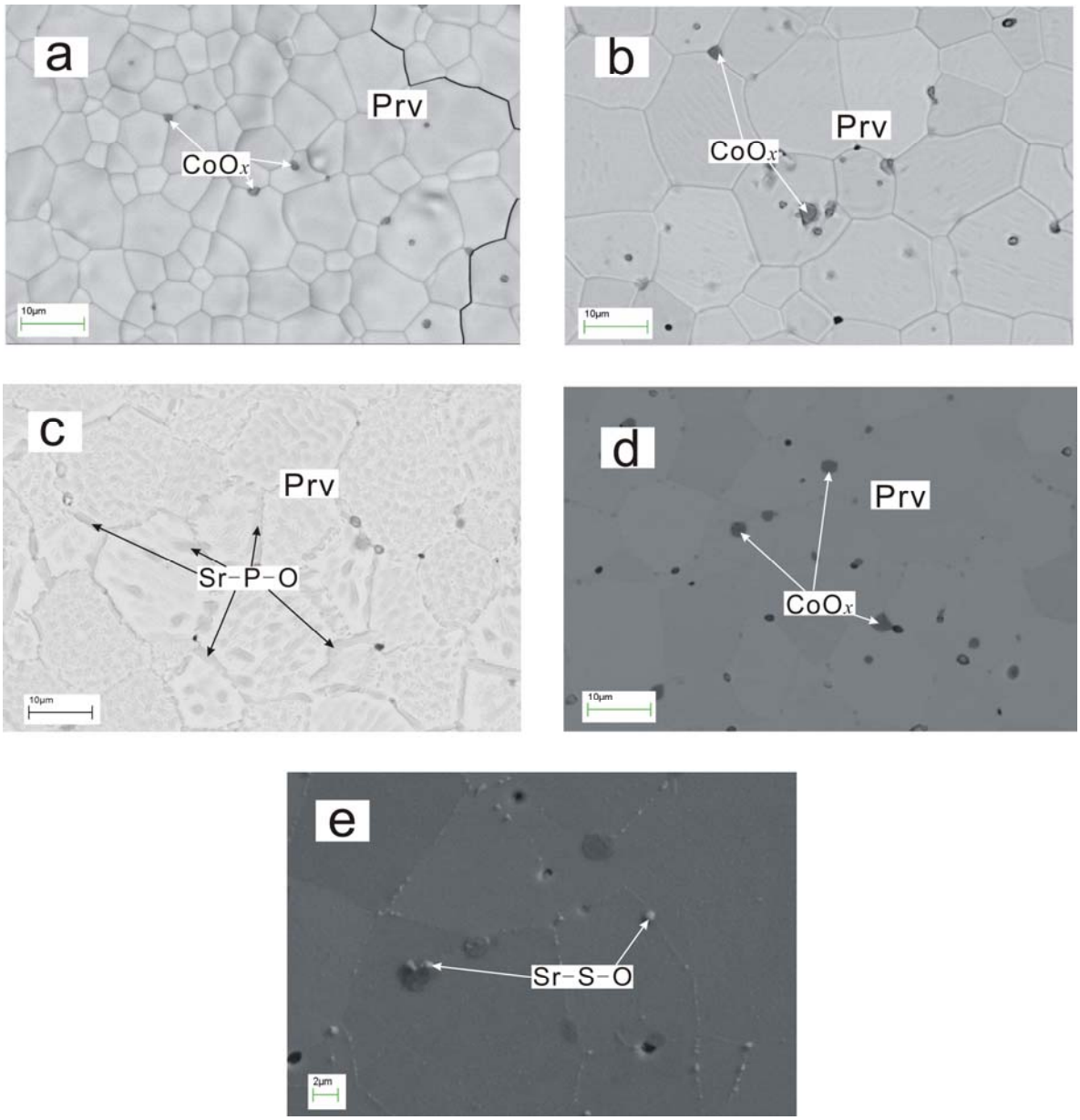

Fig. 7.9. SEM BSE images showing the upper surface of the LSCF samples annealed in N_2. (a) LSCF1250N-DH; (b) LSCF1250N-PS; (c) LSCF1000N-PS; (d) LSCF700N-PS; (e) SE image of the same place as (d) (different magnification).

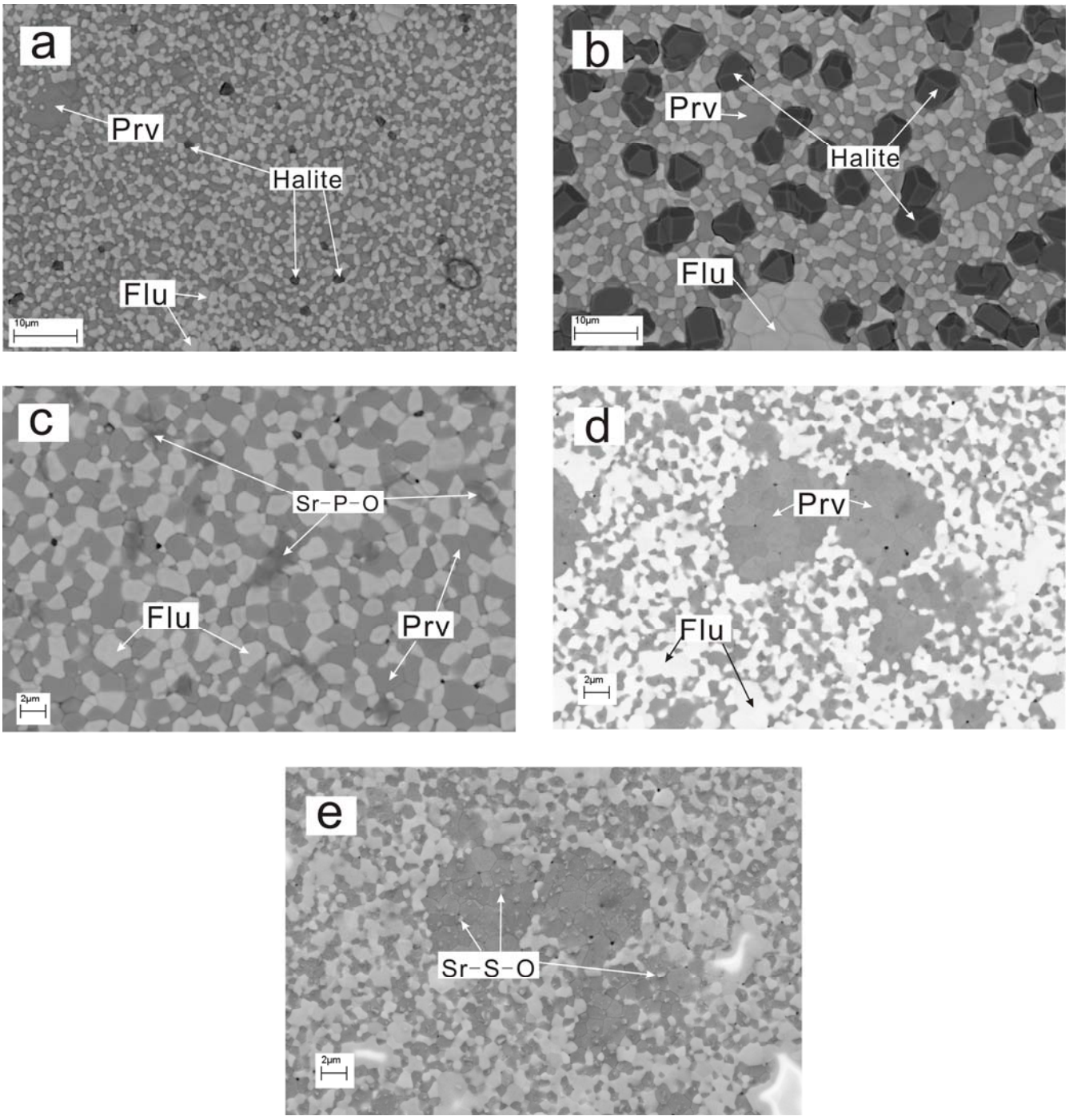

Fig. 7.10. SEM BSE images showing the upper surface of the LSCF+CGO mixture samples annealed in N_2. (a) Mix1250N-DH; (b) Mix1250N-PS; (c) Mix1000N-PS (d) Mix700N-PS; (e) SE image showing the same place as (d).

Table 7.9 Average phase compositions determined by EDS for the samples annealed at 1000°C in N_2 [§]

Sample	Phase	La cat.%	Sr cat.%	Co cat.%	Fe cat.%	Ce cat.%	Gd cat.%	P cat.%	Mg cat.%
LSCF1000N-PS	Perovskite	32.31	19.66	9.96	38.37				
	Sr-P-O		52.77					47.23	
	CoO_x	1.15	2.49	87.37	2.91			1.28	4.8
Mix1000N-PS	Fluorite	7.24				85.23	7.53		
	Perovskite	27.36	19.07	8.81	37.12	5.19	2.45		
	$Sr_3(PO_4)_2$		52.12					47.88	

[§]: The oxygen partial pressure in N_2 is close to 10^{-4} bar.

Table 7.10 Average phase compositions determined by EDS for the samples annealed at 700°C in N_2 [§]

Sample	Phase	La cat.%	Sr cat.%	Co cat.%	Fe cat.%	Ce cat.%	Gd cat.%	S cat.%	Mg cat.%
LSCF700N-PS	Perovskite	32.30	19.04	9.67	38.99				
	$(Co,Fe)O_x$	0.84		90.21	7.07				1.88
	Sr-rich precipitate	26.77	22.63	10.55	31.59			8.46	
Mix700N-PS	Fluorite	6.59				87.6	5.81		
	Perovskite	29.27	17.91	9.35	36.52	5.25	1.7		
	Sr-rich precipitate	23.11	24.5	7.74	38.18		6.74		

[§]: The oxygen partial pressure in N_2 is close to 10^{-4} bar.

7.3.2 LSCF-CGO diffusion couple

The results on the LSCF/CGO diffusion couples are presented in Table 7.11 and Fig. 7.11−7.14. On the CGO side of the interface, a significant amount of Sr-rich phase was found in the samples heat treated in air or in N_2. The Sr-rich phase appears as the dark phase in the BSE images shown in Fig. 7.12. XRD pattern fitting indicates that it is Sr_2SiO_4 for the sample annealed in air (CGO-A). The EDS determined phase compositions for CGO-A are presented in Table 7.12. No dissolution of elements from LSCF into CGO was detected by EDS. For the sample annealed in N_2, the amount of the Sr-rich phase is too small to allow for phase identification by XRD. A small peak at a 2θ angle of around 40° indicates that it is not Sr_2SiO_4. EDS analysis can only confirm that it is a Sr-rich oxide. These results indicate that during heat treatment at 1200˚C, Sr from LSCF segregated out to the LSCF-CGO interface (and may further diffuse into CGO), and reacted with impurities there. More Sr-rich phase formed in air than in N_2 which indicates the segregation of Sr is influence by oxygen partial pressure.

Table 7.11 Summary of the results obtained on the diffusion couple samples

Samples No.	Heat treatment	Phase detected by XRD¤	SEM/EDS result¤
LSCF1400	Pre-sintered reference, no heat treatment	Prv +small peak	Prv
LSCF-A*	diffusion couple, heated in air at 1200˚C for 5 days	Prv +small peak	Prv
LSCF-N	diffusion couple, heated in N_2 at 1200˚C for 5 days	Prv +small peak	Prv
CGO1450	Pre-sintered reference, no heat treatment	Flu	Flu
CGO-A	diffusion couple, heated in air at 1200˚C for 5 days	Flu + Sr_2SiO_4	Flu+ Sr_2SiO_4
CGO-N	diffusion couple, heated in N_2 at 1200˚C for 5 days	Flu +small peak	Flu + Sr-rich phase

*: A denoted samples heat treated in air and N denoted samples heat treated in N_2. The oxygen partial pressure in N_2 is close to 10^{-4} bar.
¤: Prv means the perovskite phase while Flu means the fluorite phase.

Table 7.12 Average phase compositions determined by EDS on CGO-A, CGO-N, and CGO1450 (reference)

Sample	Phase	Ce cat.%	Gd cat.%	Sr cat.%	Ca cat.%	Si cat.%	Mg cat.%	Co cat.%
CGO1450	Fluorite	90.91	9.09					
CGO-A	Fluorite	89.17	10.83					
	Sr_2SiO_4			50.16	2.47	47.37		
CGO-N	Fluorite	90.51	9.49					
	Sr-rich phase	14.97	3.05	45.73	9.67		0.76	25.82

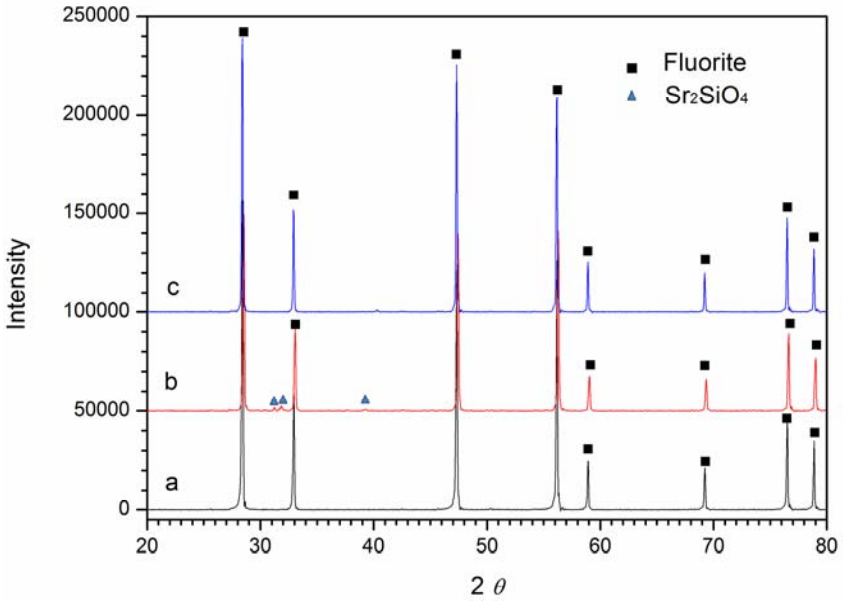

Fig. 7.10. XRD spectra on the CGO side of diffusion couples. a) CGO1450, b) CGO-A, c) CGO-N.

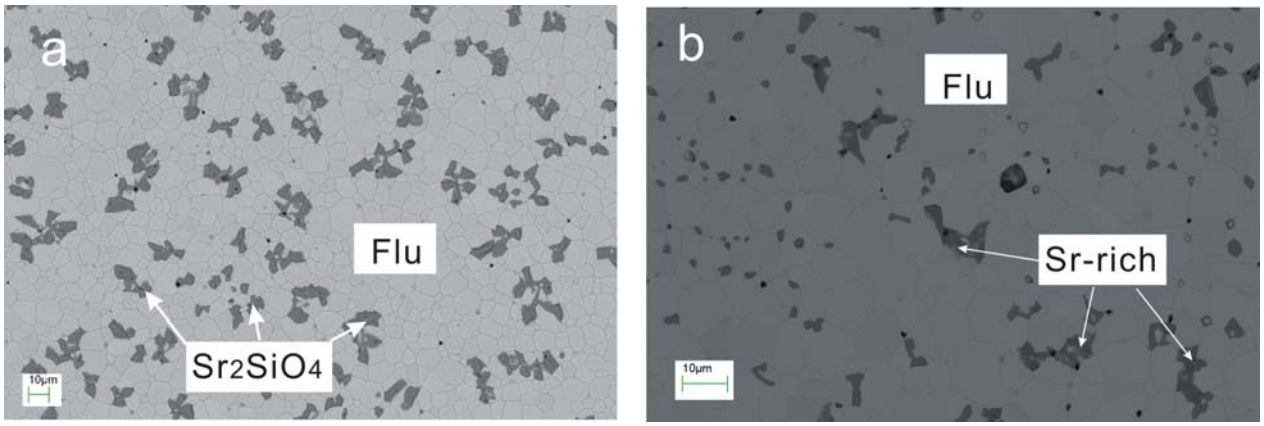

Fig. 7.11 SEM BSE images showing surface of the CGO side of the diffusion couples. a) CGO-A and b) CGO-N.

On the LSCF side, no dissolution of Ce or Gd into LSCF was detected. XRD pattern (Fig. 7.12 b and c) indicate a small amount of CGO existing along with the LSCF phase. This is due to the fact that some CGO was stuck to the LSCF pellet surface, which is clearly visible after dismounting the diffusion couples. SEM/EDS analyses (Fig. 7.13) further confirm formation of the $(Co,Fe)O_x$ phase, which exists mainly at the grain boundaries. The EDS measured phase compositions are listed in Table 7.13. Interestingly, the Sr-rich phase is found only on the CGO surface, but not on the LSCF surface.

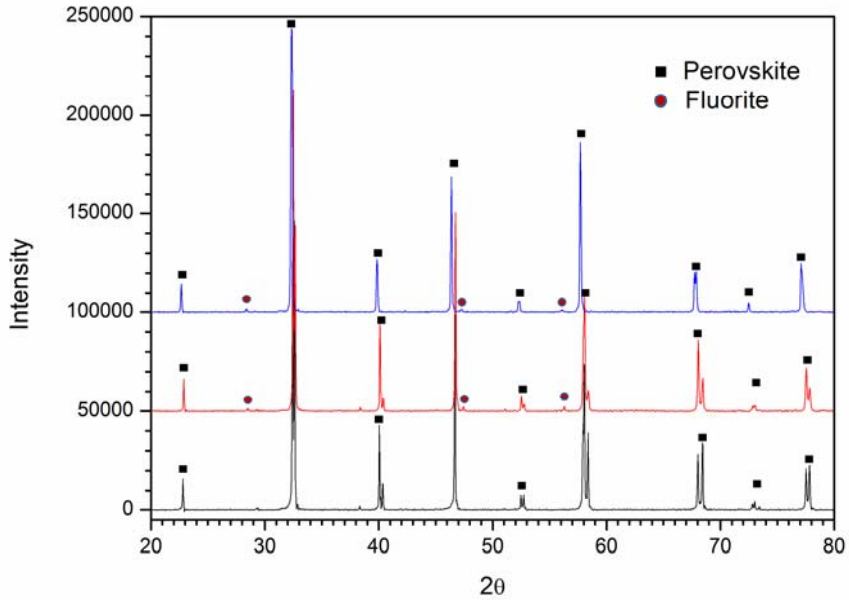

Fig. 7.12. XRD spectra of the LSCF side of diffusion couples. a) LSCF1400, b) LSCF-A, c) LSCF-N.

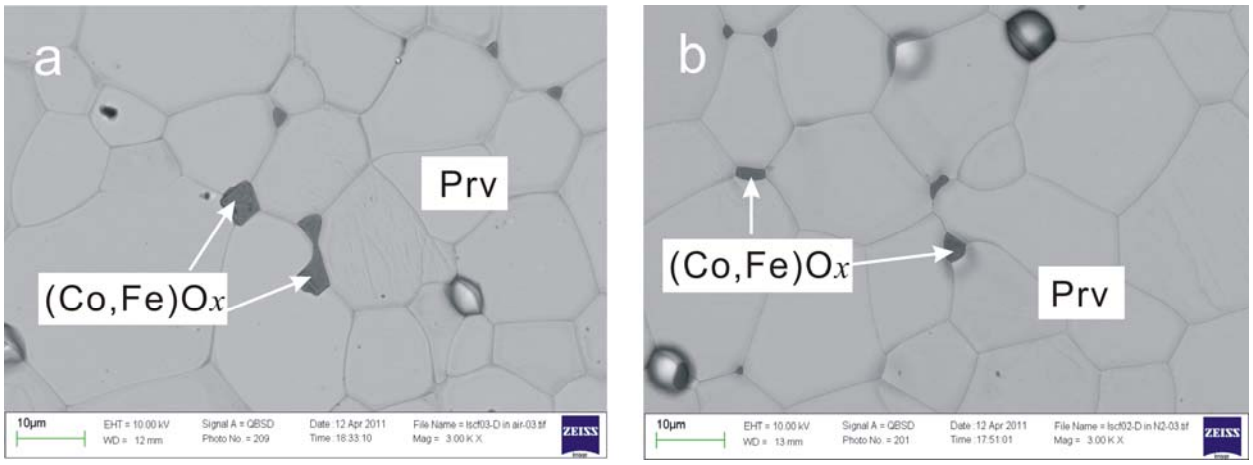

(a) (b)

Fig. 7. 13. SEM BSE images showing surface of the LSCF side of diffusion couples (a) LSCF-A and (b) LSCF-N surface.

Table 7.13 Average phase compositions determined by EDS on LSCF-A and LSCF-N as compared to the reference LSCF1400

Sample	Phase	La cat.%	Sr cat.%	Co cat.%	Fe cat.%
LSCF1400	Perovskite	32.82	19.27	9.01	38.9
	$(Co,Fe)O_x$			85.07	14.93
LSCF-A	Perovskite	31.6	18.87	10.31	38.22
	$(Co,Fe)O_x$			97.45	2.55
LSCF-N	Perovskite	30.69	18.57	11.94	38.8
	$(Co,Fe)O_x$			95.57	4.46

7.4 Discussion

7.4.1. LSCF and CGO interdiffusion

The results presented above confirm that there is no direct reaction between LSCF and CGO. However the dissolution of La into the fluorite phase and dissolution of Ce and Gd into the perovskite phase were detected in the mixture samples annealed at high temperatures (>1000°C). No dissolution of Sr, Fe and Co into CGO was found. This agrees with the results from Izuki *et al.* [7], who reported shallow diffusion profile for Sr, Fe and Co in CGO. The intensive inter-diffusion of La into CGO and Ce and Gd into LSCF is due to large phase mutual solubility. Du *et al.* reported a large solubility of La in ceria [8] (around 40 mol.% in air at 700°C). The solubility of Ce and Gd in LSCF has not been reported in the literature– however, both $Sr_{1-x}Gd_xFeO_3$ and $Sr_{1-x}Ce_xFeO_3$ phases have been synthesized and described in literatures [15-17].

Inter-diffusion between LSCF and CGO takes place predominantly at high temperatures (>1000°C), which is relevant for cell manufacturing. Izuki *et al.* [7] measured the bulk diffusion coefficients of La and Sr in CGO (Table 7.14). According to the diffusion depth equation $x_{diff} = 2\sqrt{Dt}$ derived from Fick's second law, the distance for diffusion of 1000h was calculated. It shows that the inter-diffusion at cell operating temperature at 700°C is limited.

Table 7.14 Diffusion coefficients of La and Sr in CGO10

Element	Temperature (°C)	Diffusion Coefficient (cm^2s^{-1})	Distance for 1000h diffusion (nm)
La	700	4.85×10^{-22}	0.418
	1000	4.16×10^{-17}	122.3
	1100	6.13×10^{-16}	469.8
	1250	1.76×10^{-14}	2.51×10^{3}
Sr	700	7.25×10^{-21}	1.6
	1000	8.14×10^{-17}	171.0
	1100	7.38×10^{-16}	515.4
	1250	1.17×10^{-14}	2.48×10^{3}

The present study indicates that the LSCF perovskite phase is more stable in air than in N_2. Dissolution of Ce and Gd into LSCF and loss of La in N_2 is accompanied by formation of a small amount of CoO secondary phase.

It should be noted that inter-diffusion between LSCF and CGO changes also thermal expansion of the adjacent layers which could lead to deterioration of the mechanical strength of the LSCF–CGO interface.

7.4.2. Sr segregation out of LSCF and formation of Sr-impurity phases

The present studies show Sr diffuses or volatilizes out of LSCF, and further reacts with impurities forming Sr-rich phase on the sample surface. The secondary phases and Sr-impurity prefer forming or segregating at the grain boundaries. Sr segregation on sample surface is not driven by dissolution of Ce and Gd into LSCF, as this was observed both in the LSCF+CGO mixture samples and in LSCF samples. The Sr segregation could be an intrinsic or impurity activated process. Surface precipitation of Sr-rich phase was also observed recently by Oh *et al.* [18] at 600°C–900°C in air, N_2 and 0.1%O_2 in argon. They regarded this phenomenon as an intrinsic process. The phase information or crystal structure was not determined in their study. In our study, the Sr-rich phase was determined to be a Sr-P-O phase for samples annealed at

high temperatures (≥1000°C) and a Sr-S-O phase at low temperature (700°C). The amount of the Sr-impurity phase increases with increasing temperature, which can be explained by high Sr activity in LSCF at high temperature. The influence of oxygen partial pressure on the amount of formed Sr-rich phase is however not clear from our study on the LSCF samples. On the other hand, for the diffusion couple samples, more Sr-rich phase formed in air than in N_2, which is in agreement with the findings from Oh *et al.* [18]. However, the influence of oxygen partial pressure on Sr segregation shall be further studied.

In the diffusion couple experiments, Sr-impurity phases were found on CGO surface but not on the LSCF surface.

7.5 Conclusions

In the present work, the stability of LSCF and its reaction with CGO were studied at different temperatures in air or N_2. The following can be concluded:

1) There is no direct reaction between LSCF and CGO.

2) Inter-diffusion between LSCF and CGO predominantly takes place at high temperatures (T=1400 °C or T=1250 °C). La diffusion into CGO and Ce and Gd into LSCF was detected. The inter-diffusion of La and Ce/Gd between the two phases was further observed to be accompanied by a formation of a halite secondary phase (presumably CoO). The diffusion is strongly thermally activated - there are hardly any differences to be observed between the samples aged at 700 and 1000 °C. At 1250 °C however, significant interdiffusion is observed both by EDS and by XRD. For the samples that have been presintered 5 hours at 1400 °C it makes no change to the degree of interdiffusion to heat treat the samples 100 hours at 1250 °C or for longer periods of up to 2000 hours at 700 °C.

3) Sr is a mobile element in LSCF. It diffuses or volatilizes out of LSCF, and further reacts with impurities forming Sr-rich phase on the sample surface. The Sr-rich phase was determined to be Sr-P-O for samples annealed at high temperature and Sr-S-O at low temperature. The formation of Sr-rich phase can be intrinsic, but can also be activated by presence of impurities. The tendency of Sr segregation increases with increasing temperature and maybe also with increasing oxygen partial pressure (based on the results for diffusion couples). Further studies are needed to clarify how Sr segregation is influenced by the experimental conditions.

4) At the LSCF−CGO interface, Sr-rich phases were found on CGO surface. The Sr was diffused from LSCF into CGO.

References

[1] W.G. Wang, M. Mogensen, Solid Sate Ionics 176 (2005) 457–462.

[2] A. Esquirol, J. Kilner, N. Brandon, Solid State Ionics 175 (2004) 63–67.

[3] A. Mai, V.A.C. Haanappel, F. Tietz, D. Stöver, Solid State Ionics 177 (2006) 2103–2107.

[4] N. Jordan, W. Assenmacher, S. Uhlenbruck, V.A.C. Haanappel, H.P. Buchkremer, D. Stöver, W. Mader, Solid State Ionics 179 (2008) 919–923.

[5] A. Mai, M. Becker, W. Assenmacher, F. Tietz, D. Hathiramani, E. Ivers-Tiffée, D. Stöver, W. Mader, Solid Sate Ionics, 177 (2006) 1965–1968.

[6] A. Tsoga, A. Naoumidis, D. Stöver, Solid State Ionics 135 (2000) 403–409.

[7] M. Izuki, M.E. Brito, K. Yamaji, H. Kishimoto, D.-H. Cho, T. Shimonosono, T. Horita, H. Yokokawa, J. Power Sources 196 (2011) 7232–7236.

[8] Y. Du, M. Yashima, T. Koura, M. Kakihana, M. Yoshimura, CALPHAD 20 (1996) 95–l08.

[9] A. Martínez-Amesti, A. Larraňaga, L.M. Rodríguez-Martínez, A.T. Aguayo, J.L. Pizarro, M.L. Nó, A. Laresgoiti, M.I. Arriortuaa, J. Power Sources 185 (2008) 401–410.

[10] N. Sakai, H. Kishimoto, K. Yamaji, T. Horita, M.E. Brito, H. Yokokawa, J. Electrochem. Soc. 154 (2007) B1331–B1337.

[11] N. Sakai, H. Kishimoto, K. Yamaji, T. Horita, M.E. Brito, H. Yokokawa, ECS Trans. 7 (2007) 389–398.

[12] S. Uhlenbruck, T. Moskalewicz, N. Jordan, H.-J. Penkalla, H.P. Buchkremer. Solid Sate Ionics 180 (2009) 418–423.

[13] S.P. Simner, J.F. Bonnett, N.L. Canfield, K.D. Meinhardt, J.P. Shelton, V.L. Sprenkle, J.W. Stevenson, J. Power Sources 113 (2003) 1–10.

[14] H. Yokokawa, H. Tu, B. Iwanschitz, A. Mai, J. Power Sources 182 (2008) 400–412.

[15] C.R. Dyck, R.C. Peterson, Z.B. Yu, V.D. Krstic, Solid State Ionics 176 (2005) 103-108.

[16] J. Blasco, J. Stankiewicz, J. Garcia, J. Solid State Chem. 179 (2006) 898-908.

[17] S. Deganello, L.F. Liotta, A. Longo, M.P. Casaletto, M. Scopellitti, J. Solid State Chem. 179 (2006) 3407-3419.

[18] D. Oh, D. Gostovic, E.D. Wachsman, J. Mater. Res. 27 (2012) 1992–1999.

Chapter 7 An experimental study of reactions between $La_{0.58}Sr_{0.4}Co_{0.2}Fe_{0.8}O_{3-\delta}$ and $Ce_{0.9}Gd_{0.1}O_{3-\delta}$

Chapter 8

Post-mortem analysis of an LSCF/CGO cathode after long term SOFC testing

Abstract

Degradation phenomena of LSCF/CGO cathodes were investigated via post-mortem analyses of an SOFC tested at 700 °C for 2000h using techniques including SEM, SIMS and TEM. Similar studies were also carried out on a reference non-tested cell. The analyses were focused on the LSCF/CGO cathode and the CGO barrier layer, as various evidences have pointed the degradation of this type of IT-SOFC to the cathode side. SEM/EDS and SIMS were used to investigate inter-diffusion across the barrier layer–electrolyte interface and the barrier layer–cathode interface. SIMS was employed to investigate impurity distribution. Finally TEM/EDS alone was employed to examine phase stability of the LSCF and phase separation or secondary phase formation on a nano-meter scale. The results show that the inter-diffusion across the cathode–barrier layer interface and the barrier layer – electrolyte interface happened mainly during sintering, and to a very little degree while long-term SOFC testing. Therefore, it shall not be counted as a major degradation mechanism. Partial phase separation of LSCF took place primarily at the cathode–barrier layer interface and may be a reason for the observed cell degradation.

8.1 Introduction

Recent research efforts on SOFC (solid oxide fuel cell) technology focus on cost reduction and improvement on performance, durability and reliability [1]. One strategy is to reduce the operating temperature from about 1000 °C to intermediate operating temperature (IT) of 600−800 °C which brings both economic and technical benefits. High performance cathode materials are investigated for IT-SOFCs. Lanthanum strontium cobalt ferrite (LSCF), with high electronic and ionic conductivity at intermediate temperature, is regarded as one of the best cathodes. CGO (gadolinium doped ceria) with high oxide ion conductivity, is often mixed with LSCF forming a composite cathode [2,3] in order to obtain high oxygen diffusivity and fast surface exchange kinetics. CGO is also used as an interlayer between the LSCF cathode and the YSZ (Yittria Stabilized Zirconia) electrolyte for impeding undesired secondary phase formation [4−6]. The SOFCs with LSCF/CGO cathode, CGO barrier layer, state of the art YSZ electrolyte and Ni-YSZ anode exhibit great initial performance at intermediate temperature [2, 7]. However, cells degrade over extended periods of time [8]. A number of studies on testing of such IT-SOFCs show that the degradation originated mainly from the cathode side [9−11].

To date, the degradation mechanisms for the LSCF-based cathodes are ambiguous. In literature, the degradation of IT-SOFCs with LSCF cathode and CGO barrier layer can be attributed to 1) LSCF is chemically [12] and/or structurally [2] unstable; and 2) it interacts with other components (e.g. CGO barrier layer [13] and/or YSZ electrolyte [6, 14, 15]) or other species (e.g. impurities [16, 17]). However, the processes that play a dominant role for the degradation and their relation to cell durability are not fully understood at the moment.

In the present study, in order to clarify the cell degradation mechanisms, a reference cell and a cell after 2000h testing in a stack environment were characterized by techniques including SEM (Scanning Electron Microscopy), EDS (Energy Dispersive Spectroscopy), SIMS (Secondary ion mass spectroscopy), and TEM (Transmission Electron Microscopy). The aforementioned degradation phenomena including phase separation or secondary phase formation, and inter-diffusion were studied with a main focus on cathode−barrier−electrolyte.

8.2 Experiments

8.2.1. Specimens and test condition

Cells investigated in this work were anode-supported SOFCs with Ni-YSZ anode and YSZ electrolyte. The CGO10 ($Ce_{0.9}Gd_{0.1}O_{2-\theta}$) barrier layer and LSCF ($La_{0.58}Sr_{0.4}Co_{0.2}Fe_{0.8}O_{3-\delta}$)/CGO10 cathode were screen printed and sintered separately. The cells were tested in a stack environment at 700˚C for 2000 h. The testing is outside the scope of this thesis. During the long term test, the cathode was fed with air. H_2 with 30 vol.% H_2O was supplied to the anode with a fuel utilization of 50%. The current density was set as 0.52 A/cm^2. The average degradation rate was measured to be 20 mΩ•cm^2/1000h.

8.2.2. Characterization

The cross sections of the reference and tested cells were characterized by both SEM and TEM for visualizing the microstructure, and by SIMS and EDS for elemental distribution and composition analysis. The regions of interest are: i) the LSCF cathode and ii) the cathode−barrier−electrolyte interfaces.

I. SEM/EDS

Both the reference and tested cells were fractured into small pieces and were vacuum embedded in epoxy, ground and polished, and then carbon coated to eliminate surface charging. The samples were characterized using a Zeiss Supra-35 SEM equipped with a field-emission gun and an energy-dispersive X-ray spectrometer. The EDS analysis was performed using the aforementioned SEM in conjunction with Noran System Six software. For backscattered electron (BSE) imaging, an accelerating voltage of 15 keV was used. For EDS analysis, an accelerating voltage of 10−15 keV was used.

II. TOF-SIMS (time-of-flight SIMS)

The samples were vacuum embedded in epoxy, ground and polished. A SIMS experiment was performed with a TOF-SIMS IV (ION-TOF GmbH, Germany) by Kion Norrman. TOF-SIMS imaging of the surface was performed by scanning the primary ion beam which produces a visualization of the distribution of elements or chemical compounds on the surface. Several areas were analyzed with the TOF-SIMS: (i) 500µm×500µm scans were performed on the cross sections of reference and tested cells with high mass resolution spectra (low lateral resolution) covering all

cell layers, (ii) 50μm×50μm scans were performed on the active layers of each cell, (iii) 25μm×25μm scans were acquired, which produce high lateral resolution images with about 200 nm (low mass resolution), focusing on the cathode–electrolyte side for the two cells. The data were post-processed using the TOF-SIMS IV software package (version 4.1). The mass spectral data were calibrated using the software package IonSpec.

III. TEM/EDS

TEM was performed on the tested cell only. The TEM sample was prepared using the focused ion beam (FIB) on the Zeiss Crossbeam 1540XB by Karl Thydén. The FIB was operated at 30 keV during milling. For TEM investigation, a JEOL 3000F TEM/STEM (Tokyo, Japan) operated at 300 keV equipped with a field-emission gun and an EDS system was used. An Oxford Instruments INCA system (Abingdon, United Kingdom) was used for collecting EDS spectra. The TEM analysis was carried out by Hsiang-Jen Wang and Ruth Knibbe.

8.3 Results and discussion

8.3.1 SEM

Fig. 8.1 shows the BSE images on the cross-sections of the cathode side for the reference and tested SOFCs. The white porous layer is the CGO barrier which is sandwiched between a porous LSCF/CGO cathode layer and a dense YSZ electrolyte. EDS area mappings and linescans were performed on the cathode and across the cathode–barrier and barrier–electrolyte interfaces. It was found that the cathode was homogenous, and no evidence of phase separation was found under SEM. The interface between cathode and barrier is well integrated with no reaction products observed. At the barrier–electrolyte interface, formation of a new phase was found for both the reference and tested cells, shown as small grey spots in Fig. 8.1.

Fig. 8.2 presents SEM BSE images at the interface between barrier and electrolyte for the reference and tested cells. The concentration profiles across the interface determined by EDS line scans are also presented along with the BSE images. The intensity signals of different elements were collected from the element mapping over an area shown as the yellow box in Fig. 8.2 and integrated to the line vertical to the interface. Therefore, it provides information of the averaged concentration across the interface.

An enrichment of Sr at the interface was found, indicating formation of a Sr-rich phase, which is speculated to be $SrZrO_3$ [18]. The EDS signals came from a volume of about $1\mu m^3$ in this

measurement. Thus, the lateral resolution shall be larger than 1μm. The accuracy of elemental distributions and concentration profiles is limited by the resolution.

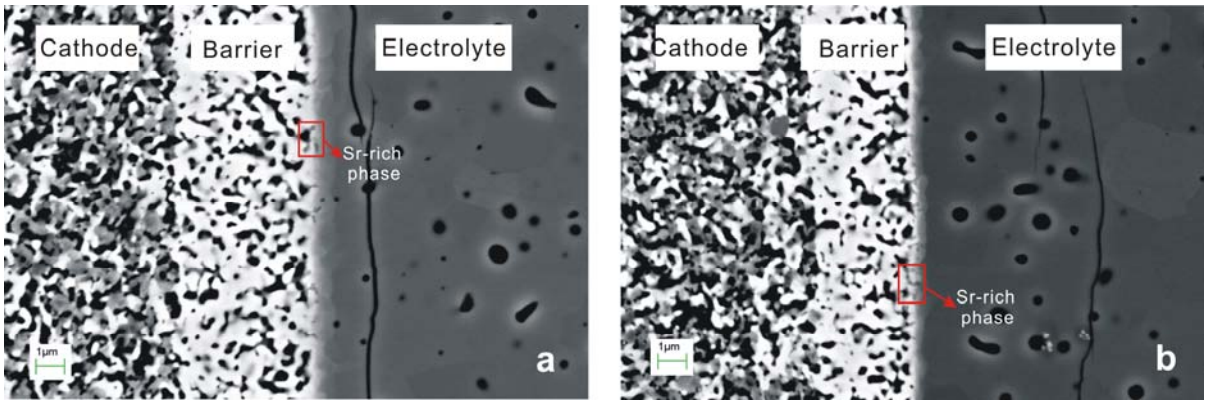

Fig. 8.1 SEM BSE images on the cross-sections of the reference and tested SOFCs (a) reference cell, (b)tesed cell.

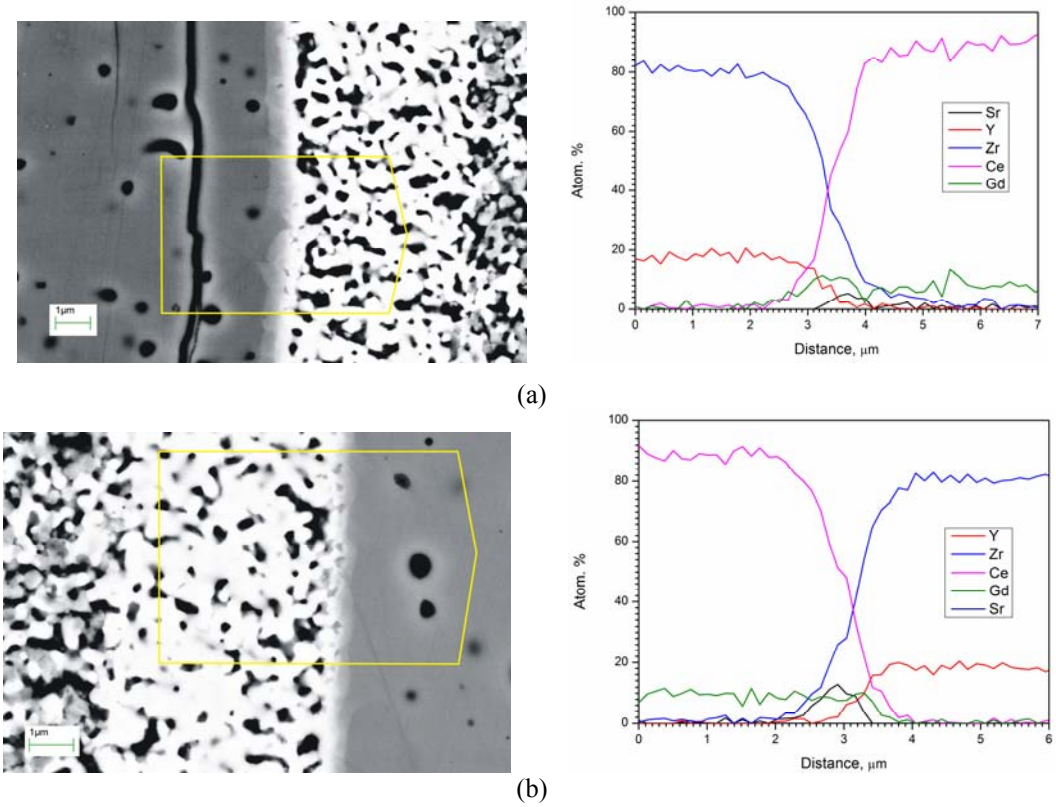

Fig. 8.2 SEM/EDS line scans across the CGO−YSZ interface for the reference and tested SOFCs, (a) reference cell and (b) tested cell.

8.3.2 TOF-SIMS

In SIMS measurements, the signal intensities were acquired by area integration of the mass spectral peaks. Assigning colour shades to the intensities results in an ion image, which displays the lateral distribution of a given species. Fig. 8.3 is the element map of Sr acquired on the reference and tested cells using SIMS. The layers from left to right are the electrolyte, the barrier and the cathode, respectively. It is clear that the SIMS measurements give more information about Sr distribution in CGO and across the CGO–YSZ interface than SEM/EDS measurements. As shown in Fig. 8.3, there is a considerable amount of Sr in the CGO layer for both the reference and tested samples. For the reference cell, Sr is enriched both at the cathode–barrier interface and at the electrolyte–barrier interface. For the tested cell, Sr is distributed all over through the barrier layer, but more at the electrolyte–barrier interface. It is however difficult to make a firm conclusion on formation of Sr zirconate is more severe in the tested cell than in the reference cell or vice versa, given that neither the barrier layer thickness nor the Sr distribution are homogeneous.

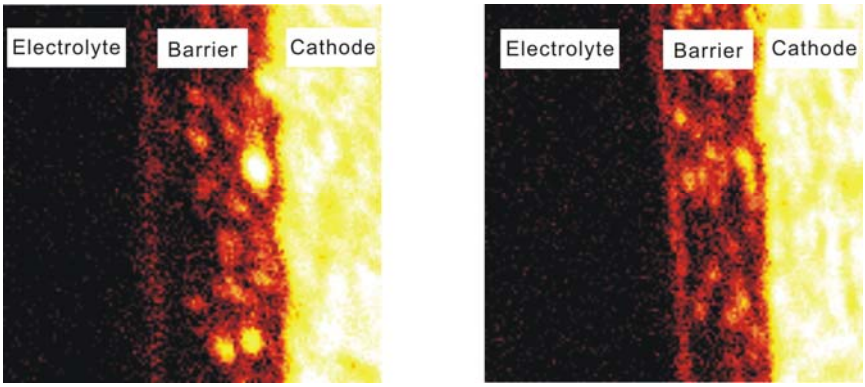

(a) (b)

Fig. 8.3 Element maps of Sr of a 25μm×25μm area over cathode–barrier–electrolyte by SIMS, (a) reference cell and (b) tested cell.

TOF-SIMS was used to determine the concentration profiles. The element line scans at the cathode–barrier and barrier–electrolyte interfaces were made on the TOF-SIMS imaging with a scanning area of 25μm×25μm. The resolution here is about 200nm. The SIMS results are therefore considered to be more accurate than the SEM/EDS results. Fig. 8.4 shows the mapping of the six main elements on the 25μm×25μm area. The diffusion profiles were constructed in the

same way as in EDS analysis. To compare the results of the reference and tested cells, corrections were made on interface position.

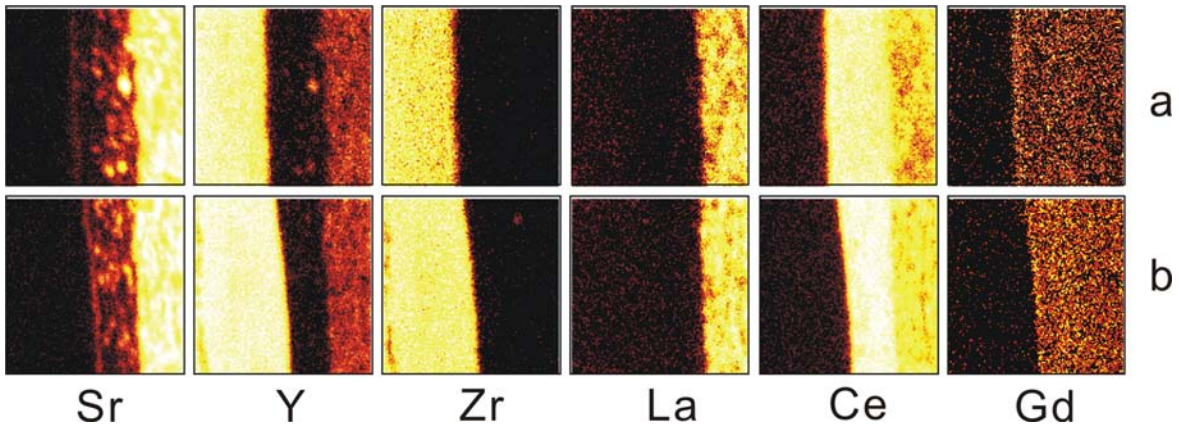

Fig. 8.4. SIMS element maps of a 25μm×25μm area over the cathode–barrier–electrolyte region, (a) reference cell and (b) tested cell. For each box, the layers from left to right are electrolyte, barrier, and cathode.

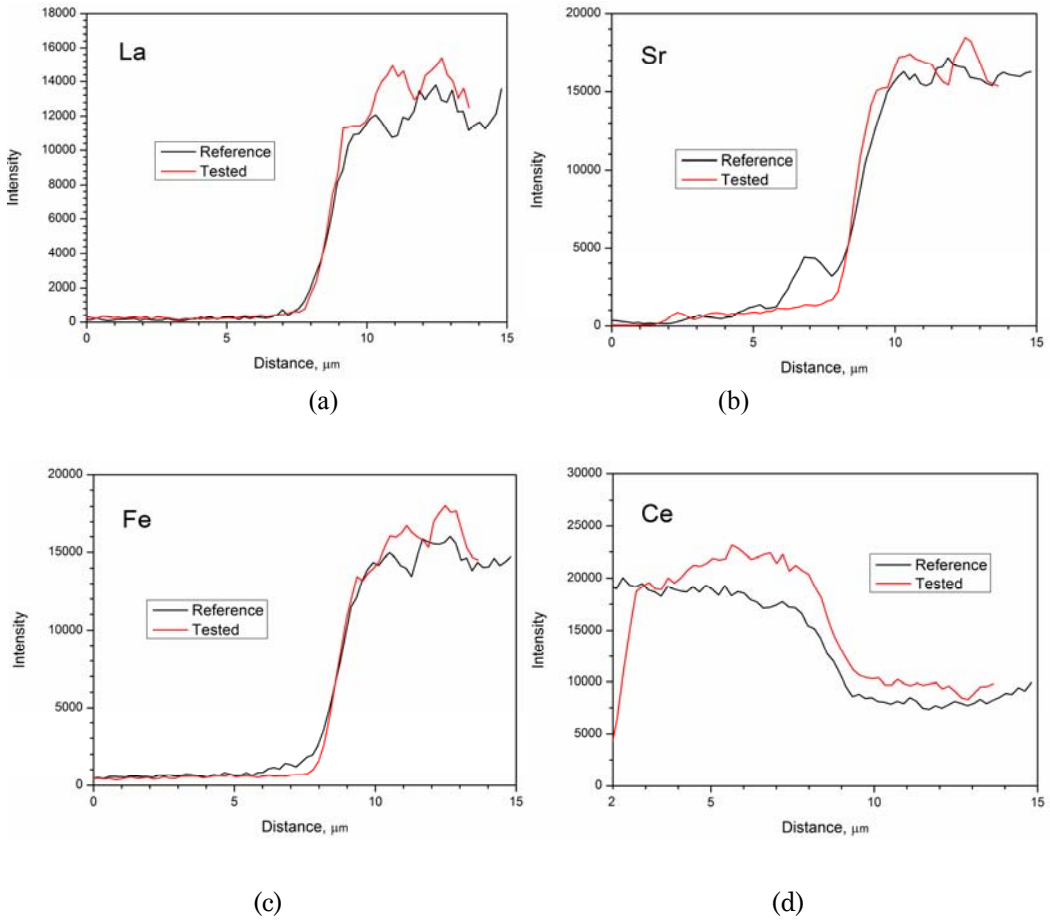

Fig. 8.5 Elemental intensity profiles measured by SIMS across the barrier–cathode interface. (a) La, (b) Sr, (c) Fe, (d) Ce.

Fig. 8.5 shows the elemental profiles across the CGO barrier layer − LSCF/CGO cathode interface, around 8 µm to the left and 6 µm to the right. The profiles indicate that the elements from the cathode side diffuse into CGO barrier layer with a diffusion distance of a few microns. In comparison with the reference cell, the tested cell has similar La inter-diffusion profile but less Fe inter-diffusion. For Ce, different intensities over the CGO layer were observed from the reference and tested cells. For comparison, the Ce intensity was normalized by the highest Ce intensity on each profile (Fig. 8.6a). After normalization, the Ce profile for the tested cell looks very similar to the one of the reference cell. As shown in Fig. 8.5, the Sr intensity in the CGO barrier layer is higher than that of La and Fe. A peak in the Sr diffusion profile was observed for the reference cell, indicating Sr enrichment. The Sr intensity was also normalized and is shown in Fig. 8.6b. The Sr profiles for the two cells are quite similar, with slightly higher intensity for the reference cell.

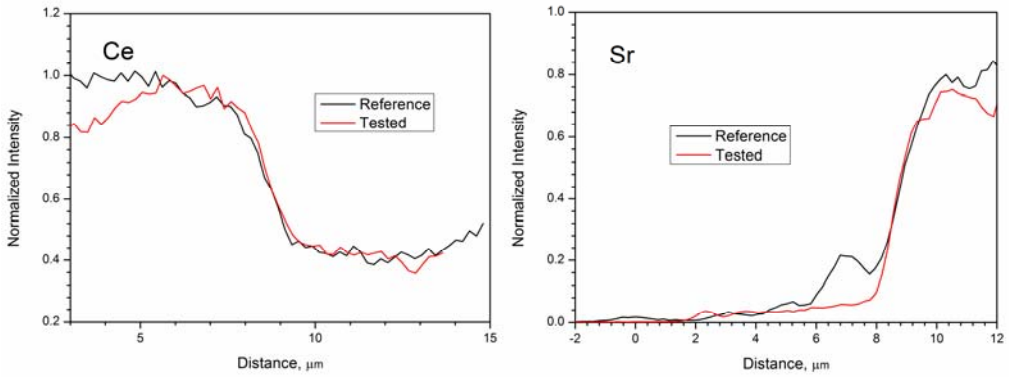

(a) (b)

Fig. 8.6 Normalized Ce and Sr intensities across the barrier−cathode interface. (a) La, (b) Sr. The Ce and Sr intensities were normalized by the highest Ce intensity in bulk CGO.

Fig. 8.7 shows the intensity profile of a linescan across the YSZ electrolyte−CGO barrier interface, around 6 µm to the left and 13 µm to the right. It is clearly shown that the inter-diffusion layer has a thickness of around 2~3 µm and it is quite similar before and after long term testing. It can therefore be concluded that the inter-diffusion layer did not grow much after 2000 hours long term testing at 700 °C.

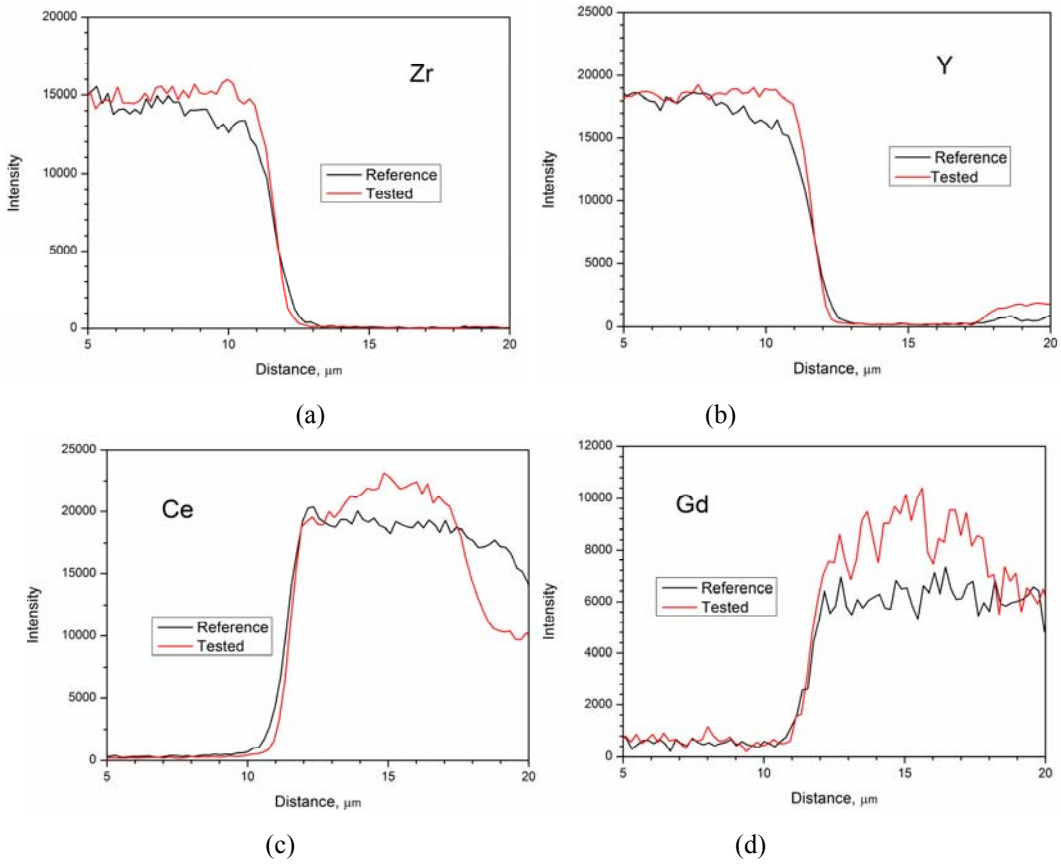

Fig. 8.7 Elemental intensity profiles across the barrier–electrolyte interface measured by SIMS. (a) Zr, (b) Y, (c) Ce, (d) Gd.

By comparing the diffusion profiles at the cathode–barrier and barrier–electrolyte interfaces before and after testing, we found that there is no considerable change in the thickness of the inter-diffusion layer, indicating slow diffusion kinetics at 700 °C. This agrees with the determined diffusion coefficients from literature [19, 20].

TOF-SIMS is very powerful in detecting impurities, especially low concentration impurities in ppm level. It is sensitive to basically all elements even light elements from H to O. SIMS is one of the most sensitive techniques among the commonly-employed surface analytical techniques. However, it cannot be directly used in quantitative analysis, since in principle different response factors associate with different species, i.e. different species produce different signal intensities for equal concentrations.

The species detected in the reference and tested cells include the main species of the cell component materials as well as the following impurities: Na, Mg, Al, Si, K, Ca, and Cr. By analyzing intensity profiles, the location of the different impurities was determined. Fig. 8.8

shows a few examples of TOF-SIMS imaging of 500μm×500μm scans on impurities. It should be noted that the different signal intensities of one element on different substrates may be caused by matrix effects. This analysis yields comprehensive information on composition and lateral distribution of impurity species as well as the size of impurity features. On the reference sample, the impurities homogenously distribute on the cross section. However, on the tested sample, the impurities preferentially congregate in some regions (Fig. 8.8b). Also the impurities signals have higher intensity in the tested cell than in the reference cell. In the cathode (Fig. 8.8), the Cr intensity is much higher in the tested cell than that in the reference one. Cr is homogeneously distributed in the LSCF/CGO cathode layer, unlike what was observed for the LSM cathode where Cr was enriched at the cathode–electrolyte interface [21]. Cr deposition in cathodes has been extensively studied [22–24] and was recently reviewed by Fergus [25]. Cr deposits in cathode as Cr_2O_3 and /or $SrCrO_4$. Its influence on cell stability was reported in a few works [22, 26], which show that both LSM/YSZ and LSCF/CGO cathodes were sensitive to chromium poisoning, with the LSCF/CGO cathode to a less extent than the LSM/YSZ cathode. Different methods to suppress the Cr volatilization are under investigation [12, 25, 27-29] including reducing chromium volatilization with alloying additions, coatings, the selection of electrolyte and electrode materials or compositions.

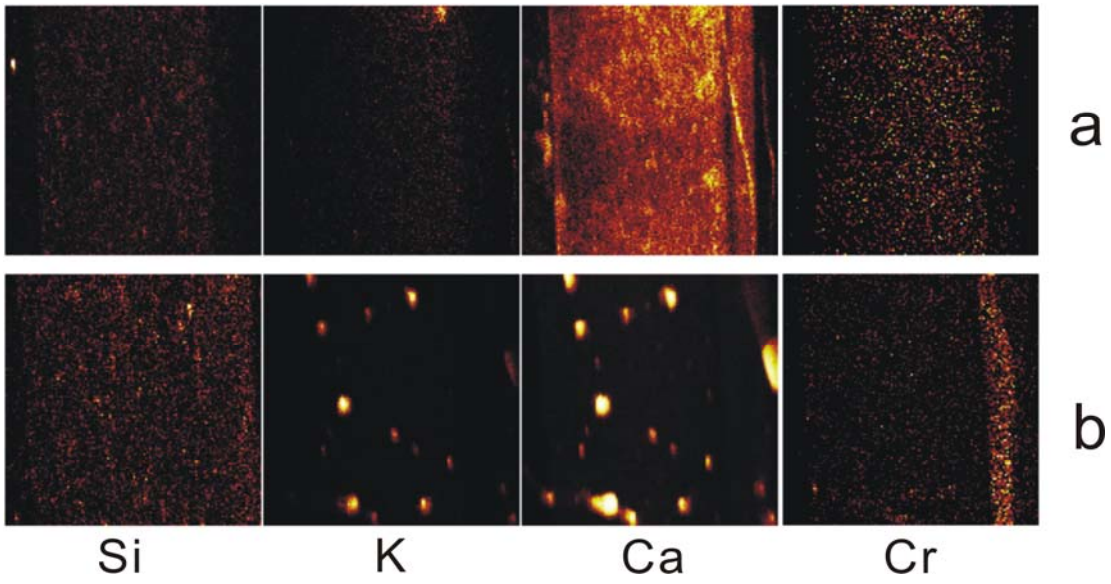

Fig. 8.8. SIMS impurity element maps on a 500μm×500μm area, (a) reference cell, (b) tested cell. For each box, the layers from left to right are anode support, anode, electrolyte, barrier and cathode, respectively.

8.3.3 TEM

The LSCF/CGO cathode investigated in this work was made from nano-sized LSCF and CGO particles, which is beyond the resolution limitation of traditional SEM&EDS. In this study, the LSCF stability and elemental distributions in the tested LSCF/CGO cathode were further examined by TEM/EDS. 14 regions inside the cathode and across the barrier layer were analyzed.

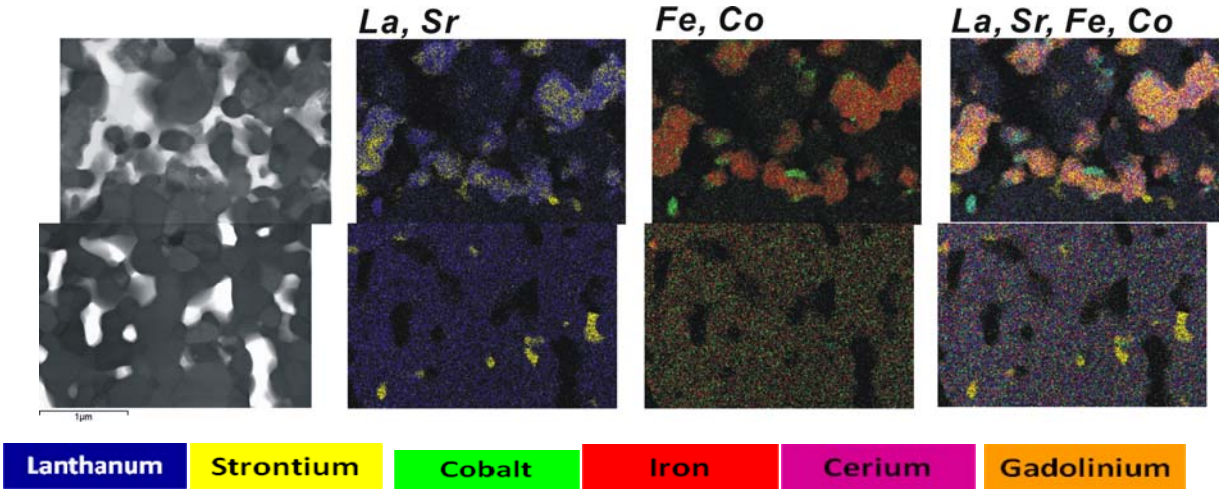

Fig. 8.9. TEM images and element maps over the LSCF/CGO cathode − CGO barrier layer interface. The top images correspond to the LSCF/CGO cathode, and the bottom ones are for the CGO barrier layer.

Fig. 8.9 presents TEM images and element maps on the LSCF/CGO cathode − CGO barrier layer interface. It is clearly shown that the elements are not homogenously distributed in the cathode. In the CGO barrier layer, Sr rich particles which diffused from the cathode are found. Fig. 8.10a shows a TEM image and element maps in a cathode region very close to the cathode−barrier layer interface. It can be observed from Fig. 8.10a that there are some particles rich in La and Co and some rich in Sr and Fe. Fig. 8.10b is an enlarged image for the region ROI8 in Fig. 8.10a – a particle rich in La and Co. A line scan cross this particle is presented in Fig. 8.10c. The particle consists mainly La and Co, while the La content is a bit higher than Co. A small amount of La was found in CGO.

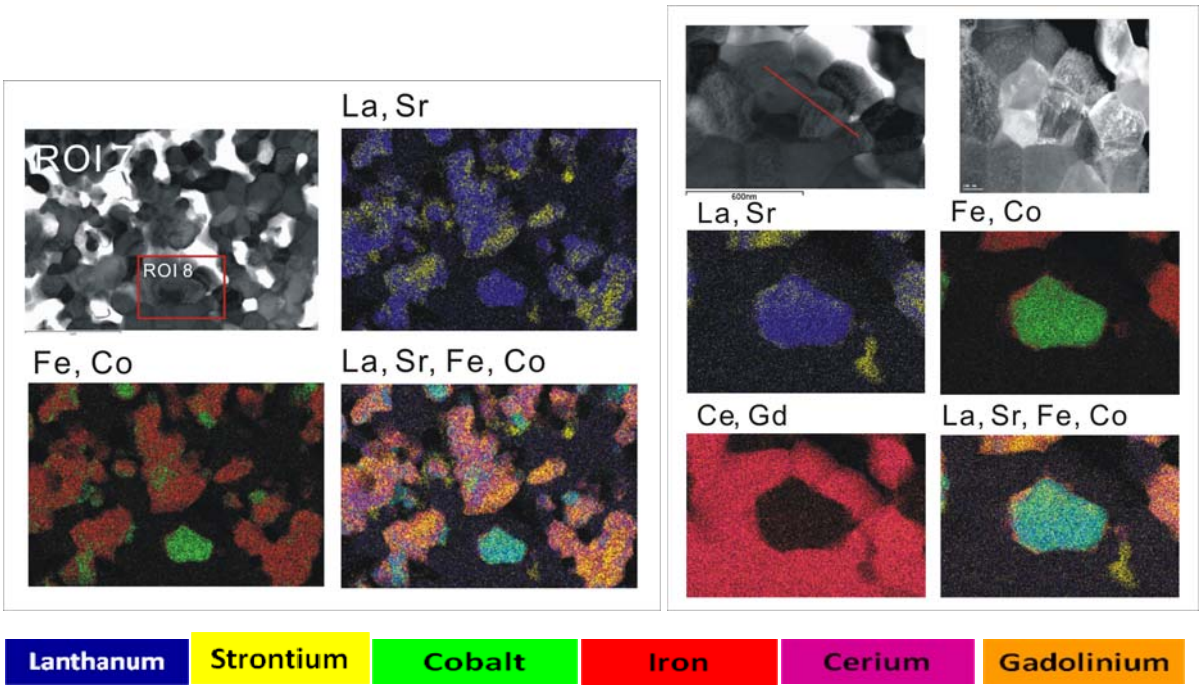

(a) (b)

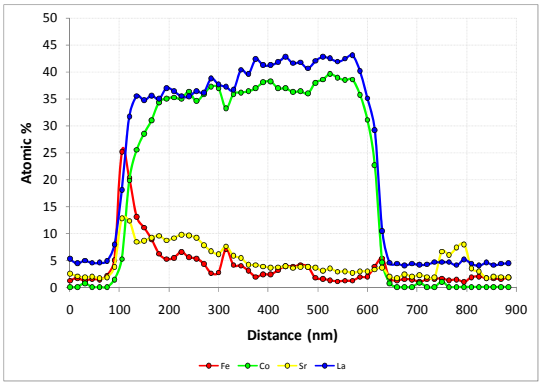

(c)

Fig. 8.10. TEM images, element map and line scan over a region close to the LSCF/CGO cathode − CGO barrier layer interface. a) TEM image and element map over the region ROI7. b) Enlarged image for the region ROI8 in a) — a particle rich in La and Co. c) Line scan on the La and Co rich particle.

Fig. 8.11 shows TEM images and element maps over different regions in the LSCF/CGO cathode. Fig. 8.11a is close to the interface with the CGO barrier layer and Fig. 8.11b is inside the LSCF/CGO cathode. It is clear that the LSCF is more homogeneous inside the cathode further away from barrier (Elements are homogenously distributed except for a few green particles which may be halite or spinel), than the LSCF around interface with barrier layer (phase separations

are clearly visible). The observed tendency that there is a partial phase separation occurring on nano-scale close to the interface, but not deep in the cathode could be a result of the different conditions in the places during test.

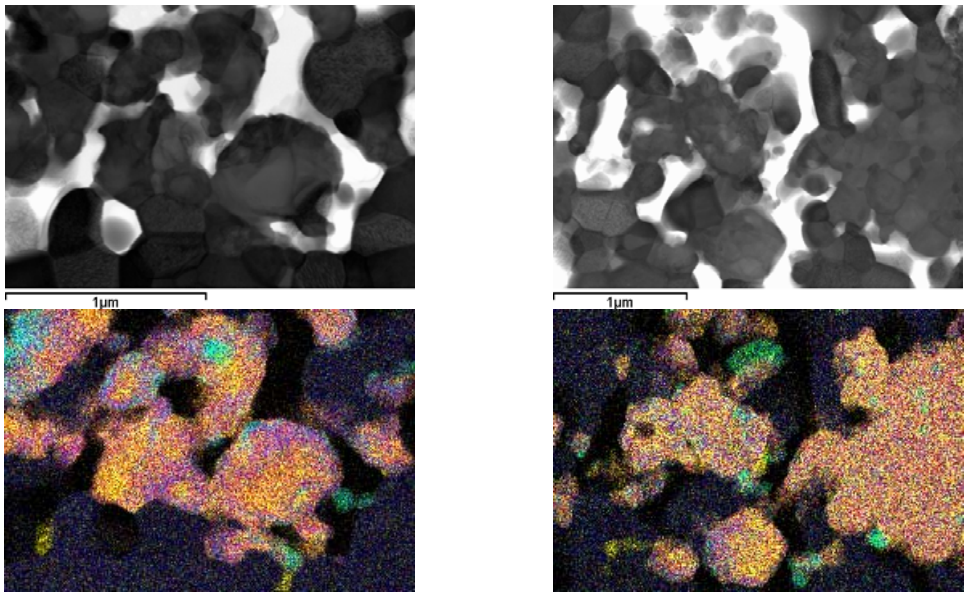

(a) (b)

Fig. 8.11. TEM images and element maps of LSCF/CGO cathode. a) a region near the CGO barrier layer. b) a region inside the LSCF/CGO cathode.

Theoretically, LSCF perovskite has largest tendency to decompose at the lowest PO_2 caused by electrochemical reactions at the active zone. However, by referring to the calculated LSCF phase diagrams (*Chapter 6*, Fig. 6.5), we found that the perovskite material is inside the safety zone during test (perovskite phase is stable at $PO_2 > 10^{-17}$ bar at 700°C). When in contact with CGO, the depletion of La and incorporation of Ce and Gd in LSCF perovskite is another possibility to cause phase decomposition. A $La_{0.58}Sr_{0.4}Gd_{0.01}Fe_{0.8}Co_{0.2}O_{3-\delta}$ powder has been prepared by Uhlenbruck et al. [14]. The powder was calcined at 900°C for 5h in air. Formation of (La, Sr)$_2$(Co, Fe)O_4 and spinel was confirmed by XRD. It can therefore be speculated that inter-diffusion across the LSCF−CGO interface may lead to phase decomposition or secondary phase formation. In *Chapter 7*, we did not detect the phase decomposition after 2000hrs heat treatment at 700 °C for neither the samples pre-sintered at 1400 °C (with La depletion and Ce, Gd incorporation) nor for the directly heated samples (where negligible La depletion and Ce, Gd incorporation is expected on the length scales accessible to XRD and SEM/EDS). As pointed in *Chapter 5*, the pre-sintered

samples reheated at 700°C do not reflect the actual phase stability, since it is hard to achieve equilibrium from sintered dense structure. Thus as a tentative explanation of the inhomogeneities on the nano scale observed by TEM we postulate that first the local composition of both phases change due to elemental inter-diffusion (La depletion and Ce, Gd incorporation in the perovskite) at the cathode sintering temperature (1100 °C). This inter-diffusion tends to destabilize both phases and further during the 2000 hour test especially close to the active cathode where PO_2 is reduced, a beginning phase separation is observed at very short length scales (50-100nm).

8.5 Conclusions

In this work, SEM/EDS, TEM and SIMS techniques were performed on a reference and a tested SOFC with a LSCF/CGO cathode. Significant Sr diffusion to the CGO−YSZ interface was observed by all three techniques for both the reference and tested cells. Sr was found inside the barrier layer and across the barrier−electrolyte interface, forming strontium zirconate. However, the increment of the Sr zirconate phase during cell testing was not verified in this study. Further investigation on contribution of Sr zirconate formation to cell degradation during testing will be needed.

The inter-diffusion regions between cathode and barrier and between barrier and electrolyte are around 2~3 μm in width and didn't grow during long term testing due to slow kinetics at 700 °C. Thus the "inter-diffusion at the interfaces and growth of an interlayer between barrier and electrolyte" does not seem to be the mechanisms to account for the observed 20 $m\Omega \cdot cm^2$/1000h degradation rate.

On the reference sample, the impurities were homogenously distributed on the cross section. However, on the tested sample, the impurities seem to agglomerate in few spots. The SIMS result show that the Cr content in the cathode has increased after cell testing which likely contributes to the observed cell degradation.

An inhomogeneity in the LSCF particles of the cathode was observed by TEM on the tested sample especially close to the electrolyte (where oxygen activity is reduced due to the cathode polarization). It is tentatively postulated that the inter-diffusion of elements occurring during cathode firing leads to a destabilization of the compound under the long term aging conditions leading to what appears to be beginning phase separation on the sub-micron length scale.

Sintering and operating at lower temperature and current density may help suppress the above processes.

References

[1] N.H. Menzler, F. Tietz, S. Uhlenbruck, H.P. Buchkremer, D. Stöver. J. Mater. Sci. 45 (2010) 3109–3135.

[2] W.G. Wang, M. Mogensen, Solid Sate Ionics, 176 (2005) 457–462.

[3] A. Esquirol, J. Kilner, N. Brandon, Solid State Ionics 175 (2004) 63–67.

[4] A. Mai, Vincent A.C. Haanappel, Frank Tietz, Detlev Stöver, Solid State Ionics 177 (2006) 2103–2107.

[5] N. Jordan, W. Assenmacher, S. Uhlenbruck, V.A.C. Haanappel, H.P. Buchkremer, D. Stöver, W. Mader, Solid State Ionics 179 (2008) 919–923.

[6] A. Mai, M. Becker, W. Assenmacher, F. Tietz, D. Hathiramani, E. Ivers-Tiffée, D. Stöver, W. Mader, Solid Sate Ionics 177 (2006) 1965–1968.

[7] A. Mai, V. A.C. Haanappel, S. Uhlenbruck, F. Tietz, D. Stöver, Solid Sate Ionics 176 (2005) 1341–1350.

[8] B.C.H. Steele, Solid State Ionics 134 (2000) 3–20.

[9] S.P. Simner, M.D. Anderson, M.H. Engelhard, J.W. Stevenson, Electrochem. Solid-State Lett. 9 (2006) A478–A481.

[10] H. Tu, U. Stimming, J. Power Sources 127 (2004) 284–293.

[11] F. Tietz, V.A.C. Haanappel, A. Mai, J. Mertens, D. Stöver, J. Power Sources 156 (2006) 20–22.

[12] H. Yokokawa, N. Sakai, T. Horita, K. Yamaji, M.E. Brito, H. Kishimoto, J. Alloys Compd. 452 (2008) 41–47.

[13] A. Martínez-Amesti, A. Larrañaga, L.M. Rodríguez-Martínez, A.T. Aguayo, J.L. Pizarro, M.L. Nó, A. Laresgoiti, M.I. Arriortuaa, Journal of Power Sources, 185 (2008) 401–410.

[14] S. Uhlenbruck, T. Moskalewicz, N. Jordan, H.-J. Penkalla, H.P. Buchkremer. Solid Sate Ionics, 180 (2009) 418–423.

[15] R. Knibbe, J. Hjelm, M. Menon, N. Pryds, M. Søgaard, H.-J. Wang, K. Neufeld, 93 (2010) 2877–2883

[16] T. Komatsu, R. Chiba, H. Arai, K. Sato, J. Power Sources 176 (2008) 132–137.

[17] T. Komatsu, K. Watanabe, M. Arakawa, H. Arai, J. Power Sources 193 (2009) 585–588.

[18] L. Kindermann, D. Das, H. Nickel, K. Hilpert, Solid State Ionics 89 (1996) 215–220.

[19] M. Izuki, M.E. Brito, K. Yamaji, H. Kishimoto, D.-H. Cho, T. Shimonosono, T. Horita, H. Yokokawa, J. Power Sources 196 (2011) 7232–7236.

[20] V.M. Bekale, A.M. Huntz, C. Legros, G. Sattonnay, F. Jomard. Philos. Mag. & Philos. Mag. Lett. 88 (2007) 1–19.

[21] S.P.S. Badwal, R. Deller, K. Fogera, Y. Ramprakash, J.P. Zhang, Solid State Ionics 99 (1997) 297–310.

[22] Y. Matsuzaki, I. Yasuda, J. Electrochem. Soc. 148 (2001) A126–131.

[23] I. Yasuda, Y. Baba, T. Ogiwara, H. Yakabe, Y. Matsuzaki, Proc. Electrochem. Soc. (2001) 131–139.

[24] J.Y. Kim, N.L. Canfield, C.A. Chick, K.D. Meinhardt, V.L. Sprenkle. Ceram. Eng. Sci. Proc. 26 (2005) 129–38.

[25] J.W. Fergus, Int. J. Hydrogen Energy 32 (2007) 3664–3671.

[26] J.J. Bentzen, J.V.T. Høgh, R. Barfod, A. Hagen, Fuel Cells 9 (2009) 823–832.

[27] J.-Y. Kim, V.L. Sprenkle, N.L. Canfield, K. D. Meinhardt, L. A. Chick, J. Electrochem. Soc. 153 (2006) A880−A886. ┌

[28] Y. Zhen, A.I.Y. Tok, F.Y.C. Boey, S.P. Jiang, Electrochem. Solid-State Lett. 11 (2008) B42−B46. ┌

[29] C.-L. Chu, J. Lee, S. Lee, The Third Asian Conference on Electrochemical Power Sources (2008) Pf−51.

Chapter 9

Conclusions and outlook

9.1 Conclusions

In this thesis, degradation phenomena of LSCF based cathodes and proposed mechanisms in the literature were first reviewed (*Chapter 1*). Thermodynamic properties of the oxide systems Co-Fe-O, La-Co-O, Sr-Co-O, Sr-Co-Fe-O, La-Sr-Co-O and La-Sr-Co-Fe-O were described using CALPHAD models and a thermodynamic database containing all the phases in the La-Sr-Co-Fe-O system has been established. It was shown that the compound energy formalism in the CALPHAD approach is well suited to describe phases in this multi-component system. The calculated phase diagrams for varying composition, temperature and oxygen partial pressure were discussed together with the calculated oxygen non-stoichiometry and cation distributions etc. Good agreement between thermodynamic calculations and experimental data was illustrated for the above mentioned systems. The developed thermodynamic database can be used to predict the regimes in terms of temperature and PO_2 where the LSCF perovskite phase is stable. Examples of such stability "windows" are presented in *Chapter 5* and *6* for a range of compositions and conditions, which can be extended by use of the thermodynamic parameters in the established database. The description also helped in understanding defect chemistry and charge disproportionation properties (for example, for the perovskite phase in La-Co-O as described in *Chapter 3*). It is noteworthy that some of the oxygen non-stoichiometry data for the perovskite phase reported in the literature actually correspond to 2- or 3-phase mixtures according to calculated stability phase diagrams (*Chapter 5*). Hence whereas such data can be

taken as a good measure of the total oxygen content of the samples, it is not correct to express it as an oxygen content in a single perovskite phase.

The calculations show that the stability of the perovskite phase decreases with increasing Co content (LSC<LSCF<LSF) as also elucidated by numerous experimental studies. Calculated stability regions for selected compositions and conditions for LSC and LSCF are presented in *Chapters 5* and *6*. LSC is stable at high temperatures (>700°C) and high oxygen partial pressures (>10^{-8} bar). LSCF is stable at high La and Fe content and/or high oxygen partial pressure. For example, at 700°C, LSCF is stable at La > 60 at.%, Fe > 75 at.%, and PO_2 > 10^{-8} bar). In general the stability of the perovskites decreases when reducing the PO_2. Hence, polarization of the cathode generally introduces conditions where the cathode materials are less stable. However, at cathode polarization less than 300 mV (vs air), most of LSCFs are well inside its stability range. Decreasing operating temperature is a good way to prevent phase decomposition for most of the compositions in the LSCF, but not for LSC, where a three-phase region (LSC+Spinel+$Sr_6Co_5O_{15}$) exist at low temperature (T≤700 °C).

An inter-diffusion of elements between LSCF and CGO was observed at high temperature. Inter-diffusion is clearly detectable after 100 hours at 1250 °C, but aging powder mixture samples for 1000 hours at 1000 °C did not lead to significant changes in compositions detectable on the characteristic length scales accessible by XRD or SEM/EDS. The inter-diffusion tends to de-stabilize the perovskite phase and accelerates decomposition (*Chapter 7*) and may thus be important in understanding degradation during long term operation. The inter-diffusion of La to the ceria and Ce/Gd into the perovksites puts an upper limit to the firing temperature of the cathode. Further, Sr was found enriched on the sample surface together with impurities. Additional studies are needed to clarify how Sr segregation is influenced by the experimental conditions.

Characterization techniques including TEM, SEM and SIMS were applied to elucidate differences between a long term (2000 hr) tested composite LSCF/CGO cathode (on a CGO barrier layer and a reference non-tested one. Sr was found inside the barrier layer and across the barrier−electrolyte interface as strontium zirconate in both cells. Further it was found that the inter-diffusion between the CGO barrier layer and the YSZ electrolyte takes place mainly during sintering and diffusion profiles as detected by SIMS and EDS were observed not to change significantly upon long term testing. Thus the inter-diffusion between ceria and zirconia and

growth of the CGO–YSZ interlayer does not seem to be the major degradation mechanism accountable for the observed electrical degradation of the cell.

SIMS result shows that the Cr content in the cathode is increased after long term cell testing in a stack environment. Also TEM results show that the LSCF phase in the active part of the cathode tends to become more inhomogeneous on the sub-micron length scale. This could be early stages of a phase separation which could potentially affect the electrical performance of the cell, however, at present the effects on performance of this beginning "phase separation" are not known.

It can be concluded that the observed Cr enrichment is a likely contributor to the observed electrical degradation whereas the consequences of the increasing sub-micron inhomogeneity are not yet known. The influence of Sr diffusion/segregation/volatilization on degradation should be further studied.

9.2 Outlook

Although this dissertation explored the possibilities of studying the degradation mechanisms for LSCF cathode by coupling CALPHAD and key experiments, challenges remain which form the basis for future work on studying the degradation of LSCF (or LSCF/CGO) cathodes and based on obtained knowledge, to improve the durability of the IT-SOFC.

First, "CALPHADly", adding the elements Cr or Ce and Gd to the thermodynamic database in the near future will be valuable for the SOFC research community, as it is then possible to calculate stable phase assemblages at the cathode side of a SOFC for a range of very relevant cathode materials and barrier layers at various operation temperatures and oxygen partial pressures, also considering Cr poisoning. Additionally the equilibrium defect chemistry of both the cathode and the electrolyte can be easily calculated. Moreover, having a Sr-Y-Zr-O database would be helpful in understanding reactions at the cathode–electrolyte interface. In the framework of the CALPHAD approach, computational kinetic modeling has been successfully coupled with thermodynamic models. Using software packages, like DICTRA, the kinetic database can be further developed based on the thermodynamic database. Different sorts of coefficients and concentration profiles in various diffusion couples at arbitrary temperature and

composition can be finally obtained, which provide a way in understanding degradation phenomena in SOFCs in a kinetic aspect.

Secondly, experimentally, new experimental data are essential to verify and improve the thermodynamic database, especially for the data at low oxygen partial pressure. From literature only La and Sr diffusion coefficients in ceria were found. The studies for Ce and Gd diffusion coefficients at different temperatures in perovskite are also needed to deduce the temperature and time dependence of the inter-diffusion. In order to study the impact of $SrZrO_3$ formation on cell degradation, long term testing could be performed on cells with different CGO barrier layer thickness (1µm, 5µm, 10µm and 15µm). With thinner CGO layer, it is easier for Sr to reach the YSZ surface. Different growth rates for $SrZrO_3$ can be obtained. By recording the degradation rates at the same testing condition, the influence of $SrZrO_3$ on cell degradation can be studied. In order to verify the source of impurities (P, S, Si *etc.*), further heat treatment with surface re-polished samples sealed in clean crucible together with post mortem characterizations is needed. Moreover, the cross sections of the pellets are valuable to be examined, in order to verify if the phase separation and secondary formation happen only on the surface.

Appendix A

Thermodynamic database of the La-Sr-Co-Fe-O system

```
$-------------------------------------------------------------------
$ LSCF.TDB: Database file for the La-Sr-Co-Fe-O system written 2012-11-23
$ Copyright holder and editor: Weiwei Zhang (wwzhangww.gmail.com)
$-------------------------------------------------------------------
$
$ I. The definition of the pure elements and species
$
 TEMPERATURE_LIMITS 298.15 6000 !
 ELEMENT     /-     ELECTRON_GAS  0.0000E+00  0.0000E+00  0.0000E+00!
 ELEMENT     VA     VACUUM        0.0000E+00  0.0000E+00  0.0000E+00!
 ELEMENT     FE     BCC_A2        5.5847E+01  4.4890E+03  2.7280E+01!
 ELEMENT     LA     DHCP          1.3891E+02  6.6651E+03  5.6902E+01!
 ELEMENT     O      1/2_MOLE_O2(G)      1.5999E+01  4.3410E+03  1.0252E+02!
 ELEMENT     SR     FCC_A1        8.7620E+01  6.5680E+03  5.5694E+01!
 ELEMENT     CO     HCP_A3        5.8933E+01  4,7656E+03  3.0400E+01!

 SPECIES CO+2              CO1/+2!
 SPECIES CO+3              CO1/+3!
 SPECIES CO+4              CO1/+4!
 SPECIES CO2               CO2!
 SPECIES COO               CO1O1!
 SPECIES CO3O4             CO3O4!
 SPECIES FE+2              FE1/+2!
 SPECIES FE+3              FE1/+3!
 SPECIES FE+4              FE1/+4!
 SPECIES FE1O2             FE1O2!
 SPECIES FE2               FE2!
 SPECIES FEO               FE1O1!
 SPECIES FE2O3             FE2O3!
 SPECIES FE3O4             FE3O4!
 SPECIES LA+2              LA1/+2!
 SPECIES LA+3              LA1/+3!
 SPECIES LA1O1             LA1O1!
 SPECIES LA1O2             LA1O2!
 SPECIES LA2O1             LA2O1!
 SPECIES LA2O2             LA2O2!
 SPECIES O-2               O1/-2!
 SPECIES O1                O!
 SPECIES O2                O2!
 SPECIES O2-2              O2/-2!
 SPECIES O3                O3!
 SPECIES SR+2              SR1/+2!
 SPECIES SR2               SR2!
 SPECIES SR2O              O1SR2!
 SPECIES SRO               O1SR1!
 SPECIES SRO2              O2SR1!
```

```
 SPECIES CO1LA1O3          CO1LA1O3!
 SPECIES CO1LA2O4          CO1LA2O4!
 SPECIES CO3LA4O10         CO3LA4O10!
 SPECIES LA2O3             LA2O3!
 SPECIES LAO15             LA1O1.5!

 $*********************************************************************
$  II.  Functions
$---------------------------------------------------------------------
$ ---------------------1U:  La----------------------------
FUNCTION GHSERLA    2.98150E+02  -7968.403+120.284604*T-26.34*T*LN(T)
     -.001295165*T**2;  5.50000E+02  Y
     -3381.413+59.06113*T-17.1659411*T*LN(T)-.008371705*T**2
     +6.8932E-07*T**3-399448*T**(-1);  2.00000E+03  Y
     -15608.882+181.390071*T-34.3088*T*LN(T);  4.00000E+03  N REF0 !
FUNCTION GLALIQ     2.98150E+02  +5332.653+18.23012*T-11.0188191*T*LN(T)
     -.020171603*T**2+2.93775E-06*T**3-133541*T**(-1);  1.13400E+03  Y
     -3942.004+171.018431*T-34.3088*T*LN(T);  4.00000E+03  N REF0 !
FUNCTION GLABCC     2.98150E+02  -3952.161+88.072353*T-21.7919*T*LN(T)
     -.004045175*T**2-5.25865E-07*T**3;  8.00000E+02  Y
     +321682.673-3565.08252*T+513.440708*T*LN(T)-.387295093*T**2
     +4.9547989E-05*T**3-36581228*T**(-1);  1.13400E+03  Y
      -16377.894+218.492988*T-39.5388*T*LN(T);  1.19300E+03  Y
      -136609.91+1123.34397*T-163.413074*T*LN(T)+.053968535*T**2
      -4.056395E-06*T**3+21167204*T**(-1);  2.00000E+03  Y
      -8205.988+174.836315*T-34.3088*T*LN(T);  4.00000E+03  N REF0 !
FUNCTION GLAFCC     2.98150E+02  -6109.797+89.878761*T-21.7919*T*LN(T)
     -.004045175*T**2-5.25865E-07*T**3;  1.13400E+03  Y
     -124598.976+955.878375*T-139.346741*T*LN(T)+.042032405*T**2
     -3.066199E-06*T**3+20994153*T**(-1);  2.00000E+03  Y
      -12599.386+178.54399*T-34.3088*T*LN(T);  4.00000E+03  N REF0 !
$ ---------------------- 2U: Sr----------------------------
FUNCTION GHSERSR    2.98150E+02  -7532.367+107.183879*T-23.905*T*LN(T)
     -.00461225*T**2-1.67477E-07*T**3-2055*T**(-1);  8.20000E+02  Y
     -13380.102+153.196104*T-30.0905432*T*LN(T)-.003251266*T**2
     +1.84189E-07*T**3+850134*T**(-1);  3.00000E+03  N REF0 !
FUNCTION GSRLIQ     2.98150E+02  +2194.997-10.118994*T-5.0668978*T*LN(T)
     -.031840595*T**2+4.981237E-06*T**3-265559*T**(-1);  1.05000E+03  Y
     -10855.29+213.406219*T-39.463*T*LN(T);  3.00000E+03  N REF0 !
FUNCTION GSRBCC     2.98150E+02  -6779.234+116.583654*T-25.6708365*T*LN(T)
     -.003126762*T**2+2.2965E-07*T**3+27649*T**(-1);  8.20000E+02  Y
     -6970.594+122.067301*T-26.57*T*LN(T)-.0019493*T**2-1.7895E-08*T**3
     +16495*T**(-1);  1.05000E+03  Y
     +8168.357+.423037*T-9.7788593*T*LN(T)-.009539908*T**2+5.20221E-07*T**3
     -2414794*T**(-1);  3.00000E+03  N REF0 !
$ ----------------------3U: Co----------------------------
FUNCTION GHSERCO    2.98000E+02  +310.241+133.36601*T-25.0861*T*LN(T)
     -.002654739*T**2-1.7348E-07*T**3+72527*T**(-1); 1768.00 Y
     -17197.666+253.28374*T-40.5*T*LN(T)+9.3488E+30*T**(-9);
     6.00000E+03  N REF0 !
FUNCTION GCOFCC     2.98150E+02  +427.59-.615248*T+GHSERCO#;   6.00000E+03
      N REF0 !
FUNCTION GCOBCC     2.98150E+02  +2938-.7138*T+GHSERCO#;   6.00000E+03 N REF0 !
FUNCTION GCOLIQ     2.98150E+02  +15395.278+124.434078*T-25.0861*T*LN(T)
     -.002654739*T**2-1.7348E-07*T**3+72527*T**(-1)-2.19801E-21*T**7;      1768.00 Y
     -846.61+243.599944*T-40.5*T*LN(T); 6.00000E+03  N REF0 !
$ ---------------------- 4U: Fe----------------------------
```

```
FUNCTION GHSERFE    2.98000E+02  +1225.7+124.134*T-23.5143*T*LN(T)
     -.00439752*T**2-5.89269E-08*T**3+77358.5*T**(-1);  1.81100E+03  Y
      -25383.581+299.31255*T-46*T*LN(T)+2.29603E+31*T**(-9);  6.00000E+03  N
    REF0 !
FUNCTION GFELIQ     2.98000E+02  +13265.87+117.5757*T-23.5143*T*LN(T)
     -.00439752*T**2-5.89269E-08*T**3+77358.5*T**(-1)-3.6751551E-21*T**7;
     1.81100E+03  Y
     -10838.83+291.302*T-46*T*LN(T);  3.00000E+03  N REF0 !
FUNCTION GFEFCC     2.98000E+02  +GHSERFE#-1462.4+8.282*T-1.15*T*LN(T)
     +6.4E-04*T**2;  1.81100E+03  Y
      -27097.266+300.25256*T-46*T*LN(T)+2.78854E+31*T**(-9);  3.00000E+03  N
    REF0 !
FUNCTION GFEHCP    2.98000E+02  -2480.08+136.725*T-24.6643*T*LN(T)
          -.00375752*T**2-5.8927E-08*T**3+77359*T**(-1);     1811.00   Y
           -29340.776+304.561559*T-46*T*LN(T)+2.78854E+31*T**(-9);
         6.00000E+03  N REF0 !
$ ---------------------- 5U: O2----------------------------
FUNCTION GHSEROO    2.98150E+02  -3480.87226-25.5028601*T
     -11.1355068*T*LN(T)-.005098873*T**2+6.6184604E-07*T**3
     -38364.8742*T**(-1);  1.00000E+03  Y
      -6568.76015+12.6600017*T-16.8138015*T*LN(T)-5.9579637E-04*T**2
     +6.78055555E-09*T**3+262904.778*T**(-1);  3.30000E+03  Y
      -13986.728+31.259625*T-18.9536*T*LN(T)-4.25243E-04*T**2
     +1.0721E-08*T**3+4383200*T**(-1);  6.00000E+03  N REF0 !
$ ---------------------1B: La-O---------------------------------
$
 FUNCTION GLA2O3LI  298.15
     -1812300+1285.34*T-200*T*LN(T); 6000 N REF1 !
$
 FUNCTION GLA2O3D  298.15
     -1835600+674.72*T-118*T*LN(T)-8E-03*T**2+620000*T**(-1);  6000 N REF1 !
$
 FUNCTION GLAO     2.98150E+02  +.3333333*GLA2O3D#+.3333333*GHSERLA#+62000;
        6.00000E+03   N REF1 !
 FUNCTION GLA2O3H  298.15
    -1789600+654.83*T-118*T*LN(T)-8E-03*T**2+620000*T**(-1); 6000  N REF1 !
 FUNCTION GLA2O3X  298.15
     -1729600+629.65*T-118*T*LN(T)-8E-03*T**2+620000*T**(-1); 6000 N  REF1 !
$-------------------2B : Sr-O---------------------
FUNCTION GSROLIQ    2.98150E+02  -566346+449*T-73.1*T*LN(T);   6.00000E+03
      N REF2 !
FUNCTION GSROSOL    2.98150E+02  -607870+268.9*T-47.56*T*LN(T)-.00307*T**2
     +190000*T**(-1);   6.00000E+03   N REF2 !
FUNCTION GSRO2SOL   2.98150E+02  +GSROSOL#+GHSEROO#-43740+70*T;
     6.00000E+03   N REF2 !
$ -----------------3B : Fe oxides---------------------------
FUNCTION GFEOLIQ    2.98000E+02  -137252+224.641*T-37.1815*T*LN(T);
     3.00000E+03  N REF4 !
FUNCTION GFEO       2.98000E+02  -279318+252.848*T-46.12826*T*LN(T)
     -.0057402984*T**2;  3.00000E+03  N REF3 !
 FUNCTION GAFEO      2.98000E+02  -55384+27.888*T;  3.00000E+03  N REF3 !
 FUNCTION GFE2O3     2.98000E+02  -858683+827.946*T-137.0089*T*LN(T)
     +1453810*T**(-1);  3.00000E+03  N REF3 !
 FUNCTION BFE3O4     2.98000E+02  +46826-27.266*T;  3.00000E+03  N REF3 !
 FUNCTION CFE3O4     2.98000E+02  +120730-20.102*T;  3.00000E+03  N REF3 !
FUNCTION GFE3O4     2.98000E+02  -161731+144.873*T-24.9879*T*LN(T)
     -.0011952256*T**2+206520*T**(-1);  3.00000E+03  N REF3 !
```

```
$ ----------------- 4B: Co oxides------------------------------
FUNCTION GCOOS      2.98150E+02  -252530+270.075*T-47.825*T*LN(T)
     -.005112*T**2+225008*T**(-1);   6.00000E+03   N REF5 !
FUNCTION NCO3O4     2.98150E+02  -969727+915.076*T-150.26*T*LN(T)
     -.004773*T**2+1358967*T**(-1);   6.00000E+03   N REF5 !
 FUNCTION ICO3O4     2.98150E+02  +NCO3O4#+95345-85.852*T;   6.00000E+03 N
   REF5  !
FUNCTION GCOOLIQ    2.98150E+02  +GCOOS#+42060-20*T;   6.00000E+03   N REF5 !
$ ---------------1T: La-Sr-O, Grundy--------------------
$
 FUNCTION SR_ALPHA   2.98150E+02  +2*GSROSOL#+25000;   6.00000E+03   N REF8 !
 FUNCTION SRH_ALPH   2.98150E+02  +2*GSROSOL#+25000;   6.00000E+03   N REF8 !
 FUNCTION SRX_ALPH   2.98150E+02  +2*GSROSOL#+25000;   6.00000E+03   N REF8 !
 FUNCTION LA_BETA    2.98150E+02  +GLA2O3D#+21580;   6.00000E+03   N REF8 !
$--------------2T : La-Fe-O, Povoden-------------------
FUNCTION GPRV       2.98150E+02  +.5*GLA2O3D#+.5*GFE2O3#-65921+18.02*T
     -1.95*T*LN(T);   6.00000E+03   N REF9 !
 FUNCTION GRPRV      2.98150E+02  +.5*GLA2O3D#+.5*GFE2O3#-65563+17.74*T
     -1.95*T*LN(T);   6.00000E+03   N REF9 !
 FUNCTION GPRVRED    2.98150E+02  +.5*GLA2O3D#+GFEO#+38364;   6.00000E+03
     N REF9 !
FUNCTION GRPRVRED   2.98150E+02  +.5*GLA2O3D#+GFEO#+101050-45.91*T;
     6.00000E+03   N REF9 !
FUNCTION GHEXLA     2.98150E+02  +.5*GLA2O3D#+5.5*GFE2O3#+GFEO#
  -139562+22.63*T;        6.00000E+03   N REF9 !
 FUNCTION GLAFE4O    2.98150E+02  +.5*GLA2O3D#+.375*GFE2O3#+.375*GHSEROO#
     -33198+26.46*T;   6.00000E+03   N REF9 !
 FUNCTION GRLAFE4O   2.98150E+02  +.5*GLA2O3D#+.375*GFE2O3#+.375*GHSEROO#
     -33198+26.46*T;   6.00000E+03   N REF9 !
 FUNCTION GVFE4O     2.98150E+02  +.333333*GLA2O3D#+.5*GFE2O3#+.5*GHSEROO#
     +5000;   6.00000E+03   N REF9 !
FUNCTION GL2O    298.15   +0.5*GLA2O3D+GMN1O1+27672;   6.00000E+03   N REF10 !
 FUNCTION GL3O 298.15 +0.5*GLA2O3D+0.5*GMN2O3-63367+51.77*T-7.19*T*LN(T)
  +232934*T**(-1);   6.00000E+03   N REF10 !
FUNCTION GMN2O3 298.15 -9.96393E+05+5.6846E+02*T-9.911E+01*T*LN(T)
  -2.056E-02*T**2+6.0822E+05*T**(-1);   6.00000E+03   N REF11 !
 FUNCTION GMN1O1 298.15  -402477.557+2.59355626E+02*T-4.68352649E+01*T*LN(T)
  -3.85001409E-03*T**2+2.12922234E+05*T**(-1);   6.00000E+03   N REF11 !
 FUNCTION GMN1O2 298.15  -545091.278+3.95379396E+02*T-6.52766201E+01*T*LN(T)
  -7.80284521E-03*T**2+6.64955386E+05*T**(-1);   6.00000E+03   N REF11 !
 FUNCTION GV4O 298.15 +0.333333*GLA2O3D+GMN1O2-5.37595761E+04; 6.00000E+03 N REF9 !
 FUNCTION GL4O 298.15 +0.5*GLA2O3D+0.75*GMN1O2-91857+20.31*T; 6.00000E+03 N REF9 !
FUNCTION GVVV 298.15 +6*GL2O+4*GL4O+3*GV4O-12*GL3O-254212; 6.00000E+03 N REF9 !
FUNCTION GS3O 298.15 GSROSOL+0.5*GMN2O3-7.73000000E+03-1.44550000E+04
  -1.70000000E+01*T;   6.00000E+03   N REF12 !
$---------------- 3T: La-Co-O, This work---------------------
 FUNCTION GLACOO4 298.15 -2095975.55+951.680046*T-167.49*T*LN(T)
  -.010645*T**2+938000*T**(-1); 6000   N REFX !
 FUNCTION GL3OSSUB 298.15
    -1261010.71-70.3237561*T+6.17*T*LN(T)-.14132*T**2-1179500*T**(-1);
   550.00  Y
    -1301031.07+751.034485*T-125.1*T*LN(T)-.009245*T**2+958500*T**(-1);
   1220.00  Y
   -1288831.07+669.968423*T-115.1*T*LN(T)-.009245*T**2+958500*T**(-1);
   3000   N REF13 !
 FUNCTION F7609T     2.98150E+02  -4694982.57+2329.48945*T-402*T*LN(T)
     -.02715*T**2+2566000*T**(-1);  3.80000E+03  N REF13 !
```

```
FUNCTION GL2OV 2.98150E+02  +.5*GLA2O3D+GCOOS+45388.14-14.7675*T;
    6.00000E+03 N REFX !
 FUNCTION GL4VO 2.98150E+02 +.5*GLA2O3D+.75*GCOOS+0.75*GHSEROO-68796.3
      -28.218*T;       6.00000E+03 N REFX !
 FUNCTION GLV4O  2.98150E+02  +.333333*GLA2O3D+GCOOS+GHSEROO
     -85014.24+223.25*T;  6.00000E+03 N REFX !
 FUNCTION GL3CO   2.98150E+02  +GL3OSSUB#-7358.08+9.50095*T; 6.00000E+03 N REFX !
$----------4T: Sr-Fe-O, Povoden------------------
FUNCTION GSR3FE2O   2.98150E+02  +2*GSRPRV#+GSROSOL#;   6.00000E+03        N REF14 !
FUNCTION GSM4_RP1   2.98150E+02  +GSRPRVOX#+GSROSOL#-1.9000000E+04;
     6.00000E+03   N REF14 !
FUNCTION GSF3O      2.98150E+02  +GSR3FE2O#+22.4772*T+GHSEROO#;
     6.00000E+03   N REF14 !
 FUNCTION GSF4V      2.98150E+02  +GSM4_RP1#-6*GHSEROO#;   6.00000E+03   N REF14 !
 FUNCTION GLF3O      2.98150E+02  +GSROSOL#+2*GPRV#+63000-62*T;
     6.00000E+03   N REF14 !
 FUNCTION GSF4O      2.98150E+02  +2*GSRPRVOX#+GSROSOL#-5000-4.71*T;
     6.00000E+03   N REF14 !
FUNCTION GSS4       2.98150E+02  +3*GSRPRVOX#+GSROSOL#-54000;   6.00000E+03
      N REF14 !
 FUNCTION GSL3       2.98150E+02  +GSROSOL#+3*GPRV#+200000;   6.00000E+03 N REF14 !
 FUNCTION GLS3       2.98150E+02  +.5*GLA2O3D#+3*GSRPRVOX#-31000-88*T;
     6.00000E+03   N REF14 !
 FUNCTION GLS4       2.98150E+02  +.5*GLS3#+.5*GSS4#;   6.00000E+03   N REF14 !
 FUNCTION GSS3       2.98150E+02  +.5*GLS3#+.5*GSS4#;   6.00000E+03   N REF14 !
 FUNCTION GLL3       2.98150E+02  +GSL3#+GLS3#-GSS3#;   6.00000E+03   N REF14 !
 FUNCTION GSL4       2.98150E+02  +GSS4#+GSL3#-GSS3#;   6.00000E+03   N REF14 !
 FUNCTION GLL4       2.98150E+02  +GSL4#+GLS4#-GSS4#;   6.00000E+03   N REF14 !
 FUNCTION GSS3OV     2.98150E+02  +GSROSOL#+3*GSRPRV#;
     6.00000E+03   N REF14 !
 FUNCTION GLS3OV     2.98150E+02  +.5*GLA2O3D#+3*GSRPRV#-9943.8-26.448*T;
     6.00000E+03   N REF14 !
FUNCTION G2HEX      2.98150E+02  +GSROSOL#+GFEO#+5.5*GFE2O3#+.5*GHSEROO#;
     6.00000E+03   N REF14 !
 FUNCTION GHEX       2.98150E+02  +GSROSOL#+6*GFE2O3#-173012+888.77*T
     -115.2*T*LN(T)+5092797.5*T**(-1);   6.00000E+03   N REF14 !
FUNCTION GSRPRVR    2.98150E+02  +GSRPRV#-.5*GHSEROO#+116977;
     6.00000E+03   N REF14 !
 FUNCTION GSRPRVOX   2.98150E+02  +GSRPRV#-60015+188.3*T-25.69*T*LN(T);
     6.00000E+03   N REF14 !
 FUNCTION GSRPRV     2.98150E+02  +GSROSOL#+.5*GFE2O3#-4.4701000E+04-8.73*T;
     6.00000E+03   N REF14 !
$--------------5T: Sr-Co-O, This work---------------------
$
 FUNCTION GS4O 298.15 GSROSOL+GCOOS +GHSEROO-86550.169+75.64357*T; 6000  N REFX !
 FUNCTION GS3OV 298.15 +GSROSOL +GCOOS+0.5*GHSEROO-20754.002+10.99699*T;
 6000   N REFX !
 FUNCTION GS2OV 298.15 +GSROSOL +GCOOS+28889.74-15.20777*T; 6000   N REFX !
FUNCTION GSRCOO4  298.15 -1591501.7+876.17*T-149.513*T*LN(T)-0.031876*T**2
   +386659.81*T**(-1); 6000   N REFX !
 FUNCTION GSR2CO2O  2.98150E+02  -1579898.9+969.424*T-213.734*T*LN(T)
     -0.023799*T**2+1635410.1*T**(-1)-285000.00+247*T;   6.00000E+03   N REFX !
$---------------6T: CO-Fe-O This work ---------------------
FUNCTION TCOFE2O4  2.98150E+02 -1106560.1+1107.2*T-184.804*T*LN(T)
     -.00763966*T**2+1597245.2*T**(-1);      6.00000E+03   N REFX !
 FUNCTION ACOFE2O4  2.98150E+02  -34161.5-10.9247*T;     6.00000E+03   N REFX !
$ 2Q))---------------LA-SR-FE-O---------
```

```
 FUNCTION  GNHEX      2.98150E+02  +.5*GLA2O3D+.5*GSROSOL
           +5.75*GFE2O3+.5*GFEO-.75*GHSEROO+53400;
     6.00000E+03   N   REF15 !
$ -------- Perovskite functions --------------
$ LAYERED PRV, LPRV
 FUNCTION GLAYS      2.98150E+02  +4*GSRPRV#+GFE2O3#-6486-6.29*T;
     6.00000E+03   N REF15 !
 FUNCTION GLAYOX     2.98150E+02  +4*GSRPRV#+GFE2O3#+GHSEROO#-14132+13.26*T;
       6.00000E+03   N REF15 !
$ 2012-07-31 SR4FE6O13
 FUNCTION GLAYRED    2.98150E+02  +4*GSRPRV#+2*GFEO#+43043-7.12*T;
     6.00000E+03   N REF15 !
 FUNCTION GLAYREF    2.98150E+02  +4*GSRPRV#+2*GFEO#+2*GHSEROO#;
     6.00000E+03   N REF15 !
$ --------  Gas functions --------------
$ La gas, from SGTE
FUNCTION F12026T    2.98150E+02  +422273.955-30.3347881*T-22.06299*T*LN(T)
     -.005444405*T**2+4.71447833E-07*T**3+102710.1*T**(-1);  6.00000E+02  Y
      +426628.905-85.4786162*T-13.83676*T*LN(T)-.011938995*T**2
     +1.33826017E-06*T**3-312130.2*T**(-1);  1.30000E+03  Y
      +404460.17+114.016725*T-42.00406*T*LN(T)+.0037094435*T**2
     -2.70261E-07*T**3+2891891*T**(-1);  3.20000E+03  Y
      +497751.747-246.085237*T+2.791973*T*LN(T)-.006002155*T**2
     +1.30043383E-07*T**3-34158815*T**(-1);  8.20000E+03  Y
      -92343.0441+773.338363*T-111.0188*T*LN(T)+.0037862445*T**2
     -2.82257667E-08*T**3+5.418475E+08*T**(-1);  1.00000E+04  N REF17 !
$ Sr gas, from SGTE
FUNCTION F15323T    2.98150E+02  +154227.522-24.1431703*T-20.98549*T*LN(T)
     +1.951298E-04*T**2-3.09095833E-08*T**3+4675.2365*T**(-1);  1.80000E+03
     Y
      +111247.483+242.365806*T-56.52776*T*LN(T)+.0133862*T**2
     -9.57800833E-07*T**3+9843260*T**(-1);  3.30000E+03  Y
      +770872.513-2114.76782*T+233.253*T*LN(T)-.04337796*T**2
     +1.134592E-06*T**3-2.7250735E+08*T**(-1);  4.90000E+03  Y
      -196742.694+263.327068*T-44.45892*T*LN(T)-.008078665*T**2
     +2.96671167E-07*T**3+3.57637E+08*T**(-1);  6.20000E+03  Y
      -949056.902+1952.13337*T-239.3059*T*LN(T)+.01421437*T**2
     -1.79062E-07*T**3+8.9842E+08*T**(-1);  9.60000E+03  Y
      +34305.7758+474.957384*T-77.25547*T*LN(T)+.00232914*T**2
     -1.54504333E-08*T**3-2.2245325E+08*T**(-1);  1.00000E+04  N REF17 !
$ Sr2(g)
 FUNCTION F15338T    2.98150E+02  +295010.66+61.845039*T-54.13634*T*LN(T)
     +.040485225*T**2-9.264165E-06*T**3-70453.75*T**(-1);  5.00000E+02  Y
      +307156.188-147.411671*T-20.95926*T*LN(T)+1.012636E-04*T**2
     -8.03856667E-09*T**3-905190.5*T**(-1);  3.00000E+03  N REF17 !
$ Sr GAS
 FUNCTION SRGAS      2.98150E+02  +204635-49.7*T-20.64*T*LN(T)-6.7E-05*T**2
     -83500*T**(-1);   6.00000E+03   N REF17 !
$ Sr2 GAS
 FUNCTION SR2GAS     2.98150E+02  +209510-23*T-37.4*T*LN(T)-4E-06*T**2
     +21000*T**(-1);   6.00000E+03   N REF17 !
$ Fe GAS
 FUNCTION F9960T     2.98150E+02  +404205.714+35.7374154*T-32.857*T*LN(T)
     +.00911365*T**2-1.35405833E-06*T**3+109770*T**(-1);  9.00000E+02  Y
      +412790.047-53.8374242*T-19.843*T*LN(T)+6.96E-05*T**2
     -1.30683333E-07*T**3-976410*T**(-1);  2.40000E+03  Y
      +409046.151-49.3274624*T-20.125*T*LN(T)-5.6655E-04*T**2
```

```
     -5.29033333E-08*T**3+887590*T**(-1);  5.50000E+03  Y
      +511845.843-358.371229*T+16.811*T*LN(T)-.00616325*T**2
     +1.00678333E-07*T**3-48193220*T**(-1);  1.00000E+04  N REF17 !
$ Fe2 GAS
 FUNCTION F10095T    2.98150E+02  +704549.824+89.2549314*T-50.743*T*LN(T)
     +.00803125*T**2-2.18098667E-06*T**3+169270*T**(-1);  8.00000E+02  Y
      +717674.096-87.8134524*T-23.957*T*LN(T)-.0157846*T**2
     +1.723485E-06*T**3-1006505*T**(-1);  1.70000E+03  Y
      +655211.274+352.671353*T-83.82001*T*LN(T)+.0095931*T**2
     -2.85336667E-07*T**3+11147285*T**(-1);  4.50000E+03  Y
      +780963.168-41.3623286*T-36.245*T*LN(T)+.00155795*T**2
     -3.05716667E-08*T**3-51729450*T**(-1);  6.00000E+03  N REF17 !
$ CO GAS, FROM CO-CR-O DATABASE
 FUNCTION F7261T     2.98150E+02  +416729.448-35.1568065*T-20.78*T*LN(T)
     -.0080941*T**2+1.95473333E-06*T**3+68440*T**(-1);  6.00000E+02  Y
      +415600.439-4.36923762*T-25.919*T*LN(T)-3.217E-04*T**2+1.228E-08*T**3
     +69800*T**(-1);  1.60000E+03  Y
      +404059.607+61.0546568*T-34.475*T*LN(T)+.00226985*T**2
     -1.11743333E-07*T**3+2845480*T**(-1);  5.30000E+03  Y
      +619409.166-455.074402*T+25.674*T*LN(T)-.00531515*T**2
     +7.04183333E-08*T**3-1.4391985E+08*T**(-1);  1.00000E+04  N REF17 !
$ CoO GAS
 FUNCTION F7356T     2.98150E+02  +275841.927+24.2052571*T-38.62*T*LN(T)
     +.0010486*T**2-5.3089E-07*T**3+44960*T**(-1);  1.00000E+03  Y
      +271341.103+44.8779144*T-41.009*T*LN(T)-1.055E-05*T**2
     -9.90866667E-08*T**3+1003100*T**(-1);  2.90000E+03  Y
      +390604.342-373.80702*T+10.233*T*LN(T)-.0095202*T**2
     +2.18581667E-07*T**3-49953335*T**(-1);  5.60000E+03  Y
      +339256.902-297.681941*T+2.109*T*LN(T)-.00931405*T**2
     +2.32998333E-07*T**3-1285140*T**(-1);  6.00000E+03  N REF17 !
$ Co2 GAS
 FUNCTION F7427T     2.98150E+02  +739344.569+228.270514*T-75.86201*T*LN(T)
     +.02653785*T**2-3.82613167E-06*T**3+589055*T**(-1);  9.00000E+02  Y
      +766271.805-69.2721005*T-32.277*T*LN(T)-.0051345*T**2+5.3545E-07*T**3
     -2559210*T**(-1);  2.50000E+03  Y
      +742734.91+122.487528*T-58.296*T*LN(T)+.0049326*T**2
     -1.22191667E-07*T**3-1487375*T**(-1);  5.80000E+03  Y
      +1148759.49-821.285063*T+51.18*T*LN(T)-.0082646*T**2
     +1.77621667E-07*T**3-2.8575475E+08*T**(-1);  6.00000E+03  N REF17 !
$ O(g)
 FUNCTION F13349T    2.98150E+02  +243206.494-20.8612582*T-21.01555*T*LN(T)
     +1.2687055E-04*T**2-1.23131283E-08*T**3-42897.09*T**(-1);  2.95000E+03
     Y
      +252301.423-52.0847281*T-17.21188*T*LN(T)-5.413565E-04*T**2
     +7.64520667E-09*T**3-3973170.5*T**(-1);  6.00000E+03  N REF17 !
$ O2(g)
 FUNCTION F13704T    2.98150E+02  -6960.6927-51.1831467*T-22.25862*T*LN(T)
     -.01023867*T**2+1.339947E-06*T**3-76749.55*T**(-1);  9.00000E+02  Y
      -13136.0174+24.7432966*T-33.55726*T*LN(T)-.0012348985*T**2
     +1.66943333E-08*T**3+539886*T**(-1);  3.70000E+03  Y
      +14154.6459-51.485458*T-24.47978*T*LN(T)-.002634759*T**2
     +6.01544333E-08*T**3-15120935*T**(-1);  9.60000E+03  Y
      -314316.629+515.068037*T-87.56143*T*LN(T)+.0025787245*T**2
     -1.878765E-08*T**3+2.9052515E+08*T**(-1);  1.85000E+04  Y
      -108797.175+288.483019*T-63.737*T*LN(T)+.0014375*T**2-9E-09*T**3
     +.25153895*T**(-1);  2.00000E+04  N REF17 !
$ O3(g)
```

```
 FUNCTION F14021T    2.98150E+02  +130696.944-37.9096643*T-27.58118*T*LN(T)
     -.02763076*T**2+4.60539333E-06*T**3+99530.45*T**(-1);  7.00000E+02  Y
      +114760.623+176.626737*T-60.10286*T*LN(T)+.00206456*T**2
     -5.17486667E-07*T**3+1572175*T**(-1);  1.30000E+03  Y
      +49468.3956+710.09482*T-134.3696*T*LN(T)+.039707355*T**2
     -4.10457667E-06*T**3+12362250*T**(-1);  2.10000E+03  Y
      +866367.075-3566.80563*T+421.2001*T*LN(T)-.1284109*T**2
     +5.44768833E-06*T**3-2.1304835E+08*T**(-1);  2.80000E+03  Y
      +409416.383-1950.70834*T+223.4437*T*LN(T)-.0922361*T**2
     +4.306855E-06*T**3-21589870*T**(-1);  3.50000E+03  Y
      -1866338.6+6101.13383*T-764.8435*T*LN(T)+.09852775*T**2
     -2.59784667E-06*T**3+9.610855E+08*T**(-1);  4.90000E+03  Y
      +97590.043+890.798361*T-149.9608*T*LN(T)+.01283575*T**2
     -3.555105E-07*T**3-2.1699975E+08*T**(-1);  6.00000E+03  N REF17 !
$ LaO gas, from SGTE
FUNCTION F12049T    2.98150E+02  -131496.968-24.5469483*T-31.53764*T*LN(T)
     -.0051956*T**2+7.60442333E-07*T**3+103677.85*T**(-1);  9.00000E+02  Y
      -133112.849+7.93847638*T-36.65559*T*LN(T)+2.4937065E-04*T**2
     -2.05688333E-07*T**3+108868.35*T**(-1);  2.50000E+03  Y
      -137735.323-23.9414477*T-31.58251*T*LN(T)-.003177688*T**2
     +6.84986667E-08*T**3+5676870*T**(-1);  5.40000E+03  Y
      -39118.6731-213.786313*T-10.21743*T*LN(T)-.005021225*T**2
     +9.162985E-08*T**3-74562000*T**(-1);  1.00000E+04  N REF17 !
$ La2O(g)
 FUNCTION F12085T    2.98150E+02  -69316.3279+46.9195461*T-51.12563*T*LN(T)
     -.005701935*T**2+8.637425E-07*T**3+212452.95*T**(-1);  1.00000E+03  Y
      -73167.5826+93.9280358*T-58.13034*T*LN(T)-1.332372E-05*T**2
     +4.41584333E-10*T**3+616730*T**(-1);  6.00000E+03  N REF17 !
$ La2O2(g)
 FUNCTION F12089T    2.98150E+02  -642532.065+54.8487791*T-51.72813*T*LN(T)
     -.028452875*T**2+4.99643833E-06*T**3+271002.95*T**(-1);  7.00000E+02  Y
      -657497.385+256.452173*T-82.32033*T*LN(T)-1.8245965E-04*T**2
     +6.891315E-09*T**3+1664162*T**(-1);  5.10000E+03  Y
      -672122.137+293.83814*T-86.72291*T*LN(T)+4.319301E-04*T**2
     -9.75906E-09*T**3+11187120*T**(-1);  6.00000E+03  N REF17 !
$ Sr oxide Gas, from SGTE
$ SrO(g)
 FUNCTION F13511T    2.98150E+02  -25476.9742+3.04351985*T-34.37623*T*LN(T)
     -.0026980695*T**2+3.78874167E-07*T**3+120146.05*T**(-1);  9.00000E+02  Y
      -44602.142+205.651627*T-63.83687*T*LN(T)+.017645965*T**2
     -2.284235E-06*T**3+2463047*T**(-1);  1.80000E+03  Y
      +243278.077-1500.21201*T+161.9497*T*LN(T)-.0612273*T**2
     +2.896125E-06*T**3-66468000*T**(-1);  2.90000E+03  Y
      -571113.316+1685.71589*T-234.6556*T*LN(T)+.024571595*T**2
     -5.82819833E-07*T**3+2.468897E+08*T**(-1);  4.50000E+03  Y
      -14433.8514+256.066959*T-66.76292*T*LN(T)+.002226246*T**2
     -2.98498E-08*T**3-97083400*T**(-1);  8.80000E+03  Y
      +52967.3441+134.904343*T-53.17021*T*LN(T)+.001008387*T**2
     -9.46948833E-09*T**3-1.6008755E+08*T**(-1);  1.00000E+04  N REF17 !
$ from Lamoreaux 1987
$ SRO
 FUNCTION SROGAS     2.98150E+02  +113551-.315*T-36.51*T*LN(T)
     -2.635E-04*T**2+183136*T**(-1);   6.00000E+03   N REF17 !
$ SR2O
 FUNCTION SR2OGAS    2.98150E+02  +100371+69.5*T-57.13*T*LN(T)
     -3.203E-04*T**2+300079*T**(-1);   6.00000E+03   N REF17 !
$
```

```
 FUNCTION F15641T    2.98150E+02  +153602.922-22.5981707*T-20.98549*T*LN(T)
     +1.951298E-04*T**2-3.09095833E-08*T**3+4675.2365*T**(-1);  1.80000E+03
     Y
      +110622.883+243.910805*T-56.52776*T*LN(T)+.0133862*T**2
     -9.57800833E-07*T**3+9843260*T**(-1);  3.30000E+03  Y
      +770247.913-2113.22282*T+233.253*T*LN(T)-.04337796*T**2
     +1.134592E-06*T**3-2.7250735E+08*T**(-1);  4.90000E+03  Y
      -197367.294+264.872067*T-44.45892*T*LN(T)-.008078665*T**2
     +2.96671167E-07*T**3+3.57637E+08*T**(-1);  6.20000E+03  Y
      -949681.502+1953.67837*T-239.3059*T*LN(T)+.01421437*T**2
     -1.79062E-07*T**3+8.9842E+08*T**(-1);  9.60000E+03  Y
      +33681.1759+476.502383*T-77.25547*T*LN(T)+.00232914*T**2
     -1.54504333E-08*T**3-2.2245325E+08*T**(-1);  1.00000E+04  N REF17 !
 FUNCTION F15650T    2.98150E+02  +296202.76+61.7700383*T-54.13634*T*LN(T)
     +.040485225*T**2-9.264165E-06*T**3-70453.75*T**(-1);  5.00000E+02  Y
      +308348.288-147.486672*T-20.95926*T*LN(T)+1.012636E-04*T**2
     -8.03856667E-09*T**3-905190.5*T**(-1);  3.00000E+03  N REF17 !
$ FeO Gas
 FUNCTION F10028T    2.98150E+02  +247269.947-13.1139445*T-32.67*T*LN(T)
     -.0075012*T**2+1.18220167E-06*T**3-34235*T**(-1);  9.00000E+02  Y
      +240957.695+66.2179313*T-44.511*T*LN(T)+.00209225*T**2
     -2.42841667E-07*T**3+572515*T**(-1);  2.80000E+03  Y
      +309524.921-212.054229*T-9.622001*T*LN(T)-.00601295*T**2
     +1.2057E-07*T**3-25282085*T**(-1);  5.80000E+03  Y
      +485837.27-638.31461*T+40.074*T*LN(T)-.01226245*T**2
     +2.68271667E-07*T**3-1.4323085E+08*T**(-1);  6.00000E+03  N REF17 !
$ Fe1O2 Gas
 FUNCTION F10034T    2.98150E+02  +58475.2387-2.12934624*T-37.569*T*LN(T)
     -.01894785*T**2+3.36232667E-06*T**3+205940*T**(-1);  7.00000E+02  Y
      +48666.2154+131.021135*T-57.802*T*LN(T)-7.83E-05*T**2
     +2.57666667E-09*T**3+1111465*T**(-1);  6.00000E+03  N REF17 !
$
$***********************************************************************
$ IV. Type definition, the reference state type for the elements
$  ---------------------------------------------------------------
 TYPE_DEFINITION % SEQ *!
 DEFINE_SYSTEM_DEFAULT ELEMENT 2 !
 DEFAULT_COMMAND DEF_SYS_ELEMENT VA /- !
$***********************************************************************
$ V. Definition of the phases
$ -------------------------------
$ 5.1 ionic_Liquid Phase, ideal extrapolation from lower-order systems
$ -------------------------------
PHASE IONIC_LIQUID:Y %  2 1   1 !
 CONSTITUENT IONIC_LIQUID:Y :CO+2,CO+3,FE+2,FE+3,LA+3,SR+2:O-2,VA: !

   PARAMETER G(IONIC_LIQUID,CO+2:O-2;0)  2.98150E+02  +2*GCOOLIQ#;
  6.00000E+03   N REF5 !
   PARAMETER G(IONIC_LIQUID,CO+3:O-2;0)  2.98150E+02  +2*GCOOS#+GHSEROO#
  -76314+103.63*T;   6.00000E+03   N REF5 !
   PARAMETER G(IONIC_LIQUID,CO+2:VA;0)  2.98150E+02  +GCOLIQ#;
  3.20000E+03  N REF REF5 !
   PARAMETER G(IONIC_LIQUID,CO+2:O-2,VA;0)  2.98150E+02  +182675-30.556*T;
  6.00000E+03   N REF5 !
   PARAMETER G(IONIC_LIQUID,CO+2:O-2,VA;2)  2.98150E+02  +54226-20*T;
  6.00000E+03   N REF5 !
   PARAMETER G(IONIC_LIQUID,CO+3:VA;0)  2.98150E+02  +2*GCOLIQ#+2*GCOOS#
```

```
  +GHSEROO#-76314+103.63*T-3*GCOOLIQ#;   6.00000E+03   N REF5 !
   PARAMETER G(IONIC_LIQUID,FE+2:O-2;0)  2.98150E+02  +4*GFEOLIQ#;
  6.00000E+03   N REF3 !
   PARAMETER G(IONIC_LIQUID,FE+3:O-2;0)  2.98150E+02  +5*GFEOLIQ#-179638
  +79.923*T;   6.00000E+03   N REF18 !
   PARAMETER G(IONIC_LIQUID,FE+2:VA;0)  2.98150E+02  +GFELIQ#;   6.00000E+03
    N REF3 !
   PARAMETER G(IONIC_LIQUID,FE+3:VA;0)  2.98150E+02  +2*GFELIQ#+5*GFEOLIQ#
  -179638+79.923*T-6*GFEOLIQ#;   6.00000E+03   N REF18 !
   PARAMETER G(IONIC_LIQUID,FE+2,FE+3:O-2;0)  2.98150E+02  -26362;
  6.00000E+03   N REF3 !
   PARAMETER G(IONIC_LIQUID,FE+2,FE+3:O-2;1)  2.98150E+02  13353;
  6.00000E+03   N REF3 !
   PARAMETER G(IONIC_LIQUID,FE+2:O-2,VA;0)  2.98150E+02  +176681-16.368*T;
  6.00000E+03   N REF18 !
   PARAMETER G(IONIC_LIQUID,FE+2:O-2,VA;1)  2.98150E+02  -65655+30.869*T;
  6.00000E+03   N REF18 !
$
   PARAMETER G(IONIC_LIQUID,LA+3:O-2;0)  2.98150E+02  +GLA2O3LI#;
  6.00000E+03   N REF1 !
   PARAMETER G(IONIC_LIQUID,LA+3:VA;0)  2.98150E+02  +GLALIQ#;   6.00000E+03
    N REF6 !
   PARAMETER G(IONIC_LIQUID,SR+2:O-2;0)  2.98150E+02  +2*GSROLIQ#;
  6.00000E+03   N REF2 !
   PARAMETER G(IONIC_LIQUID,SR+2:VA;0)  2.98150E+02  +GSRLIQ#;   6.00000E+03
    N REF0 !
   PARAMETER G(IONIC_LIQUID,FE+2,SR+2:O-2;0)  2.98150E+02  -281372;
  6.00000E+03   N REF14 !
   PARAMETER G(IONIC_LIQUID,FE+3,SR+2:O-2;0)  2.98150E+02  -281372;
  6.00000E+03   N REF14 !
   PARAMETER G(IONIC_LIQUID,FE+3,SR+2:O-2;1)  2.98150E+02  35000;
  6.00000E+03   N REF14 !
   PARAMETER G(IONIC_LIQUID,FE+3,SR+2:O-2;2)  2.98150E+02  -35311;
  6.00000E+03   N REF14 !
   PARAMETER G(IONIC_LIQUID,FE+3,LA+3:O-2;0)  2.98150E+02  -136242;
  6.00000E+03   N REF9 !
   PARAMETER G(IONIC_LIQUID,FE+3,LA+3:O-2;1)  2.98150E+02  -9285;
  6.00000E+03   N REF9 !
   PARAMETER G(IONIC_LIQUID,FE+2,LA+3:O-2;0)  2.98150E+02  -136242;
  6.00000E+03   N REF9 !
   PARAMETER G(IONIC_LIQUID,FE+2,LA+3:O-2;1)  2.98150E+02  -9285;
  6.00000E+03   N REF9 !
   PARAMETER G(IONIC_LIQUID,FE+2,LA+3:VA;0)  2.98150E+02  -41+15.2*T;
  6.00000E+03   N REF9 !
   PARAMETER G(IONIC_LIQUID,FE+2,LA+3:VA;1)  2.98150E+02  -7837+4.9*T;
  6.00000E+03   N REF9 !
   PARAMETER G(IONIC_LIQUID,LA+3,SR+2:O-2;0)  2.98150E+02  -88910;
  6.00000E+03   N REF8 !
   PARAMETER G(IONIC_LIQUID,LA+3,SR+2:O-2;1)  2.98150E+02  -73680;
  6.00000E+03   N REF8 !
   PARAMETER G(IONIC_LIQUID,LA+3,SR+2:VA;0)  2.98150E+02  +34000;
  6.00000E+03   N REF15 !
$
   PARAMETER G(IONIC_LIQUID,CO+2,FE+2:VA;0)  2.98150E+02  -9753.82;
  6.00000E+03   N REF7 !
   PARAMETER G(IONIC_LIQUID,CO+2,FE+2:VA;2)  2.98150E+02  +2757.96;
  6.00000E+03   N REF7 !
```

```
$
   PARAMETER G(IONIC_LIQUID,CO+2,LA+3:VA;0)  2.98150E+02  -35734-0.793*T;
  6.00000E+03   N REF6 !
   PARAMETER G(IONIC_LIQUID,CO+2,LA+3:VA;1)  2.98150E+02  -5150+14.181*T;
  6.00000E+03   N REF6 !
   PARAMETER G(IONIC_LIQUID,CO+2,LA+3:VA;2)  2.98150E+02  6023-0.497*T;
  6.00000E+03   N REF6 !
   PARAMETER G(IONIC_LIQUID,CO+2,LA+3:VA;3)  2.98150E+02  18450-15.756*T;
  6.00000E+03   N REF6 !
$ ---------------------------------
$ 5.2 Perovskite
$ ---------------------------------
TYPE_DEFINITION ø GES A_P_D PRV MAGNETIC  -3.0    2.80000E-01 !
 PHASE PRV  %ø  3 1   1   3 !
  CONSTITUENT PRV  :LA+3,SR+2,VA:CO+2,CO+3,CO+4,FE+2,FE+3,FE+4,VA:O-2,VA: !
   PARAMETER G(PRV,LA+3:FE+2:O-2;0)  2.98150E+02  +GRPRVRED#+.5*GHSEROO#
  +11.2386*T;   6.00000E+03   N REF9 !
   PARAMETER G(PRV,LA+3:FE+3:O-2;0)  2.98150E+02  +GRPRV#;   6.00000E+03   N
  REF9 !
   PARAMETER G(PRV,LA+3:FE+4:O-2;0)  2.98150E+02  +.66667*GLAFE4O#
  +.5*GVFE4O#-.166667*GVVV#-.5*GHSEROO#+5.76318*T;   6.00000E+03   N REF9 !
   PARAMETER G(PRV,LA+3:VA:O-2;0)  2.98150E+02  +2*GL4O#-1.5*GV4O#+.5*GVVV#
  +1.5*GHSEROO#+1.41263*T;   6.00000E+03   N REF9 !
   PARAMETER G(PRV,LA+3:FE+2:VA;0)  2.98150E+02  +GRPRVRED#-2.5*GHSEROO#
  +11.2386*T;   6.00000E+03   N REF9 !
   PARAMETER G(PRV,LA+3:FE+3:VA;0)  2.98150E+02  +GRPRV#-3*GHSEROO#;
  6.00000E+03   N REF9 !
   PARAMETER G(PRV,LA+3:FE+4:VA;0)  2.98150E+02  +.66667*GLAFE4O#+.5*GVFE4O#
  -.166667*GVVV#-3.5*GHSEROO#+5.76318*T;   6.00000E+03   N REF9 !
   PARAMETER G(PRV,LA+3:VA:VA;0)  2.98150E+02  +2*GL4O#+.5*GVVV#-1.5*GV4O#
  -1.5*GHSEROO#+1.41263*T;   6.00000E+03   N REF10 !
   PARAMETER TC(PRV,LA+3:FE+3:O-2;0) 298.15  +742.88 ;   6.00000E+03   N REF9 !
   PARAMETER BMAGN(PRV,LA+3:FE+3:O-2;0) 298.15  +0.779 ;   6.00000E+03   N REF9 !
   PARAMETER TC(PRV,LA+3:FE+2:O-2;0) 298.15  +742.88 ;   6.00000E+03   N REF9 !
   PARAMETER BMAGN(PRV,LA+3:FE+2:O-2;0) 298.15  +0.779 ;   6.00000E+03   N REF9 !
   PARAMETER TC(PRV,LA+3:FE+3:VA;0) 298.15  +742.88 ;   6.00000E+03   N REF9 !
   PARAMETER BMAGN(PRV,LA+3:FE+3:VA;0) 298.15  +0.779 ;   6.00000E+03   N REF9 !
   PARAMETER TC(PRV,LA+3:FE+2:VA;0) 298.15  +742.88 ;   6.00000E+03   N REF9 !
   PARAMETER BMAGN(PRV,LA+3:FE+2:VA;0) 298.15  +0.779 ;   6.00000E+03   N REF9 !
   PARAMETER TC(PRV,LA+3:FE+4:VA;0) 298.15  +742.88 ;   6.00000E+03   N REF9 !
   PARAMETER BMAGN(PRV,LA+3:FE+4:VA;0) 298.15  +0.779 ;   6.00000E+03   N REF9 !
   PARAMETER TC(PRV,LA+3:FE+4:O-2;0) 298.15  +742.88 ;   6.00000E+03   N REF9 !
   PARAMETER BMAGN(PRV,LA+3:FE+4:O-2;0) 298.15  +0.779 ;   6.00000E+03   N REF9 !
   PARAMETER G(PRV,VA:FE+2:O-2;0)  2.98150E+02  +GRPRVRED#+1.5*GVFE4O#
  +.5*GVVV#-2*GLAFE4O#+2*GHSEROO#+9.82596*T;   6.00000E+03   N REF9 !
   PARAMETER G(PRV,VA:FE+3:O-2;0)  2.98150E+02  +GRPRV#+1.5*GVFE4O#+.5*GVVV#
  -2*GLAFE4O#+1.5*GHSEROO#-1.41263*T;   6.00000E+03   N REF9 !
   PARAMETER G(PRV,VA:FE+4:O-2;0)  2.98150E+02  +2*GVFE4O#+.33333*GVVV#
  -1.33333*GLAFE4O#+GHSEROO#+4.35056*T;   6.00000E+03   N REF9 !
   PARAMETER G(PRV,VA:VA:O-2;0)  2.98150E+02  +GVVV#+3*GHSEROO#;
  6.00000E+03   N REF10 !
   PARAMETER G(PRV,VA:FE+2:VA;0)  2.98150E+02  +GRPRVRED#+1.5*GVFE4O#
  +.5*GVVV#-2*GLAFE4O#-GHSEROO#+9.82596*T;   6.00000E+03   N REF9 !
   PARAMETER G(PRV,VA:FE+3:VA;0)  2.98150E+02  +GRPRV#+1.5*GVFE4O#+.5*GVVV#
  -2*GLAFE4O#-1.5*GHSEROO#-1.41263*T;   6.00000E+03   N REF9 !
   PARAMETER G(PRV,VA:FE+4:VA;0)  2.98150E+02  +2*GVFE4O#+.3333*GVVV#
  -1.333*GLAFE4O#-2*GHSEROO#+4.35057*T;   6.00000E+03   N REF9 !
```

```
  PARAMETER G(PRV,VA:VA:VA;0)  2.98150E+02  +GVVV#;   6.00000E+03   N REF10 !
  PARAMETER G(PRV,SR+2:FE+2:O-2;0)  2.98150E+02  +GSRPRVR#+15.8769*T
 +GHSEROO#;   6.00000E+03   N REF14 !
  PARAMETER G(PRV,SR+2:FE+3:O-2;0)  2.98150E+02  +GSRPRV#+.5*GHSEROO#
 +11.2386*T;   6.00000E+03   N REF14 !
  PARAMETER G(PRV,SR+2:FE+4:O-2;0)  2.98150E+02  +GSRPRVOX#;   6.00000E+03
  N REF14 !
  PARAMETER G(PRV,SR+2:VA:O-2;0)  2.98150E+02  +GS3O#-GL3O#+2*GL4O#
 -1.5*GV4O#+.5*GVVV#+2*GHSEROO#+12.62121*T;   6.00000E+03   N REF14 !
  PARAMETER G(PRV,SR+2:FE+2:VA;0)  2.98150E+02  +GSRPRVR#+15.8769*T
 -2*GHSEROO#;   6.00000E+03   N REF14 !
  PARAMETER G(PRV,SR+2:FE+3:VA;0)  2.98150E+02  +GSRPRV#-2.5*GHSEROO#
 +11.2386*T;   6.00000E+03   N REF14 !
  PARAMETER G(PRV,SR+2:FE+4:VA;0)  2.98150E+02  +GSRPRVOX#-3*GHSEROO#;
 6.00000E+03   N REF14 !
  PARAMETER G(PRV,SR+2:VA:VA;0)  2.98150E+02  +GS3O#+2*GL4O#-1.5*GV4O#
 +.5*GVVV#-GL3O#-GHSEROO#+12.62121*T;   6.00000E+03   N REF14 !
  PARAMETER L(prv,SR+2:Fe+3,Fe+4:O-2;1) 298.15 -21003+20*t; 6.00000E+03  N REF14 !
  PARAMETER L(prv,SR+2:Fe+3,Fe+4:O-2;0) 298.15 -6999+6*t;  6.00000E+03   N REF14 !
  PARAMETER L(prv,SR+2,VA:FE+4:O-2;0) 298.15 73241;   6.00000E+03   N REF14 !
  PARAMETER L(prv,SR+2:FE+4,VA:O-2;0) 298.15 -117250;   6.00000E+03   N REF14 !
  PARAMETER L(PRV,LA+3,SR+2:FE+4:O-2;0) 298.15 -12026+21.67*T;
   6.00000E+03 N REF15 !
  PARAMETER L(PRV,LA+3,SR+2:FE+2:O-2;0) 298.15 -118678;   6.00000E+03   N REF15 !
  PARAMETER  G(PRV,La+3:Co+2:O-2;0) 2.98150E+02
GL2OV+0.5*GHSEROO+11.2379*T; 6000 N REF16 !
  PARAMETER  G(PRV,La+3:Co+2:VA;0) 2.98150E+02
GL2OV-2.5*GHSEROO+11.2379*T; 6000 N REF16 !
  PARAMETE  G(PRV,La+3:Co+3:O-2;0) 2.98150E+02 GL3CO; 6000 N REF16 !
  PARAMETER  G(PRV,La+3:Co+3:VA;0) 2.98150E+02
GL3CO-3*GHSEROO; 6000 N REF16 !
  PARAMETER  G(PRV,La+3:Co+4:O-2;0) 2.98150E+02
-0.166666*GVVV+0.666666*GL4VO+0.5*GLV4O-0.5*GHSEROO+5.76283*T; 6000 N REF16 !
  PARAMETER  G(PRV,La+3:Co+4:VA;0) 2.98150E+02
-0.166666*GVVV+0.666666*GL4VO+0.5*GLV4O-3.5*GHSEROO+5.76283*T; 6000 N REF16 !
  PARAMETER G(PRV,VA:CO+2:O-2;0) 2.98150E+02
0.5*GVVV+GL2OV-2*GL4VO+1.5*GLV4O+2*GHSEROO+9.82536*T; 6000  N REF16 !
  PARAMETER G(PRV,VA:CO+2:VA;0) 2.98150E+02
0.5*GVVV+GL2OV-2*GL4VO+1.5*GLV4O-GHSEROO+9.82536*T; 6000  N REF16 !
  PARAMETER G(PRV,VA:CO+3:O-2;0) 2.98150E+02
GL3CO+0.5*GVVV-2*GL4VO+1.5*GLV4O+1.5*GHSEROO-1.41254*T; 6000  N REF16 !
  PARAMETER G(PRV,VA:CO+3:VA;0) 2.98150E+02
GL3CO+0.5*GVVV-2*GL4VO+1.5*GLV4O-1.5*GHSEROO-1.41254*T; 6000  N REF16 !
  PARAMETER G(PRV,VA:CO+4:O-2;0) 2.98150E+02
0.33333*GVVV-1.33333*GL4VO+2*GLV4O+GHSEROO+4.35029*T; 6000  N  REF16 !
  PARAMETER G(PRV,VA:CO+4:VA;0) 2.98150E+02
0.33333*GVVV-1.33333*GL4VO+2*GLV4O-2*GHSEROO+4.35029*T; 6000  N REF16 !
  PARAMETER G(PRV,SR+2:Co+2:O-2;0) 2.98150E+02
GHSEROO+GS2OV+15.8759*T; 6000  N REF16 !
  PARAMETER G(PRV,SR+2:Co+2:VA;0) 2.98150E+02
 -2*GHSEROO+GS2OV+15.8759*T; 6000  N REF16 !
  PARAMETER G(PRV,SR+2:Co+3:O-2;0) 2.98150E+02
 0.5*GHSEROO+GS3OV+11.2379*T;  6000  N REF16 !
  PARAMETER G(PRV,SR+2:Co+3:VA;0) 2.98150E+02
    -2.5*GHSEROO+GS3OV+11.2379*T; 6000  N REF16 !
  PARAMETER G(PRV,SR+2:Co+4:O-2;0) 2.98150E+02 GS4O; 6000  N REF16 !
  PARAMETER G(PRV,SR+2:Co+4:VA;0) 2.98150E+02
```

```
  -3*GHSEROO+GS4O; 6000  N REF16 !
   PARAMETER G(PRV,SR+2:CO+2,CO+3:O-2;0)  2.98150E+02  -38661.9;
  6.00000E+03   N REF16 !
PARAMETER G(PRV,LA+3,SR+2:CO+4:*;0) 2.98150E+02 13510.8;
      6.00000E+03 N REF16 !
 PARAMETER G(PRV,LA+3,SR+2:CO+4:*;1) 2.98150E+02 -73293.2;
      6.00000E+03 N REF16 !
 PARAMETER G(PRV,LA+3,SR+2:CO+3:*;0) 2.98150E+02 -25713.4;
      6.00000E+03 N REF16 !
 PARAMETER G(PRV,LA+3,SR+2:CO+3:*;1) 2.98150E+02 17774.8;
  6.00000E+03 N REF16 !
 PARAMETER G(PRV,LA+3,SR+2:CO+3:*;2) 2.98150E+02 41090.7;
  6.00000E+03 N REF16 !
 PARAMETER G(PRV,LA+3,SR+2:CO+3:O-2,VA;0) 2.98150E+02 11792.1;
      6.00000E+03 N REF16 !
 PARAMETER G(PRV,LA+3,SR+2:CO+4:O-2,VA;0) 2.98150E+02 -823830.6;
      6.00000E+03 N REF16 !
   PARAMETER G(PRV,SR+2:CO+3,FE+3:*;0)  2.98150E+02  -81672.93;   6.00000E+03
   N REF16 !
   PARAMETER G(PRV,SR+2:CO+3,FE+4:*;0)  2.98150E+02  -29397.985;  6.00000E+03
   N REF16 !
   PARAMETER G(PRV,SR+2:CO+2,FE+3:*;0)  2.98150E+02  120085.95;   6.00000E+03
   N REF16 !
   PARAMETER G(PRV,LA+3,SR+2:CO+3,FE+3:*;0)  2.98150E+02  1.89713489E+04;
    6.00000E+03     N REF16 !
   PARAMETER G(PRV,LA+3,SR+2:CO+4,FE+3:*;0)  2.98150E+02  -1.31664608E+05;
     6.00000E+03     N REF16 !
   PARAMETER G(PRV,LA+3,SR+2:CO+2,FE+3:*;0)  2.98150E+02  -5.46437355E+04;
     6.00000E+03     N REF16 !
$ ---------------------------------
$ 5.3 Spinel
$ ---------------------------------
TYPE_DEFINITION W GES A_P_D SPINEL MAGNETIC  -3.0    2.80000E-01 !
PHASE SPINEL  %W  3 1   2  4 !
    CONSTITUENT SPINEL  :CO+2,CO+3,FE+2,FE+3 : CO+2,CO+3,FE+2,FE+3,VA :O-2 : !

   PARAMETER G(SPINEL,CO+2:CO+2:O-2;0)  2.98150E+02  +NCO3O4+2*ICO3O4
  +23.05272*T;   6.00000E+03   N  REF5 !
   PARAMETER G(SPINEL,CO+3:CO+2:O-2;0)  2.98150E+02  +2*ICO3O4+23.05272*T;
   6.00000E+03   N REF5 !
   PARAMETER G(SPINEL,CO+2:CO+3:O-2;0)  2.98150E+02  +NCO3O4;   6.00000E+03
    N REF5 !
   PARAMETER G(SPINEL,CO+3:CO+3:O-2;0) 298.15 0; 6000 N REF5 !
   PARAMETER G(SPINEL,CO+2,CO+3:CO+2:O-2;0)  2.98150E+02  -30847+44.249*T;
  6.00000E+03   N REF5 !
   PARAMETER G(SPINEL,CO+2,CO+3:CO+3:O-2;0)  2.98150E+02  -30847+44.249*T;
  6.00000E+03   N REF5 !
   PARAMETER G(SPINEL,FE+2:FE+2:O-2;0)  2.98150E+02  +7*GFE3O4+BFE3O4;
  6.00000E+03   N REF3 !
   PARAMETER G(SPINEL,FE+3:FE+2:O-2;0)  2.98150E+02  +7*GFE3O4;
  6.00000E+03   N REF3 !
   PARAMETER G(SPINEL,FE+2:FE+3:O-2;0)  2.98150E+02  +7*GFE3O4;
  6.00000E+03   N REF3 !
   PARAMETER G(SPINEL,FE+3:FE+3:O-2;0)  2.98150E+02  +7*GFE3O4-BFE3O4;
  6.00000E+03   N REF3 !
   PARAMETER G(SPINEL,FE+2:VA:O-2;0)  2.98150E+02  +5*GFE3O4+CFE3O4 ;
  6.00000E+03   N REF3 !
```

```
 PARAMETER G(SPINEL,FE+3:VA:O-2;0)  2.98150E+02  +5*GFE3O4+CFE3O4-BFE3O4;
6.00000E+03   N REF3 !
 PARAMETER G(SPINEL,FE+2:CO+2:O-2;0)  2.98150E+02  +2*TCOFE2O4-7*GFE3O4
+2*BFE3O4+2*ACOFE2O4+23.05272*T;   6.00000E+03   N REF16 !
 PARAMETER G(SPINEL,FE+3:CO+2:O-2;0)  2.98150E+02  +2*TCOFE2O4-7*GFE3O4
+BFE3O4+2*ACOFE2O4+23.05272*T;   6.00000E+03   N REF16 !
 PARAMETER G(SPINEL,FE+2:CO+3:O-2;0)  2.98150E+02  +7*GFE3O4-TCOFE2O4
+NCO3O4;   6.00000E+03   N REF16 !
 PARAMETER G(SPINEL,FE+3:CO+3:O-2;0)  2.98150E+02  +7*GFE3O4-BFE3O4
-TCOFE2O4+NCO3O4;   6.00000E+03   N REF16 !
 PARAMETER G(SPINEL,CO+2:FE+2:O-2;0)  2.98150E+02  +TCOFE2O4+BFE3O4;
6.00000E+03   N REF16 !
 PARAMETER G(SPINEL,CO+3:FE+2:O-2;0)  2.98150E+02  +TCOFE2O4-NCO3O4
+BFE3O4;   6.00000E+03   N REF16 !
 PARAMETER G(SPINEL,CO+2:FE+3:O-2;0)  2.98150E+02  +TCOFE2O4;
6.00000E+03   N REF16 !
PARAMETER G(SPINEL,CO+3:FE+3:O-2;0) 2.98150E+02 +TCOFE2O4-NCO3O4;
6.00000E+03   N REF16 !
 PARAMETER G(SPINEL,CO+2:VA:O-2;0)  2.98150E+02  +TCOFE2O4+CFE3O4
-2*GFE3O4 ;   6.00000E+03   N REF16 !
 PARAMETER G(SPINEL,CO+3:VA:O-2;0)  2.98150E+02  +TCOFE2O4-NCO3O4+CFE3O4
-2*GFE3O4 ;   6.00000E+03   N REF16 !
 PARAMETER G(SPINEL,CO+2,FE+3:CO+2:O-2;0)  2.98150E+02  +603917.71+404.40*T;
6.00000E+03   N REF16 !
 PARAMETER G(SPINEL,CO+3,FE+3:CO+2:O-2;0)  2.98150E+02  -59520.30+45.8467*T;
6.00000E+03   N REF16 !
 PARAMETER G(SPINEL,FE+2:CO+2,CO+3:O-2;0) 2.98150E+02  +328808.60-216.744*T;
6.00000E+03   N REF16 !
 PARAMETER G(SPINEL,FE+3:CO+2,CO+3:O-2;0)  2.98150E+02 +328808.60-216.744*T;
6.00000E+03   N REF16 !
 PARAMETER G(SPINEL,CO+2,FE+3:CO+3:O-2;0)  2.98150E+02  +603917.71+404.40*T;
6.00000E+03   N REF16 !
 PARAMETER G(SPINEL,CO+2:CO+3,FE+3:O-2;0)  2.98150E+02 +88091.749-21.7885*T;
6.00000E+03   N REF16 !
 PARAMETER G(SPINEL,CO+3,FE+3:CO+3:O-2;0)  2.98150E+02  -59520.30+45.8467*T;
6.00000E+03   N REF16 !
 PARAMETER G(SPINEL,CO+3:CO+3,FE+3:O-2;0) 2.98150E+02  +88091.749-21.7885*T;
6.00000E+03   N REF16 !
 PARAMETER G(SPINEL,FE+2:CO+3,FE+3:O-2;0)  2.98150E+02 +88091.749-21.7885*T;
6.00000E+03   N REF16 !
 PARAMETER G(SPINEL,FE+3:CO+3,FE+3:O-2;0)  2.98150E+02 +88091.749-21.7885*T;
6.00000E+03   N REF16 !
 PARAMETER G(SPINEL,CO+2,FE+3:FE+2:O-2;0)  2.98150E+02  +603917.71+404.40*T;
6.00000E+03   N REF16 !
 PARAMETER G(SPINEL,CO+3,FE+3:FE+2:O-2;0)  2.98150E+02  -59520.30+45.8467*T;
6.00000E+03   N REF16 !
 PARAMETER G(SPINEL,CO+2,FE+3:FE+3:O-2;0)  2.98150E+02  +603917.71+404.40*T;
6.00000E+03   N REF16 !
 PARAMETER G(SPINEL,CO+3,FE+3:FE+3:O-2;0)  2.98150E+02  -59520.30+45.8467*T;
6.00000E+03   N REF16 !
 PARAMETER G(SPINEL,CO+2,FE+3:VA:O-2;0)  2.98150E+02  +603917.71+404.40*T;
6.00000E+03   N REF16 !
 PARAMETER G(SPINEL,CO+3,FE+3:VA:O-2;0)  2.98150E+02  -59520.30+45.8467*T;
6.00000E+03   N REF16 !
 PARAMETER G(SPINEL,*:CO+2,FE+3:O-2;0)  2.98150E+02  +20783.780+4.96605*T;
6.00000E+03   N REF16 !
 PARAMETER TC(SPINEL,FE+2:FE+2:O-2;0)  2.98000E+02  848;  3.00000E+03  N REF3 !
```

```
   PARAMETER BMAGN(SPINEL,FE+2:FE+2:O-2;0)  2.98000E+02  44.54;  3.00000E+03
   N REF3 !
   PARAMETER TC(SPINEL,FE+3:FE+2:O-2;0)  2.98000E+02  848;  3.00000E+03  N REF3 !
   PARAMETER BMAGN(SPINEL,FE+3:FE+2:O-2;0)  2.98000E+02  44.54;  3.00000E+03
   N REF3 !
   PARAMETER TC(SPINEL,FE+2:FE+3:O-2;0)  2.98000E+02  848;  3.00000E+03  N REF3 !
   PARAMETER BMAGN(SPINEL,FE+2:FE+3:O-2;0)  2.98000E+02  44.54;  3.00000E+03
   N REF3 !
   PARAMETER TC(SPINEL,FE+3:FE+3:O-2;0)  2.98000E+02  848;  3.00000E+03  N REF3 !
   PARAMETER BMAGN(SPINEL,FE+3:FE+3:O-2;0)  2.98000E+02  44.54;  3.00000E+03
   N REF3 !
   PARAMETER TC(SPINEL,FE+2:VA:O-2;0)  2.98000E+02  848;  3.00000E+03  N REF3 !
   PARAMETER BMAGN(SPINEL,FE+2:VA:O-2;0)  2.98000E+02  44.54;  3.00000E+03 N REF3 !
   PARAMETER TC(SPINEL,FE+3:VA:O-2;0)  2.98000E+02  848;  3.00000E+03  N REF3 !
   PARAMETER BMAGN(SPINEL,FE+3:VA:O-2;0)  2.98000E+02  44.54;  3.00000E+03 N REF3 !
   PARAMETER TC(SPINEL,CO+2:FE+3:O-2;0)  2.98000E+02  775.15;  3.00000E+03
  N REF16  !
   PARAMETER BMAGN(SPINEL,CO+2:FE+3:O-2;0)  2.98000E+02  -23;
  3.00000E+03  N  REF16 !
   PARAMETER TC(SPINEL,FE+3:CO+2:O-2;0)  2.98000E+02  775.15;  3.00000E+03
  N REF16  !
   PARAMETER BMAGN(SPINEL,FE+3:CO+2:O-2;0)  2.98000E+02  -23;
  3.00000E+03  N REF16  !
$ ----------------------------------------------------------
$ 5.4 HCP-A3
$ --------------------------------
TYPE_DEFINITION . GES A_P_D HCP_A3 MAGNETIC  -3.0    2.80000E-01 !
 PHASE HCP_A3  %.  2 1   .5 !
    CONSTITUENT HCP_A3  :CO,FE : O,VA :  !

   PARAMETER G(HCP_A3,CO:O;0)  2.98150E+02  +GHSERCO#+.5*GHSEROO#-122309
  +66.269*T;   6.00000E+03   N REF5 !
   PARAMETER G(HCP_A3,FE:O;0)  2.98150E+02  +GFEHCP#+.5*GHSEROO#;
  6.00000E+03   N REF0 !
   PARAMETER TC(HCP_A3,CO:VA;0)  2.98150E+02  1396;  1.76800E+03  N REF5 !
   PARAMETER BMAGN(HCP_A3,CO:VA;0)  2.98150E+02  1.35;  1.76800E+03  N REF5 !
   PARAMETER G(HCP_A3,CO:VA;0)  2.98150E+02  +GHSERCO#;  3.20000E+03  N REF0 !
   PARAMETER G(HCP_A3,FE:VA;0)  2.98150E+02  +GFEHCP#;  3.20000E+03  N REF0 !
   PARAMETER G(HCP_A3,CO,FE:VA;0)  2.98150E+02  5000;  3.20000E+03  N REF7 !
   PARAMETER TC(HCP_A3,CO,FE:VA;0)  2.98150E+02  -253;  3.20000E+03  N REF7 !
   PARAMETER TC(HCP_A3,CO,FE:VA;1)  2.98150E+02  1494;  3.20000E+03  N REF7 !
   PARAMETER BMAGN(HCP_A3,CO,FE:VA;0)  2.98150E+02  5.41;  3.20000E+03  N
  REF7 !
   PARAMETER BMAGN(HCP_A3,CO,FE:VA;1)  2.98150E+02  -.24;  3.20000E+03  N
  REF7 !
$ --------------------------------
$ 5.5 FCC-A1
$ --------------------------------
TYPE_DEFINITION + GES A_P_D FCC_A1 MAGNETIC  -3.0    2.80000E-01 !
 PHASE FCC_A1  %+  2 1   1 !
    CONSTITUENT FCC_A1  :CO,FE,LA : O,VA :  !
  PARAMETER G(FCC_A1,CO:O;0)  2.98150E+02  +GCOFCC+GHSEROO-213318
  +107.071*T;   6.00000E+03   N REF5 !
  PARAMETER G(FCC_A1,FE:O;0)  2.98150E+02  +GFEFCC+GHSEROO+65*T;
  6.00000E+03   N REF4 !
  PARAMETER TC(FCC_A1,CO:VA;0)  2.98150E+02  1396;  1.76800E+03  N REF5 !
  PARAMETER BMAGN(FCC_A1,CO:VA;0)  2.98150E+02  1.35;  1.76800E+03  N REF5 !
```

```
  PARAMETER G(FCC_A1,LA:O;0)  2.98150E+02  +GLAFCC+GHSEROO-570000+91.4*T;
  6.00000E+03   N REF1 !
  PARAMETER G(FCC_A1,CO:VA;0)  2.98150E+02  +GCOFCC ;  3.20000E+03  N REF7 !
  PARAMETER G(FCC_A1,FE:VA;0)  2.98150E+02  +GFEFCC ;   6.00000E+03   N REF7 !
  PARAMETER TC(FCC_A1,FE:VA;0)  2.98150E+02  -201;   6.00000E+03   N REF7 !
  PARAMETER BMAGN(FCC_A1,FE:VA;0)  2.98150E+02  -2.1;   6.00000E+03   N REF7 !
  PARAMETER G(FCC_A1,LA:VA;0)  2.98150E+02  +GLAFCC ;   6.00000E+03   N REF0 !
  PARAMETER G(FCC_A1,FE:O,VA;0)  2.98150E+02  +168758+19.17*T;
  6.00000E+03   N REF4 !
  PARAMETER G(FCC_A1,FE,LA:VA;0)  2.98150E+02  +35052+22.45*T;
  6.00000E+03   N REF9 !
  PARAMETER G(FCC_A1,CO,FE:VA;0)  2.98150E+02  -8968.75;   6.00000E+03   N REF7 !
  PARAMETER G(FCC_A1,CO,FE:VA;2)  2.98150E+02  +3528.8;   6.00000E+03   N REF7 !
  PARAMETER TC(FCC_A1,CO,FE:VA;0)  2.98150E+02  +283;   6.00000E+03   N REF7 !
  PARAMETER TC(FCC_A1,CO,FE:VA;1)  2.98150E+02  +879;   6.00000E+03   N REF7 !
  PARAMETER BMAGN(FCC_A1,CO,FE:VA;0)  2.98150E+02  +8.407;   6.00000E+03   N REF7 !
  PARAMETER BMAGN(FCC_A1,CO,FE:VA;1)  2.98150E+02  -3.644;   6.00000E+03   N REF7 !
$
  PARAMETER G(FCC_A1,CO,LA:VA;0)  2.98150E+02  100000;   6.00000E+03   N REF6 !
$ ---------------------------------
$ 5.6 BCC-A2
$ ---------------------------------
TYPE_DEFINITION > GES A_P_D BCC_A2 MAGNETIC  -1.0    4.00000E-01 !
 PHASE BCC_A2  %>  2 1   3 !
    CONSTITUENT BCC_A2  :CO,FE,LA : O,VA :  !

  PARAMETER G(BCC_A2,CO:O;0)  2.98150E+02  +GCOBCC+3*GHSEROO ;
  6.00000E+03   N REF5 !
  PARAMETER G(BCC_A2,FE:O;0)  2.98150E+02  +GHSERFE+3*GHSEROO+195*T;
  6.00000E+03   N REF4 !
  PARAMETER G(BCC_A2,LA:O;0)  2.98150E+02  +GLABCC#+3*GHSEROO#-855000
  +142.5*T;   6.00000E+03   N REF1 !
  PARAMETER TC(BCC_A2,CO:VA;0)  2.98150E+02  1450;   6.00000E+03   N REF5 !
  PARAMETER BMAGN(BCC_A2,CO:VA;0)  2.98150E+02  1.35;   6.00000E+03   N REF5 !
  PARAMETER G(BCC_A2,CO:VA;0)  2.98150E+02  +GCOBCC ;   6.00000E+03   N REF5 !
  PARAMETER G(BCC_A2,FE:VA;0)  2.98150E+02  +GHSERFE ;   6.00000E+03   N REF4 !
  PARAMETER TC(BCC_A2,FE:VA;0)  2.98150E+02  1043;   6.00000E+03   N REF4 !
  PARAMETER BMAGN(BCC_A2,FE:VA;0)  2.98150E+02  2.22;   6.00000E+03   N REF4 !
  PARAMETER G(BCC_A2,LA:VA;0)  2.98150E+02  +GLABCC ;   6.00000E+03   N REF0 !
  PARAMETER G(BCC_A2,FE:O,VA;0)  2.98150E+02  -517549+71.83*T;
  6.00000E+03   N  REF4 !
  PARAMETER G(BCC_A2,CO,FE:VA;0)  2.98150E+02 -26222.7+125*T-15.502*T*LN(T)
   -0.63225E+6*T**(-1);   6.00000E+03   N REF7 !
  PARAMETER G(BCC_A2,CO,FE:VA;2)  2.98150E+02 +2686.79+0.63225E+6*T**(-1);
  6.00000E+03   N REF7 !
  PARAMETER G(BCC_A2,FE,LA:VA;0)  2.98150E+02 30358+23.67*T; 6.00000E+03  N REF9 !
  PARAMETER TC(BCC_A2,CO,FE:VA;0)  2.98150E+02  590;   6.00000E+03   N REF7 !
  PARAMETER BMAGN(BCC_A2,CO,FE:VA;0)  2.98150E+02  1.406;   6.00000E+03  N REF7 !
  PARAMETER BMAGN(BCC_A2,CO,FE:VA;1)  2.98150E+02  -0.6617; 6.00000E+03  N REF7 !
  PARAMETER G(BCC_A2,CO,LA:VA;0)  2.98150E+02 60000; 6.00000E+03  N REF6 !
$ ----------
$ 5.7 corundum phase, Fe2O3
$ ----------
TYPE_DEFINITION < GES A_P_D CORUNDUM MAGNETIC  -3.0    2.80000E-01 !
 PHASE CORUNDUM  %<  3 2   1   3 !
    CONSTITUENT CORUNDUM  :FE+2,FE+3:FE+3,VA:O-2 :  !
```

```
  PARAMETER G(CORUNDUM,FE+2:FE+3:O-2;0)  2.98150E+02  +GFE2O3+85000;
  6.00000E+03   N REF4 !
  PARAMETER G(CORUNDUM,FE+3:FE+3:O-2;0)  2.98150E+02  +GFE2O3+85000;
  6.00000E+03   N REF4 !
  PARAMETER G(CORUNDUM,FE+2:VA:O-2;0)  2.98150E+02  +GFE2O3 ;   6.00000E+03
    N REF4 !
  PARAMETER G(CORUNDUM,FE+3:VA:O-2;0)  2.98150E+02  +GFE2O3 ;   6.00000E+03
    N REF4 !
  PARAMETER TC(CORUNDUM,FE+2:FE+3:O-2;0)  2.98150E+02  -2867;  6.00000E+03 N REF4 !
  PARAMETER TC(CORUNDUM,FE+2:VA:O-2;0)  2.98150E+02  -2867;  6.00000E+03   N REF4 !
  PARAMETER TC(CORUNDUM,FE+3:FE+3:O-2;0)  2.98150E+02  -2867;  6.00000E+03 N REF4 !
  PARAMETER TC(CORUNDUM,FE+3:VA:O-2;0)  2.98150E+02  -2867;  6.00000E+03   N REF4 !
  PARAMETER BMAGN(CORUNDUM,FE+2:FE+3:O-2;0)  2.98150E+02  -25.1;
  6.00000E+03   N  REF4 !
  PARAMETER BMAGN(CORUNDUM,FE+2:VA:O-2;0)  2.98150E+02  -25.1; 6.00000E+03 N REF4 !
  PARAMETER BMAGN(CORUNDUM,FE+3:FE+3:O-2;0)  2.98150E+02  -25.1;
  6.00000E+03   N  REF4 !
  PARAMETER BMAGN(CORUNDUM,FE+3:VA:O-2;0)  2.98150E+02  -25.1; 6.00000E+03 N REF4 !
$-----------------------------------------------------------------------------
$ 5.8 HALITE Cobalt-Wuest phase, FeO-CoO
$ ----------
 TYPE_DEFINITION ) GES A_P_D HALITE MAGNETIC  -3.0    2.80000E-01 !
 PHASE HALITE  %)  2 1   1 !
    CONSTITUENT HALITE  :CO+2,FE+2,FE+3,VA : O-2 :  !
   PARAMETER TC(HALITE,CO+2:O-2;0)  2.98150E+02  -870;  3.00000E+03  N  REF5 !
   PARAMETER BMAGN(HALITE,CO+2:O-2;0)  2.98150E+02  2;  3.00000E+03  N  REF5 !
   PARAMETER G(HALITE,CO+2:O-2;0)  2.98150E+02  +GCOOS ;   6.00000E+03   N REF5 !
   PARAMETER G(HALITE,FE+2:O-2;0)  2.98150E+02  +GFEO ;   6.00000E+03   N REF3 !
   PARAMETER G(HALITE,FE+3:O-2;0)  2.98150E+02  +1.25*GFEO +1.25*GAFEO ;
  6.00000E+03   N REF3 !
   PARAMETER G(HALITE,VA:O-2;0) 298.15 0; 6000 N REF3 !
   PARAMETER G(HALITE,FE+2,FE+3:O-2;0)  2.98000E+02  -12324;  3.00000E+03  N REF3 !
   PARAMETER G(HALITE,FE+2,FE+3:O-2;1)  2.98000E+02  20070;  3.00000E+03  N REF3 !
   PARAMETER G(HALITE,CO+2,FE+2:O-2;0)  2.98000E+02 3441.85;
   3.00000E+03 N REF16 !
   PARAMETER G(HALITE,CO+2,FE+3:O-2;0)  2.98000E+02 -3766.5+9.868*T;
   3.00000E+03 N REF16 !
$ ----------
$ 5.9 La4SrO7 as BETA phase, LA-SR-O
$ ----------
PHASE BETA  %  2 2   3 !
    CONSTITUENT BETA  :LA+3,SR+2 : O-2,VA :  !

   PARAMETER G(BETA,LA+3:O-2;0)  2.98150E+02  +LA_BETA#;   6.00000E+03   N
  REF8 !
   PARAMETER G(BETA,SR+2:O-2;0)  2.98150E+02  +SR_ALPHA#+416100+GHSEROO#
  +15.87691*T;   6.00000E+03   N REF8 !
   PARAMETER G(BETA,LA+3:VA;0)  2.98150E+02  +LA_BETA#-3*GHSEROO#;
  6.00000E+03   N REF8 !
   PARAMETER G(BETA,SR+2:VA;0)  2.98150E+02  +SR_ALPHA#+416100-2*GHSEROO#
  +15.87691*T;   6.00000E+03   N REF8 !
   PARAMETER G(BETA,LA+3,SR+2:O-2;0)  2.98150E+02  -121000-237.8*T;
  6.00000E+03   N REF8 !
   PARAMETER G(BETA,LA+3,SR+2:VA;0)  2.98150E+02  -121000-237.8*T;
  6.00000E+03   N REF8 !
$ ----------
$ 5.10 A phase A-La2O3 (none-stoi), A-Sr2O3
```

```
$ ----------
PHASE LA2O3SS  %  2 2   3 !
    CONSTITUENT LA2O3SS  :LA+2,LA+3,SR+2 : O-2,VA :  !

   PARAMETER G(LA2O3SS,LA+2:O-2;0)  2.98150E+02  +GLAO#;   6.00000E+03   N
  REF1 !
   PARAMETER G(LA2O3SS,LA+3:O-2;0)  2.98150E+02  +GLA2O3D#;   6.00000E+03
  N REF1 !
   PARAMETER G(LA2O3SS,SR+2:O-2;0)  2.98150E+02  +SR_ALPHA#+GHSEROO#
  +15.87691*T;   6.00000E+03   N REF8 !
   PARAMETER G(LA2O3SS,LA+2:VA;0)  2.98150E+02  +GLAO#-GHSEROO#;
  6.00000E+03   N REF1 !
   PARAMETER G(LA2O3SS,LA+3:VA;0)  2.98150E+02  +GLA2O3D#-3*GHSEROO#;
  6.00000E+03   N REF1 !
   PARAMETER G(LA2O3SS,SR+2:VA;0)  2.98150E+02  +SR_ALPHA#-2*GHSEROO#
  +15.87691*T;   6.00000E+03   N REF8 !
   PARAMETER G(LA2O3SS,LA+3,SR+2:O-2;0)  2.98150E+02  +214900-78.1*T;
  6.00000E+03   N REF8 !
   PARAMETER G(LA2O3SS,LA+3,SR+2:VA;0)  2.98150E+02  +214900-78.1*T;
  6.00000E+03   N REF8 !
$ ----------
$ 5.11 X-phase, X-La2O3, X-Sr2O3
$ ----------
PHASE LA2O3_CUBSS  %  2 2   3 !
    CONSTITUENT LA2O3_CUBSS  :LA+3,SR+2 : O-2,VA :  !

   PARAMETER G(LA2O3_CUBSS,LA+3:O-2;0)  2.98150E+02  +GLA2O3X#;
  6.00000E+03   N REF8 !
   PARAMETER G(LA2O3_CUBSS,SR+2:O-2;0)  2.98150E+02  +SRX_ALPH#+GHSEROO#
  +15.87691*T;   6.00000E+03   N REF8 !
   PARAMETER G(LA2O3_CUBSS,LA+3:VA;0)  2.98150E+02  +GLA2O3X#-3*GHSEROO#;
  6.00000E+03   N REF8 !
   PARAMETER G(LA2O3_CUBSS,SR+2:VA;0)  2.98150E+02  +SRX_ALPH#-2*GHSEROO#
  +15.87691*T;   6.00000E+03   N REF8 !
   PARAMETER G(LA2O3_CUBSS,LA+3,SR+2:O-2;0)  2.98150E+02  +168700-78.1*T;
  6.00000E+03   N REF8 !
   PARAMETER G(LA2O3_CUBSS,LA+3,SR+2:O-2;1)  2.98150E+02  -20000;
  6.00000E+03   N REF8 !
   PARAMETER G(LA2O3_CUBSS,LA+3,SR+2:VA;0)  2.98150E+02  +168700-78.1*T;
  6.00000E+03   N REF8 !
   PARAMETER G(LA2O3_CUBSS,LA+3,SR+2:VA;1)  2.98150E+02  -20000;
  6.00000E+03   N REF8 !
$ ----------
$ 5.12 H phase  H-La2O3, H-Sr2O3
$ ----------
PHASE LA2O3_HEXSS  %  2 2   3 !
    CONSTITUENT LA2O3_HEXSS  :LA+3,SR+2 : O-2,VA :  !

   PARAMETER G(LA2O3_HEXSS,LA+3:O-2;0)  2.98150E+02  +GLA2O3H#;
  6.00000E+03   N REF8 !
   PARAMETER G(LA2O3_HEXSS,SR+2:O-2;0)  2.98150E+02  +SRH_ALPH#+GHSEROO#
  +15.87691*T;   6.00000E+03   N REF8 !
   PARAMETER G(LA2O3_HEXSS,LA+3:VA;0)  2.98150E+02  +GLA2O3H#-3*GHSEROO#;
  6.00000E+03   N REF8 !
   PARAMETER G(LA2O3_HEXSS,SR+2:VA;0)  2.98150E+02  +SRH_ALPH#-2*GHSEROO#
  +15.87691*T;   6.00000E+03   N REF8 !
   PARAMETER G(LA2O3_HEXSS,LA+3,SR+2:O-2;0)  2.98150E+02  +193600-78.1*T;
```

```
  6.00000E+03   N REF8 !
   PARAMETER G(LA2O3_HEXSS,LA+3,SR+2:VA;0)  2.98150E+02  +193600-78.1*T;
  6.00000E+03   N REF8 !
$ ----------
$ 5.13 SrO Solid Solution
$ ----------
 PHASE SRO  %  2 1   1 !
    CONSTITUENT SRO  :LA+3,SR+2,VA : O-2 :  !

   PARAMETER G(SRO,LA+3:O-2;0)  2.98150E+02  +.5*GLA2O3D#+113700;
  6.00000E+03   N REF8 !
   PARAMETER G(SRO,SR+2:O-2;0)  2.98150E+02  +GSROSOL#;   6.00000E+03   N
  REF2 !
   PARAMETER G(SRO,VA:O-2;0) 298.15 0; 6000 N REF8 !
$ ----------
$ 5.14 SrO2
$ ----------
 PHASE SRO2  %  1  1.0  !
    CONSTITUENT SRO2  :SRO2 :  !

   PARAMETER G(SRO2,SRO2;0)  2.98150E+02  +GSRO2SOL#;   6.00000E+03   N REF2 !
$ ----------
$ 5.15 La4SR3O9
$ ----------
$ La4Sr3O9, Stoichiometric
 PHASE LA4SR3O9  %  3 4   3   9 !
    CONSTITUENT LA4SR3O9  :LA+3 : SR+2 : O-2 :  !

   PARAMETER G(LA4SR3O9,LA+3:SR+2:O-2;0)  2.98150E+02  +2*GLA2O3D#
  +3*GSROSOL#+2.298E+05-1.3675E+02*T;   6.00000E+03   N REF8 !
$ ----------
$ 5.16 (LA,SR)3(FE,CO)2O7---Is it possible to simplificate
$ ----------
$
 PHASE SR3FE2O7  %  5 1   2   2   6   1 !
   CONSTITUENT SR3FE2O7 :LA+3,SR+2:LA+3,SR+2:CO+3,FE+3,FE+4:O-2,VA:O-2
    :  !

   PARAMETER G(SR3FE2O7,LA+3:LA+3:FE+3:O-2:O-2;0) 298.15 +GLF3O#-300000+115*T;
     6.00000E+03   N REF15 !
   PARAMETER G(SR3FE2O7,SR+2:LA+3:FE+3:O-2:O-2;0)  2.98150E+02  +GLF3O#;
  6.00000E+03   N REF15 !
   PARAMETER G(SR3FE2O7,LA+3:SR+2:FE+3:O-2:O-2;0)  2.98150E+02  +GSR3FE2O#
  +22.4772*T+GHSEROO#-300000+115*T;   6.00000E+03   N REF14 !
   PARAMETER G(SR3FE2O7,SR+2:SR+2:FE+3:O-2:O-2;0)  2.98150E+02  +GSR3FE2O#
  +22.4772*T+GHSEROO#;   6.00000E+03   N REF14 !
   PARAMETER G(SR3FE2O7,LA+3:LA+3:FE+4:O-2:O-2;0)  2.98150E+02  +GLF3O#
  +GSF4O#-GSF3O#-300000+115*T;   6.00000E+03   N REF15 !
   PARAMETER G(SR3FE2O7,SR+2:LA+3:FE+4:O-2:O-2;0)  2.98150E+02  +GLF3O#
  +GSF4O#-GSF3O#;   6.00000E+03   N REF15 !
   PARAMETER G(SR3FE2O7,LA+3:SR+2:FE+4:O-2:O-2;0) 298.15 +GSF4O#-300000+115*T;
     6.00000E+03   N REF15 !
   PARAMETER G(SR3FE2O7,SR+2:SR+2:FE+4:O-2:O-2;0)  2.98150E+02  +GSF4O#;
  6.00000E+03   N REF14 !
   PARAMETER G(SR3FE2O7,LA+3:LA+3:FE+3:VA:O-2;0)  2.98150E+02  +GSF4V#
  +GLF3O#-GSF4O#-300000+115*T;   6.00000E+03   N REF15 !
   PARAMETER G(SR3FE2O7,SR+2:LA+3:FE+3:VA:O-2;0)  2.98150E+02  +GSF4V#
```

```
  +GLF3O#-GSF4O#;   6.00000E+03   N REF15 !
   PARAMETER G(SR3FE2O7,LA+3:SR+2:FE+3:VA:O-2;0)  2.98150E+02  +GSR3FE2O#
  +22.4772*T-5*GHSEROO#-300000+115*T;   6.00000E+03   N REF15 !
   PARAMETER G(SR3FE2O7,SR+2:SR+2:FE+3:VA:O-2;0)  2.98150E+02  +GSR3FE2O#
  +22.4772*T-5*GHSEROO#;   6.00000E+03   N REF14 !
   PARAMETER G(SR3FE2O7,LA+3:LA+3:FE+4:VA:O-2;0)  2.98150E+02  +GSF4V#
  +GLF3O#+GSF4O#-GSF3O#-GSF4O#-300000+115*T;   6.00000E+03   N REF15 !
   PARAMETER G(SR3FE2O7,SR+2:LA+3:FE+4:VA:O-2;0)  2.98150E+02  +GSF4V#
  +GLF3O#+GSF4O#-GSF3O#-GSF4O#;   6.00000E+03   N REF15 !
   PARAMETER G(SR3FE2O7,LA+3:SR+2:FE+4:VA:O-2;0)  2.98150E+02  +GSF4O#
  -6*GHSEROO#-300000+115*T;   6.00000E+03   N REF15 !
   PARAMETER G(SR3FE2O7,SR+2:SR+2:FE+4:VA:O-2;0)  2.98150E+02  +GSF4O#
  -6*GHSEROO#;   6.00000E+03   N REF14 !
   PARAMETER G(SR3FE2O7,SR+2:SR+2:CO+3:O-2:O-2;0)  2.98150E+02  +3*GSROSOL
  +2*GCOOS +2*GHSEROO+15000;   6.00000E+03   N REF16 !
   PARAMETER G(SR3FE2O7,SR+2:SR+2:CO+3:VA:O-2;0)  2.98150E+02  +3*GSROSOL
  +2*GCOOS -4*GHSEROO;   6.00000E+03   N REF16 !
   PARAMETER G(SR3FE2O7,SR+2:SR+2:CO+3,Fe+3:O-2:O-2;0)  2.98150E+02
    -165000;   6.00000E+03   N REF16 !
   PARAMETER G(SR3FE2O7,SR+2:SR+2:CO+3,Fe+3:VA:O-2;0)  2.98150E+02
    -100000;   6.00000E+03   N REF16 !
   PARAMETER G(SR3FE2O7,SR+2:LA+3,SR+2:FE+3:O-2:O-2;0)  2.98150E+02  -150000;
    6.00000E+03   N REF15 !
   PARAMETER G(SR3FE2O7,SR+2:LA+3,SR+2:FE+3:O-2:O-2;1)  2.98150E+02  +200000;
    6.00000E+03   N REF15 !
$ ----------
$ 5.17 SR3CO2O7
$ ----------
 PHASE SR3CO2O7   %  5 1   2   2   6   1  !
    CONSTITUENT  SR3CO2O7 :SR+2 : SR+2 : CO+3: O-2,VA : O-2 :  !

   PARAMETER G(SR3CO2O7,SR+2:SR+2:CO+3:O-2:O-2;0)  2.98150E+02  +3*GSROSOL
  +2*GCOOS#+2*GHSEROO#-100000+60*T;   6.00000E+03   N REF16 !
   PARAMETER G(SR3CO2O7,SR+2:SR+2:CO+3:VA:O-2;0)  2.98150E+02  +3*GSROSOL
  +2*GCOOS#-4*GHSEROO#;   6.00000E+03   N REF16 !
$ ----------
$ 5.18 La2SrFe2O7
$ ----------
 PHASE L2SF2O7  %  5 1   2   2   6   1 !
    CONSTITUENT L2SF2O7  :SR+2 : LA+3,SR+2 : FE+3,FE+4 : O-2 : O-2 :  !

   PARAMETER G(L2SF2O7,SR+2:LA+3:FE+3:O-2:O-2;0)  2.98150E+02  +GLF3O#
  -20*T;   6.00000E+03   N REF15 !
   PARAMETER G(L2SF2O7,SR+2:SR+2:FE+3:O-2:O-2;0)  2.98150E+02  +GSR3FE2O#
  +22.4772*T+GHSEROO#;   6.00000E+03   N REF15 !
   PARAMETER G(L2SF2O7,SR+2:LA+3:FE+4:O-2:O-2;0)  2.98150E+02  +GLF3O#
  -20*T+GSF4O#-GSF3O#;   6.00000E+03   N REF15 !
   PARAMETER G(L2SF2O7,SR+2:SR+2:FE+4:O-2:O-2;0)  2.98150E+02  +GSF4O#;
  6.00000E+03   N REF15 !
$ ----------
$ 5.19 (La,Sr)2FeCoO4  $ rhombohedral PEROVSKITE
$ ----------
PHASE SR2FEO4  %  4 2   1   4   1 !
    CONSTITUENT SR2FEO4  :LA+3,SR+2:CO+2,CO+4,FE+4:O-2:O-2,VA:  !
   PARAMETER G(SR2FEO4,Sr+2:Co+4:O-2:Va;0) 298.15 GSRCOO4; 6000  N REF16 !
   PARAMETER G(SR2FEO4,La+3:Co+2:O-2:Va;0) 298.15 GLACOO4; 6000  N REF16 !
   PARAMETER G(SR2FEO4,Sr+2:Co+2:O-2:Va;0) 298.15 GLACOO4-GLA2O3D+2*GSROSOL;
```

```
    6000  N REF16 !
   PARAMETER G(SR2FEO4,La+3:Co+4:O-2:Va;0) 298.15 GSRCOO4+GLA2O3D-2*GSROSOL;
    6000  N REF16 !
   PARAMETER G(SR2FEO4,Sr+2:Co+4:O-2:O-2;0) 298.15 GSRCOO4+GHSEROO; 6000  N REF16 !
   PARAMETER G(SR2FEO4,La+3:Co+2:O-2:O-2;0) 298.15 GLACOO4+GHSEROO+1000000;
    6000  N REF16 !
   PARAMETER G(SR2FEO4,Sr+2:Co+2:O-2:O-2;0) 298.15 GLACOO4-GLA2O3D+2*GSROSOL
   +GHSEROO;    6000  N REF16 !
   PARAMETER G(SR2FEO4,La+3:Co+4:O-2:O-2;0) 298.15 GSRCOO4+GLA2O3D-2*GSROSOL
   +GHSEROO+1000000;    6000  N REF16 !
   PARAMETER G(SR2FEO4,La+3,Sr+2:Co+2:O-2:Va;0) 298.15 -83000-60*t; 6000 N REF16 !
   PARAMETER G(SR2FEO4,La+3,Sr+2:Co+4:O-2:Va;0) 298.15 -83000-60*t; 6000 N REF16 !
      PARAMETER G(SR2FEO4,LA+3:FE+4:O-2:O-2;0)  2.98150E+02
  +GSM4_RP1-2*GSROSOL+GLA2O3D+30000-21*t;   6.00000E+03 N REF15 !
   PARAMETER G(SR2FEO4,SR+2:FE+4:O-2:O-2;0)  2.98150E+02
  +GSM4_RP1#+GHSEROO#;   6.00000E+03   N REF14 !
   PARAMETER G(SR2FEO4,LA+3:FE+4:O-2:VA;0)  2.98150E+02
   +GSM4_RP1-2*GSROSOL+GLA2O3D-GHSEROO#-80000;   6.00000E+03   N REF15 !
   PARAMETER G(SR2FEO4,SR+2:FE+4:O-2:VA;0)  2.98150E+02  +GSM4_RP1#;
     6.00000E+03   N REF14 !
   PARAMETER G(SR2FEO4,LA+3,SR+2:FE+4:O-2:O-2;0)  2.98150E+02  -0;
     6.00000E+03   N REF15 !
   PARAMETER G(SR2FEO4,LA+3,SR+2:FE+4:O-2:O-2;1)  2.98150E+02
  280000;   6.00000E+03   N REF15 !
$ ----------
$ 5.20 (LA,SR)4FE3O10
$ ----------
 PHASE SR4FE3O10  %  5 1   3   3   9   1 !
    CONSTITUENT SR4FE3O10  :LA+3,SR+2 : LA+3,SR+2 : FE+3,FE+4 : O-2,VA : O-2
    :  !

   PARAMETER G(SR4FE3O10,LA+3:LA+3:FE+3:O-2:O-2;0)  2.98150E+02  +GSL3#
  +GLS3#-GSS3#;   6.00000E+03   N REF15 !
   PARAMETER G(SR4FE3O10,SR+2:LA+3:FE+3:O-2:O-2;0)  2.98150E+02  +GSL3#;
  6.00000E+03   N REF15 !
   PARAMETER G(SR4FE3O10,LA+3:SR+2:FE+3:O-2:O-2;0)  2.98150E+02  +GLS3#;
  6.00000E+03   N REF15 !
   PARAMETER G(SR4FE3O10,SR+2:SR+2:FE+3:O-2:O-2;0)  2.98150E+02  +.5*GLS3#
  +.5*GSS4#;   6.00000E+03   N REF15 !
   PARAMETER G(SR4FE3O10,LA+3:LA+3:FE+4:O-2:O-2;0)  2.98150E+02  +GSL4#
  +GLS4#-GSS4#;   6.00000E+03   N REF15 !
   PARAMETER G(SR4FE3O10,SR+2:LA+3:FE+4:O-2:O-2;0)  2.98150E+02  +GSS4#
  +GSL3#-GSS3#;   6.00000E+03   N REF15 !
   PARAMETER G(SR4FE3O10,LA+3:SR+2:FE+4:O-2:O-2;0)  2.98150E+02  +.5*GLS3#
  +.5*GSS4#;   6.00000E+03   N REF15 !
   PARAMETER G(SR4FE3O10,SR+2:SR+2:FE+4:O-2:O-2;0)  2.98150E+02  +GSS4#;
  6.00000E+03   N REF15 !
   PARAMETER G(SR4FE3O10,LA+3:LA+3:FE+3:VA:O-2;0)  2.98150E+02  +9*GLS3OV#
  -9*GLS3#+234.93*T+GLL3#;   6.00000E+03   N REF15 !
   PARAMETER G(SR4FE3O10,SR+2:LA+3:FE+3:VA:O-2;0)  2.98150E+02  +GSS3OV#
  -6*GSS3#+202.295*T+GSL3#;   6.00000E+03   N REF15 !
   PARAMETER G(SR4FE3O10,LA+3:SR+2:FE+3:VA:O-2;0)  2.98150E+02  +9*GLS3OV#
  -8*GLS3#+234.93*T;   6.00000E+03   N REF15 !
   PARAMETER G(SR4FE3O10,SR+2:SR+2:FE+3:VA:O-2;0)  2.98150E+02  +GSS3OV#
  -5*GSS3#+202.295*T;   6.00000E+03   N REF15 !
   PARAMETER G(SR4FE3O10,LA+3:LA+3:FE+4:VA:O-2;0)  2.98150E+02  +9*GLS3OV#
  -9*GLS3#+234.93*T+GLL4#;   6.00000E+03   N REF15 !
```

```
   PARAMETER G(SR4FE3O10,SR+2:LA+3:FE+4:VA:O-2;0)  2.98150E+02  +GSS3OV#
  -6*GSS3#+202.295*T+GSL4#;   6.00000E+03   N REF15 !
   PARAMETER G(SR4FE3O10,LA+3:SR+2:FE+4:VA:O-2;0)  2.98150E+02  +9*GLS3OV#
  -9*GLS3#+234.93*T+GLS4#;   6.00000E+03   N REF15 !
   PARAMETER G(SR4FE3O10,SR+2:SR+2:FE+4:VA:O-2;0)  2.98150E+02  +GSS3OV#
  -6*GSS3#+202.295*T+GSS4#;   6.00000E+03   N REF15 !
   PARAMETER L(SR4FE3O10,LA+3,SR+2:SR+2:FE+3:O-2:O-2;0) 2.98150E+02 0;
   6.00000E+03 N REF15 !
   PARAMETER L(SR4FE3O10,LA+3,SR+2:SR+2:FE+4:O-2:O-2;0) 2.98150E+02 0;
   6.00000E+03 N REF15 !
$ ----------
$ 5.21 (LA,SR)4FE6O13
$ ----------
 PHASE SR4FE6O13  %  5 4   4   2   12   2 !
    CONSTITUENT SR4FE6O13  :LA+3,SR+2 : FE+3 : CO+3,FE+2,FE+3,FE+4 : O-2
    : O-2,VA:  !

   PARAMETER G(SR4FE6O13,LA+3:FE+3:FE+2:O-2:O-2;0)  2.98150E+02  +GLAYREF#
  -900000;   6.00000E+03   N REF15 !
   PARAMETER G(SR4FE6O13,SR+2:FE+3:FE+2:O-2:O-2;0)  2.98150E+02  +GLAYREF#;
   6.00000E+03   N REF14 !
   PARAMETER G(SR4FE6O13,LA+3:FE+3:FE+3:O-2:O-2;0)  2.98150E+02  +GLAYS#
  -.5*GLAYRED#+.5*GLAYREF#+11.5264*T-900000;   6.00000E+03   N REF15 !
   PARAMETER G(SR4FE6O13,SR+2:FE+3:FE+3:O-2:O-2;0)  2.98150E+02  +GLAYS#
  -.5*GLAYRED#+.5*GLAYREF#+11.5264*T;   6.00000E+03   N REF14 !
   PARAMETER G(SR4FE6O13,LA+3:FE+3:FE+4:O-2:O-2;0)  2.98150E+02  +GLAYOX#
  -900000;   6.00000E+03   N REF15 !
   PARAMETER G(SR4FE6O13,SR+2:FE+3:FE+4:O-2:O-2;0)  2.98150E+02  +GLAYOX#;
  6.00000E+03   N REF14 !
   PARAMETER G(SR4FE6O13,LA+3:FE+3:FE+2:O-2:VA;0)  2.98150E+02  +GLAYRED#
 -900000;   6.00000E+03   N REF15 !
   PARAMETER G(SR4FE6O13,SR+2:FE+3:FE+2:O-2:VA;0)  2.98150E+02  +GLAYRED#;
  6.00000E+03   N REF14 !
   PARAMETER G(SR4FE6O13,LA+3:FE+3:FE+3:O-2:VA;0)  2.98150E+02  +.5*GLAYRED#
  -.5*GLAYREF#+GLAYS#+11.5264*T-900000;   6.00000E+03   N REF15 !
   PARAMETER G(SR4FE6O13,SR+2:FE+3:FE+3:O-2:VA;0)  2.98150E+02  +.5*GLAYRED#
  -.5*GLAYREF#+GLAYS#+11.5264*T;   6.00000E+03   N REF14 !
   PARAMETER G(SR4FE6O13,LA+3:FE+3:FE+4:O-2:VA;0)  2.98150E+02  +GLAYOX#
  +GLAYRED#-GLAYREF#-900000;   6.00000E+03   N REF15 !
   PARAMETER G(SR4FE6O13,SR+2:FE+3:FE+4:O-2:VA;0)  2.98150E+02  +GLAYOX#
  +GLAYRED#-GLAYREF#;   6.00000E+03   N REF14 !
   PARAMETER G(SR4FE6O13,SR+2:FE+3:FE+3,FE+4:O-2:O-2;0)  2.98150E+02  +9982;
    6.00000E+03   N REF14 !
   PARAMETER G(SR4FE6O13,SR+2:FE+3:FE+3:O-2:O-2,VA;0)  2.98150E+02  +15000;
  6.00000E+03   N REF14 !
   PARAMETER G(SR4FE6O13,SR+2:FE+3:FE+4:O-2:O-2,VA;0)  2.98150E+02  +15000;
  6.00000E+03   N REF14 !
   PARAMETER G(SR4FE6O13,SR+2:FE+3:FE+3,FE+4:O-2:VA;0)  2.98150E+02  +9982;
   6.00000E+03   N REF14 !
$$ CO SOLUBILITY (SR-CO-FE-O)
   PARAMETER G(SR4FE6O13,SR+2:FE+3:CO+3:O-2:O-2;0)  2.98150E+02  +4*GSRPRV
   +2*GHSERCO +4*GHSEROO -478000;   6.00000E+03   N !
   PARAMETER G(SR4FE6O13,SR+2:FE+3:CO+3:O-2:VA;0)  2.98150E+02  +4*GSRPRV
   +2*GHSERCO +2*GHSEROO -170000;   6.00000E+03   N !
$$ Nothing but two end members have no contribution!
   PARAMETER G(SR4FE6O13,LA+3:FE+3:CO+3:O-2:O-2;0)  2.98150E+02  +4*GSRPRV
   +2*GHSERCO +4*GHSEROO;   6.00000E+03   N !
```

```
   PARAMETER G(SR4FE6O13,LA+3:FE+3:CO+3:O-2:VA;0)  2.98150E+02  +4*GSRPRV
   +2*GHSERCO +2*GHSEROO;   6.00000E+03   N !
$ ----------
$ 5.22 (LA,SR)FE12O19, SRFE12O19
$ ----------
 PHASE SRFE12O19  %  4 1   1   11   19 !
    CONSTITUENT SRFE12O19  :LA+3,SR+2 : FE+2,FE+3 : FE+3 : O-2 :  !

   PARAMETER G(SRFE12O19,LA+3:FE+2:FE+3:O-2;0)  2.98150E+02  +GHEXLA#;
  6.00000E+03   N REF9 !
   PARAMETER G(SRFE12O19,SR+2:FE+2:FE+3:O-2;0)  2.98150E+02  +G2HEX#;
  6.00000E+03   N REF14 !
   PARAMETER G(SRFE12O19,LA+3:FE+3:FE+3:O-2;0)  2.98150E+02  +GHEX#+GHEXLA#
  -G2HEX#;   6.00000E+03   N REF9 !
   PARAMETER G(SRFE12O19,SR+2:FE+3:FE+3:O-2;0)  2.98150E+02  +GHEX#;
  6.00000E+03   N REF14 !
   PARAMETER G(SRFE12O19,LA+3,SR+2:FE+2:FE+3:O-2;0)  2.98150E+02  +53400;
  6.00000E+03   N REF15 !
   PARAMETER G(SRFE12O19,LA+3,SR+2:FE+3:FE+3:O-2;0)  2.98150E+02  +53400;
  6.00000E+03   N REF15 !
$ ----------
$ 5.23 Sr6Co5O15, SR-CO-O
$ ----------
 PHASE  Sr6Co5O15 % 4 6 4 1 15 !
    CONSTITUENT Sr6Co5O15 :SR+2: CO+4: CO+2: O-2:   !
   PARAMETER G(Sr6Co5O15,Sr+2:Co+4:Co+2:O-2;0) 298.15 -5599515.9+3551.83*T
  -602.231*T*LN(T)-0.08953*T**2+4863524*T**(-1)-300000.00+255*T; 6000   N REF16 !
$ ----------
$ 5.24 Sr2Co2O5, SR-CO-O SAAL + this work
$ ----------
 PHASE  Sr2Co2O5 % 4 2 1 1 5 !
    CONSTITUENT Sr2Co2O5 :SR+2: CO+2: CO+4: O-2:    !
   PARAMETER G(Sr2Co2O5,Sr+2:Co+2:Co+4:O-2;0) 298.15 +GSR2CO2O; 6000  N REF16 !
$ ----------
$ 5.25 CO3LA4O10_S, LA-CO-O SAAL
$ ----------
    PHASE CO3LA4O10_S  %  1 1.0  !
   CONSTITUENT CO3LA4O10_S  :CO3LA4O10 :  !
   PARAMETER G(CO3LA4O10_S,CO3LA4O10;0)  2.98150E+02  +F7609T#+10000-4*T;
  6.00000E+03   N REF16 !
$ ----------
$ 5.26 DHCP
$ ----------
PHASE  DHCP %  2 1  .5 !
    CONSTITUENT DHCP :LA : O,VA :  !
   PARAMETER G(DHCP,LA:O;0)  2.98150E+02  +GHSERLA+.5*GHSEROO-285000
 +42.4*T;  3.20000E+03  N REF1 !
   PARAMETER G(DHCP,LA:VA;0)  2.98150E+02  +GHSERLA ;  3.20000E+03  N REF0 !
$ ----------
$ 5.27 Gas
$ ----------
PHASE GAS %  1  1.0  !
    CONSTITUENT GAS :CO,CO2,COO,SRO,SR,SR2,O,O2,O3,LA,LA1O1,LA2O1,LA2O2 :  !

   PARAMETER G(GAS,CO;0)  2.98150E+02  +F7261T#+RTLNP#;   6.00000E+03   N
  REF17 !
   PARAMETER G(GAS,CO2;0)  2.98150E+02  +F7427T#+RTLNP#;   6.00000E+03   N
```

```
  REF17 !
   PARAMETER G(GAS,COO;0)  2.98150E+02  +F7356T#+RTLNP#;   6.00000E+03   N
   PARAMETER G(GAS,O;0)  2.98150E+02  +F13349T#+RTLNP#;   6.00000E+03   N
  REF17 !
   PARAMETER G(GAS,O2;0)  2.98150E+02  +F13704T#+RTLNP#;   6.00000E+03   N
  REF17 !
   PARAMETER G(GAS,O3;0)  2.98150E+02  +F14021T#+RTLNP#;   6.00000E+03   N
  REF17 !
   PARAMETER G(GAS,SR;0)  2.98150E+02  +F15641T#+RTLNP;
  6.00000E+03   N !
   PARAMETER G(GAS,SR2;0)  2.98150E+02  +F15650T#+RTLNP;
  6.00000E+03   N !
     PARAMETER G(GAS,SRO;0)  2.98150E+02  +F13511T#+RTLNP;
  6.00000E+03   N !
     PARAMETER  G(GAS,LA;0)     298.15  +F12026T#+RTLNP#;   6000  N !
     PARAMETER  G(GAS,LA1O1;0)  298.15  +F12049T#+RTLNP#;   6000  N  !
     PARAMETER  G(GAS,LA2O1;0)  298.15  +F12085T#+RTLNP#;   6000  N  !
     PARAMETER  G(GAS,LA2O2;0)  298.15  +F12089T#+RTLNP#;   6000  N !
$ ----------
$ 5.28 CO13LA
$ ----------
 PHASE CO13LA %  2 0.929 0.071 !
 CONST CO13LA :CO:LA: !

 PARAMETER G(CO13LA,CO:LA;0) 298.15 -8589.5+3.262*T
 +0.071*GHSERLA+0.929*GHSERCO; 6000.0 N REF6 !
  PARAMETER TC(CO13LA,CO:LA;0)  2.98150E+02  +1290;   6.00000E+03   N REF6 !
  PARAMETER BMAGN(CO13LA,CO:LA;0)  2.98150E+02  +20.5;   6.00000E+03   N REF6 !
$ ----------
$ 5.29 CO5LA
$ ----------
PHASE CO5LA %  2 0.833 0.167 !
 CONST CO5LA :CO:LA: !

 PARAMETER G(CO5LA,CO:LA;0) 298.15 9434.8+1.441*T
 +0.167*GHSERLA+0.833*GHSERCO; 6000.0 N REF6 !
  PARAMETER TC(CO5LA,CO:LA;0)  2.98150E+02  +840;   6.00000E+03   N REF6 !
  PARAMETER BMAGN(CO5LA,CO:LA;0)  2.98150E+02  +20.5;   6.00000E+03   N REF6 !
$ ----------
$ 5.30 CO19LA5
$ ----------
PHASE CO19LA5 %  2 0.792 0.208 !
 CONST CO19LA5 :CO:LA: !

 PARAMETER G(CO19LA5,CO:LA;0) 298.15 -10729.3+1.912*T
 +0.208*GHSERLA+0.792*GHSERCO; 6000.0 N REF6 !
  PARAMETER TC(CO19LA5,CO:LA;0)  2.98150E+02  +616;   6.00000E+03   N REF6 !
  PARAMETER BMAGN(CO19LA5,CO:LA;0)  2.98150E+02  +1.93;   6.00000E+03   N REF6 !
$ ----------
$ 5.31 CO7LA2
$ ----------
PHASE CO7LA2 %  2 0.777 0.223 !
 CONST CO7LA2 :CO:LA: !

 PARAMETER G(CO7LA2,CO:LA;0) 298.15 -10728.5+1.746*T
 +0.223*GHSERLA+0.777*GHSERCO; 6000.0 N REF6 !
  PARAMETER TC(CO7LA2,CO:LA;0)  2.98150E+02  +490;   6.00000E+03   N REF6 !
```

```
  PARAMETER BMAGN(CO7LA2,CO:LA;0)  2.98150E+02  +6.9;   6.00000E+03   N REF6 !
$ ----------
$ 5.32 CO3LA2
$ ----------
PHASE CO3LA2 %  2 0.6 0.4 !
 CONST CO3LA2 :CO:LA: !

 PARAMETER G(CO3LA2,CO:LA;0) 298.15 -11550.6+1.397*T
 +0.4*GHSERLA+0.6*GHSERCO; 6000.0 N REF6 !
$ ----------
$ 5.33 CO23LA27
$ ----------
PHASE CO23LA27 %  2 0.46 0.54 !
 CONST CO23LA27 :CO:LA: !

 PARAMETER G(CO23LA27,CO:LA;0) 298.15 -10857+1.495*T
 +0.54*GHSERLA+0.46*GHSERCO; 6000.0 N REF6 !
$ ----------
$ 5.34 COLA3
$ ----------
 PHASE COLA3 %  2 0.25 0.75 !
 CONST COLA3 :CO:LA: !

PARAMETER G(COLA3,CO:LA;0) 298.15 -5120-2.453*T
 +0.75*GHSERLA+0.25*GHSERCO; 6000.0 N REF6 !
$ --------------------------------------------------------------------------
 LIST_OF_REFERENCES
 NUMBER     SOURCE
$ 1U-5U      La, Sr, Co, Fe, O
REF0         A.T. Dinsdale, CALPHAD 15 (1991) 317-425.
$ 1B         La-O:
REF1         A.N. Grundy, B. Hallstedt, L.J. Gauckler, J. Phase Equilib. 22 (2001) 105-113
$ 2B         Sr-O:
 REF2        D. Risold, B. Hallstedt, L.J. Gauckler, CALPHAD, 20 (1996) 353-361.
$ 3B         Fe-O:
REF3         B. Sundman, J. Phase equilib. 12 (1991) 127-140.
REF4         L. Kjellqvist, M. Selleby, B. Sundman, CALPHAD 32 (2008) 577-592.
$ 4B         Co-O:
REF5         M. Chen, B. Hallstedt, L.J. Gauckler, J. Phase Equilib. 24 (2003) 212
$ 5B         La-Co
REF6         C.P. Wang, J. Wang, X.J. Liu, I. Ohnuma, R. Kainuma, K. Ishida, J. Alloys
Compd. 453 (2008) 174-179.
$ 6B         Co-Fe
REF7         I. Ohnuma, H. Enokia, O. Ikeda, R. Kainuma, H. Ohtani, B. Sundman, K. Ishida,
Acta Mater. 50 (2002) 379–393.
$ 1T         La-Sr-O:
REF8         A.N. Grundy, B. Hallstedt,et al, Acta Mater. 50 (9) (2002)  2209-2222.
$ 2T         La-Fe-O:
REF9         E. Povoden,A.N. Grundy,et al. J. Phase Equilib. Diff. 30 (2009) 351
REF10  A.N. Grundy, M. Chen, B. Hallstedt, L.J. Gauckler, J. Phase Equilib. . Diff. 26
(2005) 131. (La-Mn-O)
REF11        A.N. Grundy, B. Hallstedt, L.J. Gauckler, J Phase Equilib 24 (2003) 21-39. (Mn-
O)
REF12        A.N. Grundy, B. Hallstedt, L.J. Gauckler, J Phase Equilib. Diff. 25 (2004) 311-
319. (Sr-Mn-O)
REF13        H. Yokokawa, T. Kawada, M. Dokiya, J. Am.Ceram. Soc. 72 (1989) 2104-2110.
$ 4T         Sr-Fe-O:
```

```
REF14         E. Povoden unpublished results.
$ 2Q          La-Sr-Fe-O:
REF15         E. Povoden unpublished results.
$ 3T          La-Co-O
$ 5T          Sr-Co-O
$ 6T          Fe-Co-O
$ 1Q          La-Sr-Co-O
$ 3Q          Sr-Co-Fe-O
$ 4Q          La-Co-Fe-O   #
$ 1W          La-Sr-Co-Fe-O
REF16         This work
REF17  S.G.T.E. Thermodynamic Properties of Inorganic Materials, volume 19 of Landolt-
Börnstein New Series, Group IV. Springer, Verlag Berlin Heidelberg, (1999).
REF18         J.R. Taylor, A.T. Dinsdale, Z. Metallkd. 84 (1993) 335-345.
 !
```

Appendix B

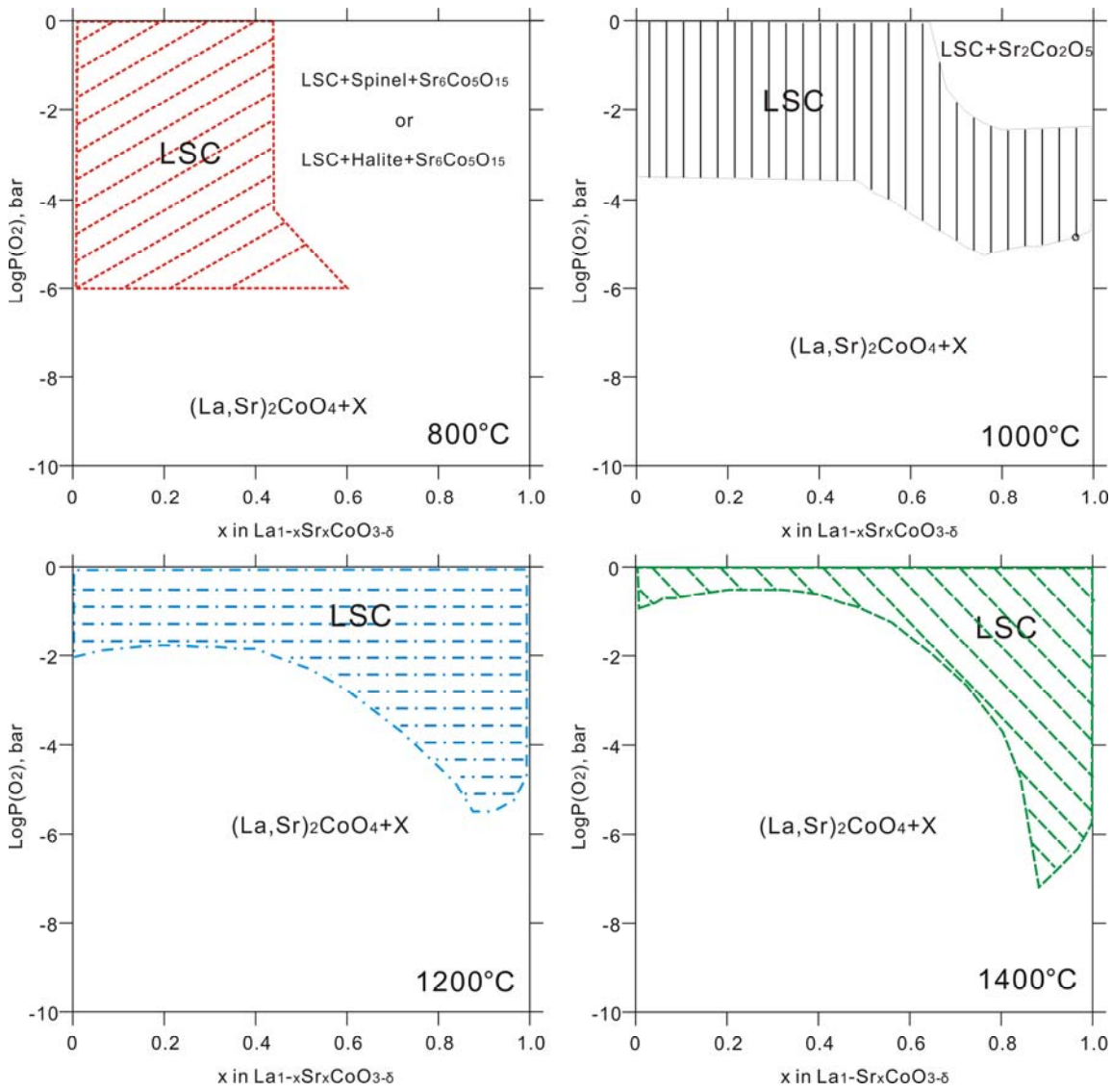

Fig. B.1. Calculated stability diagram ("stability window") for LSC at different temperatures.